

In compliance with the
Canadian Privacy Legislation
some supporting forms
may have been removed from
this dissertation.

While these forms may be included
in the document page count,
their removal does not represent
any loss of content from the dissertation.

STUDIES OF MAGNETISM IN
RHENIUM AND MANGANESE BASED PEROVSKITE
OXIDES

By

CHRISTOPHER RYAN WIEBE, B. Sc., M. Sc.

A Thesis

Submitted to the School of Graduate Studies

In Partial Fulfilment of the Requirements

For the Degree

Doctor of Philosophy

McMaster University

@ Copyright by Christopher Ryan Wiebe, November 2002

**MAGNETISM IN RHENIUM AND MANGANESE BASED
PEROVSKITE OXIDES**

DOCTOR OF PHILOSOPHY (2002) McMaster University
(Physics) Hamilton, ON

TITLE: Studies of Magnetism in Rhenium and Manganese Based
Perovskite Oxides

AUTHOR: Christopher Ryan Wiebe,
B. Sc. (University of Winnipeg), M. Sc. (McMaster University)

SUPERVISOR: Professor John E. Greedan

NUMBER OF PAGES: xvii, 207

Abstract

The bulk of this thesis consists of studies of geometric frustration in $S = \frac{1}{2}$ FCC perovskites based upon the chemical formula A_2BReO_6 . The magnetism of these materials is expected to exhibit geometric frustration, a situation in which the ideal spin arrangements cannot be achieved for antiferromagnetic interactions between adjacent spins. It is proposed that subtle quantum effects are driving these systems to unique ground states in the absence of chemical disorder. Both compounds Sr_2CaReO_6 and Sr_2MgReO_6 exhibit spin glass behaviour at low temperatures ($T_G \sim 14$ K and $T_G \sim 50$ K respectively), in which the magnetic moments freeze out in random orientations instead of an ordered array. This work shows that these materials possess several unconventional properties, which suggest that interesting spin dynamics may be present.

Other perovskite and perovskite-related materials studied in this thesis include the magnetoresistive $CaMnO_{3-\delta}$ and the "pillared" material $La_5Re_3MnO_{16}$. Neutron diffraction studies have shown that both $CaMnO_{2.94}$ and $CaMnO_{2.89}$ order at $T_N \sim 125$ K, but possess unique yet related magnetic structures. $CaMnO_{2.94}$ orders into a simple G-type magnetic structure, as observed in the compound $CaMnO_3$. The slightly more doped sample $CaMnO_{2.89}$, on the other hand, orders into a magnetic structure related to the G-type, and involves a Mn^{3+}/Mn^{4+} charge ordering over every four lattice spacings.

The new material $La_5Re_3MnO_{16}$ consists of layers of corner shared ReO_6 and MnO_6 octahedra that are separated by layers of Re_2O_{10} dimer units. Metal-metal bonding involving Re atoms have been postulated for these dimers which separate the Re/Mn layers by approximately 10 Å. The magnetic behaviour exhibited by this new class of materials is rich and complex. Despite the large distances separating the perovskite layers, the Re and Mn magnetic moments order into a ferrimagnetic $Q = (0, 0, \frac{1}{2})$ structure below a relatively high T_N of 161 K. There may be an additional spin rearrangement at lower temperatures as evidenced by weak magnetic Bragg peaks below ~ 50 K.

Acknowledgements

I would first like to thank my supervisor, Dr. John E. Greedan, for taking a chance with a physicist in a solid state chemistry laboratory. His knowledge and intuition as a scientist were inspiring for me in many ways.

I would also like to thank the other members of my supervisory committee, Dr. Bruce Gaulin, Dr. Malcolm Collins, and Dr. Graeme Luke. They were all excellent resources to draw upon during my years at McMaster, and above all the best that one could hope for in colleagues and friends. I would like to particularly thank Bruce for his gentle encouragings to continue my graduate studies, and the words of wisdom he gave during the long battle towards the end of my PhD.

The names of people that have helped me along the way would fill an entire thesis itself, but I will try to list some of them here. To my colleagues in the lab over the years, Craig Bridges, Rob Lam, Mario Bieringer, Andrew Wills, Hyunsoo Park, Athena Safa-Sefat, Jim Garrett, Jim Britten, Bruce Collier, Hanna Dabkowska, Anton Dabkowski and many others I have missed, I thank you sincerely for everything. In the physics department, Mike Dunlavy, Roby Austin, Paul Dube, Marcy Lumsden, Mike Lewis, Joost van Duijn, Josie Lee, Pat Byrne, Daniel Knapp, and others too numerous to list, I thank you for your camaraderie. Life at McMaster wouldn't have been the same without you. I also could not have survived without the secretaries, Wendy Malarek, Rosemary McNeice, Anne Taylor, Cheryl Johnston, and Daphne Kilgour who weathered my little crises with ease over the years.

I would like to thank Michelle Arnold for showing me the path, as difficult as it may be sometimes. May you always find happiness and the best in life.

My closest friends, Anton North, Derek and Kathryn Smyk, Aaron Wells, Stuart Allison, and David de Jong - words cannot describe the journeys we have taken with each other. I am a better person for having known you all.

To my dearest Angela, who has shown me what true love, courage, and passion is

all about, thank you. You have been the beacon I have been moving towards all these years without even knowing it myself. I love you with all of my heart.

Last, but not the least, I must credit what I have done in these pages to my family, who have been the foundation of who I am as a person and everything I do. I am blessed by all of their support over their years, and it is their love that has made this possible. Thank you for believing in me Mom, Dad, and Amber. This is for you.

Table of Contents

Chapter 1: Introduction.....	1
Outline of thesis.....	1
The Perovskite Structure.....	3
Magnetism.....	5
Magnetic Transitions.....	11
Magnetic Ground States.....	13
Magnetoresistance.....	16
Low Dimensional Perovskite-Based Materials.....	19
FCC Perovskites.....	22
Geometric Frustration.....	26
References.....	32
Chapter 2: Experimental Techniques.....	35
Basics of Diffraction.....	35
Elastic Scattering and Bragg's Law.....	37
Powder Diffraction Formulism.....	42
X-ray Diffraction.....	44
Neutron Diffraction.....	46
Magnetic Neutron Diffraction.....	50
The Rietveld Method.....	53
Oxidation State Analysis.....	56
DC Magnetic Susceptibility.....	57
Heat Capacity Measurements.....	62
μ SR Experiments.....	68
References.....	74

Chapter 3: Charge and Magnetic Ordering in the Electron-Doped Magnetoresistive	
Materials $\text{CaMnO}_{3-\delta}$ ($\delta = 0.06, 0.11$).....	76
Abstract.....	77
Introduction.....	78
Experimental Procedures.....	79
Results.....	80
Structure of $\text{CaMnO}_{2.94}$	80
Structure of $\text{CaMnO}_{2.89}$	83
Magnetism in $\text{CaMnO}_{2.94}$	87
Magnetism in $\text{CaMnO}_{2.89}$	92
Discussion.....	93
Conclusions.....	95
Acknowledgements.....	96
References.....	96
Chapter 4: Synthesis, Structure, and Magnetic Behaviour of $\text{La}_5\text{Re}_3\text{MnO}_{16}$: A New-	
Perovskite-Like Material.....	98
Abstract.....	99
Introduction.....	100
Experimental.....	100
Preparation of $\text{La}_5\text{Re}_3\text{MnO}_{16}$	100
Magnetic Measurements.....	101
X-ray Powder Diffraction.....	101
Results and Discussion.....	102
Crystal Structure.....	102
Magnetism in $\text{La}_5\text{Re}_3\text{MnO}_{16}$	114
Acknowledgements.....	120
References.....	120
Appendix: Magnetic Structure of $\text{La}_5\text{Re}_3\text{MnO}_{16}$	121

Experimental.....	121
Preparation of $\text{La}_5\text{Re}_3\text{MnO}_{16}$	121
X-ray Diffraction.....	121
Neutron Diffraction.....	121
Results and Discussion.....	122
X-ray Diffraction.....	122
Crystal Structure.....	122
Magnetic Structure.....	126
Future Work.....	132
Acknowledgements.....	134
References.....	135
Chapter 5: Spin Glass Behaviour in the $S=1/2$ FCC Ordered Perovskite	
$\text{Sr}_2\text{CaReO}_6$	136
Abstract.....	137
Introduction.....	138
Experimental Procedures.....	139
Results and Discussion.....	141
Part A: Crystal Structure.....	141
Part B: Magnetic Susceptibility Experiments.....	149
Part C: μSR Experiments.....	155
Part D: Heat Capacity Measurements.....	158
Conclusions.....	165
Acknowledgements.....	165
References.....	166
Chapter 6: Frustration-driven Spin Freezing in the $S=1/2$ FCC Perovskite	
$\text{Sr}_2\text{MgReO}_6$	169
Abstract.....	170

Introduction.....	171
Experimental Procedures.....	173
Results and Discussion.....	174
Part A: Crystal Structure.....	174
Part B: Magnetic Susceptibility Experiments and Neutron Diffraction.....	184
Part C: μ SR Experiments.....	191
Part D: Heat Capacity Measurements.....	197
Conclusions.....	202
Acknowledgements.....	202
References.....	203
Chapter 7: Conclusions.....	205

List of Figures

Chapter 1

Figure I: The idealized perovskite structure, as shown for SrTiO_3	3
Figure II: Direct exchange between magnetic species for J positive.....	6
Figure III: Super exchange for $\text{Mn}^{3+}\text{-O-Mn}^{3+}$ with a 180° bonding angle and an octahedral crystal field on the Mn sites.....	7
Figure IV: Double exchange for $\text{Mn}^{3+}\text{-O-Mn}^{4+}$ with a 180° bonding angle and an octahedral crystal field on the Mn sites.....	8
Figure V: Examples of Magnetic Ordering.....	14
Figure VI: Various ordered states for the system $\text{La}_{1-x}\text{Ca}_x\text{MnO}_3$	15
Figure VII: Phase diagram of the $\text{La}_{1-x}\text{Ca}_x\text{MnO}_3$ system.....	18
Figure VIII : The MR as a function of temperature for the series $\text{CaMnO}_{3-\delta}$ in an applied field of 5 T.....	19
Figure IX: The Ruddlesden-Popper phases for the system $\text{Ca}_{n+1}\text{Mn}_n\text{O}_{3n+1}$	20
Figure X: The crystal structure of $\text{La}_5\text{Re}_3\text{MnO}_{16}$ in the ac-plane.....	21
Figure XI: Antiferromagnetic orderings of the first, second, and third kinds as predicted by mean field theory.....	24
Figure XII: Geometric Frustration on Triangular Plaquettes.....	26
Figure XIII: Types of frustrated lattices consisting of triangular networks.....	27
Figure XIV: Exotic magnetic ground states shown upon triangular lattices.....	31

Chapter 2

Figure I: A representation of Bragg's law for lattice spacing d.....	38
Figure II: Ewald's sphere representation in 2D.....	39
Figure III: Transmission geometry powder diffraction.....	40
Figure IV: X-ray powder diffraction pattern for silicon.....	41

Figure V: Neutron and x-ray scattering coherent scattering lengths.....	43
Figure VI: X-ray transitions for Cu and Mo radiation.....	44
Figure VII: Maxwell distribution of speeds.....	47
Figure VIII: Scattering geometry for neutron scattering experiments.....	48
Figure IX: The Inverse Susceptibility for various kinds of magnetic behaviour.....	58
Figure X: Diagram of a RF SQUID system.....	60
Figure XI: Response of the SQUID to a paramagnetic sample.....	61
Figure XII: The Temperature (T) and Power (P) dependence as a function of time for an adiabatic calorimeter.....	65
Figure XIII: The Temperature (T) and Power (P) dependence as a function of time for the relaxation method.....	66
Figure XIV: Sample mount for the Oxford Instruments Heat Capacity probe...	67
Figure XV: TF- μ SR.....	70
Figure XVI: ZF- μ SR.....	71
Figure XVII: The Kubo-Toyabe lineshape, dynamic fluctuation spectra, and typical spin glass lineshape.....	73

Chapter 3

Figure I: The crystal structure of $\text{CaMnO}_{2.94}$	82
Figure II: (a) The neutron diffraction pattern of $\text{CaMnO}_{2.94}$ at $T = 14$ K and $T = 130$ K.....	84
Figure II: (b) The neutron diffraction pattern of $\text{CaMnO}_{2.89}$ at $T = 11$ K and $T = 130$ K.....	85
Figure III: Evidence of possible vacancy ordering in $\text{CaMnO}_{2.89}$	86
Figure IV: The magnetic susceptibility of $\text{CaMnO}_{2.94}$ (top) and $\text{CaMnO}_{2.89}$ (bottom) for an applied field of $H = 0.01$ T.....	89
Figure V: The magnetic structure of $\text{CaMnO}_{2.94}$ (G-type structure, on the left) and $\text{CaMnO}_{2.89}$ (G-type charge-ordered structure).....	90
Figure VI: The ordered moment as a function of temperature for	

CaMnO _{2.94} (top) and CaMnO _{2.89} (bottom).....	91
---	----

Chapter 4

Figure I: Projection along [0 0 1].....	105
Figure II: Projection along [0 1 0].....	106
Figure III: Projection along [1 0 0] indicating where the mirror planes occur for the space group C2/m.....	108
Figure IV: The Re-Re bioctahedra.....	109
Figure V: The magnetic susceptibility as a function of temperature for an applied field of 0.05 T.....	115
Figure VI: The high temperature magnetic susceptibility as a function of temperature for an applied field of 0.05 T.....	116
Figure VII: Magnetization as a function of applied field for 5 K, 60 K and 120 K.....	118
Figure VIII: Rietveld refinement of the 250K neutron diffraction data for La ₅ Re ₃ MnO ₁₆	125
Figure IX: Low angle neutron diffraction data for La ₅ Re ₃ MnO ₁₆	128
Figure X: The temperature dependence of the strongest magnetic reflections belonging to the $k = (0\ 0\ \frac{1}{2})$ magnetic structure along with an additional weak reflection indexed with $k = (\frac{1}{2}\ \frac{1}{2}\ \frac{1}{2})$	129
Figure XI: Simultaneous crystal structure/magnetic structure Rietveld refinement of the 10 K data for La ₅ Re ₃ MnO ₁₆	130
Figure XII: The refined magnetic structure for La ₅ Re ₃ MnO ₁₆	131
Figure XIII: Possible magnetic frustration in La ₅ Re ₃ MgO ₁₆	134

Chapter 5

Figure I: Powder neutron diffraction refinements of Sr ₂ CaReO ₆ at T = 4 K with $\lambda = 1.3284(2)$ Å neutrons.....	142
Figure II: The crystal structure of Sr ₂ CaReO ₆ as viewed from the ab plane	

at T = 4 K.....	146
Figure III: The crystal structure of Sr ₂ CaReO ₆ as viewed from the ac plane....	147
Figure IV: The ordered Re ions in the FCC-based lattice.....	148
Figure V: DC magnetic susceptibility results for powder Sr ₂ CaReO ₆ samples.	150
Figure VI: Powder neutron diffraction profiles at T = 4 K and T = 40 K with $\lambda = 2.3688(3)$ Å.....	153
Figure VII: DC magnetization measurements as a function of field for T = 5 K, T = 25 K and T = 40 K.....	154
Figure VIII: ZF μ SR measurements of Sr ₂ CaReO ₆ at T = 2.5 K, 12.5 K, 17.5 K, and 28 K.....	156
Figure IX: The heat capacity of Sr ₂ CaReO ₆ at H = 0 T and H = 6 T, the heat capacity of the lattice model compound Sr ₂ CaWO ₆ at H = 0 T, and the calculated lattice heat capacity of Sr ₂ CaReO ₆ based upon the model material.....	160
Figure X: The magnetic heat capacity of Sr ₂ CaReO ₆ calculated by subtracting the lattice component.....	161
Figure XI: The magnetic heat capacity of Sr ₂ CaReO ₆ as a function of T ³	163

Chapter 6

Figure I: Powder x-ray diffraction refinements of Sr ₂ MgReO ₆ at T = 298 K with Cu K α radiation.....	176
Figure II: Powder neutron diffraction refinements of Sr ₂ MgReO ₆ at T = 6 K with $\lambda = 1.3285(3)$ Å	177
Figure III: Powder neutron diffraction refinements of Sr ₂ MgReO ₆ at T = 298 K with $\lambda = 1.3285(3)$ Å.....	178
Figure IV: The crystal structure of Sr ₂ MgReO ₆ as viewed from the ac plane...	179
Figure V: The crystal structure of Sr ₂ MgReO ₆ as viewed from the ab plane....	180
Figure VI: The FCC ordered sublattice of Sr ₂ MgReO ₆	181

Figure VII: DC magnetization measurements as a function of temperature.....	185
Figure VIII: DC magnetic susceptibility runs for $H = 100$ G, 500 G and 1000 G.....	186
Figure IX: The magnetic susceptibility taken with the RSO mode, clearly showing the FC/ZFC divergence at ~ 175 K.....	187
Figure X: Powder neutron diffraction scans taken at 6 K and 298 K with $\lambda = 1.3285(3)$ Å.....	188
Figure XI: Magnetic hysteresis runs at 5K and 250 K.....	191
Figure XII: LF- μ SR data as a function of temperature.....	192
Figure XIII: LF- μ SR runs as a function of field at $T = 5$ K.....	194
Figure XIV: The fluctuation rate as a function of temperature, indicating moment freezing below T_G	195
Figure XV: The heat capacity as a function of temperature and field for $\text{Sr}_2\text{MgReO}_6$	198
Figure XVI: The main graph is the scaled lattice component plotted with the raw data, suggesting that a weak magnetic component is present.....	199
Figure XVII: The magnetic specific heat, as determined by a subtraction of the lattice portion calculated from Figure XVI.....	200

List of Tables

Chapter 1

Table I: The positions for the idealized perovskite structure in space group $Pm\bar{3}m$	4
Table II: Ordering of magnetic models as a function of d and D.....	12
Table III: Exchange Interactions in Face-Centered Cubic Antiferromagnets.....	25
Table IV: Properties of Strongly Frustrated Geometric Antiferromagnets.....	28

Chapter 2

Chapter 3

Table I. Room temperature lattice parameters and magnetic properties of $\text{CaMnO}_{3-\delta}$	81
Table II. Refined Atomic Positions and Their Estimated Standard Deviations at T = 11 K ($\text{CaMnO}_{2.89}$) and T = 14 K ($\text{CaMnO}_{2.94}$).....	81
Table III. Selected Interatomic Distances and Bond Angles.....	87

Chapter 4

Table I: Experimental Data and Structural Refinement Parameters for $\text{La}_5\text{Re}_3\text{MnO}_{16}$	103
Table II: Refined Atomic Positions and Their Estimated Standard Deviations.....	104
Table III: Selected Interatomic Distances.....	111
Table IV: Selected Bond Angles.....	112
Table V: Results from VaList Bond Valence Calculation.....	113
Table VI: Positional parameters refined from powder neutron diffraction data for $\text{La}_5\text{Re}_3\text{MnO}_{16}$ for 10 K and 250 K.....	123

Table VII: Cell parameters, magnetic moments and agreement indices for $\text{La}_5\text{Re}_3\text{MnO}_{16}$ for 10 K and 250 K.....	124
Table VIII: Néel temperatures for the series $\text{La}_5\text{Re}_3\text{XO}_{16}$ (X = Fe, Co, Ni)....	133

Chapter 5

Table I: Lattice parameters for $\text{Sr}_2\text{CaReO}_6$ at 4 K (short wavelength neutron data) and 295 K (x-ray data) as determined by powder diffraction.....	143
Table II: Refined lattice positions and temperature factors for $\text{Sr}_2\text{CaReO}_6$ ($\lambda = 1.3284(2)$ Å) at 4 K.....	143
Table III: Bond distances and angles for $\text{Sr}_2\text{CaReO}_6$ at T = 4 K and T = 20 K as determined by powder neutron diffraction (short wavelength).....	145

Chapter 6

Table I: Lattice parameters for $\text{Sr}_2\text{MgReO}_6$ at 6 K (neutron data) and 295 K (neutron and x-ray data) as determined by powder diffraction.....	177
Table II: Refined lattice positions and temperature factors for $\text{Sr}_2\text{MgReO}_6$ ($\lambda = 1.3285(3)$ Å) at 6 K.....	182
Table III: Bond distances and angles for $\text{Sr}_2\text{MgReO}_6$ at T = 6 K and T = 298 K as determined by powder neutron diffraction.....	183

For My Parents

Chapter One

Introduction

Outline of thesis

Transition metal oxides occupy a realm of condensed matter physics which is arguably the most extensive to date.¹ The wide variety of properties exhibited by these materials, from high- T_C superconductivity² to magnetoresistance phenomena³ to magnetic frustration⁴, has provided a fruitful arena for investigation. The bulk properties of these materials are all governed by the electronic configuration of the d elements, which, when combined with the geometry of the lattice, give rise to these varied sets of magnetic ground states. The rich nature of the d-block elements has granted chemists the power to design materials with novel and unusual properties.⁵

In particular, the perovskite structure can accommodate many transition metal ions. The ubiquitous nature of these materials is due to the remarkable stability of the perovskite framework. It should be no surprise then, that perovskites, and materials related to them, have provided entire series of technologically and theoretically important systems of study.

The general theme of this thesis is the study of the magnetic properties of new transition metal oxides. More specifically, it centres on the study of perovskite oxides containing manganese and rhenium. Manganese is of interest as a magnetic species due to the wide range of stable oxidation states observed. This provides a way to finely tune materials to exhibit new magnetic phenomena through doping or the creation of defects that slightly alter the populations of oxidation states. Rhenium, on the other hand, has only a few stable oxidation states, and the list of known rhenium oxides is dwarfed by the manganese oxides in comparison. The search for new materials and the synthesis methods needed to create them is a focus of current activity driven by recent discoveries such as the half-metallic $\text{Sr}_2\text{FeReO}_6$ ⁶ and the superconducting pyrochlore $\text{Cd}_2\text{Re}_2\text{O}_7$.⁷

The structure of this thesis will be as follows. Chapter one will briefly describe perovskites, their magnetic properties, phase transitions, and magnetic ground states. Chapter two will introduce the reader to the experimental methods used to study these materials by the author. The remaining chapters will be the thesis proper, where the published works of the author are presented. The electron-doped magnetoresistive materials $\text{CaMnO}_{3.8}$ are investigated by neutron diffraction with convincing evidence that a new charge-ordered structure is seen for the moderately doped phase.⁸ The crystal⁹ and magnetic structure¹⁰ of the pillared perovskite $\text{La}_5\text{Re}_3\text{MnO}_{16}$ is presented, which is the first in a new series of materials that exhibit metal-metal bonding within a layered network. The remainder of the thesis presents the detailed study of the frustrated materials Sr_2XReO_6 ($X = \text{Ca}$,¹¹ Mg ¹²), which form unconventional spin-glass ground states. The thesis is completed with some closing remarks.

The Perovskite Structure

The ideal perovskite structure, denoted by the chemical formula ABO_3 , is cubic and of space group $Pm\bar{3}m$ (see figure I). A common description of the structure is that of a framework of corner-shared BO_6 octahedra, with the A cations occupying the interstices, which are 12-fold coordinate.¹³ Both the A and B atoms form a cubic close packed array. All of the atoms in the structure lie at special positions (table I).

Figure I: The idealized perovskite structure, as shown for $SrTiO_3$. ($a = 3.90 \text{ \AA}$)

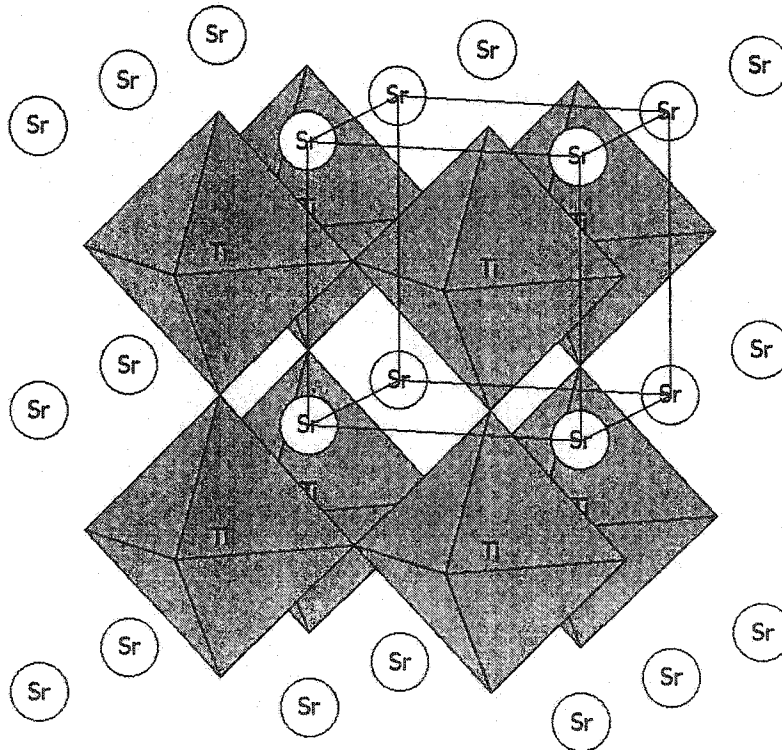


Table I: The positions for the idealized perovskite structure in space group $Pm\bar{3}m$

	Site	Wyckoff symmetry
A	0, 0, 0	1a
B	0.5, 0.5, 0.5	1b
X	0.5, 0.5, 0; 0.5, 0, 0.5; 0, 0.5, 0.5	3c

Various distortions away from cubic symmetry are possible. There are three different hettotypes, or distortions, which have been identified: distortions of the BO_6 octahedra, B-cation displacements, and tilting of the BO_6 octahedra. The latter is the most common type of distortion, resulting in structures of lower symmetries. Glazer,¹⁴ and recently Woodward,¹⁵ have developed various systems to describe such distortions and the space groups associated with them. The dominant driving forces beyond such transformations are the size and charge differences on the A and B sites.

One can define a tolerance factor¹³ which characterizes the stability of the perovskite structure as a function of A and B cation sizes and the oxygen crystalline radius

$$(1) \quad t = \frac{r_A + r_O}{\sqrt{2}(r_B + r_O)}$$

Goldschmidt¹⁶ was the first to discover that perovskites are stable within the range $0.8 \leq t \leq 1$. Otherwise, other phases such as the hexagonal structures of the formula ABO_3 are more stable. The most stable perovskites are those in which the A sites have larger radii than the B sites. If these ratios are not ideal, distortions away from cubic symmetry are noted.

Magnetism

Magnetism, it has been observed, is “the oldest and greatest mystery of solids, [and] ... one of the most difficult to explain.”¹⁷ Since antiquity, the Greeks knew that lodestone, $\text{FeO-Fe}_2\text{O}_3$, attracted iron, but it wasn't until much later that magnets were used for practical purposes such as in the manufacture of crude compasses.¹⁸ Some of the first studies in phase transitions were made with iron, with Gilbert¹⁷ (1600) noticing that one can “apply a red-hot iron rod to a magnetized needle and the needle stands still, not turning to the iron; but as soon as the temperature has fallen somewhat it at once turns to it.”

Physicists now know that the origin of magnetism in magnetic insulators is due to unpaired electrons on the constituent atoms.¹⁹ The Pauli principle dictates that no two electrons may occupy a given orbital unless their spins are paired. This pairing argument determines the electronic structure of atoms, and the number of electrons within a given oxidation state which will be unpaired. These electrons form magnetic dipoles which interact only very weakly with one another, as the interaction energy is related to the distance as $1/r^3$ via the following relation:²⁰

$$(2) \quad U = \frac{1}{r^3} \left\{ \bar{m}_i \cdot \bar{m}_j - 3(\bar{m}_i \cdot \hat{r}_{ij})(\bar{m}_j \cdot \hat{r}_{ij}) \right\}$$

where \bar{m}_i and \bar{m}_j are the magnetic dipoles vectors and \hat{r}_{ij} is a unit vector in the direction of the shortest distance from i to j . This equation, which has a maximum magnitude when $\bar{m}_i // \bar{m}_j$ has an energy scale U :

$$(3) \quad U \sim \frac{1}{r^3} (g\mu_B)^2 \sim \frac{1}{r^3} \left(\frac{eh}{2\pi mc} \right)^2$$

U has a value of about 1 meV, or a temperature on the order of 1 K, for moments

that are $\sim 2 \text{ \AA}$ apart. It is clear then that the classical explanation for magnetism is inadequate for describing phase transitions of typical magnetic insulators, let alone for materials such as iron which has a transition at well over 1000 K. The answer to this problem came with the advent of quantum mechanics in the 20th century. Physicists now understand magnetism in terms of exchange interactions between electronic orbitals. This is often expressed as

$$(4) \quad H = -J \sum_{ij} \bar{s}_i \cdot \bar{s}_j$$

where \bar{s}_i and \bar{s}_j are the values for the spin of two electrons, and J is known as the exchange integral. For J positive, the system prefers a ferromagnetic interaction between the two electrons. For J negative, an antiferromagnetic interaction is dominant, which minimizes the energy of the system (see figure II).

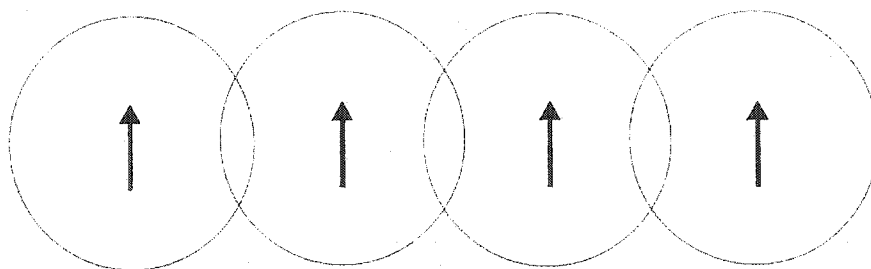


Figure II: Direct exchange between magnetic species for J positive. Orbital overlap between the magnetic species leads to a ferromagnetic interaction.

The type of interaction described above is known as direct exchange. For magnetic insulators, one would expect a superexchange process to be dominant, as is the case for transition metal oxides. In these instances, a diamagnetic oxygen atom resides between two transition metal cations, mediating the exchange (see figure III).

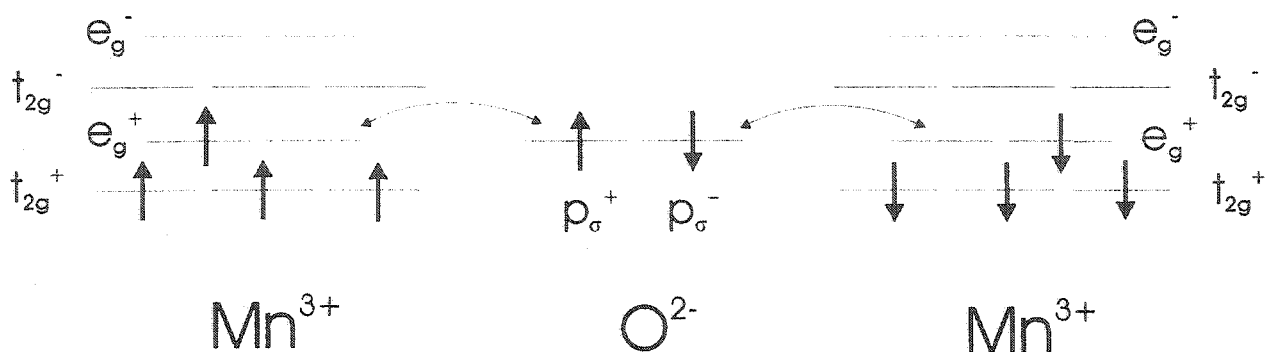


Figure III: Super exchange for $\text{Mn}^{3+}\text{-O-Mn}^{3+}$ with a 180° bonding angle and an octahedral crystal field on the Mn sites. The overlap between the manganese 3d orbitals and the oxygen 2p orbitals results in a net antiferromagnetic coupling between the sites (adapted from M. Bieringer²¹).

From the overlap of the transition metal d orbitals and the 2p orbitals on the oxygen atom, and the application of the Pauli principle, one can readily conclude that an antiferromagnetic alignment is energetically preferred. It should be noted that the bond angles here are 180° , and for angles of 90° for example, the exchange would be expected to be different (it is ferromagnetic in the general case). A proper treatment of the magnetic exchange interaction among atomic species would be to consult the Goodenough-Kanamori rules.²²

All of these arguments have been made assuming that there are identical transition metal species on either side of the ligand. One can also have the scenario where there are different atoms present, such as the $\text{Mn}^{3+}\text{-O-Mn}^{4+}$ array (see figure IV below).

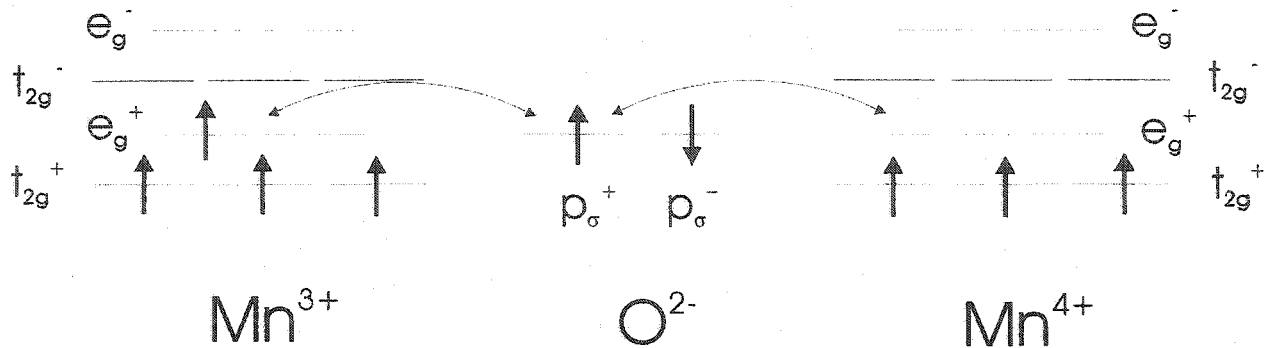


Figure IV: Double exchange for $\text{Mn}^{3+}\text{-O-Mn}^{4+}$ with a 180° bonding angle and an octahedral crystal field on the Mn sites. The overlap between the manganese 3d orbitals and the oxygen 2p orbitals results in a net ferromagnetic coupling between the sites (adapted from M. Bieringer²¹).

This double exchange mechanism gives rise to a ferromagnetic alignment between the two magnetic species. This is important for an understanding of ferromagnetic impurities in materials (which may be due to defects, for example, which results in a variance of oxidation states within a sample), and magnetoresistance in manganates, which will be discussed later in this chapter.

There is a third type of exchange process which usually occurs with less extended electron orbitals, such as partially filled f-electron shells. This is known as indirect exchange, with a simple example being the RKKY (Ruderman-Kittel-Kosuda-Yosida) interaction.²³ In this case, the exchange process is governed by the conduction electrons which interact with the f electrons. However, this mechanism is rarely seen beyond the rare earth materials.

A common method to determine the magnitude of the magnetic interactions within a solid is to measure the magnetic susceptibility. If one is in a temperature regime $k_B T$ which is much higher than the interaction energy between the constituent magnetic moments, one would expect the Curie-Weiss law to be applicable:

$$(5) \quad \chi = \frac{C}{T - \theta} + \alpha$$

Where C is known as the Curie constant, θ is known as the Weiss constant, T is the temperature, and α is a temperature independent term. One can derive this equation using simple statistical mechanics arguments to obtain:²⁴

$$(6) \quad \chi = \frac{Ng^2J(J+1)\mu_B^2}{3k_B(T - \theta)} + \alpha$$

Where N is Avogadro's number, μ_B is a constant known as the Bohr magneton, J is the total angular momentum quantum number (not to be confused with the exchange constant, J), and g is the Landé factor. In this interpretation, the Weiss constant θ is the interaction energy between the magnetic moments. This sets the energy scale for which the Curie-Weiss law is applicable. Above these temperatures, the material is paramagnetic, a state in which the moments are fluctuating. Below this temperature, one would expect this law to break down, as the magnetic interaction energies become comparable to thermal fluctuations. For positive values of θ , the dominant interactions are ferromagnetic and for negative, antiferromagnetic.

It is worth noting at this point that the magnetic susceptibility is assumed to be positive in the above argument, which is expected for unpaired electrons. If the electrons are paired, one would expect the susceptibility to be negative, and the material is said to be diamagnetic. A crude explanation of this effect is that the electrons form orbits that act as shielding currents, and therefore the material obtains a small moment that tends to align itself against an applied field.

From equation 1.6 above, one can equate the Curie constant to

$$(7) \quad C = \frac{Ng^2J(J+1)\mu_B^2}{3k_B}$$

And define an effective magnetic moment, μ_{eff} , to be

$$(8) \quad \mu_{\text{eff}} = g\sqrt{J(J+1)}\mu_B$$

This is not to be confused with the magnetic moment associated with an atom

$$(9) \quad \mu = gJ = g(L + 2S)$$

Where L is the orbital angular momentum and S is the spin angular momentum. Fortunately, for transition metal oxides, the orbital angular momentum is usually quenched due to crystal field effects, and only the net spin of the constituent electrons contributes to the magnetic moment. Thus we have

$$(10) \quad \mu_{\text{eff}} = g\sqrt{S(S+1)}\mu_B$$

$$(11) \quad \mu = 2gS$$

The Landé g factor for a free atom is defined as

$$(12) \quad g = 1 + \frac{J(J+1) + S(S+1) - L(L+1)}{2J(J+1)}$$

With $L = 0$ and $J = S$, this equation essentially reduces to the g -factor for an electron, which is $2.0023193043737(82)$.²⁵ This celebrated value has been predicted to great precision using QED (quantum electrodynamics), a triumph of theoretical physics.

For most purposes, the value $g = 2$ can be used for the calculation of effective moments in magnetic insulators (with some exceptions due to such factors as incomplete quenching of the moments, hyperfine coupling, or relativistic effects).

Magnetic transitions

The Hamiltonian expressed above to describe interactions between magnetic atoms via exchange is a simplified case. The general Hamiltonian for a magnetic system, under the influence of a magnetic field h is:

$$(13) \quad H = -2 \sum_{\langle ij \rangle} J_{ij} (aS_i^z S_j^z + b(S_i^x S_j^x + S_i^y S_j^y)) - g\mu_B h \sum_i S_i$$

Where J_{ij} is the exchange constant, and the coefficients a and b are constants which depend on the dimensionality of moments, or the anisotropy of the system. This is distinct from the dimensionality of the system, d , which is purely a matter of crystallography. For $D = 1$, the spins are Ising-like, which only have one component ($a=1, b=0$). $D = 2$ is the XY-model ($a=0, b=1$), where spins can align in a plane, and $D = 3$ is the Heisenberg model, where the spins are isotropic ($a=b$). The dimensionality of the system, d , is determined by the exchange paths of the system, such as a linear chain ($d=1$), a planar structure ($d=2$), or a fully three dimensional network of interacting moments ($d=3$). Using this Hamiltonian, physicists have shown that magnetic phase transitions only exist in certain combinations of these two dimensionalities, as displayed in the table below.

		d = 1	d = 2	d = 3
Ising	D = 1	X	✓	✓
XY	D = 2	X	*	✓
Heisenburg	D = 3	X	X	✓

Table II: Ordering of magnetic models as a function of d and D .⁴ The “X” indicates no long range ordering, ✓ the presence of a long range ordered state at $T > 0$ K, and * is a special case. For the $D=2$ XY model in two dimensions, there is a phase transition to a low temperature ordered state with $\langle S \rangle = 0$. This is known as the Kosterlitz-Thouless transition²⁰, where spin configurations known as vortices form in pairs and stabilize the magnetic ground state.

The beauty of the study of magnetic systems is in the simplicity of the interactions between the moments. This is in stark contrast to, for example, the study of standard states of matter, where very complicated Hamiltonians are known to exist, such as for liquids. The quantum mechanical nature of exchange provides some simple Hamiltonians to solve.

Magnetic phase transitions have been studied intensely for this purpose over the last century. The concept of universality has been applied with great success in the modelling of these systems. Universality states that for a continuous phase transition, critical exponents can be calculated to describe the transition which are only based upon the dimensionality of the system, d , the dimensionality of the order parameter, D (or in the case of magnetic interactions, the anisotropy of the Hamiltonian), and whether the forces are of short or long range.²⁶ The designation between a discontinuous, or first-order phase transition, and second-order, or a continuous phase transition, is made by investigating the derivative of the free energy as a function of the state variables. If there is a discontinuity in the first derivative, the phase transition is first order; for a discontinuity in the second derivative, the transition is second order. The distinction is almost moot for magnetic systems, which are by and large second order due to symmetry.

Critical exponents describe how the state variables change as one approaches a transition. For magnetic systems, the following state variables and exponents are most relevant:

$$(14) \quad M \propto \left(\frac{T - T_C}{T_C} \right)^\beta$$

$$(15) \quad \chi \propto \left(\frac{T_C - T}{T_C} \right)^{-\gamma}$$

$$(16) \quad C_p \propto \left(\frac{T_C - T}{T_C} \right)^{-\alpha}$$

Where M , χ , and C_p are the magnetization, magnetic susceptibility, and the heat capacity, and α , β , and γ are known as critical exponents. The literature of phase transitions is replete with verifications of these exponents in magnetic systems.

Magnetic Ground States

In magnetic insulators, the nature of the exchange usually promotes antiferromagnetic interactions between the moments. The bulk of transition metal oxides, as a result, have ordered antiferromagnetic ground states below some Néel temperature T_N . However, some materials, such as the archetypical magnet Fe have ferromagnetic orderings at T_C (the Curie temperature). The distinction between these two lies with the observation of a spontaneous magnetic moment at low temperatures. Below the transition, the net moment of a true antiferromagnet is zero, whereas a ferromagnet is defined as when all the moments align in a particular direction. Solids which have spontaneous moments which do not satisfy this condition are known as ferrimagnets. In these cases, the net interactions between moments may be antiferromagnetic, but if there are different magnetic species, the moments may not

cancel and thus a residual moment may appear. A canted antiferromagnet is another example of weak ferrimagnetism, in which there is a component of ferromagnetic alignment due to a slight tilting of the ordered moments. Such situations arise among mixed valent materials and are often difficult to distinguish by neutron diffraction. Very complex incommensurate orderings, such as a helical arrangement of spins seen in rare earth metals like holmium, or spin density waves such as those seen in chromium have been observed but these are less common in transition metal oxides.

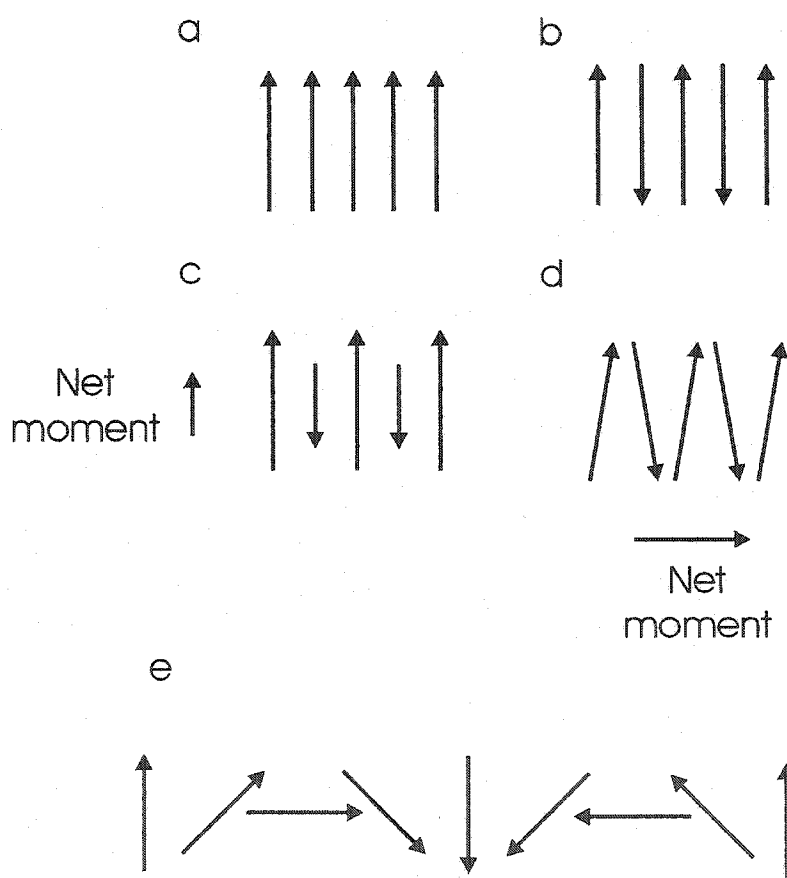


Figure V: Examples of Magnetic Ordering: (a) simple ferromagnetic ordering (b) simple antiferromagnetic ordering (c) ferromagnetic ordering (d) canted antiferromagnetism and (e) a spin density wave.

One of the first detailed magnetic structure determinations of the perovskites were made by Wollan and Koehler in their pioneering neutron scattering experiments on the manganate series $\text{La}_{1-x}\text{Ca}_x\text{MnO}_3$.²⁷ The observation of a change in the magnetic behaviour as a function of doping (and therefore the relative $\text{Mn}^{3+}/\text{Mn}^{4+}$ concentrations), from antiferromagnetic insulating through ferromagnetic metallic to finally ferromagnetic insulating ground states prompted a more detailed investigation of these. What was found was a rich and diverse set of magnetic orderings, some of them accompanied by charge ordering for certain doping levels. These are summarized in the table below:

LABEL	ONE OCTANT OF MAGNETIC UNIT CELL	IONS PER UNIT CELL				NEIGHBOR RELATIONS	RELATIVE NUMBER OF BONDS		
		$\text{Mn}^{3+} - \text{B}$	6	4	2		0	F	A
		$\text{Mn}^{4+} - \text{O}$	2	4	6		8		
A								4	2
B								6	
C		(C-E) STRUCTURE						2	4
D		(C-E) STRUCTURE				FOR C-E STRUCTURE		2	4
E						FOR D-E STRUCTURE		2	4
F						FOR D-F STRUCTURE		3	3
G		(D-E)	(D-F)					8	6

THESE CELLS REQUIRE DOUBLING IN THIS PLANE
HEAVY CIRCLES INDICATE CELL EDGE

Figure VI: Various ordered states for the system $\text{La}_{1-x}\text{Ca}_x\text{MnO}_3$

It was only later discovered that these materials exhibit magnetoresistive effects, which revitalized the field over the last ten years. There is still considerable effort devoted to how these magnetic structures are related to electrical properties of these systems.

Magnetoresistance

The recent surge of interest in the study of perovskite manganates has been due to a phenomena known as magnetoresistance. Formally, the definition of a magnetoresistant material is one that exhibits a significant change in the resistance with the application of an applied field H . The parameter which quantifies the magnetoresistive effect, MR, has been defined as:

$$(17) \quad MR(T,H) = \frac{\rho(T,0) - \rho(T,H)}{\rho(T,H)} \times 100\%$$

The drive to study these materials is for the most part technological, as they are used routinely in magnetic information storage devices or as magnetic field sensors. The above quantity, MR, is related to the efficiency of the device. Of course, small fields are preferred in these devices, which provides a great challenge to the solid state community to design new materials that exhibit large magnetoresistance in a small field range. The current material used as a magnetic sensor for hard drives is Permalloy, which has a MR of 2-3 % at room temperature for small magnetic fields.

Recently, attention has turned to the mixed-valent manganate perovskites, which display very large magnetoresistant effects. For example, $\text{Sr}_{0.05}\text{Ca}_{0.25}\text{Pr}_{0.7}\text{MnO}_{3-\delta}$ has a MR of 2.5×10^7 % at 85 K in an applied field of 5 T²⁸. The gigantic change in MR has led scientists to dub these as CMR, or “colossal magnetoresistant” oxides. These

materials have been finely tuned to have a delicate balance of Mn^{3+} and Mn^{4+} species which gives rise to the double exchange mechanism. The basic theory behind this was first elucidated by Zener²⁹ and de Gennes.³⁰ In simple terms, this mechanism can be understood as a delocalization of electrons in a $\text{Mn}^{3+}\text{-O-Mn}^{4+}$ array. The singly occupied e_g level of the high-spin Mn^{3+} state lies above the triply occupied t_{2g} level, and thus will hop from one site to the next if the spins are mutually aligned (see the double exchange interaction noted above). Thus, the mobility of the electrons is increased significantly if a magnetic field is applied to the system. This is a greatly simplified model, however, and a complete understanding is mired by such complications as the role of reduced dimensionality via layered variants of the perovskite structure³¹, and the interplay of charge and magnetic ordering³². Moreover, MR and CMR are found in some materials such as the Ruddlesden-Popper phases which do not involve this ferromagnetic interaction, and thus do not involve the double-exchange mechanism.

Despite the many years of interest in manganate perovskites, there is still a lack of understanding of the magnetoresistive phenomena. For example, for a broad range of doping, the system $\text{La}_{1-x}\text{Ca}_x\text{MnO}_3$ exhibits a ferromagnetic to paramagnetic transition that is only just now being understood (see figure VII).³³ In the ferromagnetic regime, there is colossal magnetoresistance which is as much as 100 000 % in thin films.³⁴ In bulk materials though, the best magnetoresistance is $\sim 35\%$ (for $0.15 < x < 0.50$) below T_C . Domain effects are now known to be very important, in which electrons crossing domain walls become minority spin electrons, and are scattered by Fermi surface effects. In the AFM range of doping levels, however, the mechanism is unknown, and magnetoresistance is seen in the presence of ordered antiferromagnetic domains which clearly cannot be explained by double exchange.

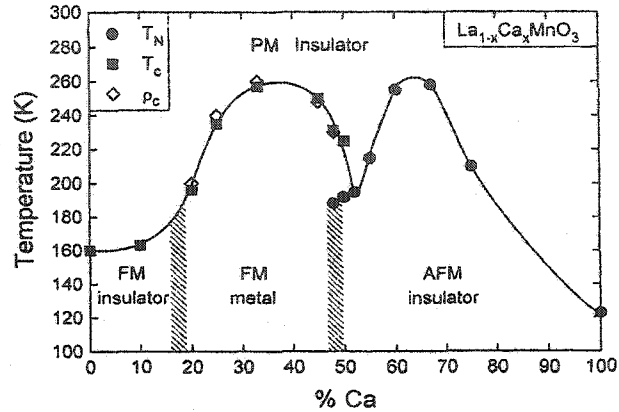


Figure VII: Phase diagram of the $\text{La}_{1-x}\text{Ca}_x\text{MnO}_3$ system (as determined by Schiffer³³ *et al*)

In contrast to the system $\text{La}_{1-x}\text{Ca}_x\text{MnO}_3$, in which the route to MR is obtained by hole doping, one can also electron dope these materials by starting with CaMnO_3 and creating oxygen defects. By this method, a large MR can be produced even in the presence of antiferromagnetic ordering (as much as 20 % for $\text{CaMnO}_{2.94}$ and 40 % for $\text{CaMnO}_{2.89}$ for $H = 5$ T at 20 K).³⁵ These materials have been studied for some time, and it has been found that there is oxygen vacancy ordering for some doping levels. However, it is only recently with the discovery of MR that they have been revisited and studied in more detail. In particular, the scenario of AFM ordering with the presence of MR provides a challenge for solid state physicists to describe within current theoretical frameworks. The work of Wollan and Koehler suggests that these materials should have the G-type AF ordering at temperatures close to $T_N \sim 130$ K, but detailed studies of the magnetic structure have been sparse up until now. Chapter three of this thesis details a new kind of charge ordering which is observed in the moderately doped $\text{CaMnO}_{2.89}$. The G-type structure is preserved with the addition of layers of ordered Mn^{3+} moments every 4 lattice spacings in the c-direction. This is in sharp contrast to $\text{CaMnO}_{2.94}$, which has the simple G-type structure as expected for CaMnO_3 .

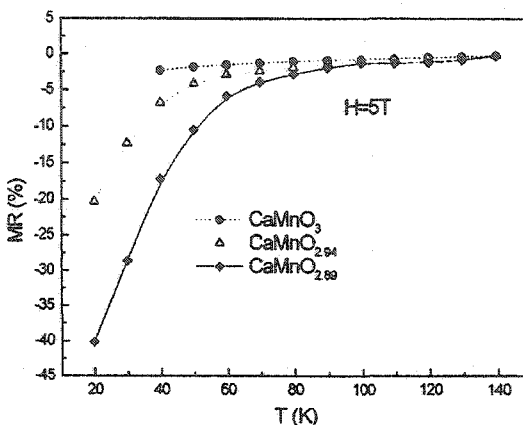


Figure VIII : The MR as a function of temperature for the series $\text{CaMnO}_{3-\delta}$ in an applied field of 5 T (from Zeng³⁵ *et al*).

Low Dimensional Perovskite-Based Materials

The search for new low dimensional materials with perovskite related structures has become a focal point for many research efforts due to the wide number of interesting systems observed. One of the best known examples is the high temperature superconductors, which by and large all have layered structures. The reduced dimensionality has been shown to be critical to an understanding of the condensation of the superconducting state. In the magnetoresistive community, layered materials such as the Ruddlesden-Popper phases $\text{Ca}_{n+1}\text{Mn}_n\text{O}_{3n+1}$ have relatively high MR values that are related to the 2D character of the Mn oxide planes.³¹ In particular, one of the more common theoretical arguments to describe these systems, the double exchange interaction, fails to provide an appropriate explanation for the observed behaviour. The search for new low dimensional systems, and in particular those of mixed valence, is an extremely active and changing field.

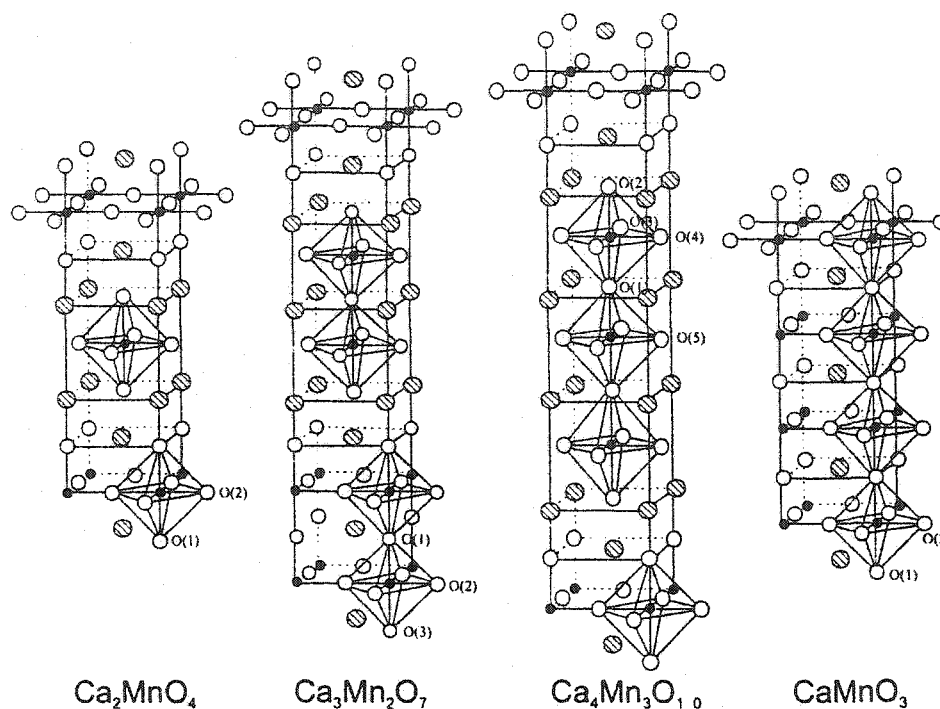
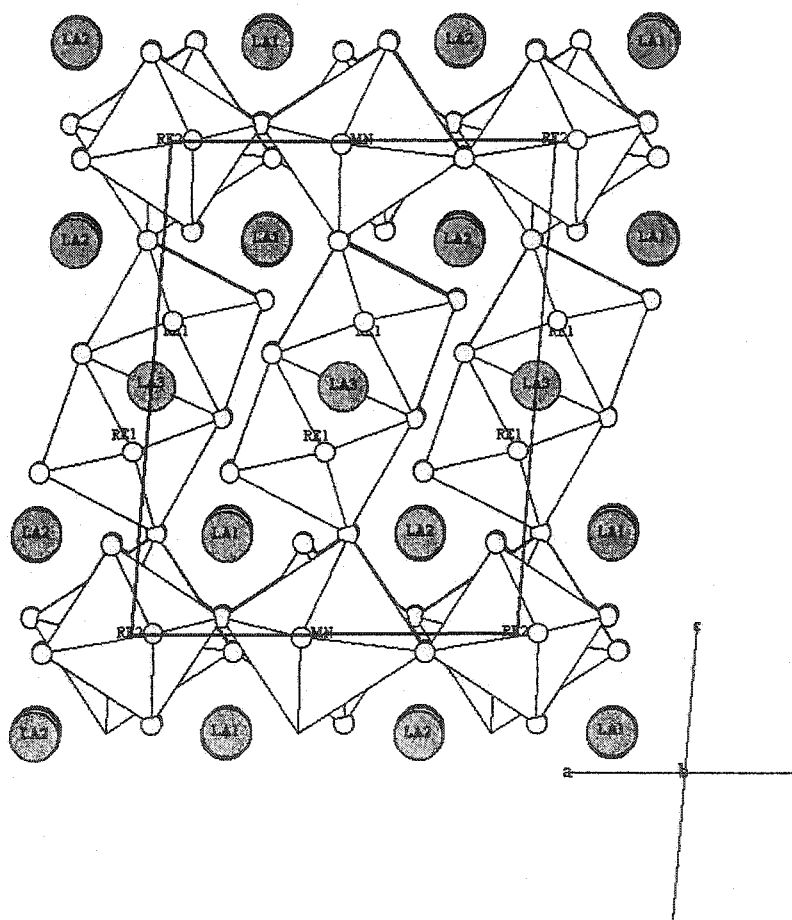


Figure IX: The Ruddlesden-Popper phases for the system $\text{Ca}_{n+1}\text{Mn}_n\text{O}_{3n+1}$. From left to right, are have $n = 1$ (Ca_2MnO_4), $n = 2$ ($\text{Ca}_3\text{Mn}_2\text{O}_7$), $n = 3$ ($\text{Ca}_4\text{Mn}_3\text{O}_{10}$) and $n = \infty$ (CaMnO_3).³¹

Chapter four of this thesis is dedicated towards the synthesis, crystal and magnetic structure of a new layered material, $\text{La}_5\text{Re}_3\text{MnO}_{16}$. This is the first in a new class of materials built upon what has been dubbed a “pillared” perovskite unit. Essentially, layers of perovskite-like ReO_6 and MnO_6 octahedra are connected in the c -direction by dimer units of Re_2O_{10} (see figure X). These dimers separate the layers by about 10 Å, which one would expect to reduce the dimensionality of the magnetic interactions. Nonetheless, long range order is observed at a relatively high T_N of 161 K, and a lower temperature FC/ZFC divergence in the susceptibility. The dimers themselves

are also believed to be involved in a double bond between the Re atoms, which leads to interesting exchange interactions mediated through the layers.

Figure X: The crystal structure of $\text{La}_5\text{Re}_3\text{MnO}_{16}$ in the ac-plane. Note the perovskite-like $\text{MnO}_6 - \text{ReO}_6$ layers in the ab planes which are separated by Re_2O_{10} dimers, which are actually edge-shared octahedra.



The low temperature magnetic structure is discussed in an appendix to this chapter. Even though one would expect a two-dimensional structure with only weak interactions between the planes, one finds that the material orders into a relatively simple three dimensional A-type structure (as defined by the scheme for perovskites by Wollan

and Koehler²⁷). There is some evidence for a slight spin reorientation at lower temperatures (in accordance with the field dependant susceptibility), but a corresponding structure cannot be ascertained with the weak features seen in the neutron scattering.⁹ The future work on this class of materials completes this chapter, which mentions further efforts to understand the exchange interactions between the layers, and the possibility of magnetic frustration playing a role for certain species substituted on the ab-perovskite layers.

FCC Perovskites

The remainder of this thesis discusses the properties of the ordered FCC perovskites Sr_2XReO_6 ($X = \text{Ca}, \text{Mg}$).^{11,12} The purpose of this work was to design new materials which would have frustrated networks of $S = \frac{1}{2}$ moments. Rhenium was chosen as a magnetic species for several reasons. The ease of preparing the Re^{6+} state, which occurs in the well studied oxide ReO_3 , was appealing, as was the extended nature of the 5d orbitals, which ensures that there are adequate exchange paths throughout the frustrated substructure. However, this feature of the 5d orbitals can be a problem if the Re^{6+} cations are too close, which will result in metallic behaviour, mimicking the parent compound ReO_3 .

Compounds of the general formula $\text{A}_2\text{BB}'\text{O}_6$ are known to be quite stable under substitution upon the B and B' sites.³⁶ For choices of cations that have similar sizes and charge, chemical disorder is common. However, in some cases, one can produce ordered structures, as in the combination of alkaline earths and 5d elements upon the B and B' sites. In these situations, the resulting sublattices form ordered face-centred cubic arrays. The magnetism of FCC topologies has been studied a great deal experimentally^{4,41} and theoretically.^{37,38} Basically, one of two types of behaviour is noted: long-ranged magnetic ordering, or geometrically frustrated phenomena. The difference between these two cases lies within the nature of the exchange interactions, which is largely determined by degree of overlap of the magnetic orbitals. For near or next-nearest neighbour

interactions, which one would expect for the 3d block of transition metals for instance, one can show through simple mean-field theory that these systems order. Stern³⁷ and Li³⁸ have identified several kinds of ordering based upon the strength of the nearest (NN) and next-nearest neighbour (NNN) interactions. Anderson³⁹ later identified a third, which is detailed below. The easiest way to describe these structures is in terms of four separate sublattices. Each of the structures has a net ordered spin of zero, as expected for true antiferromagnetism. Antiferromagnetic ordering of the first kind involves a simple layered stacking of ferromagnetic moments with antiferromagnetic coupling between the layers. The second case has six antiparallel nearest neighbours, with sheets of ordering in planes perpendicular to a cube diagonal. The third is complicated, and seen most easily by taking the first kind and translating along a cube edge to reverse the spins along every other pair perpendicular to this direction. All of these spin arrangements have been seen in real materials, but other interactions such as dipolar interactions or crystal field effects have been known to complicate the ordering. Nonetheless, these models provide good starting places for magnetic structure determination.

In the case of very strong NN interactions, the case of geometric frustration is favoured. The NNN interactions cannot stabilize the long-range ordered state upon the FCC lattice. Experimentally, the signature for such a situation is a large Weiss constant, or a small J_2/J_1 ratio. For some magnetic sublattices, the presence of a large NNN interaction (such that $J_2 \gg J_1$) favours the formation of a frustrated ground state such as for square planar topologies. It is less clear which is the case for the FCC antiferromagnet. However, in the specific scenario of the ordered perovskite, the distances between the NN are large, on the order of 5 Angstroms. Magnetic species with extended orbitals, such as the 5d transition metals, are needed to ensure good overlap and therefore strong antiferromagnetic interactions.

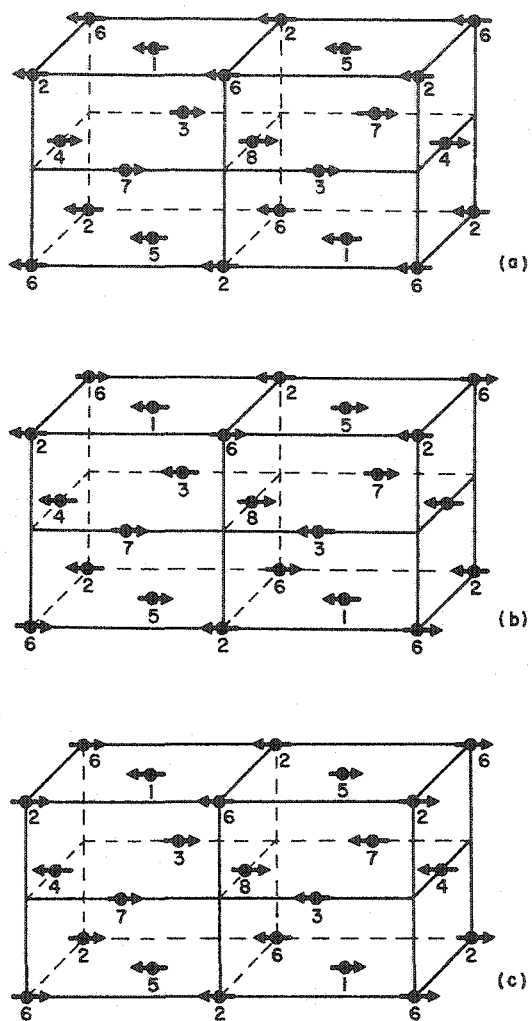


Figure XI: Antiferromagnetic orderings of the (a) first, (b) second, and (c) third kinds as predicted by mean field theory.⁴⁰

Table III: Exchange Interactions in Face-Centered Cubic Antiferromagnets (adapted from Smart⁴⁰)

	T_N (K)	θ_w (K)	$-\theta_w/T_N$	$-J_1$ (K)*	$-J_2$ (K)*	J_2/J_1	Type cal	Type obs
MnO	116	-610	5.3	7.0	3.3	0.46	2,3	2
FeO	198	-570	2.9	7.8	8.2	1.1	2	2
CoO	292	-330	1.1	1.3	19.5	15	2	2
NiO	523	-1310	2.5	82	65	1.3	2	2
α -MnS	154	-465	3.0	4.4	4.4	1.0	2	2
MnS ₂ **	60	-592	9.9	5.5	5.9	1.1	2	3
MnTe ₂	100	-528	5.3	6.7	1.6	0.24	3	1

* The values for J_1 and J_2 , the size of the nearest and next nearest neighbour exchange constants, were calculated by mean field theory. The ratio of the two determines the kind of ordering seen. The last two columns represent the type of order expected by these ratios (type calculated), and are compared to the experimentally observed orderings (type observed).

** The case of MnS₂ is interesting, as it has a high $-\theta/T_N$ value. As will be discussed below, this suggests a highly frustrated situation, and the mean field theory prediction for the kind of order observed breaks down. Recent neutron scattering measurements on a similar material, NiS₂ have shown evidence that spin fluctuations common to frustrated systems coexist with the ordered ground state.⁴¹

Geometric Frustration

The inability of a magnetic system to satisfy all of its constraints was first recognized by Tolouse⁴² and Anderson⁴³ to be magnetically frustrated. When such a situation arises due to the geometry of the lattice, this is called geometric frustration. A simple example of this is the triangular lattice in which a magnetic ion lies at the corner of each unit. If the dominant interactions between these ions are antiferromagnetic, then only two out of the three spins can align antiparallel to one another. Lattices made up of networks of triangles, therefore, tend to form exotic ground states in which the systems cannot order in the usual fashion (figure XIII).⁴ There are some orderings possible for various combinations of magnetic species on specific sublattices, but even in such cases the spin arrangement is a compromise and not a true eigenstate of the system.

Figure XII: Geometric Frustration on Triangular Plaquettes. Fig (A) illustrates geometric frustration, where only 2 bond constraints can be satisfied for magnetic spins on a triangle. Figures (B) and (C) show how some systems may try to reach a compromise by forming $q = 0$ ordered states, such as for the kagomé lattice (B) and the pyrochlore lattice (C).

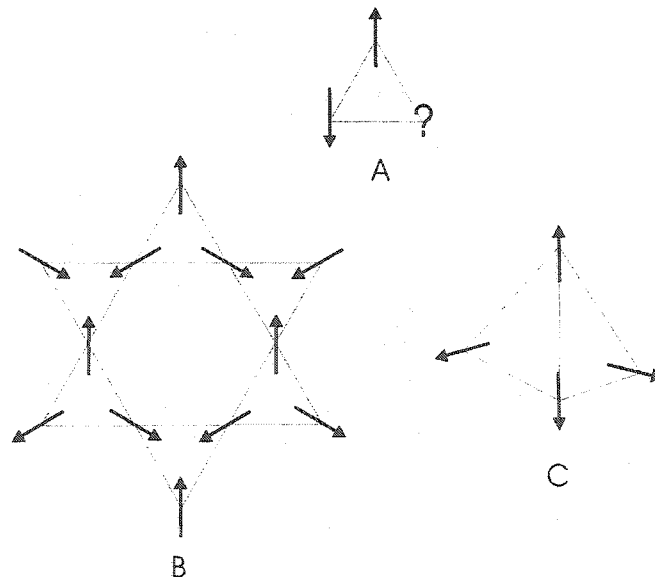
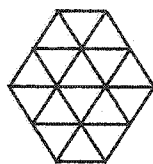


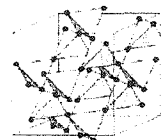
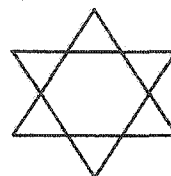
Figure XIII: Types of frustrated lattices consisting of triangular networks. Two dimensional examples include the triangular and kagomé lattices, and in three dimensions, the FCC and pyrochlore lattices are shown.

2D Lattices:

Triangular Lattice



Kagome Lattice



3D Lattices:

FCC Lattice

Pyrochlore Lattice

In the absence of frustration, one would expect these systems to order on a temperature scale that is governed by the Weiss temperature, or at least show strong deviations from typical paramagnetic Curie-Weiss behaviour. For systems that exhibit ferromagnetic interactions, one would expect that $T_C \sim \theta_w$, and thus that $|\theta_w|/T_C \sim 1$. For systems with antiferromagnetic nearest neighbour interactions, as is usually the case with many transition metal oxides, one would also expect this ratio to be of the same order of magnitude, with some variance depending on the exact nature of the interactions and the type of magnetic order. Empirically, this ratio is found to vary between 2 and 4 for typical antiferromagnets.

The case of extreme frustration is classified as when the energy scale for the magnetic interactions is much higher than the observed transition temperature. This translates to a $|\theta_w|/T_C$ ratio which is large, typically on the order of 10 or higher. However, the definition of the transition temperature can be somewhat ambiguous. For

systems that show glassy behaviour, for example, where the moments freeze into a random network of loosely correlated spins, the transition temperature is replaced by T_G , the freezing temperature. The transition may not be well defined in such a case.

	Lattice	$-\theta_w$ (K)	T_C (K)	f_{frus}	Order	Electron Config.
				$ \theta_w /T_C$		
LiCrO_2	Triangular	490	15	33	AF	$3d^3$
$\text{SrCr}_8\text{Ga}_4\text{O}_{19}$	Kagomé	515	3.5	150	SG	$3d^3$
$\text{KCr}_3(\text{OH})_6(\text{SO}_4)_2$	Kagomé	70	1.8	39	AF	$3d^3$
ZnCr_2O_4	B-spinel	390	16	24	AF	$3d^3$
K_2IrCl_6	FCC	32	3.1	10	AF	$5d^5$
$\text{Gd}_3\text{Ga}_5\text{O}_{12}$	Garnet	2	0.1	20	SG	$4f^7$
$\text{Sr}_2\text{NbFeO}_6$	FCC	840	28	30	SG	$3d^4$
$\text{Gd}_2\text{Ti}_2\text{O}_7$	Pyrochlore	10	1.0	10	AF	$4f^7$
$\text{Y}_2\text{Mo}_2\text{O}_7$	Pyrochlore	200	22	9	SG	$4d^2$
$\text{Tb}_2\text{Ti}_2\text{O}_7$	Pyrochlore	19	<0.07	>270	?	$4f^8$

Table IV: Properties of Strongly Frustrated Geometric Antiferromagnets (adapted from Ramirez⁴⁴). Under the column “Order” is listed the kinds of magnetic ground states observed, where AF denotes antiferromagnetism and SG denotes a spin-glass like state. $\text{Tb}_2\text{Ti}_2\text{O}_7$ does not order, but instead enters a “cooperative paramagnetic” phase.

The literature on geometric frustration is considerable, consisting mostly of systems based on triangular plaquettes. As mentioned above, the most common systems of study are the 2D kagomé lattices, and the 3D pyrochlores and spinels (which have a pyrochlore magnetic sublattice). Reports on other systems based on more complicated networks of triangles, such as the FCC lattice, which can be thought of as a system of edge-shared tetrahedra, are few in comparison, and perhaps theoretically more challenging to describe due to the complicated exchange pathways. A summary of some

representative materials of these classes is presented in table IV above, along with the magnetic behaviour noted at low temperatures and the corresponding frustration index.

That many of these materials fail to exhibit long range order is not surprising and it is indeed these states which are often the most interesting. It is only among the triangular AF that long range ordered states are most common. Complex spin orderings are possible in such materials as the spinels⁴⁵, but more and more systems are being discovered which do not order at all. Instead, cooperative paramagnetic states are emerging as a common theme. All frustrated systems in principle have an enormous ground state degeneracy, which has its origin in the many ways that one can minimize the ground state energy within a given plaquette. As one approaches Avogadro's number N of these units, the ground state acquires a tremendous number of possible configurations, also approaching N and thus no long range order should be expected. The term "cooperative paramagnetism," first coined by Villain⁴⁶, to describe such a state suggests that the system is dynamic, with spin fluctuations playing an important role even as $T \rightarrow 0$ K. $\text{Tb}_2\text{Ti}_2\text{O}_7$ is an example of such a state⁴⁷, where the moments are fluctuating over a single tetrahedron, hinting at interesting dynamics such as the spin roton mode. There is no long-range ordered Néel state observed down to 0.07 K.

The second most common ground state beyond the ordered Néel state for geometrically frustrated systems is the spin glass. Most spin glasses are driven by disorder effects such that the spins themselves freeze out in random orientations at a freezing temperature T_g . However, in the case of spin glasses such as $\text{Y}_2\text{Mo}_2\text{O}_7$, there is little or no apparent disorder, and the glassiness is driven by frustration effects⁴⁸. Since the correlations are only significant over single tetrahedra in this material (as evidenced by neutron scattering measurements), the possible number of spin arrangements that preserve $S = 0$ upon each plaquette is macroscopic, and glassy behaviour is noted. Typical spin glasses show several characteristic features, such as a divergence in the field cooled and zero-field cooled magnetic susceptibility below T_g , a characteristic line shape observed through μSR (which is often accompanied by strong spin fluctuations noted in inelastic neutron scattering measurements), a linear heat capacity dependence at lower

temperatures, and an absence of long range magnetic order from neutron scattering.⁴ The latter two signatures have been known to vary for unconventional spin glasses such as $(D_3O)Fe_3(SO_4)_2(OD)_6$,⁴⁹ which is a two dimensional system comprised of Fe^{3+} spin 5/2 moments on a layered kagomé lattice. The signatures of an apparent T^2 dependence of the heat capacity, and a Warren-like line shape, are both indicative of strongly two dimensional correlations. The heat capacity exponent T^2 can be explained by using the following canonical expression:

$$(18) \quad C_v \sim aT^{d/\nu}$$

where a is a constant, d is the dimensionality, and ν is the exponent in the dispersion relation for spin waves, $\omega \sim k^\nu$.⁵⁰ The results for 3D antiferromagnets, for which $\omega \sim k$, gives the result $C \sim T^3$, and thus for 2D antiferromagnets, $C \sim T^2$. 3D ferromagnets, on the other hand, have a $\omega \sim k^2$, and therefore one has the result $C \sim T^{3/2}$.

Recently, research on geometrically frustrated antiferromagnets has focussed on systems in which quantum effects are important and cooperative paramagnetism plays a strong role in the determination of the magnetic ground state. One such state is the celebrated "spin liquid", in which the spins do not freeze out due to fluctuations which stabilize the system into pairs of spin-singlets (see figure XIV). Quantum spin systems of $S=1/2$ moments were predicted to form the Resonating Valence Bond State by Anderson in the 1970s, but very few examples of such materials have been realized experimentally. The remainder of this thesis investigates the effects of frustration in the perovskites Sr_2XReO_6 ($X = Ca, Mg$). The ordered FCC arrays of $S = 1/2$ Re^{6+} moments are believed to form spin-glass like states that are driven by quantum effects.

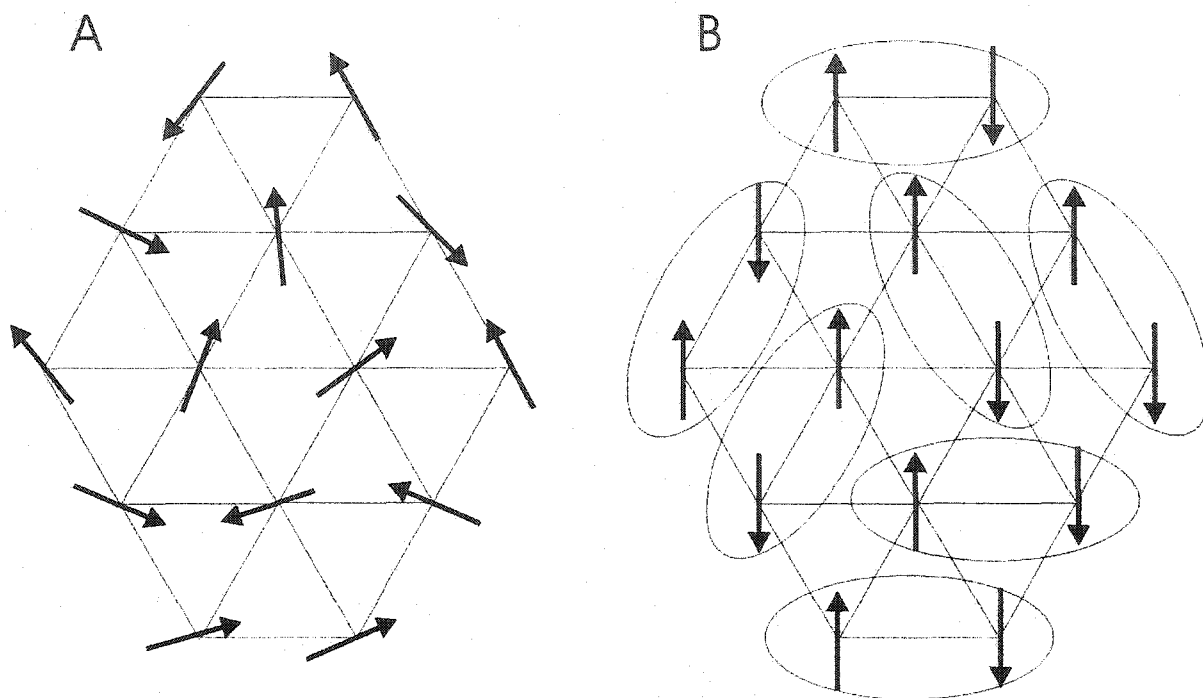


Figure XIV: Exotic magnetic ground states shown upon triangular lattices. Figure (A) gives an example of a spin glass, in which the moments freeze out in random orientations. Figure (B) illustrates a spin liquid, in which the moments are still fluctuating due to quantum effects, but they are paired into spin singlets.

References

- (1) P. A. Cox, *Transition Metal Oxides* (Clarendon Press, Oxford, 1992).
- (2) J. Orenstein and A. J. Millis, *Science*, **288**, 468 (2000).
- (3) Y. Tokura and N. Nagosa, *Science*, **288**, 462 (2000).
- (4) J. E. Greedan, *Journal of Mat. Chem.*, **11**, 37 (2001).
- (5) R. M. Hazen, *Sci. Amer.* **358**, 52 (1988).
- (6) H. Kato, T. Okuda, Y. Okimoto, Y. Tomioka, K. Oikawa, T. Kamiyama, Y. Tokura, *Phys. Rev B*, **65**, 144404 (2002).
- (7) M. Hanawa, Y. Muraoka, T. Tayama, T. Sakakibara, J. Yamaura, Z. Hiroi, *Phys. Rev. Lett.*, **87**, 187001 (2001).
- (8) C. R. Wiebe, J. E. Greedan, J. S. Gardner, Z. Zeng, M. Greenblatt, *Phys. Rev. B*, **64**, 064421 (2001).
- (9) C. R. Wiebe, A. Gourrier, T. Langet, J. F. Britten, J. E. Greedan, *J. Solid State Chem.*, **151**, 31 (2000).
- (10) A. E. C. Green, C. R. Wiebe, J. E. Greedan, *Solid State Sciences*, **4**, 305 (2002).
- (11) C. R. Wiebe, J. E. Greedan, G. M. Luke, and J. S. Gardner, *Phys. Rev. B*, **65**, 144413 (2002).
- (12) C. R. Wiebe, J. E. Greedan, P. P. Kyriakou, G. M. Luke, J. S. Gardner, I. M. Malureanu, P. Russo, A. Savici, Y. J. Uemura, submitted to *Phys. Rev B* December, 2002.
- (13) A. R. West, *Solid State Chemistry* (John Wiley and Sons, Essex, 1989).
- (14) A. M. Glazer, *Acta. Crys. B*, **28**, 3384 (1972).
- (15) P. M. Woodward, *Acta. Crys. B*, **53**, 32 (1997).
- (16) V. M. Goldschmidt, *Mat.-Naturv. Kl.*, **2**, 117 (1926).
- (17) W. Gilbert, *On the Loadstone and Magnetic Bodies, and on the Great Magnet the Earth* (John Wiley and Sons, New York, 1893).

- (18) M. P. Marder, *Condensed Matter Physics* (John Wiley and Sons, New York, 2000).
- (19) D. L. Goodstein, *States of Matter* (Dover, New York, 1985).
- (20) N. W. Ashcroft and N. D. Mermin, *Solid State Physics* (Holt, Rinehart and Wilson, New York, 1976).
- (21) M. Bieringer, *Ph. D. Thesis* (McMaster University, Hamilton, 2000).
- (22) J. B. Goodenough, *Magnetism and the Chemical Bond* (Interscience, New York, 1963).
- (23) C. Kittel, *Introduction to Solid State Physics* (John Wiley and Sons, New York, 1986).
- (24) A. Earnshaw, *Introduction to Magnetochemistry* (Academic Press, London, 1968).
- (25) A. Beiser, *Concepts of Modern Physics* (McGraw-Hill, Inc., New York, 1987).
- (26) M. Collins, *Magnetic Critical Scattering* (Oxford University Press, New York, 1989).
- (27) E. O. Wollan and W. C. Koehler, *Phys. Rev.* **100**, 545 (1955).
- (28) V. Caignaert, A. Maignan, Ch. Simon, B. Raveau, E. Suard, *J. Magn. Magn. Mat.* **153**, 1260 (1996).
- (29) C. Zener, *Phys. Rev.* **83**, 299 (1951).
- (30) P. G. de Gennes, *Phys. Rev.* **118**, 141 (1960).
- (31) I. D. Fawcett, J. E. Sunstrom IV, M. Greenblatt, M. Croft, K. V. Ramanujachery, *Chem. Mater.* **10**, 3643 (1998).
- (32) C. Frontero, J. L. Garcia-Munos, M. A. G. Aranda, C. Ritter, A. Llobet, M. Respaud, J. Vanacken, *Phys. Rev. B* **64**, 054401 (2001)
- (33) P. Schiffer, A. P. Ramirez, W. Bao, S.-W. Cheong, *Phys. Rev. Lett.* **75**, 3336 (1995).
- (34) S. Jin, T. H. Tiefel, M. McCormack, R. A. Fastnacht, R. Ramesh and L. H. Chen, *Science*, **264**, 413 (1994).

- (35) Z. Zeng, M. Greenblatt, and M. Croft, *Phys Rev B* **59**, 8784 (1999).
- (36) J. Longo and R. Ward, *J. Am. Chem. Soc.* **83**, 2816 (1961).
- (37) F. Stern, *Phys. Rev.* **94**, 1412 (1954).
- (38) Y. Y. Li, *Phys. Rev.* **100**, 627 (1955).
- (39) P. W. Anderson, *Phys. Rev.* **79**, 705 (1950).
- (40) J. S. Smart, *Effective Field Theories of Magnetism* (Saunders, Philadelphia, 1966).
- (41) M. Matsuura, Y. Endoh, H. Hiraka, K. Yamada, K. Hirota, A. S. Mishchenko, N. Nagaosa, I. V. Solovyev, *cond-mat/0104233* (2001).
- (42) G. Toulouse, *Commun. Phys.*, **2**, 115 (1977).
- (43) P. W. Anderson, *Phys. Rev.*, **102**, 1008 (1956).
- (44) A. P. Ramirez in *Handbook of Magnetic Materials*, edited by K. H. J. Buschow (North-Holland, Amsterdam, 2001), Vol. 13, p. 423.
- (45) A. S. Wills, N. P. Raju, J. E. Greedan, *Chem. Mater.*, **11**, 1510 (1999).
- (46) J. Villain, *Z. Phys. B*, **33**, 31 (1979).
- (47) J. S. Gardner, S. R. Dunsiger, B. D. Gaulin, M. J. P. Gingras, J. E. Greedan, R. F. Kiefl, M. D. Lumsden, W. A. MacFarlane, N. P. Raju, J. E. Sonier, I. Swainson, Z. Tun, *Phys. Rev. Lett.* **82**, 1012 (1999).
- (48) J. S. Gardner, B. D. Gaulin, S.-H. Lee, C. Broholm, N. P. Raju, J. E. Greedan, *Phys. Rev. Lett.*, **83**, 211 (1999).
- (49) A. S. Wills, A. Harrison, S. A. M. Mentink, T. E. Mason, Z. Tun, *Europhys. Lett.*, **42**, 325 (1998).
- (50) A. P. Cracknell and A. O. Tooke, *Contemp. Phys.*, **20**, 55 (1979).

Chapter Two

Experimental Techniques

Basics of Diffraction

Neutrons and x-rays are among the primary probes of the structure and behaviour of condensed matter systems. With the rise of increasingly powerful synchrotron and ultra-cold neutron sources, the fields of x-ray and neutron scattering have entered a golden age. The theory behind these techniques, however, is nearly a century old, beginning with the work of Laue and Bragg's first explanation of x-ray diffraction in solids.¹ The use of neutrons, with the rise of reactor technology, was later popularized by Schull and Brockhouse.² The property which both of these probes share, however, is the magnitude of their respective wavelengths. For typical x-ray sources, such as the ones originally used at the turn of the century, these wavelengths are on the order of angstroms, albeit with energies of several thousand electron volts. This is due to the fundamental energy-momentum relationship:³

$$(1) \quad E_{x\text{-ray}} = \frac{hc}{\lambda}$$

This is much greater than the average energy of excitations in solids at room temperature, making conventional x-rays (such as from a rotating anode or tube source) well suited to the study of the static properties of materials, such as the structure. Typical energies for thermal neutrons, on the other hand, are defined by:

$$(2) \quad E_{neutron} = \frac{p^2}{2M_n} = \frac{h^2}{2M_n\lambda^2}$$

which are not only on the order of $k_B T$ for excitations in solids, but they also have de Broglie wavelengths on the order of interatomic distances. Thus, neutrons are popular for both elastic and inelastic studies of materials. Neutrons have the added advantage of possessing a magnetic moment, which enables the determination of the magnetic structure of ordered systems, as well as the magnetic excitations. X-rays are only now being used for magnetic scattering, but due to the weak nature of the magnetic field associated with electromagnetic radiation, it is only at the most powerful synchrotron sources that this option is commonly exercised.

X-ray scattering is more commonly used for the routine structure determination of materials due to the relative ease and inexpensive nature of the technique. However, x-rays only penetrate solid matter to lengths on the order of microns, and are scattered very strongly from bound electrons within a solid. Neutrons, on the other hand, have penetration lengths on the order of centimeters for some samples. The mechanism for the scattering is fundamentally different, arising predominantly from nuclear scattering. However, the phenomena of scattering in both cases can be described by the same laws of diffraction. The first part of this chapter will discuss diffraction with a general overview of neutron and x-ray scattering. Neutron scattering will then be discussed in detail, and this will be followed by a formal explanation of magnetic neutron scattering. The Rietveld method which is used in the structure determination of powders will conclude the discussion on diffraction.

Elastic Scattering and Bragg's Law

Most of what scientists know today about the structure of materials is from the diffraction of electrons, neutrons, or photons. The diffraction of x-rays from a NaCl crystal by W. L. Bragg at the dawn of the 20th century ushered in a new era of understanding in materials science. By directing beams of x-rays upon simple crystalline materials, Bragg noted characteristic patterns of diffracted x-ray beams on photographic plates. The locations of these lines (for powder samples) or singular peaks (for single crystals) was dependent upon the wavelength of the incoming radiation. Bragg explained these results by considering the lattice to be a diffraction grating, upon which parallel planes of atoms could diffract an incoming beam.³ For elastic scattering, one would expect the angle of the incoming beam to be equal to the angle of the reflected beam, but a certain amount of momentum could be transferred to the lattice. Using this idea, Bragg formulated the law that bears his name to describe the condition for constructive interference of these diffracted photons:

$$(3) \quad 2d \sin \theta = m\lambda$$

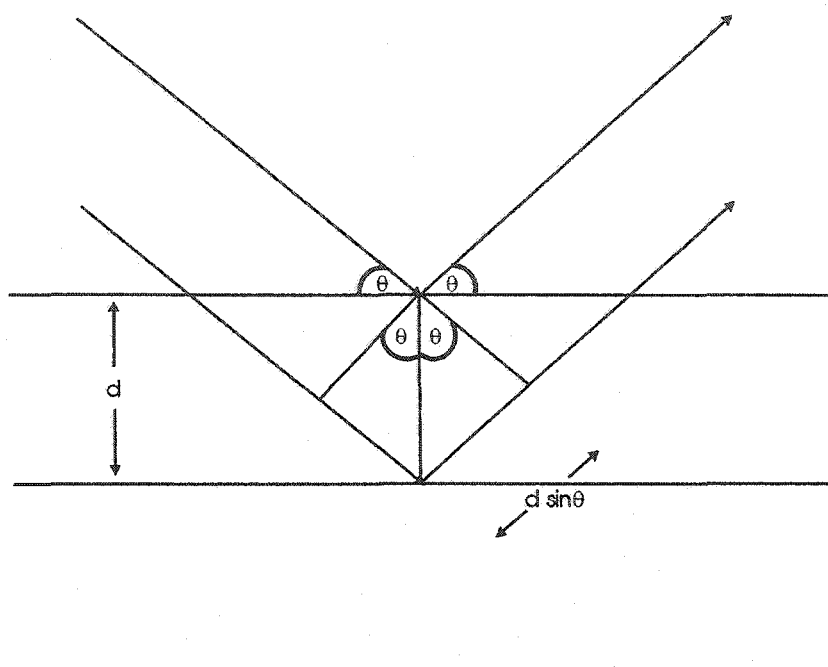


Figure I: A representation of Bragg's law for lattice spacing d .

The interatomic spacings, d , can be inferred from this law, and in theory one can imagine how the structure of an atomic lattice can be derived. However, a more useful construct in the calculation of crystal structures is to approach this problem from what is known as reciprocal space. Although there is no energy transferred to the lattice for elastic scattering, there is a finite amount of momentum transferred, which one can quantify as $\vec{Q} = \vec{k} - \vec{k}'$. Here, \vec{k} and \vec{k}' are defined as the incident and reflected wavevectors, and are equal in magnitude with $|\vec{k}| = 2\pi/\lambda$. The vector difference between these two wavevectors, however, has a special condition for diffraction. Ewald expressed the condition for diffraction in reciprocal space geometrically by constructing a sphere in reciprocal space of radius k as in Fig II.

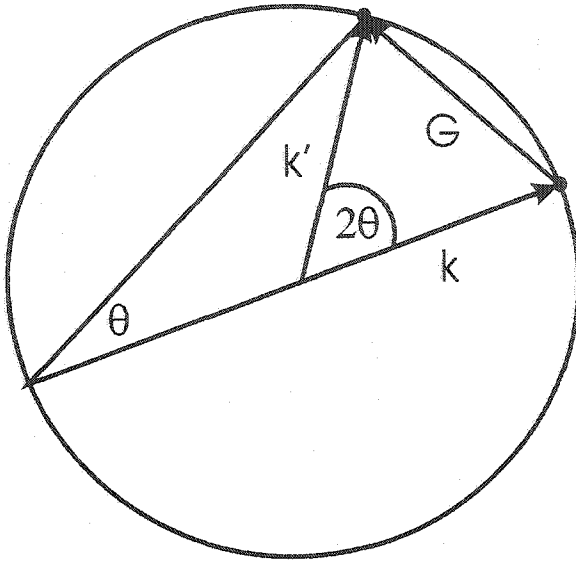


Figure II: Ewald's sphere representation in 2D

One can readily show that for Bragg's law to be valid, \vec{Q} , the vector difference of \vec{k} and \vec{k}' , must be equal to a reciprocal lattice vector \vec{G} which is defined by

$$(4) \quad \vec{G} = \frac{2\pi}{d_{hkl}} = h\vec{b}_1 + k\vec{b}_2 + l\vec{b}_3$$

Where h, k, and l are Miller indices which describe the vector space \vec{G} .¹ The connection between these reciprocal space lattice vectors ($\vec{b}_1, \vec{b}_2, \vec{b}_3$) and their real space counterparts ($\vec{a}_1, \vec{a}_2, \vec{a}_3$) is defined to be:

$$(5) \quad \vec{b}_1 = 2\pi \frac{\vec{a}_2 \times \vec{a}_3}{|\vec{a}_1 \cdot (\vec{a}_2 \times \vec{a}_3)|}$$

$$(6) \quad \vec{b}_2 = 2\pi \frac{\vec{a}_3 \times \vec{a}_1}{|\vec{a}_1 \cdot (\vec{a}_2 \times \vec{a}_3)|}$$

$$(7) \quad \vec{b}_3 = 2\pi \frac{\vec{a}_1 x \vec{a}_2}{|\vec{a}_1 \bullet (\vec{a}_2 x \vec{a}_3)|}$$

The approach of solving crystal structures in reciprocal space proves to be a much more elegant method than the visualization of complicated scattering planes d_{hkl} in real space. The Ewald sphere is a beautiful construction which provides experimentalists with an excellent visual aid for an understanding of the diffraction process.

The diffraction pattern observed for a single-crystalline sample would consist of an array of points in space which satisfy Ewald's condition. However, for a powder, or multicrystalline sample, which is made up of many randomly oriented crystals, the expected diffraction pattern would be a series of Debye cones, each of which defining a reciprocal point \vec{G} .

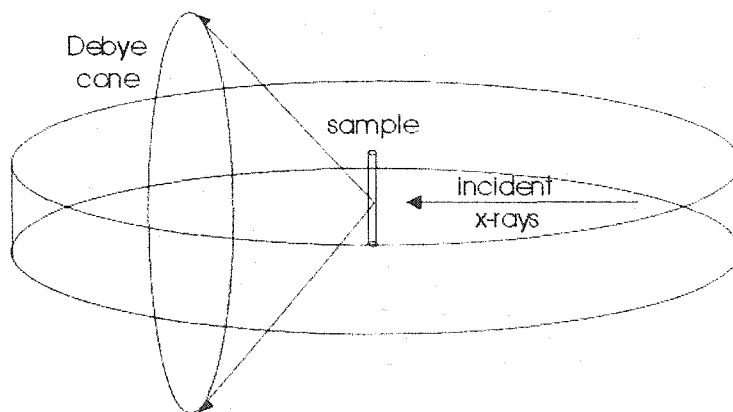


Figure III: Transmission geometry powder diffraction showing how Debye cones of scattering arise

The fundamental problem of overlap between numerous Bragg peaks with the same d_{hkl} makes powder diffraction a less powerful technique than single crystal

diffraction for the determination of structures (see figure IV below). However, modern methods, such as the Rietveld approach to refinement and the use of synchrotron beams for example, are now providing more routine structural determination of powder samples.

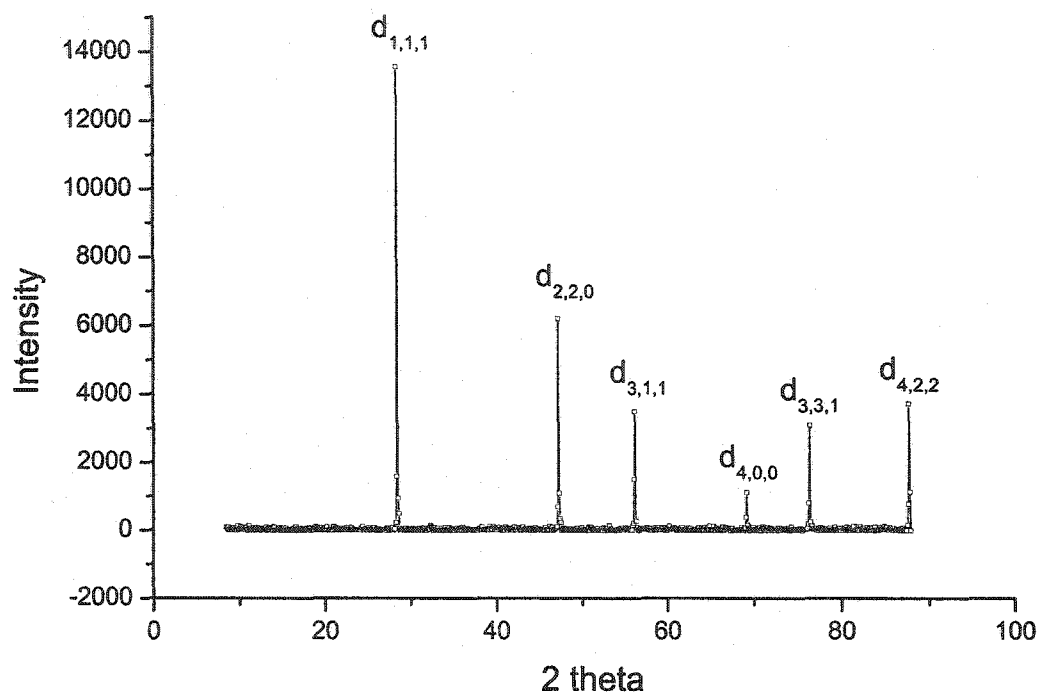


Figure IV: X-ray powder diffraction pattern for silicon. The d_{hkl} for the reflections are listed. Due to the cubic symmetry, there is significant overlap of Bragg peaks. For example, $d_{+2,+2,0}$, $d_{+2,0,+2}$ and $d_{0,+2,+2}$ are all superimposed upon the $d_{2,2,0}$ peak.

Powder Diffraction Formalism

The deconvolution of a diffraction pattern to deduce a crystal structure involves the indexing of the Bragg peaks upon a unit cell, and then defining the contents of that unit cell from the intensities of the reflections. The intensity of a Bragg reflection is defined by ⁴

$$(8) \quad I = S_{hkl} S_{hkl}^* \exp\left[-2B \frac{\sin^2 \theta}{\lambda^2}\right]$$

where the exponential is known as the Debye-Waller factor and S_{hkl} is the structure factor. The Debye-Waller factor describes the displacement of atoms from their equilibrium positions. The variable B is defined in terms of the mean square displacement of the atoms, u :

$$(9) \quad B = 8\pi^2 \langle u^2 \rangle$$

The structure factor S_{hkl} is defined by

$$(10) \quad S_{hkl} = \sum_{n=1}^N f_n(2\theta) \exp(i2\pi(hx_n + ky_n + lz_n))$$

where x_n , y_n , and z_n are the atomic positions for each atom n with respect to the unit cell and h , k , and l are the Miller indices defining the reciprocal lattice vector.

The $f_n(2\theta)$ is the atomic form factor. For x-rays, this defines the number and distribution of the atomic electrons for atom n in the unit cell, and falls off rapidly as a function of scattering angle.

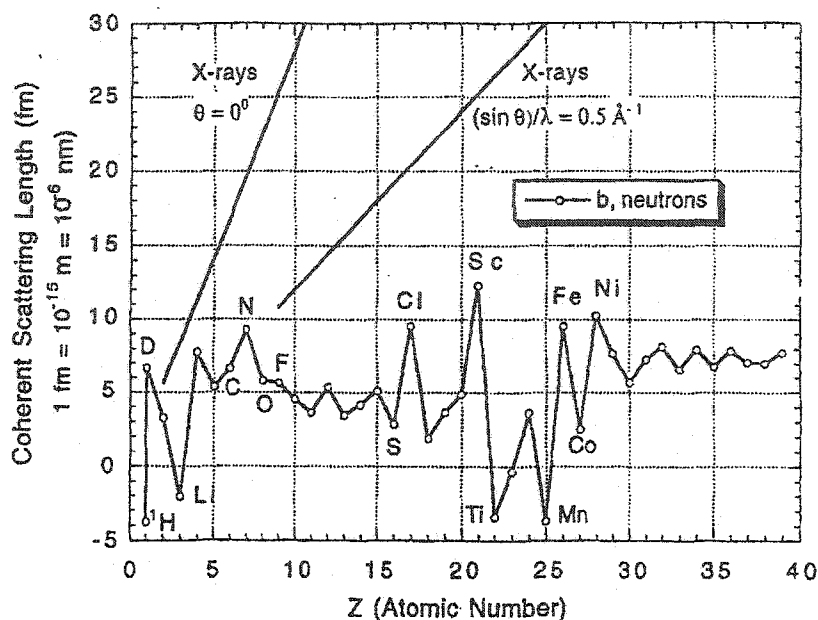


Figure V: Neutron and x-ray scattering coherent scattering lengths⁵

The integral of f_n over each atomic site yields Z , the total number of electrons for each atom n . Thus, the intensity of scattered reflections for x-rays is approximately governed by $I \sim Z^2$, showing that x-rays are rather insensitive to determining the atomic positions of light atoms as compared to heavy atoms.

Neutrons, on the other hand, scatter largely from the atomic nucleus of a given atom. The dependence of the scattering factor f_n for neutrons is much more complex, as determined from nuclear interactions (see figure V above). Since the cross-sections are more uniform across the periodic table, neutrons are useful for the determination of structures with low Z atoms, such as hydrogen or oxygen. However, other effects such as strong absorption among particular isotopes must be considered for neutron scattering. Absorption is usually a much stronger effect for x-rays as compared to neutrons, and care is needed in the choice of one probe over the other.

X-ray diffraction

Conventional x-rays are produced in much the same manner that William Röntgen first did in 1895 via the inverse photoelectric effect. Electrons, usually produced by thermionic emission from a heated cathode, are accelerated in evacuated tubes towards a metal target. Upon colliding with the surface of the metal, these electrons are immediately decelerated by bremsstrahlung, where most of their kinetic energy is lost as a continuous spectrum of background radiation. However, some of these electrons undergo atomic collisions within the metal lattice and induce inner shell electron transitions. Characteristic x-rays are produced when these atoms de-excite to their ground state by reshuffling their electron configurations. A typical x-ray source has a spectrum which has several of these sharp features (which are classified as K_{α} , K_{β} , etc.) and a low intensity background which is due to bremsstrahlung.

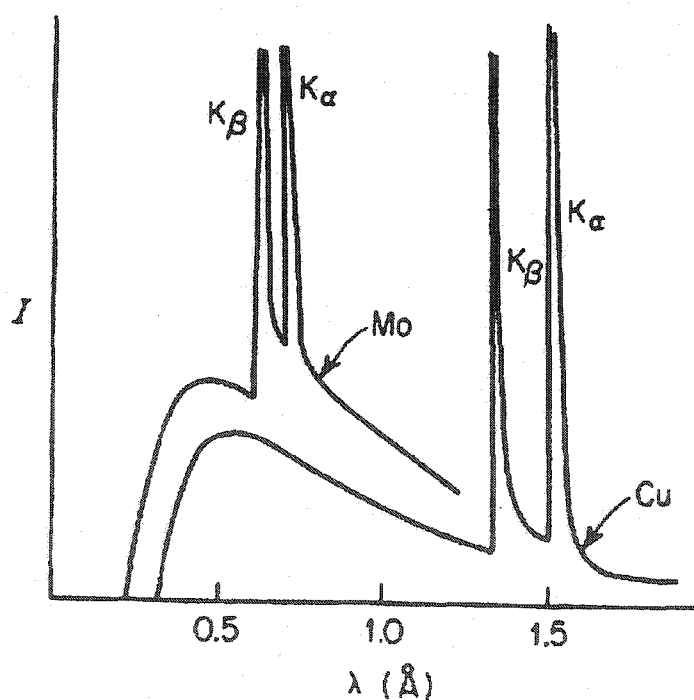


Figure VI: X-ray transitions for Cu and Mo radiation⁶

The cryptic classification of these lines is based upon which “shells” or atomic orbitals that are involved in the electronic transition. K_{α} and K_{β} , for example, represent transitions from the L shell to the K shell and the M shell to the K shell respectively. Closer examination of these lines reveals that they are further split by the two electrons which occupy the shells, which due to the Pauli principle have opposite spin and slightly different energies due to spin-orbit coupling (these are designated as $K_{\alpha 1}$ and $K_{\alpha 2}$ for example). In order to obtain a single wavelength beam, an experimentalist will typically use a monochromator such as single crystal graphite or germanium. Bragg reflection from this crystal can be used to separate these emission lines, although the angular resolution may not be good enough to separate the closely spaced doublets mentioned above.

The geometry of an x-ray experiment is very important, as x-rays are strongly absorbed by most materials. Most experiments are completed in reflection geometry, or Bragg-Brentano mode to minimize absorption. X-rays are reflected from a sample to a scintillation counter where the x-ray intensities are measured as a function of angle. Alternatively, film may be used to record the positions of the Bragg peaks, which is particularly useful for powder work where high resolution diffraction patterns can be measured via a focussed Guinier-Hägg camera. The film, once briefly exposed to x-rays, can be developed and with the aid of a line scanner, one can obtain very accurate cell parameters. The use of charge-coupled devices (CCDs) and phosphor screens are rapidly replacing film techniques in more modern laboratories.

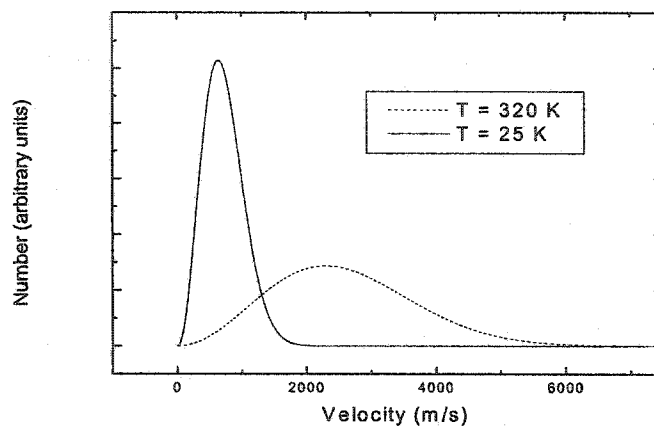
Single crystal experiments are usually completed in transmission, or Debye-Scherrer geometry. As a result, very small crystals are actively sought to eliminate absorption effects as much as possible. Even with crystals on the order of hundreds of microns in size, however, absorption effects can be significant, as is the case with transition metals or rare-earth materials. One approach to coping with this problem is to apply a correction based upon the geometry of the crystal and the known elements within.⁷ By indexing the faces and identifying the orientation of each face relative to the

next, sophisticated software can approximate the absorption that is observed for single crystal x-ray diffraction experiments and produce more refined structures.

Neutron diffraction

The most common method to produce thermal neutrons is via fission reactions at a nuclear reactor. However, spallation sources are becoming more and more popular due to the high intensities of neutrons produced and the advantages to using the time-of-flight method over conventional diffraction techniques. The wavelengths of neutrons produced at a reactor source depend upon the temperature of the moderator, a cavity within the reactor itself which brings the particles to thermal equilibrium. The neutrons emerge with a Maxwellian distribution of velocities which is peaked at an energy corresponding to the temperature of the moderator (see figure VII). Thermal neutrons have a peak usually near 300 K, and a much wider distribution than a cold source for example, which has a liquid hydrogen moderator and a peak near 25 K. With the aid of a monochromator, and usually a filter to remove higher order wavelengths via absorption, one can choose a wavelength to conduct experiments. Cold neutron sources produce longer wavelength neutrons than conventional sources, which have various advantages for elastic and inelastic experiments (predominantly the high resolution which can be obtained, and therefore the ability to discern closely spaced Bragg peaks and probe very small energy excitations).

Figure VII: Maxwell distribution of speeds produced from moderators of $T = 320 \text{ K}$ and $T = 25 \text{ K}$.²



Elastic Neutron Scattering

There are several excellent references on neutron diffraction. The remainder of this section will be dedicated to the basic concepts of neutron scattering theory as used in Squires⁸ and Collins.⁹

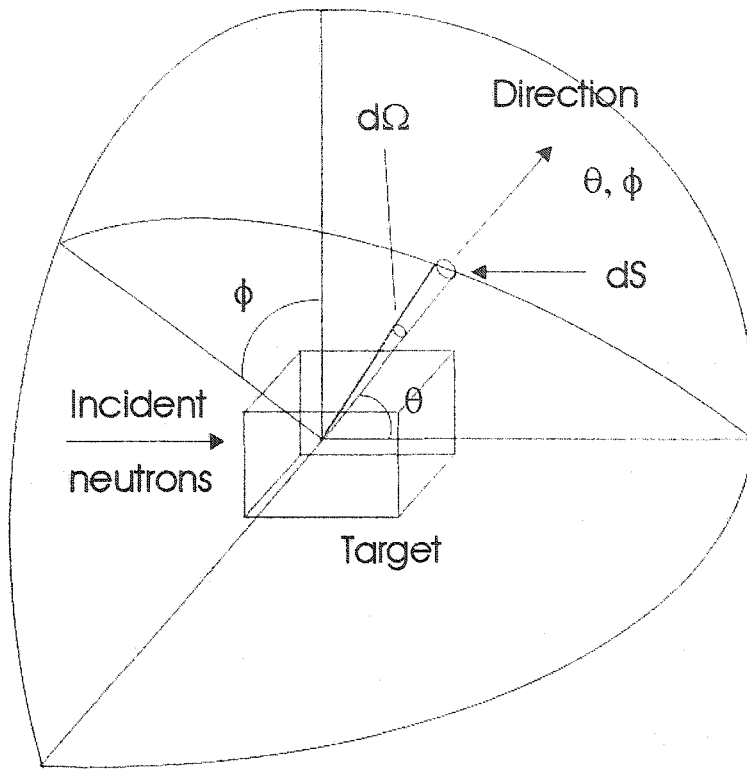


Figure VIII: Scattering geometry for neutron scattering experiments⁸

It is convenient now to introduce the concept of a cross-section. Most neutron scattering experiments measure a flux in a particular direction (θ, ϕ) with a certain energy E_f (see figure VIII). For large distances, one can define dS to be the solid angle covered by the detector, and the partial differential cross-section can be defined as:

$$(11) \quad \frac{d^2\sigma}{d\Omega dE_f} = (\text{number of neutrons scattered/unit time into } dS \text{ in the direction } \theta, \phi$$

with final energy between E_f and $E_f + dE_f$)/ $\Phi d\Omega dE_f$

where Φ is the incident neutron flux. Elastic scattering is defined with the final energy E_f equal to the incident energy E_i (with the definition $E_f - E_i = \hbar\omega$, $\omega = 0$), and inelastic

scattering in the converse case.

Since neutrons interact only with nuclei (in the case of non-magnetic scattering), one can use the Fermi pseudopotential $V(\vec{r})$ to calculate the partial differential cross-section.

$$(12) \quad V(\vec{r}) = \frac{2\pi\hbar^2}{m} b_i \delta(\vec{r} - \vec{R}_i)$$

where b_i is defined as the scattering length of the nuclei located at \vec{R}_i . The typical approach to calculating the cross-section is to use Fermi's golden rule:

$$(13) \quad \frac{d^2\sigma}{d\Omega dE_F} = \frac{k'}{k} \left(\frac{m}{2\pi\hbar^2} \right)^2 \sum_{\lambda} p_{\lambda} \sum_{\lambda'} \left| \langle k'\lambda' | V | k\lambda \rangle \right|^2 \delta(E_{\lambda} - E_{\lambda'} - E_i - E_F)$$

where k and E_i are the incident wavevector and energy of the neutron, and p_{λ} is the thermal population of the state λ of the system. The coherent partial differential cross section is

$$(14) \quad \frac{d^2\sigma}{d\Omega dE_F} = \frac{k'}{k} N b^2 S(\vec{Q}, \omega)$$

where the scattering vector is $\vec{Q} = \vec{k} - \vec{k}'$. The dynamical structure factor $S(\vec{Q}, \omega)$ has been introduced here, which is the Fourier transform of the nuclear correlation function:

$$(15) \quad S(\vec{Q}, \omega) = \frac{1}{hN} \sum_{i,j} \int_{-\infty}^{\infty} \exp(i\omega\tau) \langle (\exp(-i\vec{Q} \cdot \vec{R}_j(0)) (\exp(i\vec{Q} \cdot \vec{R}_i(\tau))) \rangle d\tau$$

$\bar{R}_j(\tau)$ is the position of the j^{th} atom at time τ . This correlation function is measured in neutron scattering experiments.

It is useful at this point to introduce the concepts of coherent and incoherent scattering. For a collection of nuclei with scattering lengths b_i , the coherent cross-section is defined as:

$$(16) \quad \left(\frac{d^2\sigma}{d\Omega dE_f} \right)_{\text{coherent}} = \frac{k'}{k} N(\bar{b})^2 S_{\text{coherent}}(\bar{Q}, \omega)$$

where there is no restriction on the sum for the dynamical structure factor. For the case of incoherent scattering, the cross-section is defined as:

$$(17) \quad \left(\frac{d^2\sigma}{d\Omega dE_f} \right)_{\text{incoherent}} = \frac{k'}{k} N(\bar{b}^2 - (\bar{b})^2) S_{\text{incoherent}}(\bar{Q}, \omega)$$

where there is now a restriction on the sum for the incoherent dynamical structure factor such that one is only taking the contributions from an individual atom. Coherent scattering gives rise to structural information, such as Bragg peaks or diffuse scattering from short-range ordering, since it measures correlations with other atoms. Incoherent scattering measures the “self correlation function”, which correlates an atom at time zero to another time τ . This results in a relatively weak background function.

Magnetic Neutron Diffraction

Magnetic neutron scattering measures the magnetic cross-section, which has a similar form to equation 14. In the case, however, the formal expression is a second-rank tensor.² To derive this result, the pseudopotential must be replaced with U , the operator

which represents the interaction between the magnetic moment of the neutron and the electrons of the solid.

$$(18) \quad U = \bar{\mu} \cdot \bar{H} = -\gamma \mu_N \bar{\sigma} \cdot \bar{H}$$

where γ is known as the gyromagnetic ratio (which is 1.91 for the neutron), μ_N is the nuclear magneton (5.501×10^{-27} J/T), $\bar{\mu}$ is the magnetic moment operator and $\bar{\sigma}$ is the Pauli spin operator. The magnetic field produced by the electrons, \bar{H} , is defined as:

$$(19) \quad \bar{H} = \text{curl} \left[\frac{\bar{\mu} \times \bar{R}}{|\bar{R}|^3} \right] - \frac{e \bar{v}_e \times \bar{R}}{c |\bar{R}|^3}$$

where \bar{v}_e is the velocity of the charge, \bar{R} is the position vector relating the electron to the point where the magnetic field is being measured, and e and c are fundamental constants ($e = 1.602 \times 10^{-19}$ C, $c = 2.98 \times 10^{10}$ cm/s). The first term in this equation is from the spin of the electron; the latter has its origin in the orbital motion. The electronic magnetic moment operator is:

$$(20) \quad \bar{\mu}_e = -2\mu_B \bar{s}$$

The spin operator of the electron is defined here as \bar{s} .

The proper form for the magnetic cross-section can be calculated by substituting these terms into equation 13. Halpern and Johnson first completed this considerable task in 1939.¹⁰ The final result of this work is listed below for N identical atoms with magnetic moments:

$$(21) \quad \frac{d^2\sigma}{d\Omega dE_F} = \frac{k'}{k} \frac{N}{h} (\gamma r_o)^2 |F(\vec{Q})|^2 \sum_{\alpha, \beta} (\delta_{\alpha\beta} - \hat{Q}_\alpha \hat{Q}_\beta) S^{\alpha\beta}(\vec{Q}, \omega)$$

One can compare this equation to its nonmagnetic analog equation 14. For example, the scattering length is now replaced by the length $\gamma r_o = 5.391$ fm. $F(\vec{Q})$ is known as the magnetic form factor, which is analogous to the atomic form factor that was discussed for x-ray scattering. This equation is the Fourier transform of the magnetic moment distribution, which has a finite spatial extent. One key difference between x-ray and neutron scattering is the introduction of a polarization factor $\delta_{\alpha\beta} - \hat{Q}_\alpha \hat{Q}_\beta$. The α and β indices refer to spin components in the tensor. The inclusion of this term signifies that neutrons can only couple to moments and spin fluctuations which are perpendicular to \vec{Q} . The scattering function $S^{\alpha\beta}(\vec{Q}, \omega)$ is the Fourier transform of the spin-spin correlation function for tensor components α and β . One can compare the form of this equation:

$$(22) \quad S^{\alpha\beta} = \frac{1}{2\pi} \sum_R \exp(i\vec{Q} \cdot \vec{R}) \int_{-\infty}^{\infty} \exp(i\omega\tau) \langle S_{0\alpha}(0) S_{R\beta}(\tau) \rangle d\tau$$

to equation 15 in the nonmagnetic case. The $S_{R\beta}(\tau)$ terms now represent the β component of the spin at site \vec{R} and at time τ . It is this quantity, the spin-spin correlation function, which is measured by the magnetic partial cross-section.

In the specific case of diffraction from an ordered magnetic structure, one obtains a delta function in the spin-spin correlation function (since the spins are essentially static in the classical sense) which indicates zero energy transfer.

$$(23) \quad S_{el}^{\alpha\beta}(\vec{k}, \omega) = \delta(\omega) \sum_R \exp(i\vec{k} \cdot \vec{R}) \langle S_{0\alpha}(0) S_{R\beta}(\infty) \rangle$$

To illustrate how this can give rise to magnetic Bragg scattering, consider the case of an ordered ferromagnet of the same spin S aligned in the z -direction, following Collins.⁹ One can simplify the spin-spin correlation function to:

$$(24) \quad S_{el}^{\alpha\beta}(\vec{k}, \omega) = \delta(\omega) \delta_{\alpha z} \delta_{\beta z} (S_z)^2 \frac{(2\pi)^3}{v_o} \sum_{\vec{g}} \delta(\vec{k} - \vec{g})$$

This equation describes delta function Bragg peaks at reciprocal lattice positions \vec{g} . The intensity of the Bragg peaks is proportional to $(S_z)^2$, the ordered magnetic moment along z . This is how one can calculate magnetic structures, and determine the magnitude of ordered magnetic moments using neutron scattering.

The Rietveld Method

The refinement of crystal structures from powder diffraction patterns is complicated by the fundamental problem of Bragg peak overlap. For high symmetry structures, this can for the most part be dealt with (at least for small scattering angles), since the peaks are often well resolved. However, even minor distortions away from these structures can lead to a very difficult deconvolution problem. Fortunately, Rietveld has discovered a method to address this issue by fitting the entire data profile to a model rather than the individual reflections. The following function is minimized via a least-squares refinement procedure:⁴

$$(25) \quad F = \sum_i w_i (y_i, obs - \frac{1}{c} y_i, calc)^2$$

where y_i obs and y_i calc are the observed and calculated intensities, w_i is a weighing function, and c is a scaling factor. The observed y_i are first corrected for a

background function:

$$(26) \quad y_{i,obs} = Y_i - B_i$$

The calculated pattern is based in the general case upon a Gaussian line-shape for individual Bragg peaks. Other line shapes, such as a Lorentzian, or the Pseudo-Voigt (which is a convolution of Gaussian and Lorentzian shapes) can be used as well. For a given position $2\theta_i$, the intensity is calculated based upon the following equation:

$$(27) \quad y_i = t S_k^2 j_k L_k \frac{2\sqrt{2 \ln 2}}{H_k \sqrt{\pi}} \exp\left(-4 \ln 2 \left(\frac{(2\theta_i - 2\theta_k)}{H_k}\right)^2\right)$$

where t is the step width, j_k is the multiplicity of the reflection, L_k is the Lorentz factor, $2\theta_k$ is the calculated Bragg position peak, H_k is the peak width (at half maximum), and S_k^2 is the structure factor. The Lorentz factor is a geometric correction which is made to account for how a reciprocal lattice point passes through the Ewald sphere. It is highly dependant upon the direction from which the point approaches the sphere.

Note that there is an implied assumption here that the contributions from each Bragg peak will add algebraically to contribute to the diffraction pattern. This holds for both multi-phase and magnetic structures.

The variation of the width of the diffraction peaks as a function of angle is characterized by the following empirical relation:

$$(28) \quad H_k^2 = U \tan^2 \theta_k + V \tan \theta_k + W$$

The U , V , and W parameters are specific to the instrument used.

The structure factor, S_k^2 , can be divided into the atomic and magnetic components:

$$(29) \quad S_k^2 = (F_k^2 + J_k^2) \exp\left(\frac{-2Q \sin^2 \theta_k}{\lambda^2} + G\alpha^2\right)$$

where F_k is the nuclear contribution, J_k is the magnetic contribution, Q is an overall isotropic temperature factor, and $G\alpha^2$ is a preferred orientation correction factor.

The asymmetry of the lineshape (which can arise, for example, from the vertical divergence of the neutron beam) can be accounted for by a factor of:

$$(30) \quad 1 - P(2\theta_i - 2\theta_k)^2 S / \tan \theta_k$$

where P is defined as the asymmetry parameter and S is a numerical constant to ensure that the difference $2\theta_i - 2\theta_k$ is positive. More complicated asymmetry parameters are now available with modern Rietveld refinement software, along with other parameters to account for the form factors of various atomic species, absorption corrections, etc.

There are several parameters which are used to gauge the quality of the refinement. The most intuitive choice is R_p :

$$(31) \quad R_p = \frac{\sum_i |y_{i,obs} - y_{i,calc}|}{\sum_i |y_{i,obs}|}$$

However, this parameter does not properly account for the statistical weighing of peaks over all angular ranges. Therefore, a modified R factor, known as R_{wp} is typically quoted:

$$(32) \quad R_{wp} = \left(\frac{\sum w(2\theta_i)(y_i,obs - y_i,calc)^2}{\sum w_i(y_i,calc)^2} \right)^{1/2}$$

where $w(2\theta_i)$ is the weighing parameter. Comparisons are often made between R_{wp} and the expected error value, R_{exp}

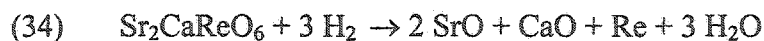
$$(33) \quad R_{exp} = \left(\frac{(N - P + C)}{\sum_i w_i(y_i,obs)^2} \right)^{1/2}$$

where N is the number of observations, P is the number of variables in the refinement, and C is the number of constraints. For most refinements, the R_{exp} and R_{wp} parameters should show good agreement. However, a caveat is needed for magnetic structures, which commonly report much higher R factors. This is due to the definition of the magnetic unit cell, which is often in a low symmetry space group. This tends to generate many low intensity reflections which results in higher error values than expected.

Oxidation State Analysis

There are two common methods of estimating the oxidation states of chemical species within a solid: one experimental, the other a theoretical argument. The experimental technique is Thermal Gravimetric Analysis, or TGA for short. TGA involves a reaction of the material of interest in an attempt to fully reduce or oxidize the sample. By comparison of the theoretical and experimental weight loss, the oxidation states of the chemical species within can be inferred. For example, in the case of the

perovskite $\text{Sr}_2\text{CaReO}_6$, the sample was reduced in a hydrogen atmosphere:¹¹



The resulting powder sample was found to have no traces of $\text{Sr}_2\text{CaReO}_6$ left. The experimental weight loss was compared to the theoretical, which agreed quite well. Therefore, the Re^{6+} oxidation state was assumed to be present.

The oxidation states of a given sample can also be calculated based upon Linus Pauling's Bond Valence Theory. Pauling,¹² and later Brown and Shannon,¹³ found that an empirical relationship exists between the bond distances, and the corresponding oxidation states given by the following equation:

$$(35) \quad V_j = \sum_i^n S_{ij} = \sum_i^n \exp\left(\frac{R_o - R_{ij}}{b}\right)$$

Where for a given ion j , V_j is the valence - the sum of contributions S_{ij} from n bonds. The values for R_o have been tabulated from known values in the literature and b is an empirical constant (0.37 Å). Using this equation, the theoretical bond valencies can be calculated. However, a caveat is needed here in the case of severe distortions, such as Jahn-Teller active ions, or with poorly investigated species (such as Re^{6+}), where this analysis may lose some validity. In most cases, though, bond valence theory provides an excellent agreement with nominal oxidation states (typically to within 10%).

DC Magnetic Susceptibility

The magnetic susceptibility of a material is defined to be

$$(36) \quad \chi = \frac{\partial M}{\partial H}$$

where M is the magnetization of the sample, and H the applied field. As discussed in Chapter 1, the susceptibility of a given material can give insight on the magnetic interactions between the various species within. It is also diagnostic of magnetic phase transitions in general. For example, conventional long-range antiferromagnetically ordered systems typically show a sharp cusp at T_N , whereas short-range order is marked by a broad anomaly (see figure IX). Ferromagnetic systems show more complex behaviour near the transition temperature.

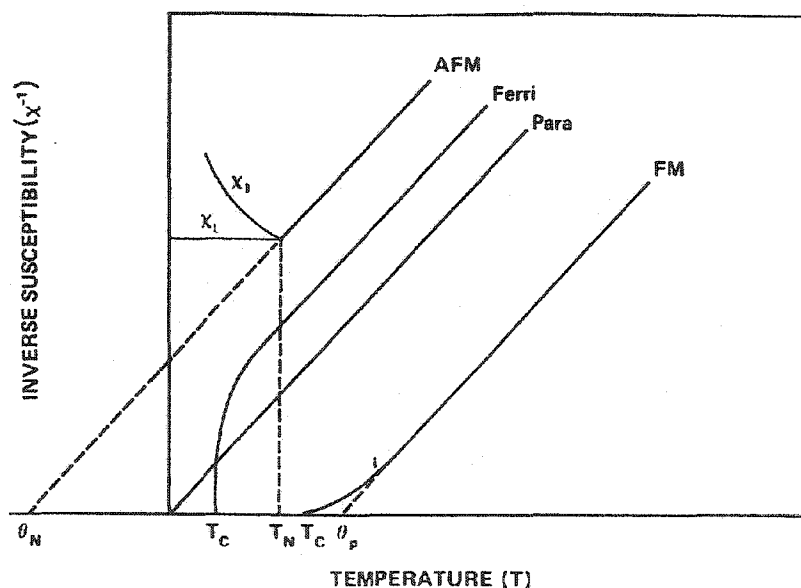


Figure IX: The Inverse Susceptibility for various kinds of magnetic behaviour. Ferri and FM denote ferrimagnetic and ferromagnetic magnetism respectively.¹⁴

The application of a magnetic field upon reaching, or after reaching a base temperature is known as field or zero-field cooling. The divergence between these two data sets can be diagnostic of either a different choice of magnetic ground states (such as for a frustrated system), or the rearrangement of domains for long-range ordered

materials. The exact nature of the ground state cannot be verified by this method alone.

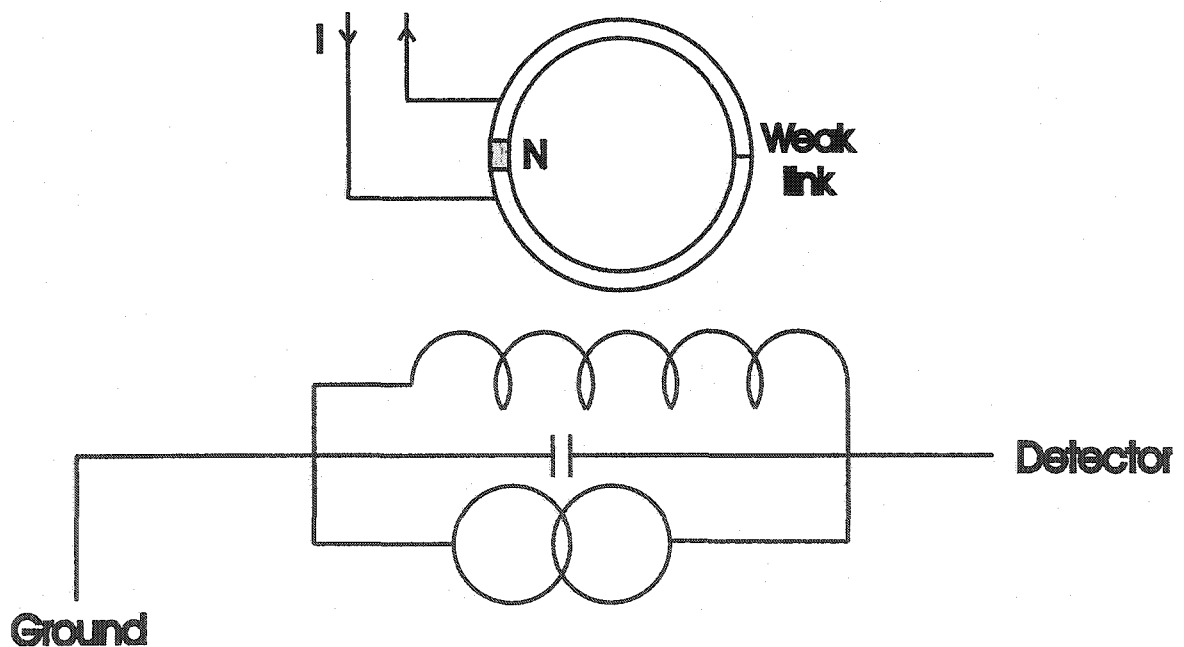
Historically, measurements of the magnetic susceptibility of a material were made with techniques such as the Gouy or Faraday method. However, measurements of increasing sensitivity, such as for studies of dilute or low spin magnetism, require other methods such as SQUID magnetometry. A SQUID is the most sensitive device for measuring very small magnetic fields, although it does not measure the magnetic susceptibility directly. SQUID magnetometry is an inductance method, in which the magnetization is determined by the current induced in a small wire loop that the sample passes through. What is actually measured is the output voltage from this small current, from which one can calculate the magnetic field and therefore the susceptibility for a given sample.¹⁵

The Josephson junction is crucial for the operation of a SQUID device, as it is responsible for the amplification of small changes in magnetic field to large electric currents. In 1962, Josephson discovered this effect by taking two superconductors and separating them by an insulating layer.¹⁶ The quantum mechanical wave functions which describe the Cooper pairs responsible for superconductivity leak into the forbidden insulating region from either side of the layer. As a result, for a very thin layer, the two wavefunctions will overlap, and the Cooper pairs can effectively tunnel between the two superconducting regions without breaking up. There are two different effects which can be observed, which depend upon the nature of the bias across the junction. The DC Josephson effect occurs in the absence of an applied field (electric or magnetic), in which a DC current flows across the junction due to tunneling. The AC Josephson effect manifests itself with the application of a DC current across the junction, which results in current oscillations in the radio frequency range.

From these two types of junctions, two different kinds of SQUIDs have been developed: DC (direct current) and RF (radio frequency).¹⁶ In general, the DC SQUIDs have a higher degree of sensitivity when compared to the RF SQUIDs, but RF SQUIDs are usually sufficient for studies of magnetism in transition metal oxides. The RF device consists of a single Josephson junction mounted upon a superconducting loop. This is

turn is coupled to a parallel resonant LC circuit (an inductor connected across a capacitor, see figure X). Applying a DC current to the SQUID sends Cooper pairs across the junction in an oscillating manner, as discussed above. However, if there is a magnetic field present within the loop, the flow of the Cooper pairs will be changed accordingly, as the Meissner effect will produce currents to oppose changes in magnetic flux in quantized amounts of $hc/2e = 2 \times 10^{-7} \text{ Oe/cm}^2$. The net effect of these two competing currents is that the phase of the wavefunction changes, which in turn alters the AC voltage induced in the loop. A resonant LC circuit, which is set up in parallel to the loop picks up these changes in the AC voltage, and this signal is fed through a lock-in amplifier. It is these changes in the AC voltage which are analyzed to determine the magnetic flux through the loop, and thus a measure of the susceptibility.

Figure X: Diagram of a RF SQUID system, showing the Josephson junction (top) and the LC circuit (bottom) ¹⁶



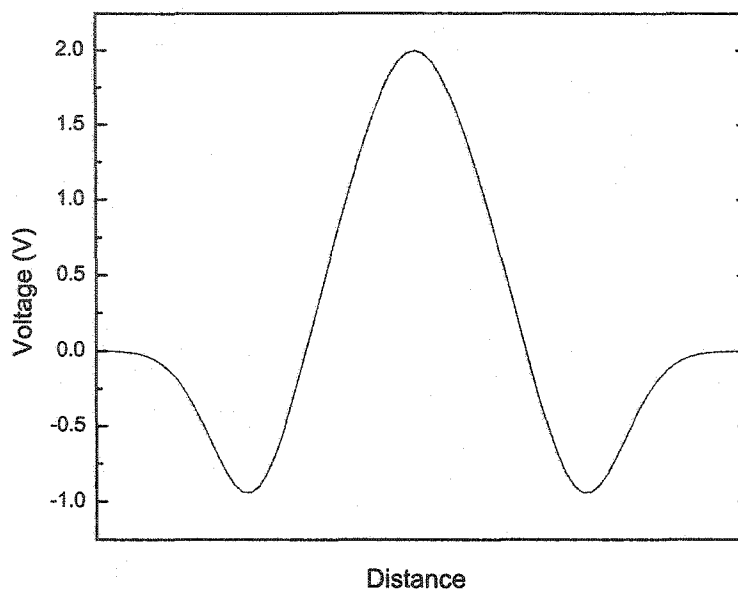


Figure XI: Response of the SQUID to a paramagnetic sample as it passes through the second-order gradiometer pickup coil.

The Quantum design SQUID magnetometer consists of three inductance coils, which are wound in opposite directions. As a result, the output voltage will appear as figure XI. There is a superconducting shield which encloses the entire device and generates a low but stable magnetic field in which the SQUID can operate. The SQUID itself can be run in two different modes: (1) what is known as the DC, or Direct Current mode and (2) the RSO, or Reciprocating Sample Option mode. The DC mode is the traditional method of slowly passing the sample through the three coils, usually multiple times for each measurement to obtain an average signal with relatively small error bars. The RSO mode involves the rapid oscillation of the sample through the detection coils, which in theory results in higher data acquisition times (which reduces the experiment time and therefore the nonlinear SQUID drift) and greater sensitivity (usually by several

orders of magnitude over DC). The reduction in noise of this technique is significant over the DC method. However, for powder samples, one must exercise caution, as certain frequencies may cause the sample to shift over a period of time and therefore skew the results.

Heat Capacity Measurements

The heat capacity of a system at constant volume is defined as: ¹

$$(37) \quad C_v = \lim_{\Delta T \rightarrow 0} \frac{Q}{\Delta T}$$

The heat capacity of a solid can convey a great deal of information. Ideally, all materials will obey the empirical heat capacity law at low temperatures:

$$(38) \quad C_v = \gamma T + \beta T^3$$

where γ is known as the electronic component of the specific heat, and β is the phonon contribution. One can use simple theory to motivate these terms. Physically, the γ term is related to the density of states of the conduction electrons in a material, as it can be derived using free electron theory to give:

$$(39) \quad C_v = \frac{\pi^2}{2} (k_B T / \epsilon_F) n k_B$$

where ϵ_F is the Fermi energy and n is the electronic density of states. Thus, for magnetic insulators, this term should be expected to be much smaller than for conductors. There is a special case with spin glasses, where a linear heat capacity dependence is noted which is due to the degeneracy of the magnetic ground state.

The cubic term is related to the phonon contribution of the specific heat of solids. Simple Debye theory can be used to derive the following expression for the low temperature specific heat:

$$(40) \quad C_v \sim \frac{2\pi^2}{5} k_B \left(\frac{k_B T}{\hbar c} \right)^3$$

With these two terms, one would expect the low-temperature specific heat to have a linear dependence, which is quickly overcome by the cubic component at higher temperatures. The simple relationships above hold only for low temperatures, however. A detailed knowledge of the phonon modes are needed to extract the proper heat capacity in a moderate temperature regime. One approach to doing this is to use the Debye function:

$$(41) \quad C_v = 9nk_B \left(\frac{T}{\theta_D} \right)^3 \int_0^{\theta_D/T} \frac{e^x x^4 dx}{(e^x - 1)^2}$$

This model assumes that the vibrational spectrum is replaced with three acoustic branches, each with a linear dispersion relation $\omega = ck$, and the upper limit of the integral is the Debye frequency ω_D . One can define a Debye temperature, θ_D which defines the temperature scale for which the modes begin to be frozen out. Obviously, such an approach is valid only for highly symmetric, monoatomic materials. It is found empirically that this law breaks down for complicated materials; however one alternative to approximating the specific heat contribution is to define a temperature dependant Debye temperature. This is only practical at low temperatures where one would expect the acoustic modes to be the most thermally populated. Optical modes typically require larger excitation energies, and are thus frozen out at low temperatures.

For magnetic systems, the specific heat can be diagnostic of the nature of a phase transition. For example, a transition to a long-range ordered state is usually heralded by a

lambda-anomaly, or a sharp asymmetric spike in the specific heat. If one integrates the area under this curve, the following thermodynamic relationship can be used to solve for the entropy removal as one passes through the transition:

$$(42) \quad S = \int_0^T \frac{C_v}{T} dT$$

where S is the entropy. For a system of spins, the molar entropy removal is expected to be equal to $S = R \ln (2J+1)$, where J is the spin quantum number. This gives a rough estimate of the number of spins which are static, as compared to dynamic or fluctuating components, in the low temperature ordered state. For systems which do not order, this technique can still be used to determine the nature of the ground state. Heat capacity anomalies are usually quite small for low spin systems however, and often obscured by the lattice component.

The traditional method of measuring the heat capacity of a material is through adiabatic calorimetry. This involves applying a known pulse of heat to a thermally insulated sample, and then measuring the corresponding change in temperature (see figure XII). The heat capacity is measured by simply taking the quantity of heat and dividing it by the change in temperature.¹⁷

$$(43) \quad C = \frac{\Delta q}{\Delta T}$$

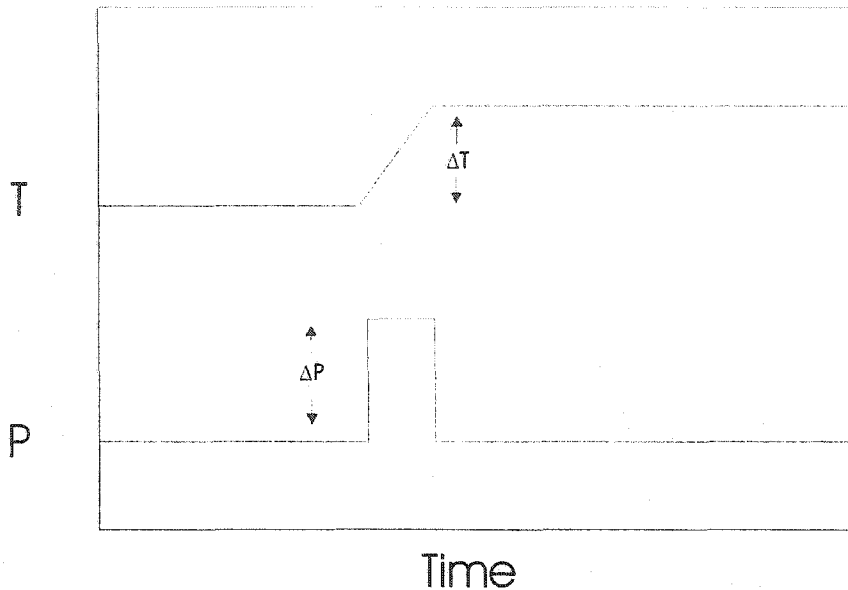


Figure XII: The Temperature (T) and Power (P) dependence as a function of time for an adiabatic calorimeter (adapted from Oxford Instruments).¹⁷

The assumption here is that the sample has reached thermal equilibrium, and that it is well insulated so that the heat losses are negligible.

An alternative technique to measure the heat capacity is via the relaxation method. The sample is isolated upon a sample platform, which is connected to a thermal bath only by very weak thermal links. The power introduced to the sample is still introduced in the form of a heat pulse, but the magnitude is now dependant upon the final temperature of the system. However, each pulse is made such that the heat loss is equal to the heat supplied to the sample at the final equilibrium temperature (see figure XII). The final temperature T_o is reached by an exponential relationship:

$$(44) \quad T = T_i + \Delta T_o (1 - \exp^{-t/\tau})$$

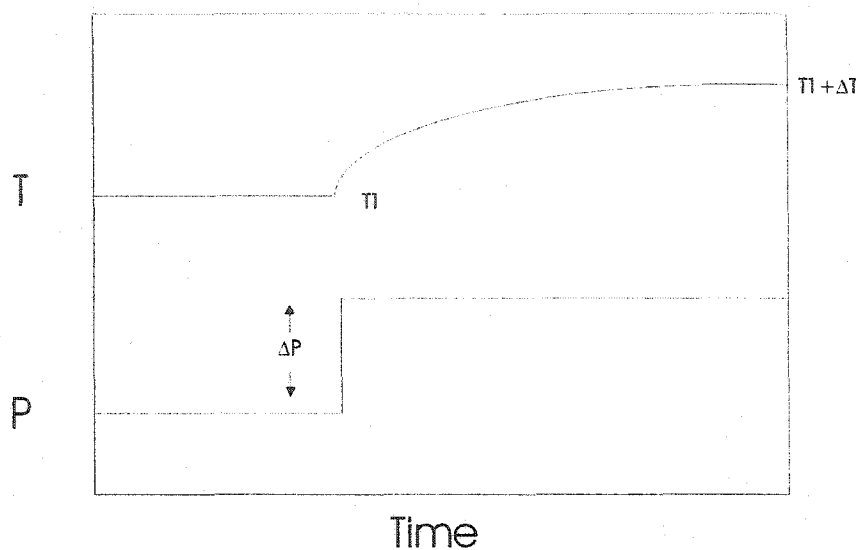


Figure XIII: The Temperature (T) and Power (P) dependence as a function of time for the relaxation method (adapted from Oxford Instruments).¹⁷

The heat capacity is measured by obtaining the time constant τ , which is determined by finding the thermal resistance between the sample and its surroundings:

$$(45) \quad \tau = R_{TH} C$$

where the thermal resistance R_{TH} is:

$$(46) \quad R_{TH} = \frac{\Delta T_o}{\Delta P}$$

The advantage to using this technique over the adiabatic method is that now a measurement of R_{TH} is being made, whereas it is assumed to be infinite in the latter case. The sample itself is quite well insulated from its surroundings, as in the case of the Oxford Instruments Heat Capacity Probe, where it sits upon a sapphire chip connected to the probe by 8 thin (20 μm) gold plated tungsten leads (see figure XIV). A Cernox

temperature sensor is connected to the chip by 50 μm gold leads. Since the thermal link is very weak, very small heat pulses result in large temperature changes which must be monitored carefully. The heat capacity of the leads, and the grease which holds the sample in place, is corrected for by the software accompanying the instrument.

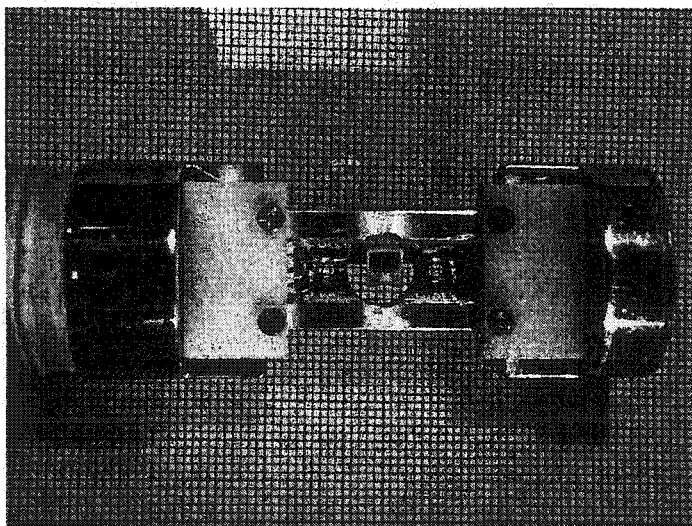
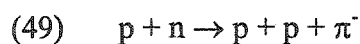
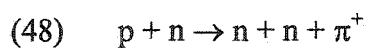
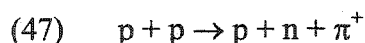


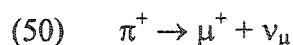
Figure XIV: Sample mount for the Oxford Instruments Heat Capacity probe. The sapphire chip is linked to the probe by 4 gold plated platinum leads on each side. The chip is located on the bottom, and linked by 4 gold leads. The sample sits above the chip.¹⁸

μ SR Experiments

The sensitivity of the muon to local magnetic fields has made muon spin relaxation, or μ SR (which is used synonymously with muon spin rotation or resonance), an invaluable technique for investigating magnetism in solids.¹⁹ The muon is a lepton, which can for the purposes of condensed matter physics be thought of as a light proton (with a mass of $m_\mu \sim 0.11 m_p$ and spin = $\frac{1}{2}$). Muons are produced via high energy collisions (> 500 MeV) at accelerators such as TRIUMF (the Tri-University Meson Facility), at the University of British Columbia. High energy proton beams strike a low Z material, such as carbon, to produce a stream of elementary particles:



The pions, π^+ or π^- , are unstable particles with a half-life of $\tau = 26$ ns. Typically, the positive pions are used, but the negative species can be used for μ^- SR studies. The decay of the pion produces a muon and a neutrino:

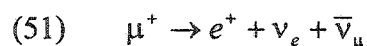


These muons are emitted isotropically from the parent pion with a momentum of 29.8 MeV/c and kinetic energy of 4.119 MeV (from the rest frame of the muon).

Two particular properties of the pion and muon decay make the μ SR technique feasible as a probe of condensed matter systems. One is the ease of producing 100% spin polarized muon beams, which is due to the weak interaction governing the decay of

the parent pions. The weak interaction does not conserve parity, and as a result, surface muons are spin polarized in a direction which is opposite to their momentum. Other resonance probes such as NMR or ESR depend upon other methods to create sufficient spin polarization within a sample.

The second important property is with the decay of the muon, which is also due to the weak interaction:



The lifetime for such a decay is $\tau_\mu = 2.2 \mu\text{s}$. Upon entering the sample, the muon is quickly thermalized, whereas it loses considerable energy. At these lower speeds, the muon readily finds a rest site and then undergoes the decay process. The direction of the positron emitted is preferentially along the direction of the spin of the muon, thanks to the non-conservation of parity. Thus, the detection of these particles can reveal information about the precession of the muon at a given site, and thus an accurate determination of the local field. However, one cannot determine the direction of the muon spin for a given decay positron, since the decay is a statistical process which is governed by a probability distribution. A solution to this problem is to measure the decays of many muons, each injected one at a time into a sample. The anisotropy of the directions of the decay positrons can then be used to reconstruct the behaviour of the muons within the sample. The time evolution of the muon spin polarization can reveal crucial information about the spatial distribution of the magnetic field, and spin fluctuations which perturb this field.

There are basically two modes of operation for μSR , which essentially differ by the direction of the applied magnetic field (see figure XV). Transverse Field Muon Spin Rotation uses a field which is perpendicular to the muon spin polarization, whereas the field is parallel for Longitudinal Field Muon Spin Relaxation. Both techniques use a clock which times the arrival of a muon into the sample, and correlates this with the detection of a positron at the detector. The anisotropy of the decay positrons is calculated

by measuring the difference between the counts of the forward and backward detector positions.

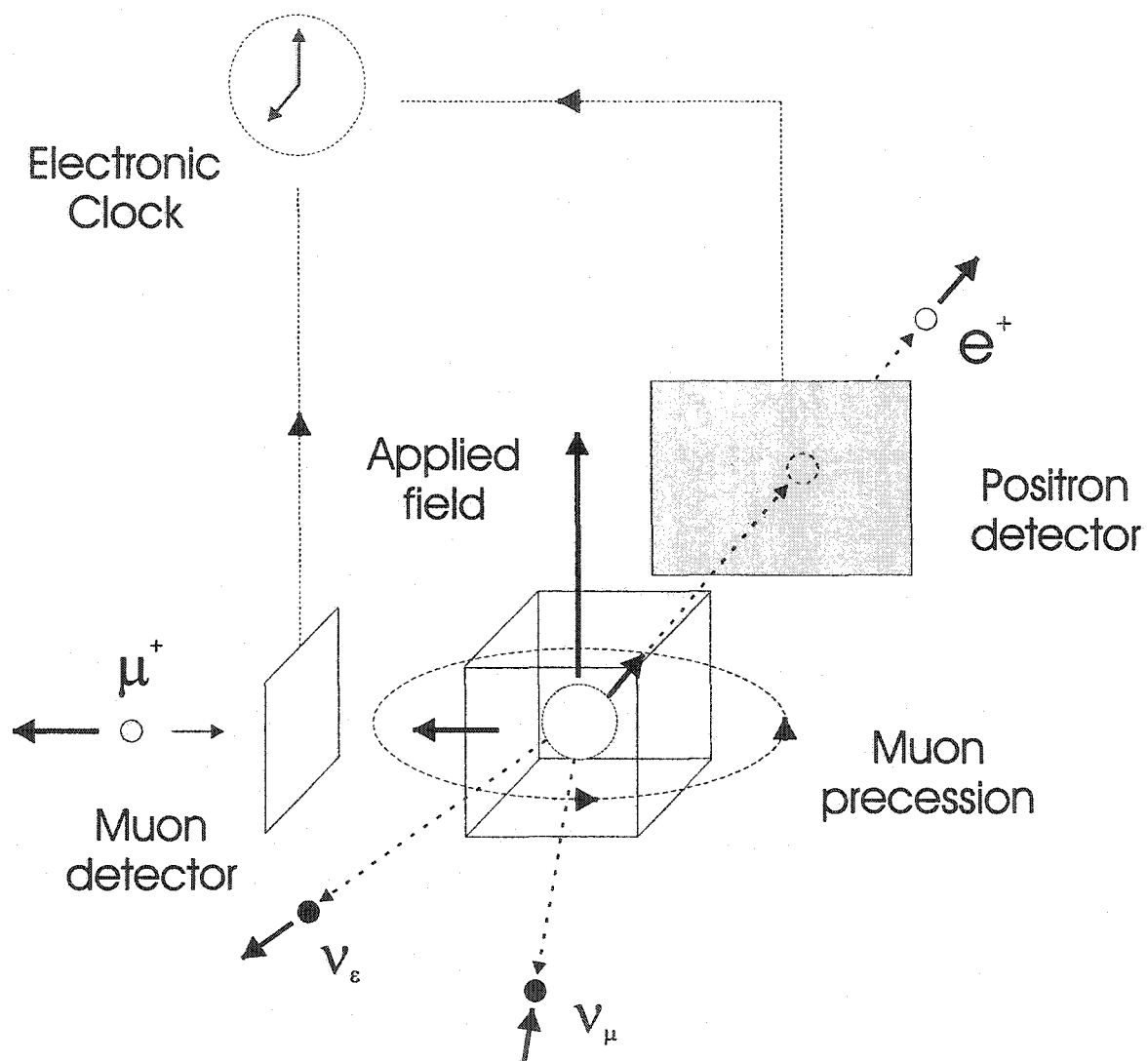


Figure XV: TF- μ SR (adapted from J. Sonier).²⁰ The smaller arrows in bold near the particles indicate the direction of their respective momenta.

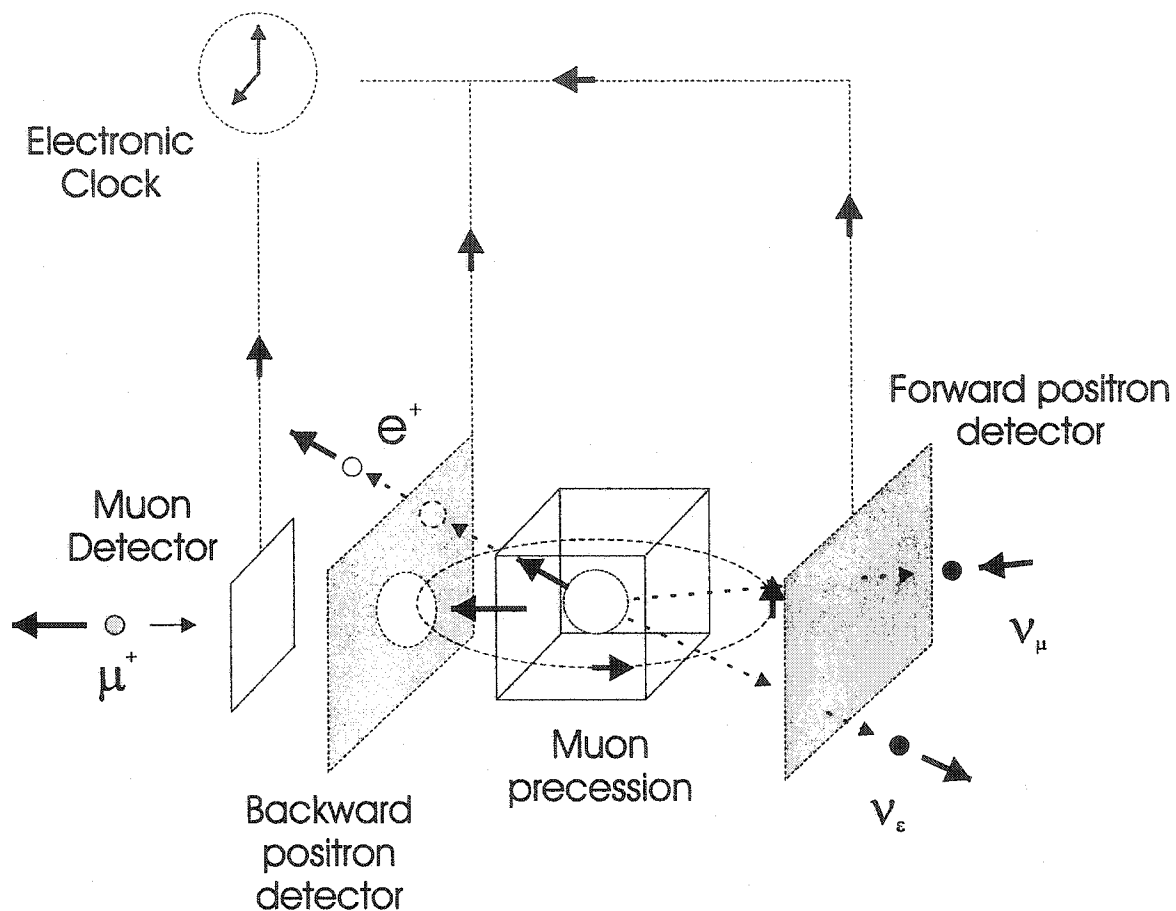


Figure XVI: ZF- μ SR (adapted from J. Sonier).²⁰ The smaller arrows in bold near the particles indicate the direction of their respective momenta.

The transverse technique, TF- μ SR, measures the precession of the muon about the applied field with a frequency that is proportional to the internal field at the muon site (the Larmor frequency). The longitudinal technique, LF- μ SR, is adept at measuring weak magnetism. The zero field method, or ZF- μ SR, is particularly well-suited for studies of very weak magnetism, such as small ordered moments or random moments that are seen in spin glasses. It is this technique which will be described in the rest of this chapter.

As mentioned above, the asymmetry function is measured in the LF/ZF- μ SR method, which is expressed as $G_z(t)$ (for a field applied in the z-direction):

$$(52) \quad G_z(t) = \frac{P_z(t)}{P_z(0)} \sim \frac{F(t) - \alpha B(t)}{F(t) + \alpha B(t)}$$

where the ratio $P_z(t)/P_z(0)$ is the normalized asymmetry, which can be calculated as a difference between the forward detector $F(t)$ and backward detector $B(t)$ counting rates. The ratio α is a correction for the counting efficiency of the two detectors, $\alpha = A_F/A_B$.

For a muon at rest in an array of static, but randomly oriented distribution of dense magnetic fields, the Kubo-Toyabe function describes the spin polarization function, P_μ , which is measured as the anisotropy in a LF/ZF- μ SR experiment:²¹

$$(53) \quad G_z(t) = \frac{1}{3} + \frac{2}{3}(1 - \Delta^2 t^2) \exp\left(-\frac{1}{2} \Delta^2 t^2\right)$$

where Δ/γ_μ is the width of the local magnetic field distribution and γ_μ is the gyromagnetic ratio of the muon ($0.085 \mu\text{s}^{-1} \text{G}^{-1}$). For long time scales, this function relaxes to a value of 1/3, whereas for short time scales there is a gaussian lineshape (see figure XVII).

For dynamic fields, the polarization function has an exponential decay which is described by:

$$(54) \quad G_z(t) \sim \exp(-\Lambda t)^{1/2}$$

where Λ is the fluctuation rate. This lineshape usually appears at the onset of fluctuations near a phase transition, or with strong paramagnetism.

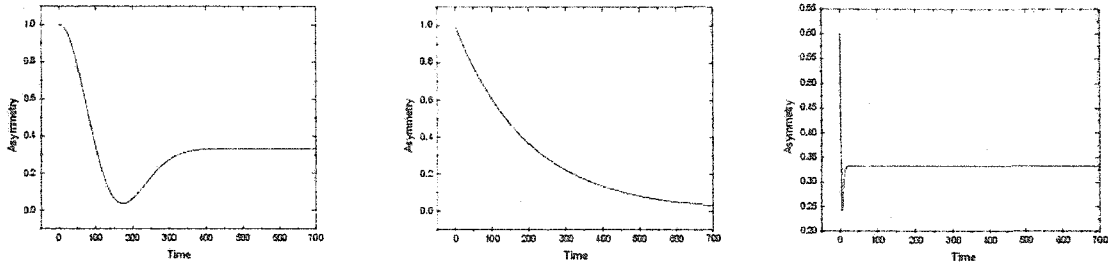


Figure XVII: The Kubo-Toyabe lineshape, dynamic fluctuation spectra, and typical spin glass lineshape.

Weak magnetism, such as that seen for spin glasses, will result in a broad distribution of local fields, and a modification of the Kubo-Toyabe function that includes a sharp increase at short time intervals (as first done by Uemura *et al*):²²

(55)

$$G_z(t) = \frac{1}{3} \left[\exp\left(-\left(4\alpha_d^2 t / \nu\right)^{1/2}\right) \right] + \frac{2}{3} \left[1 - \frac{\alpha_s^2 t^2}{\left(4\alpha_d^2 t / \nu + \alpha_s^2 t^2\right)^{1/2}} \right] \exp\left[-\left(4\alpha_d^2 t^2 / \nu + \alpha_s^2 t^2\right)^{1/2}\right]$$

where ν is the spin fluctuation rate, and α_s and α_d are the static and dynamic spin components. This increase in relaxation is interpreted as an order parameter, but it is often difficult to quantify unless one has a conventional spin glass. Note here that the function is modified by an exponential term, which accounts for spin fluctuations. Loss of muon polarization could also occur by slow movements of the muon probe throughout the lattice.

For very dilute spin glasses, this function reduces to the Lorentzian distribution, which one can readily derive by taking the limit of equation 55 as the dynamic component, α_d , approaches zero.

$$(56) \quad G(t) = \frac{1}{3} + \frac{2}{3}[1 - \alpha_s t] \exp(-\alpha_s t)$$

This expression is typically used for a system of dilute, random moments as opposed to the gaussian distribution, which is for more dense systems. For temperatures much smaller than the freezing temperature, equation 56 can be used to describe the data. However, a more rigorous approach is to use Uemura's function (55), which includes the dynamics which may still be present.

References

- (1) N. W. Ashcroft and N. D. Mermin, *Solid State Physics* (Holt, Rinehart and Wilson, New York, 1976).
- (2) S. W. Lovesey, *Theory of Neutron Scattering from Condensed Matter* (Oxford, New York, 1984).
- (3) A. Beiser, *Concepts of Modern Physics* (McGraw-Hill, Inc., New York, 1987).
- (4) R. A. Young, *The Rietveld Method* (Oxford University Press, Oxford, 1993).
- (5) J. S. Higgins and H. C. Benoît, *Polymers and Neutron Scattering* (Oxford University Press, Oxford, 1994).
- (6) G. Stout and L. Jensen, *X-ray Structure Determination; a practical guide* (Macmillan, New York, 1968).
- (7) SHELX software refinement manual
- (8) G. L. Squires, *Introduction to the Theory of Neutron Scattering* (Dover, Mineola, 1996).
- (9) M. Collins, *Magnetic Critical Scattering* (Oxford University Press, New York, 1989).

- (10) O. Halpern and M. H. Johnson, *Phys. Rev.*, **55**, 898 (1939).
- (11) C. R. Wiebe, J. E. Greedan, G. M. Luke, and J. S. Gardner, *Phys. Rev. B*, **65**, 144413 (2002).
- (12) L. Pauling, *Z. Krist.*, **67**, 377 (1928).
- (13) I. D. Brown and R. D. Shannon, *Acta. Crys.*, **A29**, 266 (1973).
- (14) R. White, *Long Range Order in Solids* (Academic Press, New York, 1979).
- (15) Quantum Design. *Fundamentals of magnetism and magnetic measurements*, 1994.
- (16) J. Clarke, *Scientific American*, **8**, 46 (1994).
- (17) Oxford Instruments. *MAGLAB Heat Capacity Manual*, 1999.
- (18) http://muon2.physics.mcmaster.ca/luke/Luke_GM_h.html
- (19) S. L. Lee, S. H. Kilcoyne, R. Cywinski, *Muon Science: Muons in Physics, Chemistry and Materials* (Institute of Physics Publication, Philadelphia, 1999).
- (20) Courtesy of J. Sonier
- (21) R. Kubo, *Hyperfine Interactions*, **8**, 731 (1981).
- (22) Y. J. Uemura, T. Yamazaki, D. R. Harshman, M. Senba, E. J. Ansaldo, *Phys. Rev. B*, **31**, 546 (1985).

Chapter Three
Charge and Magnetic Ordering in the
Electron-Doped Magnetoresistive
Materials $\text{CaMnO}_{3-\delta}$ ($\delta = 0.06, 0.11$)

This chapter incorporates the article “Charge and Magnetic Ordering in the Electron-Doped Magnetoresistive Materials $\text{CaMnO}_{3-\delta}$ ($\delta = 0.06, 0.11$)” which has been published in Physical Review B (Physical Review B, Volume 64, 064421, 2001).

Charge and Magnetic Ordering in the Electron-Doped Magnetoresistive Materials $\text{CaMnO}_{3-\delta}$ ($\delta = 0.06, 0.11$)

C. R. Wiebe and J. E. Greedan

*The Brockhouse Institute for Materials Research, McMaster University, Hamilton, ON
L8S 4M1, Canada*

J. S. Gardner

*The Neutron Program for Materials Research, NRC, Chalk River Labs, Chalk River, ON
K0J 1J0, Canada*

Z. Zeng and M. Greenblatt

*Chemistry Department, Rutgers University, Piscataway, NJ
08854-8087, USA*

ABSTRACT

The magnetoresistive “electron”-doped materials $\text{CaMnO}_{3-\delta}$ ($\delta = 0.06, 0.11$) have been investigated using powder neutron diffraction. The two materials are n-type semiconductors which exhibit antiferromagnetic ordering at $T_N \sim 125$ K, but they have different magnetic structures. The $\text{CaMnO}_{2.94}$ sample orders in a simple G-type antiferromagnetic structure, which is also observed in CaMnO_3 . The $\text{CaMnO}_{2.89}$ sample, on the other hand, exhibits two magnetic features: the G-type reflections as noted above, and a set of reflections that can be indexed on a $k = (0, 0, \frac{1}{4})$ ordering wavevector. A model for the magnetic structure is proposed which involves $\text{Mn}^{3+}/\text{Mn}^{4+}$ charge ordering concomitant with the magnetic ordering. The presence of a set of weak, temperature independent structural reflections which can also be indexed on a $k = (0, 0, \frac{1}{4})$ supercell suggests an oxygen vacancy ordering which may play a role in the charge ordering.

INTRODUCTION

The search for new magnetoresistive materials has commanded much attention for the past few years due to the enormous variety of fascinating physical properties exhibited.^{1,2,3} The need for new magnetic recording devices has provided a further impetus for the discovery of CMR and GMR materials, and an understanding of the phenomena at some fundamental level. In recent years, the perovskite LaMnO_3 has been the target of extensive doping, usually by "hole"-doping, i.e. substituting the La^{3+} ion by M^{2+} ions such as Ca, Sr, Ba, or Pb. The $\text{La}_{1-x}\text{M}_x\text{MnO}_3$ system has been studied extensively, and has been found to exhibit a wide range of magnetic structures, and varying levels of magnetoresistance (MR) effects depending on the dopant concentration.^{4,5,6} The interplay between magnetic, charge, and orbital ordering in particular has been the target of intense activity leading to the discovery of a rich and varied set of phase diagrams of these materials in different doping regimes.

In contrast, the system $\text{CaMnO}_{3-\delta}$ offers another route to explore the mechanisms of magnetoresistance by providing a means to control the electron doping levels rather than the hole concentrations.⁷ The $\text{CaMnO}_{3-\delta}$ system has been studied for stoichiometric concentrations (such as $\delta = 0$ and $\delta = 0.5$)⁸ but it has been only recently that other compounds in this series have been revisited. Previous electron diffraction experiments have revealed the existence of possible oxygen vacancy ordering for commensurate values of δ (0.2, 0.25, 0.33, 0.5) as evidenced through observed superlattice reflections.⁹ As each oxygen vacancy creates two Mn^{3+} sites, this indicated that there should exist exchange pathways of Mn(III)-O-Mn(IV) , which could possibly lead to interesting one-dimensional properties in these materials.¹⁰

The demonstration of magnetoresistance in the $\text{CaMnO}_{3-\delta}$ system which is heavily dependant on the oxygen vacancy concentration has rekindled interest in this material, and the connection with magnetic double exchange interactions and possible CMR.⁷ Magnetic susceptibility measurements have indicated the presence of a large and negative Weiss constant and several unusual low temperature features, which include a divergence in the

field-cooled and zero-field cooled data at about $T_N \sim 125$ K.¹⁰ This has been interpreted as an antiferromagnetic phase transition, as noted by Wollan and Koehler¹¹ in the parent compound CaMnO_3 , but as of yet no magnetic neutron scattering measurements have been made on this series of materials.

This work details the first such study of $\text{CaMnO}_{3-\delta}$. An understanding of the subtle ordering in these materials is crucial to a complete understanding of the magnetoresistance phenomena.

EXPERIMENTAL PROCEDURES

Powder samples of $\text{CaMnO}_{3-\delta}$ ($\delta = 0.06, 0.11$) were prepared by the Pechini citrate gel process.⁷ Stoichiometric quantities of $\text{Mn}(\text{NO}_3)_2$ (Aldrich, 49.7% w/w aqueous solution) and CaCO_3 (Aldrich, 99+ %) were dissolved in excess amounts of nitric acid, citric acid, and ethylene glycol. After drying, the resin was heated to 600°C to decompose the organic impurities, and the resultant material was pressed into pellets for firing. The samples were sintered in air to 1100°C for 24 h, and then quenched, at 1100 and 1000°C for the $\delta = 0.11$ and 0.06 , respectively, to room temperature.

The products were characterized using the facilities at Rutgers University. Powder x-ray diffraction data was obtained using a SCINTAG PAD V diffractometer with Cu K_α radiation and a silicon standard. The resultant lattice parameters were refined using a least squares minimization technique. The magnetic susceptibility from $4 - 400$ K was measured using a SQUID magnetometer (MPMS, Quantum Design), and magnetoresistive properties were observed using a standard four-probe technique.⁷

Magnetic measurements were confirmed at McMaster University using a Quantum Design MPMS SQUID magnetometer. Field cooled (FC) and zero field cooled runs (ZFC) were completed in a temperature range of 5 to 350 K with an applied magnetic field of 0.01 T.

Neutron scattering experiments were completed on the powder samples at the

Dualspec C2 beamline operated by the Neutron Program for Materials Research of the National Research Council of Canada at the Chalk River Laboratory. The wavelength of the neutrons was $\lambda = 2.37086(9)$ Å. The samples were sealed in vanadium cans in a He atmosphere with an indium wire gasket. Data were taken over a temperature range of 11 K to room temperature, covering a range in 2θ of 10° to 90° . The room temperature data sets were obtained out to $2\theta = 120^\circ$ to obtain a very accurate determination of the crystallographic unit cell. The Rietveld refinements of the datasets were completed using FULLPROF (FULL98). The $\text{CaMnO}_{2.89}$ sample was found to have two very similar crystallographic phases (one of them comprising approximately 25 % of the material), which was confirmed by x-ray experiments done at McMaster using a Cu $K_{\alpha 1}$ source and a Guinier-Hägg camera with Si as an internal standard. As a result, a three-phase refinement was carried out on this material, two crystallographic and one magnetic in origin.

RESULTS

Structure of $\text{CaMnO}_{2.94}$

The crystal structure and lattice parameters of $\text{CaMnO}_{2.94}$ were consistent with the values found using x-ray diffraction at Rutgers University. $\text{CaMnO}_{2.94}$ crystallizes in an orthorhombic perovskite structure with space group $Pnma$ (table I). The Mn ions form a network of corner-shared octahedra, with Ca ions occupying the interstitial positions (figure I). The increased size of the unit cell as oxygen defects are introduced is expected as the Mn^{3+} ion has a slightly larger radius than Mn^{4+} .¹² The oxygen defects are found from refinement to be on the shared corners of the equatorial plane of the Mn octahedra; the O2 positions of $8d$ symmetry (table II and figure IIa). The defect concentration correlates well with the titration analysis (roughly 6 % oxygen defects, or 12 % Mn^{3+} concentration for $\text{CaMnO}_{2.94}$). Each O defect creates two Mn^{3+} sites in the lattice, which effectively provides a method for electron doping these materials, in contrast to hole doping as in the $\text{La}_{1-x}\text{Ca}_x\text{MnO}_3$ series.¹³

	a	b	c	T _N	μ _{ordered}	μ _{eff} (exp) μ _{eff} (calc)	θ _C
CaMnO _{2.94}	5.2729(6) Å	7.4416(6) Å	5.2554(6) Å	126.0(8) K	2.36(4) μ _B	4.44(1) μ _B 3.99 μ _B	-529(1)K
CaMnO _{2.89}	5.270(2) Å	7.473(2) Å	5.284(2) Å	126(2) K 127(3) K	2.45(20) μ _B 4.00(30) μ _B	4.89(1) μ _B 4.10 μ _B	-450(2)K
CaMnO _{2.89} impurity	5.220(2) Å	7.483(3) Å	5.325(2) Å	-	-	-	-

Table I. Room temperature lattice parameters and magnetic properties of CaMnO_{3-δ}. The Néel temperatures and ordered moments are quoted from the refinements. The two values under the CaMnO_{2.89} compound are for the Mn⁴⁺ and Mn³⁺ sites respectively. The lattice constants for the CaMnO_{2.89} impurity phase are listed for comparison.

CaMnO _{2.89}	x	y	z	Occ.	CaMnO _{2.94}	x	y	z	Occ.	B _{iso} (Å ²)
Ca	.043(8)	.25	-.004(12)	1.0	Ca	.033(1)	.25	-.013(3)	1.0	0.58(21)
Mn	0	0	0.5	1.0	Mn	0	0	0.5	1.0	0.05(27)
O(1)	.480(7)	.25	-.079(6)	1.0	O(1)	.489(1)	.25	.055(2)	1.0	0.42(22)
O(2)	.271(9)	.0180(6)	-.293(6)	0.92(4)	O(2)	.288(1)	.038(1)	-.287(1)	0.96(2)	0.42(22)

Table II. Refined Atomic Positions and Their Estimated Standard Deviations at T = 11 K (CaMnO_{2.89}) and T = 14 K (CaMnO_{2.94}). The thermal parameters were refined from the CaMnO_{2.94} data and left constant in the CaMnO_{2.89} refinements.

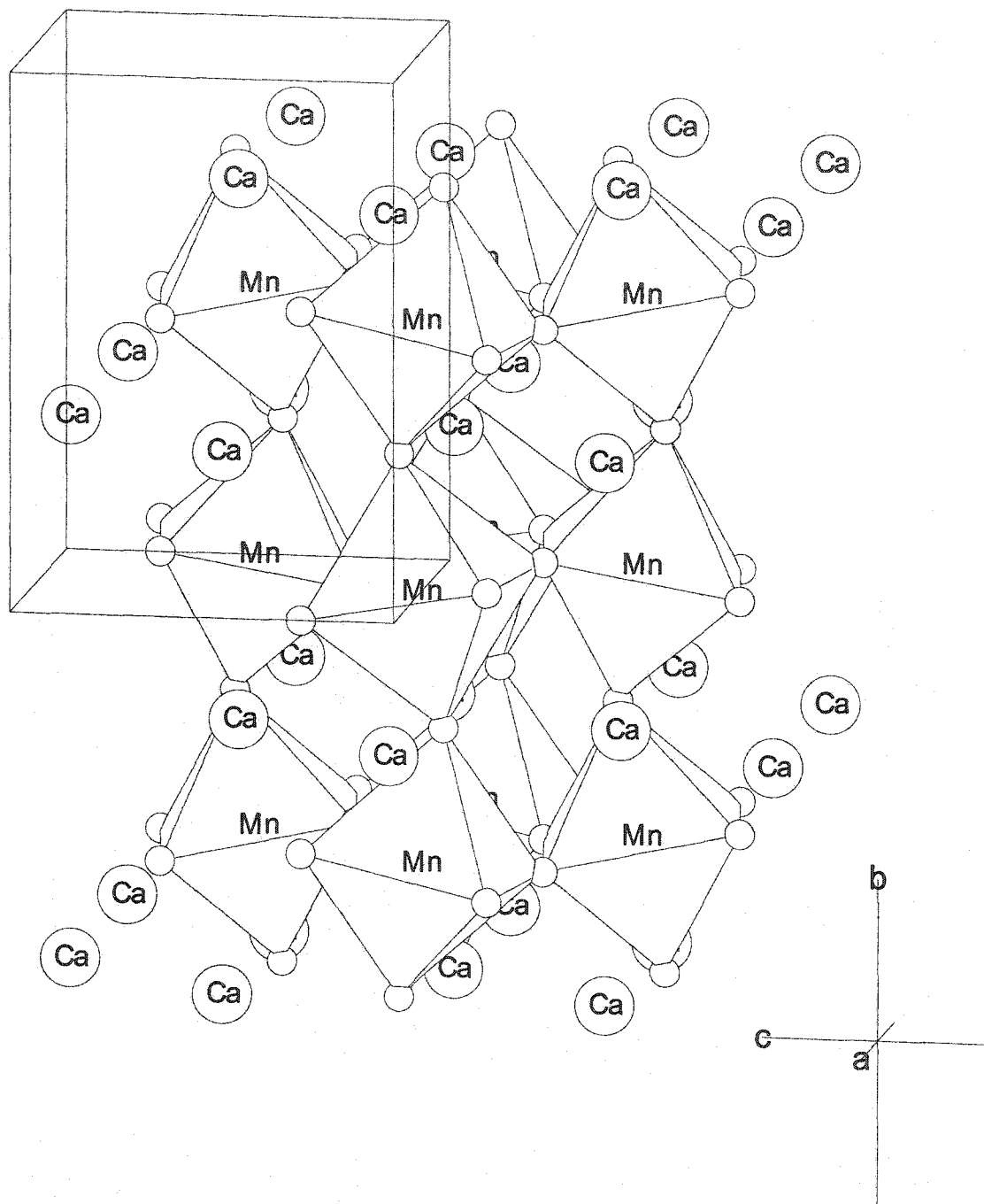


Figure I. The crystal structure of $\text{CaMnO}_{2.94}$

Structure of CaMnO_{2.89}

The full refinement of the CaMnO_{2.89} sample proved to be much more difficult than the CaMnO_{2.94} member in the series. Attempts were first made using the lattice constants and space group Pnma as reported previously.⁷ The results of these refinements were not unreasonable, but upon closer examination, it was clear that some relatively strong reflections, in particular the strong secondary peak at $2\theta \sim 66^\circ$ could not be indexed (see figure IIb). There were also a set of weak peaks which were first thought to be due to an impurity phase.

In a first attempt to analyze the data the presence of a structurally similar impurity phase was assumed. In this doping regime, reports of impurity phases are not uncommon. For example, Chiang and Poeppelmeier found such an impurity phase in CaMnO_{2.75}.¹⁴ Santhosh *et al.* investigated the series of related materials Ca_{1-x}Bi_xMnO₃ in the regime $x \leq 0.25$, and found that for the Bi_{0.18}Ca_{0.82}MnO₃ compound in particular, a crystallographically similar impurity phase was present at about 29 % wt concentration.¹⁵ Clearly, this region of the phase diagram is prone to phase separation.

Cell constants for a perovskite-like orthorhombic impurity phase were refined from powder x-ray data obtained with Cu K α_1 radiation and a Guinier-Hägg camera ($a = 5.228(1)$ Å, $b = 7.488(1)$ Å, and $c = 5.3302(9)$ Å at $T = 290$ K). In the two phase refinement the atomic positions of the impurity phase were fixed to those of CaMnO_{2.94} and the scale factor was varied. The concentration of the impurity phase was seen to be ~ 25 wt % by comparison of the scale factor for the two phases. Final atomic positions for the majority phase are listed in Table IIb. The temperature factors were found to be unstable in the refinements, and were set to the values found for CaMnO_{2.94}.

While the two phase approach accounts for the strong reflections in the powder pattern, several very weak reflections (< 1 % intensity of a strong reflection) remained unindexed (figure III). Thus, an attempt was made to index these on a supercell. Again, Chaing and Poeppelmeier observed a set of weak reflections in CaMnO_{2.75} which could be indexed on a $a \times b \times 4c$ supercell (Pnma setting) which they attributed to the ordering of

oxygen vacancies. They were not successful, however, in refining an unique model for the vacancy ordering. Using 8 – 10 weak reflections of the type shown in figure 3, a supercell, also of dimensions $a \times b \times 4c$ (Pnma subcell setting) could be assigned to the major phase in $\text{CaMnO}_{2.89}$.

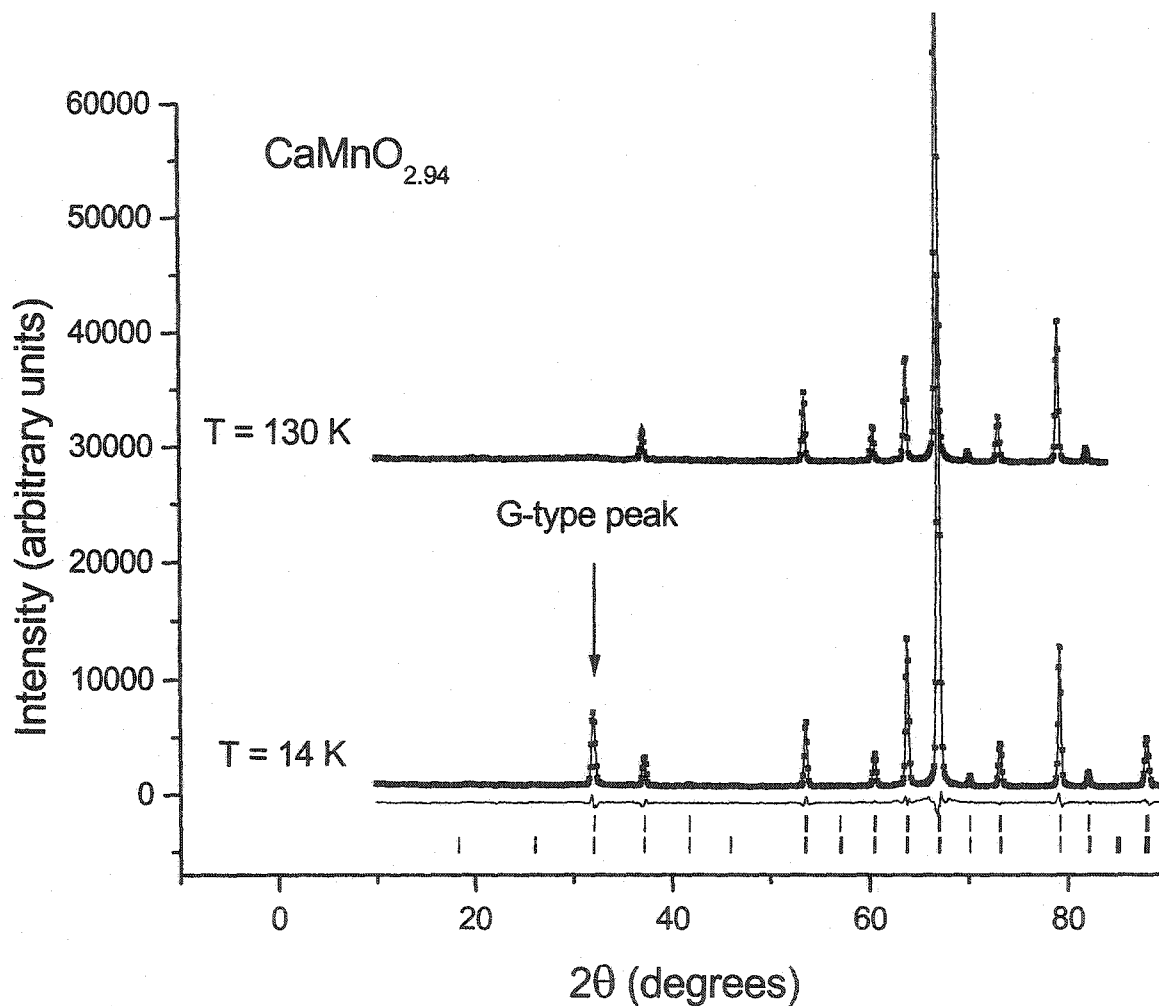


Figure II. (a) The neutron diffraction pattern of $\text{CaMnO}_{2.94}$ at $T = 14 \text{ K}$ and $T = 130 \text{ K}$. The upper set of tickmarks are for the crystallographic reflections, and the lower are for the magnetic phase.

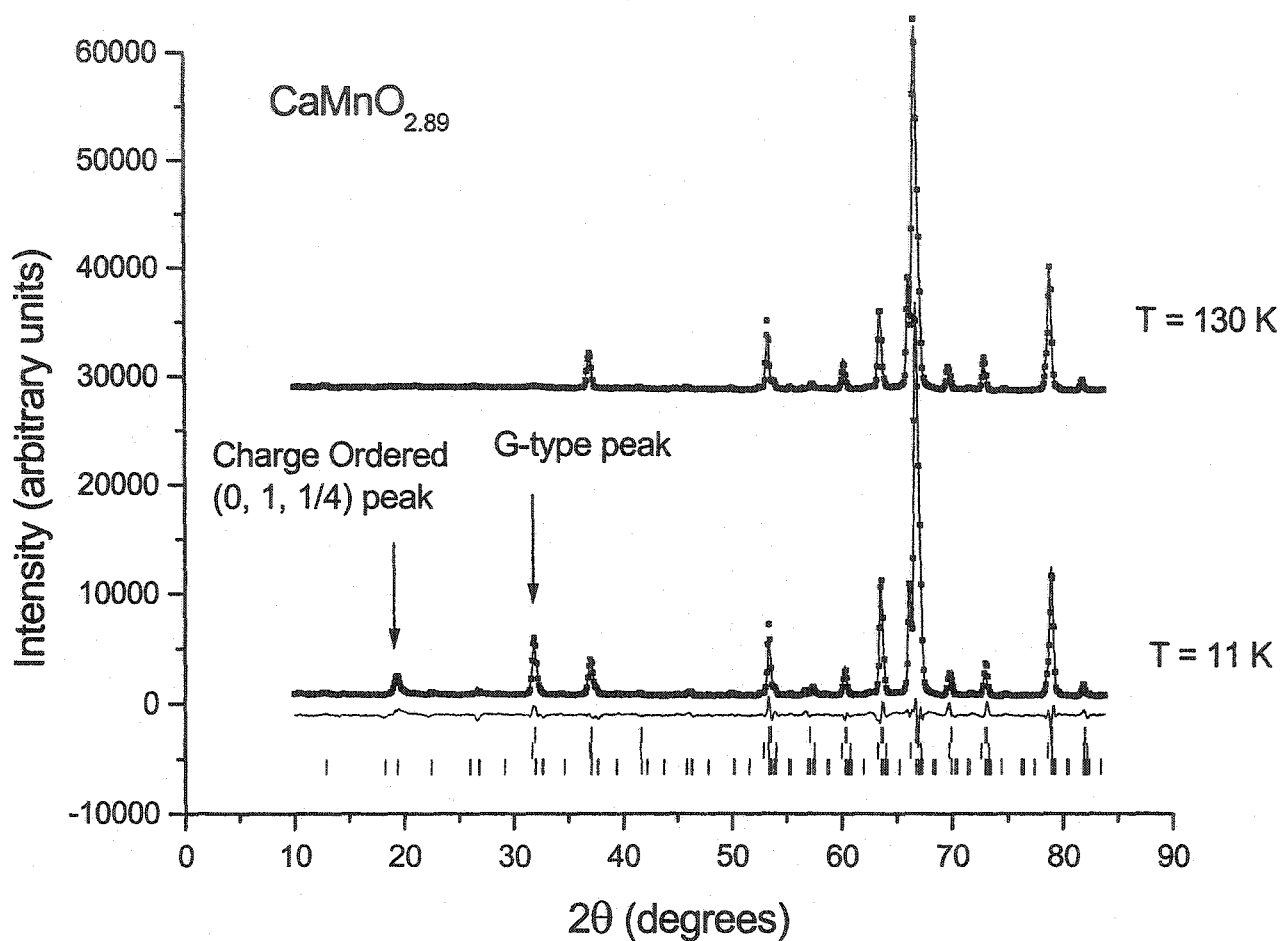
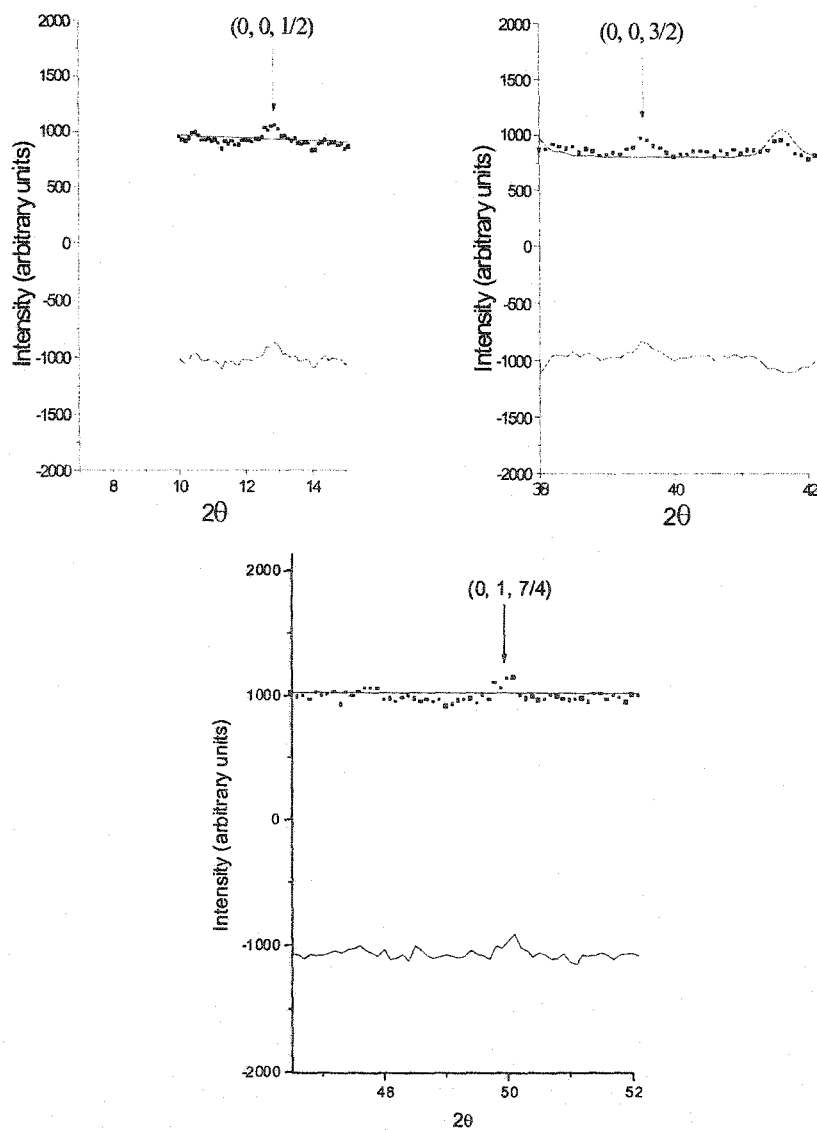


Figure II. (b) The neutron diffraction pattern of CaMnO_{2.89} at T = 11 K and T = 130 K. The upper set of tickmarks are for the primary CaMnO_{2.89} phase, the middle set are for the crystallographic impurity, and the bottom set is for the G-type + charge-ordered structures.

As in the case of Chiang and Poeppelmeier, attempts to refine a unique model for the

vacancy ordering were unsuccessful due in part to the weakness of the superlattice reflections and the complicating factor of the second phase. It is thus likely that even at room temperature there exists oxide vacancy ordering in the majority phase in $\text{CaMnO}_{2.89}$ but a detailed model is not available. Although it has been suggested that oxide vacancy ordering may induce $\text{Mn}^{3+}/\text{Mn}^{4+}$ charge ordering, this cannot be confirmed from the present data.

Figure III. Evidence of possible vacancy ordering in $\text{CaMnO}_{2.89}$. The superstructure peaks $(0, 0, 1/2)$, $(0, 0, 3/2)$, and $(0, 1, 7/4)$ are shown here at $T = 130$ K, which along with other weak reflections can be indexed on the cell $a \times b \times 4c$.



	CaMnO _{2.94}	CaMnO _{2.89}
	(T = 14 K)	(T = 11K)
Mn – O(1)	1.8840(14) Å x2	1.9173(74) Å x2
Mn – O(2)	1.9077(14) Å x2	1.965(40) Å x2
	1.8986(52) Å x2	1.806(45) Å x2
O(2)-Mn-O(2)	88.89(36)	89.82(79)
	91.11(39)	90.18(91)
O(1)-Mn-O(2)	87.63(38)	84.16(86)
	92.37(34)	95.84(88)
	91.75(22)	95.20(84)
	88.25(36)	85.81(80)
Mn-O(1)-Mn	161.850(64)	154.04(31)
Mn-O(2)-Mn	155.87(22)	163.28(92)

Table III. Selected Interatomic Distances and Bond Angles

Magnetism in CaMnO_{2.94}

The magnetic structure of CaMnO₃ was among the first to be studied with neutron diffraction.¹¹ The magnetic Mn⁴⁺ sublattice consists of two interpenetrating face centred arrays of moments with antiparallel nearest neighbour spin arrangements, the so-called type G structure (figure V). The Néel temperature is 130 K, and the effective magnetic moment is 2.43 μ_B, which agrees well with the spin-only value for Mn⁴⁺ (3.00 μ_B).¹¹

Previous magnetic susceptibility measurements indicated a feature at 125 K which implied the possibility of long range antiferromagnetic ordering in both CaMnO_{2.94} and CaMnO_{2.89}.⁷ Our measurements confirm this in the FC/ZFC CaMnO_{2.94} and CaMnO_{2.89} data sets (figure IV). The sharp cusp in the ZFC susceptibility at T ~ 125 K is a telltale sign of antiferromagnetic ordering in both materials. The values for the effective moments and the Weiss constants extracted from high temperature Curie-Weiss fits (T = 300 – 350 K) agreed

well with the published results, indicating a mixture of Mn^{3+} and Mn^{4+} moments and strong antiferromagnetic interactions.⁷ The differences between the experimental and calculated effective moments have been attributed to ferromagnetic interactions from Mn^{3+} - Mn^{4+} clusters.¹⁰

From the neutron diffraction data, figure IIa, the magnetic structure of $\text{CaMnO}_{2.94}$ was readily identified as the G-type found for CaMnO_3 (figure V). The Rietveld refinements produced very acceptable R-values for the crystallographic and magnetic phases ($R_p = 4.02$, $R_{wp} = 5.58$, $R_{mag} = 2.12$ at $T = 14$ K). The value for the ordered moment was found to be slightly smaller, $\mu = 2.36(4) \mu_B$, compared to the value for CaMnO_3 of $2.43 \mu_B$.¹¹ This is somewhat surprising as the average Mn moment should be larger, given that a larger spin-only moment ($4.0 \mu_B$) should be associated with Mn^{3+} which comprise $\sim 12\%$ of the Mn sites.

The behaviour of the ordered moment as a function of temperature is typical of 3d Heisenburg-like ordering (figure VI). More precise measurements of the order parameter are needed to get an exact determination of the phenomena, but a guide to the eye has been drawn based upon the following scaling relationship¹⁶

$$(1) \quad M(T) \sim \{(T-T_C)/T_C\}^{2\beta}$$

The values extracted from the fit, $\beta = 0.32(4)$ and $T_C = 126.0(8)$ K, are consistent with $\beta = 0.33$ and $T_C \sim 125$ K, as determined from the magnetic susceptibility measurements.

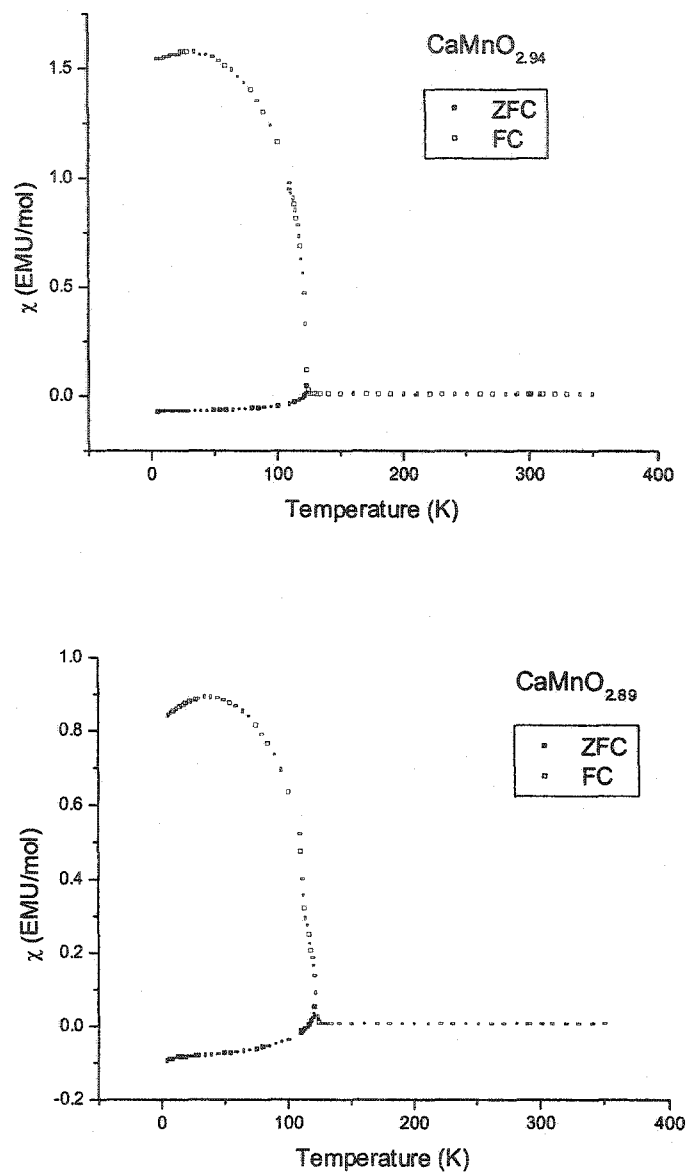


Figure IV. The magnetic susceptibility of $\text{CaMnO}_{2.94}$ (top) and $\text{CaMnO}_{2.89}$ (bottom) for an applied field of $H = 0.01$ T.

Figure V. The magnetic structure of $\text{CaMnO}_{2.94}$ (G-type structure, on the left) and $\text{CaMnO}_{2.89}$ (G-type charge-ordered structure)

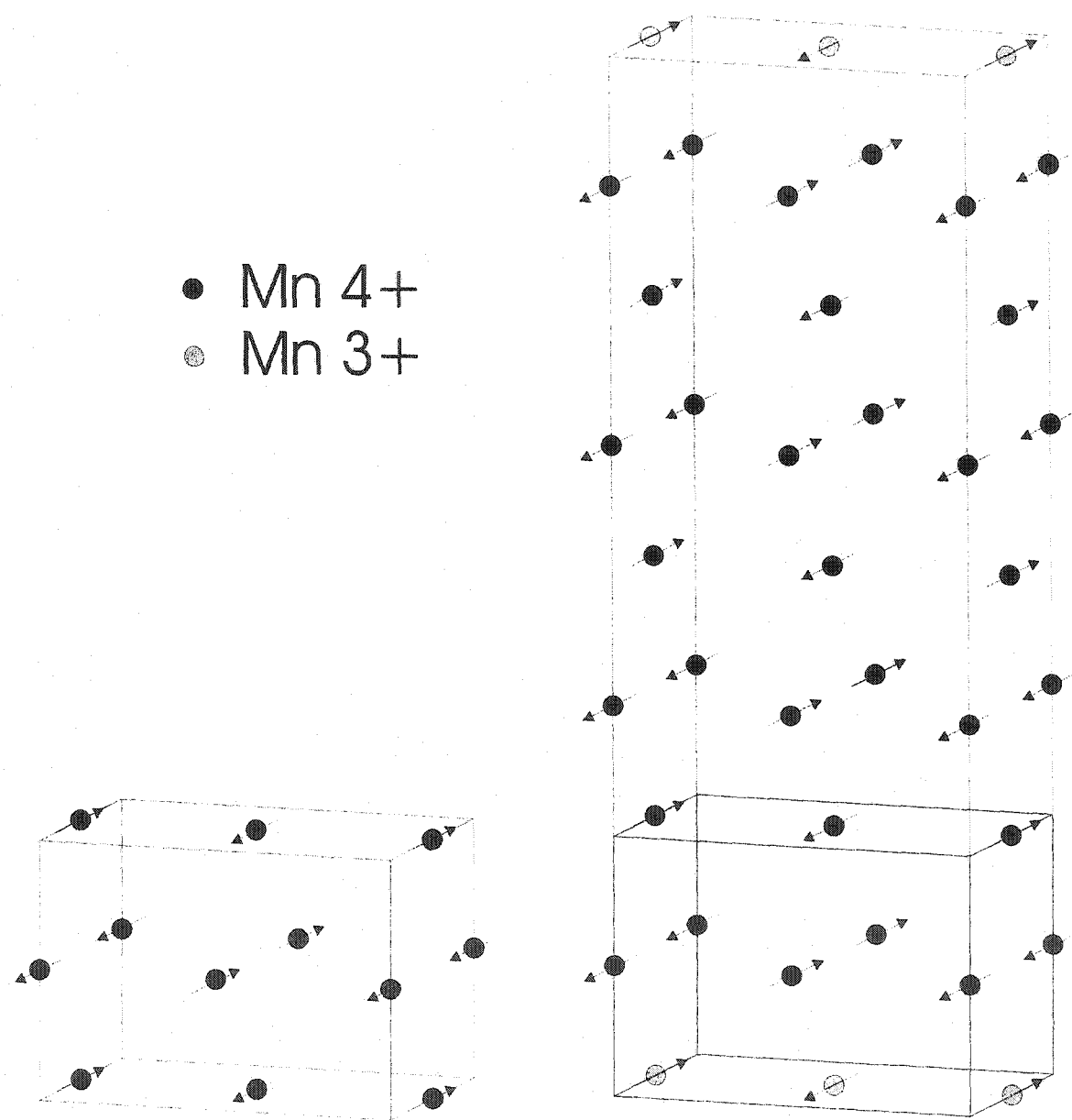
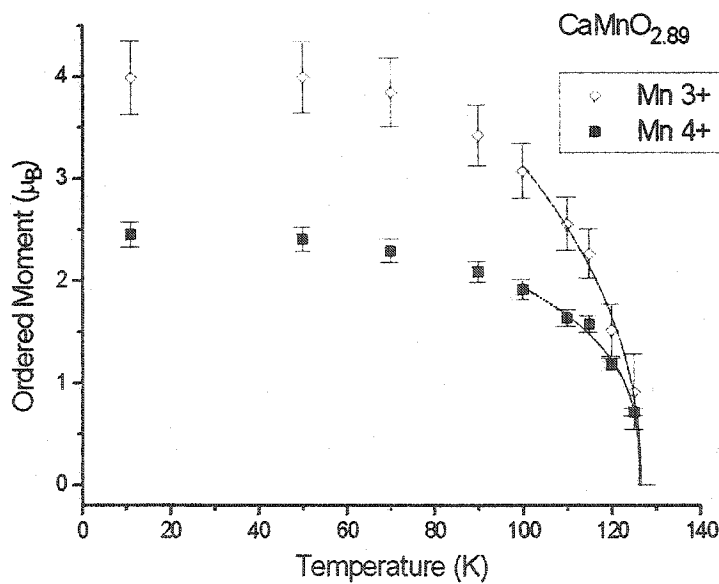
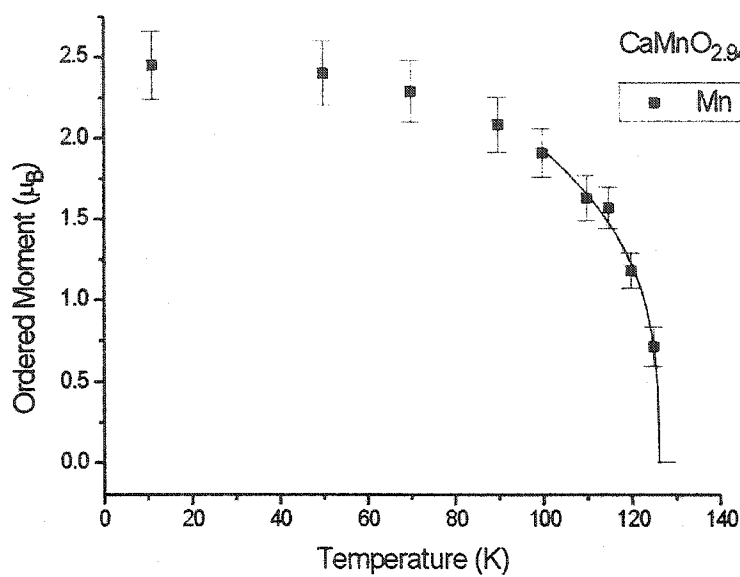


Figure VI. The ordered moment as a function of temperature for $\text{CaMnO}_{2.94}$ (top) and $\text{CaMnO}_{2.89}$ (bottom) as determined from neutron scattering measurements. The fits are guides to the eye based on the power law $M(T) \sim \{(T-T_C)/T_C\}^{2\beta}$



Magnetism in CaMnO_{2.89}

The magnetic Bragg peaks which appear below $T_N \sim 125$ K can be divided into two categories: the same “G-type” reflections as CaMnO_{2.94}, albeit of slightly altered intensities, and a set of reflections that can be indexed on a $(0, 0, \frac{1}{4})$ ordering wavevector (such as $(0, 1, \frac{1}{4})$, $(1, 1, \frac{1}{4})$, and $(0, 1, \frac{5}{4})$). Since the CaMnO_{2.89} sample has a higher concentration of oxygen defects, and hence a larger density of Mn³⁺ moments than CaMnO_{2.94}, it was hypothesized that the new Bragg peaks were due to an ordering of Mn³⁺ moments in the Mn⁴⁺ G-type network. The strongest new magnetic reflection in the diffraction pattern can be indexed as $(0, 1, \frac{1}{4})$. This points to an arrangement of Mn³⁺ moments that are antiferromagnetically coupled in rows along the b-direction and stacked with a periodicity of four in the c-axis direction (figure V). This model is appealing in that the G-type structure of CaMnO₃ and CaMnO_{2.94} is preserved for low Mn³⁺ doping levels while allowing for charge-ordering at higher doping levels. The full refinement of this model for the CaMnO_{2.89} dataset was complicated by a number of factors. Among them include the existence of a second crystallographic phase (comprising 25% of the sample), and a set of weak supercell reflections indicative of oxygen vacancy ordering. Several refinements were completed of the magnetic and charge ordered structures independently of one another until a suitable model was found to describe the observed diffraction pattern. Once a proper model was found, the charge and spin ordered phases were combined into one coherent model ($R_p = 7.86\%$, $R_{wp} = 10.71\%$, $R_{mag} = 25.6\%$ at $T = 11$ K).

However, the concentration of ordered Mn³⁺ ions in the model, 12.5 %, is not consistent with the concentration, 22 %, expected from the chemical analysis if one assumes that the electrons are completely localized on the Mn³⁺ sites. This suggests only partial charge ordering, with the residual Mn³⁺ moments distributed randomly on the lattice. Previous works have indicated that there is a significant reduction in the resistivity of this sample as compared to CaMnO_{2.94},⁷ which suggests that there is an increase in the density of states at the Fermi energy even below the ordering temperature. Further transport studies are needed to resolve this problem.

Although the magnetic structure described above appears to be unique for manganate perovskites, there is a recent report by Santhosh *et al.* which indicates that a weak magnetic superstructure has been reported for $\text{Bi}_{0.18}\text{Ca}_{0.82}\text{MnO}_3$ of the form $a \times b \times 4c$ but no detailed model has been proposed.¹⁵ As well, a C-type, not G-type AF order is found. There is clearly a structural analogy between the two materials, and further work is needed to understand them both.

The ordered moments for the two kinds of magnetic species seem to correlate well with the expected spin-only values for Mn^{4+} and Mn^{3+} ($2.45(20) \mu_B$ and $4.00(30) \mu_B$ respectively). The Néel temperatures for the type G and $k = (0, 0, \frac{1}{4})$ components, as determined by power law fits, agree to within experimental error ($126(2) \text{ K}$ and $127(3) \text{ K}$ respectively, figure VI).

DISCUSSION

It is natural to compare and contrast the results obtained for the oxygen vacancy doped compounds, $\text{CaMnO}_{3-\delta}$, with trivalent cation doped materials of similar electron doping levels (Mn^{3+} concentrations) in terms of issues such as charge-ordering and magnetic ordering, including the magnetic structure and magneto-transport properties. In fact, data on such systems are relatively sparse as most attention has been focussed on the hole-doped regime, i.e. Mn^{3+} concentrations $> 50 \%$ where CMR effects are observed. Nonetheless, the available data on systems such as $\text{M}_{0.20}\text{Ca}_{0.80}\text{MnO}_3$, where $\text{M} = \text{La}^{3+}$ or Bi^{3+} ,¹⁷ indicates that significant differences exist.

In the case of transport behaviour, the $\text{CaMnO}_{3-\delta}$ materials are much less conducting than their cation doped counterparts. As the previous study indicated,⁷ the room temperature resistivities for $\text{CaMnO}_{3-\delta}$ are in the range from 2 to $10 \Omega\text{-cm}$ even for relatively high doping levels, $\delta = 0.11$ ($\sim 22 \%$ Mn^{3+}) whereas the corresponding cation doped materials show values which are lower by factors of 10^2 to 10^3 , i.e., approaching (but not quite reaching) the metallic regime. This shows either that the e_g electrons are much less mobile or that the

nominal carrier density is much lower in the oxide vacancy than in the cation doped systems. Nonetheless, the observed negative magneto-resistances are of the same order of magnitude, 40-50 % for both series.

Concerning the issues of charge and magnetic ordering, for the cation doped compounds anomalies in the resistivity and magnetization at temperatures above T_C for magnetic AF order have been taken as evidence of charge ordering.¹ For example, $\text{La}_{0.20}\text{Ca}_{0.80}\text{MnO}_3$ shows such anomalies at about 195 K whereas AF order sets in only below ~ 120 K.^{18,19} Similar results are found for $\text{Bi}_{0.18}\text{Ca}_{0.82}\text{MnO}_3$ where T_{CO} (charge ordering) is 210 K and T_C (AF) = 160 K. In sharp contrast $\text{CaMnO}_{2.94}$ and $\text{CaMnO}_{2.89}$ show only a single anomaly in the susceptibility at 125 K which corresponds to T_C (AF) already shown. There is no indication of a higher temperature, T_{CO} , up to 300 K for either material, although, as has been argued, it is difficult to understand the magnetic structure of the majority phase in $\text{CaMnO}_{2.89}$ without postulating charge ordering. One is left with (at least) two alternatives, namely, that T_{CO} and T_C (AF) are coincident for $\text{CaMnO}_{2.89}$ or that $T_{CO} > 300 \text{ K} > T_C$ (AF). Possible support for the latter hypothesis is found in the form of the weak supercell reflections present already at 300 K which could be attributed to oxide vacancy ordering which may induce charge ordering as well by trapping Mn^{3+} centers in the vicinity of the vacancy. It should be noted that the charge ordering wave vector for $\text{Bi}_{0.18}\text{Ca}_{0.82}\text{MnO}_3$ was found to be incommensurate, while the oxide vacancy ordering wave vector appears to be commensurate, $k = (0, 0, \frac{1}{4})$. In $\text{La}_{0.20}\text{Ca}_{0.80}\text{MnO}_3$ two supercells were found from electron diffraction with “four-fold” and “23-fold” periodicities which were attributed to charge ordering.¹⁷ It is not clear at present if the “four-fold” structure is truly commensurate or if it is related to the one found in $\text{CaMnO}_{2.89}$ in the neutron diffraction data.

Finally, the basic magnetic structures are different for the cation and oxide vacancy doped phases. The C-type structure is found for both $\text{La}_{0.20}\text{Ca}_{0.80}\text{MnO}_3$ and $\text{Bi}_{0.18}\text{Ca}_{0.82}\text{MnO}_3$, while the G-type structure of CaMnO_3 is conserved for both oxide vacancy compounds studied here. In the C-type structure, one has ferromagnetic chains which are coupled antiparallel to nearest neighbour chains while all near neighbour correlations are antiferromagnetic in the G-type structure. We note that for $\text{Bi}_{0.18}\text{Ca}_{0.82}\text{MnO}_3$, $\theta_C = 160 \text{ K}$, a

large positive value consistent with dominant ferromagnetic exchange, whereas, $\theta_C = -529$ K and -450 K for $\text{CaMnO}_{2.94}$ and $\text{CaMnO}_{2.89}$, respectively, which demonstrate dominant antiferromagnetic exchange.

Further work on these materials, especially $\text{CaMnO}_{2.89}$, should include high resolution x-ray diffraction, as for example reported recently for several members of the series, $\text{Bi}_x\text{Ca}_{1-x}\text{MnO}_3$ and $\text{La}_{0.333}\text{Ca}_{0.667}\text{MnO}_3$,²⁰ in order to establish definitively the nature of the phase separated material near $\text{CaMnO}_{2.89}$. Electron diffraction studies should be carried out to determine if the formation of stripe domains, reported recently for the cation doped systems, is also a feature of the vacancy doped materials.

CONCLUSIONS

The electron-doped MR materials $\text{CaMnO}_{2.94}$ and $\text{CaMnO}_{2.89}$ have been investigated using powder neutron diffraction. The $\text{CaMnO}_{2.94}$ structure orders in the G-type AF structure as reported by Wollan and Koehler, but the $\text{CaMnO}_{2.89}$ exhibits charge ordering of the $\text{Mn}^{3+}/\text{Mn}^{4+}$ moments in a new magnetic structure, $k = (0, 0, \frac{1}{4})$, that has not been reported before. The G-type arrangement of the moments is preserved as in $\text{CaMnO}_{2.94}$, but now there is an ordering of the Mn^{3+} moments in layers along the c-axis. There is some evidence for an ordering of the oxygen vacancies, which has the same supercell as the magnetic/charge ordered cell, illustrating the strong interplay between the structure, electronic, and magnetic properties of these materials. A complete model of the MR mechanism in these materials is still elusive.

ACKNOWLEDGEMENTS

The authors would like to express their gratitude to Ron Donaberger who assisted with the technical work involved with the neutron scattering experiments. C. R. Wiebe gratefully acknowledges support for this work from the Natural Sciences and Engineering Research Council in the form of a PGS B. This project was also supported through a research grant to J. E. Greedan through the Natural Sciences and Engineering Research Council. The work at Rutgers (M.G. and Z. Z.) was supported by NSF-DMR-96-13106.

REFERENCES

- 1) Y. Tokura and N. Nagaosa, *Science* **288**, 462 (2000).
- 2) S. Jin, T. H. Tiefel, M. McCormack, R. A. Fastnacht, R. Ramesh and L. H. Chen, *Science*, **264**, 413 (1994).
- 3) R. von Helmolt, J. Wecker, B. Holzapfel, L. Schultz, and K. Samwer, *Phys. Rev. Lett.* **71**, 2331 (1993).
- 4) Q. Huang, J. W. Lynn, R. W. Erwin, A. Santoro, D. C. Dender, V. N. Smolyaninova, K. Ghosh, R. L. Greene, *Phys. Rev. B* **61**, 8895 (2000).
- 5) P. M. Levy, *Science* **256**, 972 (1992).
- 6) P. Schiffer, A. P. Ramirez, W. Bao, S.-W. Cheong, *Phys. Rev. Lett.* **75**, 3336 (1995).
- 7) Z. Zeng, M. Greenblatt, and M. Croft, *Phys Rev B* **59**, 8784 (1999).
- 8) K. R. Poeppelmeier, M. E. Leonowicz, J. C. Scanlon, J. M. Longo, and W. B. Yelon, *J. Solid State Chem.* **45**, 71 (1982).
- 9) A. Reller, J. M. Thomas, D. A. Jefferson, and M. K. Uppal, *Proc. R. Soc. Lond.*

- A 394, 223 (1984).
- 10) J. Briátco, B. Alascio, R. Allub, A. Butera, A. Caneiro, M. T. Causa, and M. Tovar, *Phys. Rev. B* **53**, 14020 (1996).
 - 11) E. O. Wollan and W. C. Koehler, *Phys. Rev.* **100**, 545 (1955).
 - 12) R. D. Shannon, *Acta Cryst.* **A32**, 751 (1976).
 - 13) E. Herrero, J. Alonso, J. L. Martínez, M. Vallet-Regí, and J. M. González-Calbet, *Chem. Mater.* **12**, 1060 (2000).
 - 14) C. C. K. Chiang and K. R. Poeppelmeier, *Mat. Lett.* **12**, 102 (1991).
 - 15) P. N. Santhosh, J. Goldberger, P. M. Woodward, T. Vogt, W. Lee, A. Epstein, *Phys Rev B* **62**, 22 (2000).
 - 16) M. F. Collins, *Magnetic Critical Scattering* (Oxford, New York, 1989).
 - 17) Y. Murakami, D. Shindo, H. Chiba, M. Kikuchi, and Y. Syono, *J. Solid State Chem.* **140**, 331 (1998).
 - 18) P. N. Santhosh, A. Arulraj, P. V. Vanitha, R. S. Singh, K. Sooryanarayana, C. N. R. Rao, *J. Phys. Cond. Matt.* **11**, L27 (1999).
 - 19) Wei Bao, J. D. Axe, C. H. Chen, and S.-W. Cheong, *Phys. Rev. Lett.* **78**, 543 (1997).
 - 20) P. G. Radaelli, D. E. Cox, L. Capogna, S.-W. Cheong, and M. Marezio, *Phys. Rev. B* **59**, 14440 (1999).

Chapter Four

Synthesis, Structure, and Magnetic Behaviour of $\text{La}_5\text{Re}_3\text{MnO}_{16}$: A New Perovskite-Like Material

This chapter incorporates the article “Synthesis, Structure, and Magnetic Behaviour of $\text{La}_5\text{Re}_3\text{MnO}_{16}$: A New Perovskite-Like Material” which has been published in the Journal of Solid State Chemistry (Journal of Solid State Chemistry, Volume 151, Number 1, 31-39, 2000).* An appendix has been included which details the author’s contribution towards the article “Magnetism and the Magnetic Structure of the Pillared Perovskite $\text{La}_5\text{Re}_3\text{MnO}_{16}$ ”, which at the time of writing has been accepted for publication in the journal Solid State Sciences.**

* © 2000 Elsevier Science

** © 2002 Elsevier Science

**Synthesis, Structure, and Magnetic Behaviour of
 $\text{La}_5\text{Re}_3\text{MnO}_{16}$:
A New Perovskite-like Material**

C. R. Wiebe, A. Gourrier, T. Langet, J. F. Britten, and J. E. Greedan

*The Brockhouse Institute for Materials Research, McMaster University, Hamilton, ON
L8S 4M1, Canada*

ABSTRACT

Single crystals of $\text{La}_5\text{Re}_3\text{MnO}_{16}$ have been grown and characterized by x-ray diffraction. The crystal structure was found to be of triclinic symmetry, but with strong monoclinic pseudosymmetry and related to the structure of $\text{La}_5\text{Mo}_4\text{O}_{16}$.⁵ The atomic parameters were refined in the unconventional C-1 space group, which is derived from C2/m by suppressing the 2-fold axis. The structure is similar to the perovskites, consisting of layers of slightly distorted corner-sharing ReO_6 and MnO_6 octahedra. The layers are connected by Re_2O_{10} units which consist of distorted edge-sharing ReO_6 octahedra. The Re-Re bond in these units is found to be unusually short (2.4068(5) Å). The La atoms are in 3 different crystallographic environments. La(1) and La(2) are 8- and 7- fold coordinated respectively, and lie in chains in the ReO_6 and MnO_6 network. La(3) has a distorted cubic coordination in a cage formed by the Re_2O_{10} units. Bond valence sums are consistent with Mn^{2+} and Re^{5+} . Powder samples have also been synthesized for magnetic susceptibility measurements. The magnetic properties are complex. Curie-Weiss behaviour occurs only in the range 400 K – 600 K giving $C = 4.43 \text{ emu}\cdot\text{K}/\text{mol}$ and $\theta = -48(5) \text{ K}$, consistent with Mn^{2+} as the only magnetic ion and net antiferromagnetic coupling. A transition to a long range ordered state occurs below 160 K and a field-induced irreversibility sets in below 50 K. Isothermal magnetization-field data imply a complex H-T phase diagram and magnetic structure.

INTRODUCTION

The great interest in perovskite and layered perovskite-like materials over the last several decades in solid state chemistry has been driven by frequent discoveries of the fascinating electronic and magnetic properties that they possess.^{1,2} The accommodating nature of the octahedral framework of this structure has led to a plethora of compounds with a wide variety of physical properties by varying the cations A and B in the ABX_3 formula. Mixed valence materials have in particular shown promise as new candidates for exotic superconducting and magnetic ground states. The synthesis of lanthanum-transition metal oxides of mixed valence, for example, has led to the discovery of the celebrated high T_c superconducting ceramic, $La_{2-x}Ba_xCuO_4$,³ and other materials with low-dimensional electronic properties, such as $La_4Re_6O_{19}$,⁴ which both have perovskite-related structures. Although there are many such examples in the literature, new compounds are continually being discovered in this vast field of solid state science. This paper reports the synthesis of a new perovskite-like material, $La_5Re_3MnO_{16}$, which consists of two distinct layers: a rhenium-manganese layer of corner-shared octahedra and a rhenium-rhenium layer of edge-shared bioctahedra. The magnetic properties have also been investigated and the results point to a complex behaviour.

EXPERIMENTAL

Preparation of $La_5Re_3MnO_{16}$

Single crystals of $La_5Re_3MnO_{16}$ resulted during attempts to prepare La_3ReO_7 from a reactant mixture comprising of stoichiometric ratios of La_2O_3 and ReO_2 . A pellet of MnO_2 , intended to function as an oxygen source, was wrapped in platinum foil and included in the reaction tube. The powder mixture was well homogenized and pressed into a pellet, which was then placed in a sealed platinum tube under an argon atmosphere. The reaction was carried out at $1400^\circ C$ for 12 h. The product was a black powder containing small plate-like

crystals, which were investigated under polarized light for quality. The chemical composition was confirmed to be $\text{La}_5\text{Re}_3\text{MnO}_{16}$ by x-ray diffraction, which indicated unintentional mixing of the two pellets.

The synthesis of polycrystalline $\text{La}_5\text{Re}_3\text{MnO}_{16}$ was accomplished by the following reaction:



The reactants were mixed well and pressed into pellets, which were then sealed in a quartz tube under vacuum (5×10^{-5} Torr). The final product was obtained by two firings at 1050°C for 48 h, with an intermediate regrinding stage. The resulting sample was found to clearly contain two phases – an outer transparent layer of material, and a small amount of black powder within. The black powder was found to be the compound of interest.

Magnetic Measurements

Magnetic measurements were performed on the polycrystalline sample using a Quantum Design MPMS SQUID magnetometer. Field cooled (FC) and zero field cooled runs (ZFC) were done in a temperature range of 2 K to 600 K in an applied magnetic field of 0.05 T. Magnetization runs as a function of field were also done up to fields of 5.5 T.

X-ray Powder Diffraction

The polycrystalline product was examined using a Guinier-Hagg camera with $\text{Cu K}\alpha_1$ radiation ($\lambda = 1.54056 \text{ \AA}$) and silicon as an internal standard. The lattice constants were refined using the program LSUDF, and reasonable agreement was found with the single crystal measurements ($a = 7.984(7) \text{ \AA}$, $b = 8.020(3) \text{ \AA}$, $c = 10.255(8) \text{ \AA}$, $\alpha = 90.19(4)^\circ$, $\beta = 95.29(3)^\circ$, $\gamma = 90.17(4)^\circ$).

Single crystal x-ray diffraction data were collected using a P4 Siemens diffractometer on a $\text{Mo K}\alpha$ rotating anode source ($\lambda = 0.71073 \text{ \AA}$) which was equipped with a 1 K Charge-

Coupled Device (CCD) Area Detector. The software programs SAINT and SADABS were used to account for the three-dimensional Lorentz and polarization factors, and the absorption corrections, respectively. Face-indexed absorption corrections were applied at a later stage in view of the plate-like habit of the crystals. The crystal structure was solved using the SHELXTL 5.03 software package.

RESULTS AND DISCUSSION

Crystal Structure

The unit cell of $\text{La}_5\text{Re}_3\text{MnO}_{16}$ was found to possess triclinic symmetry with unit cell parameters $a = 7.9885(5) \text{ \AA}$, $b = 8.0322(5) \text{ \AA}$, $c = 10.2413(5) \text{ \AA}$, $\alpha = 90.200(1)^\circ$, $\beta = 95.160(2)^\circ$, $\gamma = 89.920(2)^\circ$. The above parameters are very similar to those reported for $\text{La}_5\text{Mo}_4\text{O}_{16}$ which was described in the monoclinic space group $C2/m$, so an initial model was based on the structure of this compound.⁵ The refinement was ultimately improved by lowering the symmetry to the unconventional $C-1$ space group. The results from the final refinement are listed in Table I, with a final R factor of 0.0343 and R_w factor of 0.0854. The atomic positions were determined in this space group, which are listed in Table II.

Table I. Experimental Data and Structural Refinement Parameters for $\text{La}_5\text{Re}_3\text{MnO}_{16}$

Crystal Size and Shape	124 μm x 94 μm x 3 μm , thin black plate
Lattice Parameters	$a = 7.9885(5)$ \AA , $b = 8.0322(5)$ \AA , $c = 10.2413(5)$ \AA , $\alpha = 90.200(1)^\circ$, $\beta = 95.160(2)^\circ$, $\gamma = 89.920(2)^\circ$, $V = 654.47(7)$ \AA^3
Space Group	C-1
D_c ; Z	7.937 g/cm ³ ; 2
Data collection technique	Siemens P4 diffractometer
Scan mode	$\theta - \phi$
Wavelength	Mo (K_α) $\lambda = 0.71073$ \AA
Number of measured reflections	7590, $-13 < h < 11$, $-13 < k < 10$, $-16 < l < 15$
Number of reflections used in refinement	3021 with $I > 2 \sigma(I)$
Absorption Corrections	Face-indexed correction based on crystal morphology
Absorption Coefficient	μ (Mo K_α) = 44.567 cm ⁻¹
R, R_w	0.0343, 0.0854
(Shift/e.s.d.) _{max}	< 0.001

Table II. Refined Atomic Positions and Their Estimated Standard Deviations

Atom	x	Y	z	B (\AA^2)
La(1)	0.22985(4)	0.74460(4)	0.80072(4)	0.00999(8)
La(2)	0.23097(4)	0.26311(4)	0.79498(4)	0.00858(8)
La(3)	0.5	0.5	0.5	0.00835(10)
Re(1)	0.05587(3)	0.50019(2)	0.39472(2)	0.00475(7)
Re(2)	0	0	0	0.00679(8)
Mn	0	0.5	0	0.0065(2)
O(1)	0.1910(5)	0.5020(6)	0.5651(4)	0.0083(7)
O(2)	0.2754(5)	0.5022(5)	0.3262(4)	0.0075(7)
O(3)	-0.0432(6)	0.4996(5)	0.2023(4)	0.0083(7)
O(4)	0.0716(6)	0.0012(6)	0.1827(5)	0.0101(8)
O(5)	0.0340(6)	0.7342(5)	0.3676(4)	0.0083(7)
O(6)	0.0403(6)	0.2645(5)	0.3670(5)	0.0089(7)
O(7)	-0.0565(6)	0.2420(5)	0.0039(5)	0.0123(9)
O(8)	0.2322(5)	0.0548(6)	-0.0348(5)	0.0114(8)

Figure I shows a projection of the crystal structure of $\text{La}_5\text{Re}_3\text{MnO}_{16}$ along the $[0\ 0\ 1]$ direction. The structure is related to the perovskites, with a layered stacking of two distinct motifs in the a-b plane. One layer consists of octahedrally coordinated rhenium and manganese atoms, which are interconnected by corner-sharing oxygen atoms. Each rhenium unit is connected to four manganese units in the a-b plane, with two apexes that are free. The manganese units are likewise linked to the rhenium units in the a-b basal plane, and are also linked to rhenium layers which lie above and below the rhenium-manganese layer. Figure II shows this explicitly as a projection of the structure along the $[0\ 1\ 0]$ direction.

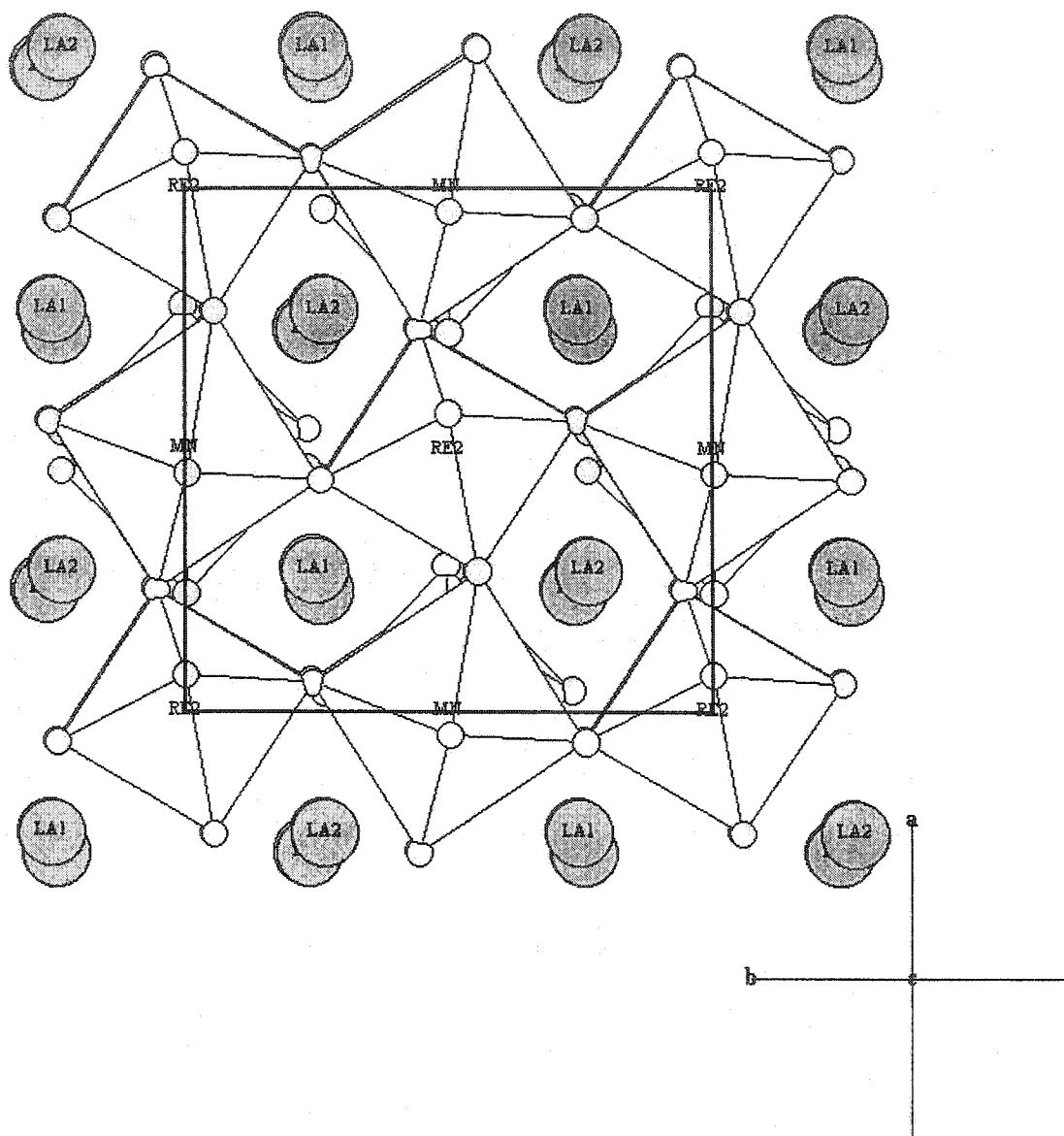
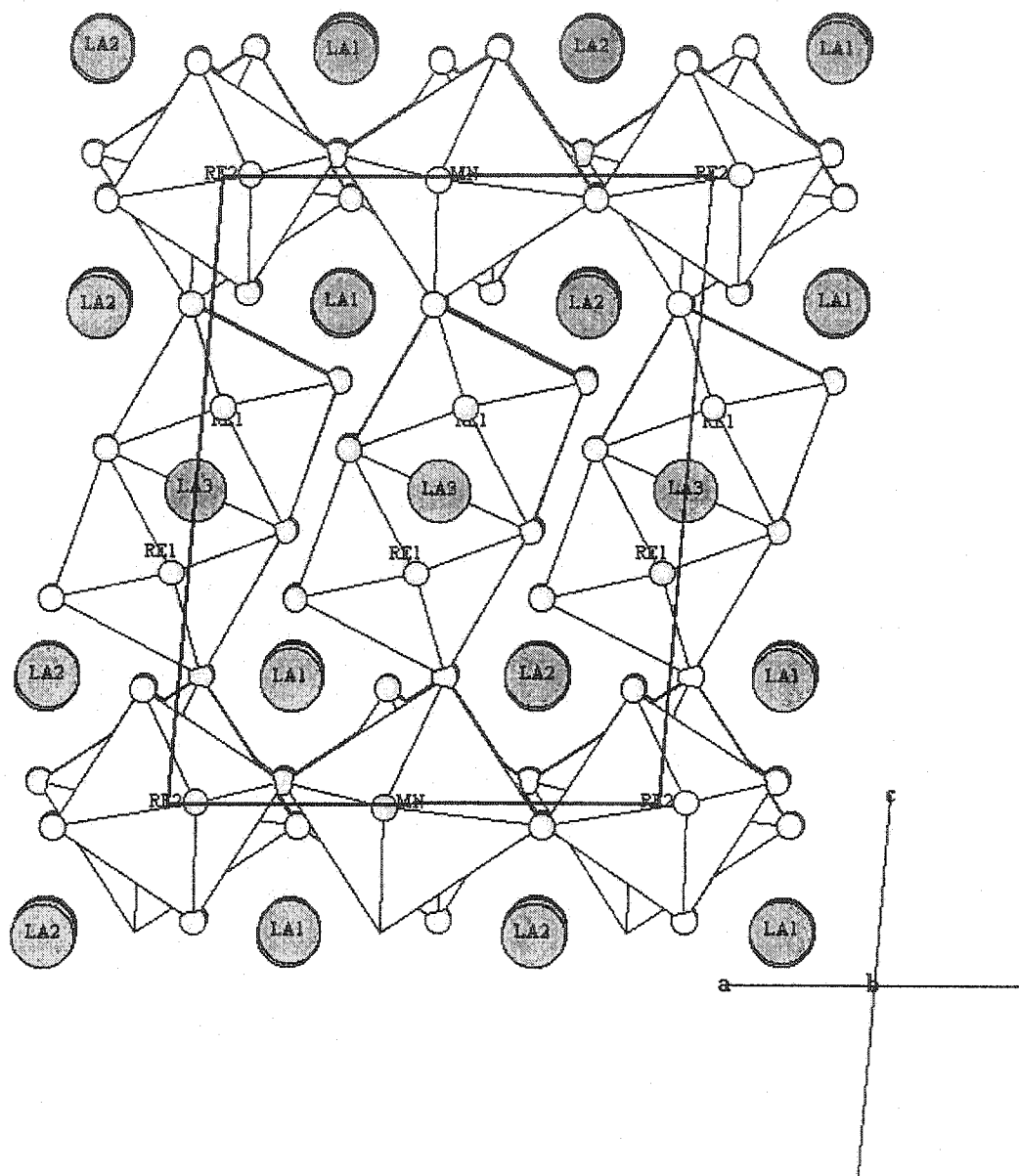
Figure I. Projection along $[0 0 1]$.

Figure II. Projection along [0 1 0].



The octahedra in the rhenium-manganese layer exhibit a slight misalignment of their equatorial planes with the a-b plane of the unit cell (the distortion is quite distinct when viewed from the [0 1 0] direction). This misalignment is significant since it plays a vital role in the determination of the proper space group of this crystal. Other refinements of the crystal structure were attempted in the monoclinic space groups Cm and C2/m. All of these refinements seemed to be reasonable, but upon closer examination, it was deduced that this distortion of the octahedra breaks the mirror symmetry at [0 1 0]. Consequentially, the residuals of these monoclinic refinements would split the oxygen positions (O(8)) and therefore suggest that there is disorder at these sites (see Figure III). This was the approach of Ledesert *et al.*,⁵ who solved the structure of La₅Mo₄O₁₆ in C2/m with disorder at the same oxygen site. The conclusion that is reached here is that the distortion appears to be real in this material, and is significant enough to lower the symmetry to a triclinic, C-1 space group (the twisting of the octahedra that is observed is typical in perovskite structures with relatively small cations such as La). Attempts were made to refine the structure in monoclinic symmetry with disorder on O(8), but these were ultimately abandoned due to indications that the crystal was indeed triclinic (with strong angular deviations from 90 degrees for α and γ), and the distortions of the octahedra in this layer appear to be genuine.

One of the more interesting aspects of this crystal structure lies in the consecutive layer of rhenium atoms, which are connected in dimers of edge-sharing octahedra. The close proximity of the octahedra causes a notable distortion of the oxygen positions, as noted in Figure IV. It also leads to an off-centering of the rhenium atoms and thus an exceptionally short Re-Re bond distance of 2.4068(5) Å. Such short bond distances in edge-shared octahedra have been observed for Ti-Ti bonds in Nd₃Ti₄O₁₂ (2.760(3) Å)⁶ and for Mo-Mo bonds in the La₅Mo₄O₁₆ structure, which were reported to be 2.406 Å by Ledesert *et al.*⁵ There are also reports of extremely short Re-Re bonds in other La-Re-O systems such as La₆Re₄O₁₈, La₄Re₆O₁₉, and La₃Re₂O₁₀.⁷ In the case of La₄Re₆O₁₉, isolated edge-sharing units of rhenium-oxygen octahedra of the crystallographic formula Re₂O₁₀ are observed in the same manner as our material. The Re-Re bond distance reported, 2.42 Å, is in good agreement with the bond distance in La₅Re₃MnO₁₆, and it is interpreted as a true metal-metal

bond. Strong distortions of the oxygen positions are observed as well, with the Re atoms similarly displaced from the centers of their respective octahedra. The nature of the bonding cannot be ascertained with the data presented here, but double or triple Re-Re bonding may indeed be present.

Figure III. Projection along $[1\ 0\ 0]$ indicating where the mirror planes occur for the space group $C2/m$ (bold lines). Note the positions of O(8), oxygen positions in bold, which do not obey the mirror plane symmetries at $b = 0$, $b = 0.5$ and $b = 1.0$, and thus lower the symmetry of the crystal structure to $C-1$.

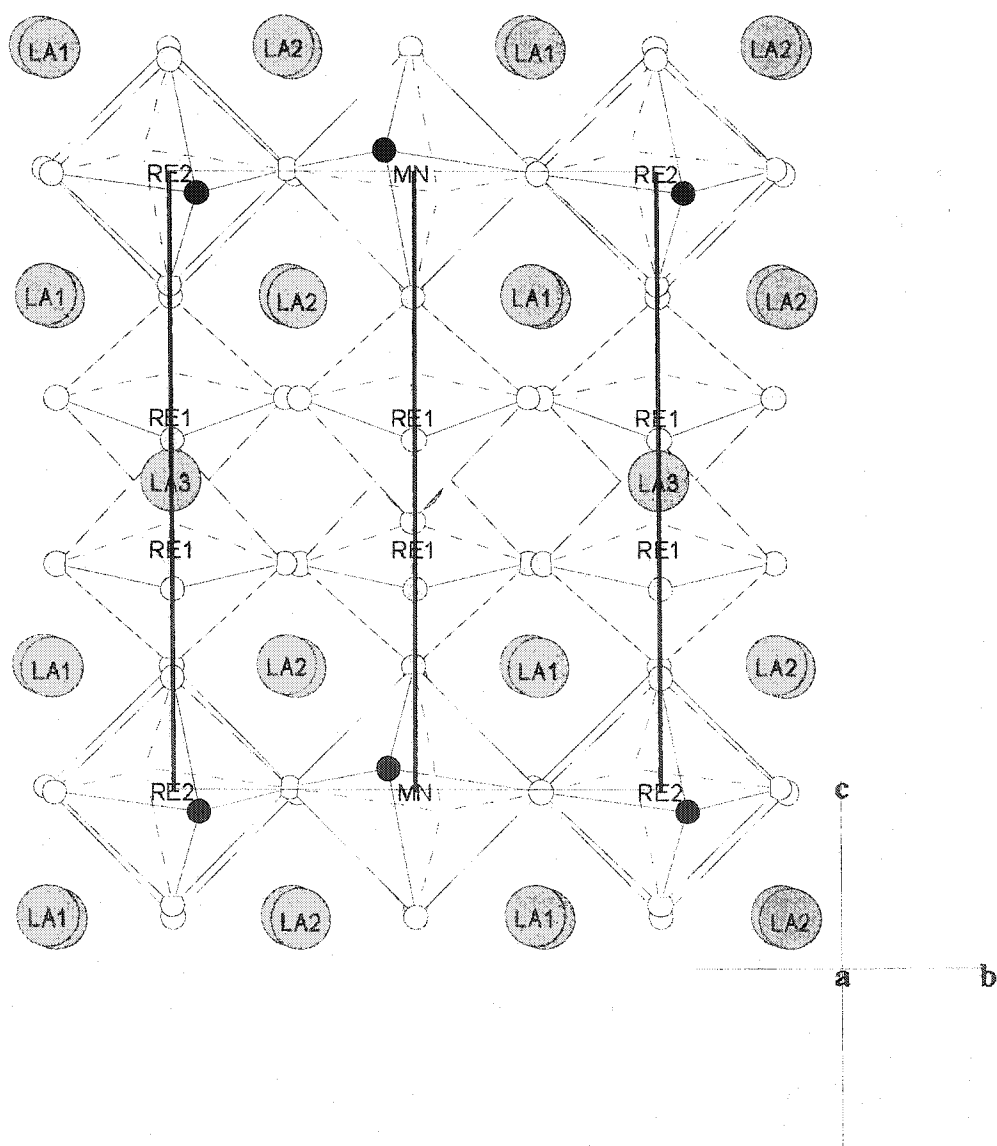
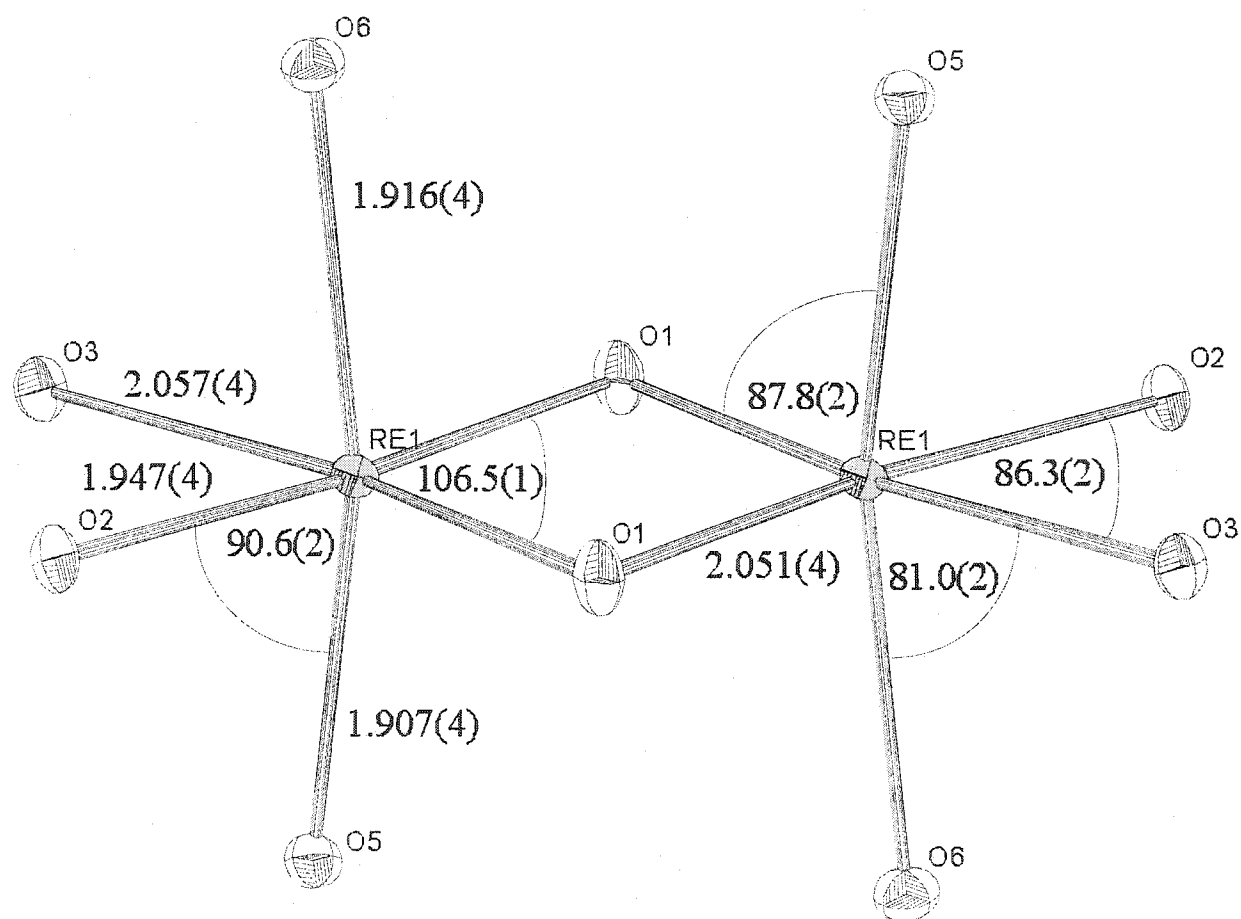


Figure IV. The Re-Re bioctahedra. The edge-sharing of the octahedra provides significant distortions as indicated by the deviations of the angles from their ideal values. It is believed that the close proximity of the Re atoms ($2.4068(5)$ Å) is evidence for a true Re-Re bond.



Quadruple Re-Re bonds have been observed in other exotic materials such as the rhenium halides (ie. $\text{K}_2\text{Re}_2\text{Cl}_8$)⁷, but these are usually characterized by very short Re-Re bond distances on the order of 2.2 Å or less and are very rare.

The lanthanum atoms are found to reside in three distinct crystallographic sites. The La(1) and La(2) atoms are distributed in chains along the [0 1 0] direction that lie in the interstitial positions in the $\text{Re}(2)\text{O}_6$ and MnO_6 framework. For ease of presentation, the polyhedra which correspond to the coordination of the lanthanum atoms have been omitted from the figures, but they are seven- and eight-fold coordinated respectively with oxygen. The La(3) atoms are located in cages delimited by the $\text{Re}(1)_2\text{O}_{10}$ dimers, and thus possess a distorted cubic coordination.

All of the relevant bonds and bond angles for the atomic polyhedra found in this crystal structure are listed in Tables III and IV. These parameters were analyzed using VaList⁸ to determine the proper oxidation states of the constituent cations. The results from this analysis are listed in Table V. All of the bond valence calculations agree to within roughly 10 % of the formal oxidation states of +3, +5, and +2 on the lanthanum, rhenium, and manganese sites respectively.

An interesting comparison can be made with the nearly isostructural $\text{La}_5\text{Mo}_4\text{O}_{16}$. The stacking is nearly identical in this material, with two distinct alternating layers of corner-sharing Mo octahedra and edge-sharing Mo-Mo bioctahedra. The difference in these two materials is that the replacement of Mo by Mn and Re in the corner-shared octahedral layer results in a distortion away from monoclinic to pseudomonoclinic (C-1 triclinic) symmetry. The positioning of the Re and Mn atoms in this layer is interesting, since Ledesert found through bond valence analysis that the two Mo sites displayed slightly lower and higher oxidation states than the commonly accepted +4 value (with reported values of 3.84 and 4.68)⁵. The Mn and Re atoms in our structure occupy the sites of lower and higher oxidation states, respectively, in $\text{La}_5\text{Re}_3\text{MnO}_{16}$, re-enforcing the close structural relationship of these compounds.

Table III. Selected Interatomic Distances (in Angstroms)

La(1) -	O(2)	2.415(4)	La(3) -	O(1)	2.614(4) x2
	O(3)	2.463(5)		O(2)	2.411(4) x2
	O(4)	2.527(5)		O(5)	2.553(4) x2
	O(5)	2.536(5)		O(6)	2.564(4) x2
	O(6)	2.635(4)			
	O(7)	2.570(5)	Re(1) -	O(1)	1.968(4)
	O(7)	2.536(5)		O(1)	2.051(4)
	O(8)	3.002(5)		O(2)	1.947(4)
				O(3)	2.057(4)
La(2) -	O(2)	2.461(4)		O(5)	1.907(4)
	O(3)	2.425(4)		O(6)	1.916(4)
	O(4)	2.463(5)			
	O(5)	2.572(4)	Re(2) -	O(4)	1.907(5) x2
	O(6)	2.584(5)		O(7)	1.996(4) x2
	O(8)	2.420(5)		O(8)	1.971(5) x2
	O(8)	2.847(5)			
			Mn -	O(3)	2.131(5) x2
Re(1) -	Re(1)	2.4068(5)		O(7)	2.123(4) x2
				O(8)	2.182(4) x2

Table IV. Selected Bond Angles (in degrees)

O(1)-	Re(1)-	O(1)	106.5(1)	Re(1)-	O(3)-	Mn	148.2(2)
O(2)-	Re(1)-	O(5)	90.6(2)				
O(1)-	Re(1)-	O(5)	87.8(2)	Re(2)-	O(7)-	Mn	154.3(3)
O(2)-	Re(1)-	O(3)	86.3(2)				
O(6)-	Re(1)-	O(3)	81.0(2)				
O(4)-	Re(2)-	O(8)	88.4(2)	O(3)-	Mn-	O(7)	85.6(2)
			91.6(2)				94.4(2)
O(4)-	Re(2)-	O(7)	88.4(2)	O(3)-	Mn-	O(8)	85.3(2)
			91.6(2)				94.7(2)
O(7)-	Re(2)-	O(8)	89.9(2)	O(7)-	Mn-	O(8)	89.6(2)
			90.1(2)				90.4(2)

Table V. Results from VaList Bond Valence Calculation

Cation	Valence	Cation-oxygen bond valence							
		O(1)	O(2)	O(3)	O(4)	O(5)	O(6)	O(7)	O(8)
La(1)	2.8	-	0.52	0.46	0.38	0.37	0.29	0.37	0.11
		-	-	-	-	-	-	0.34	-
La(2)	2.8	-	0.46	0.50	0.46	0.34	0.33	-	0.51
		-	-	-	-	-	-	-	0.16
La(3)	3.1	0.30	0.52	-	-	0.36	0.35	-	-
		0.30	0.52	-	-	0.36	0.35	-	-
Re(1)	4.5	0.75	0.79	0.59	-	0.88	0.86	-	-
		0.60	-	-	-	-	-	-	-
Re(2)	4.6	-	-	-	0.88	-	-	0.69	0.74
		-	-	-	0.88	-	-	0.69	0.74
Mn	2.3	-	-	0.40	-	-	-	0.41	0.35
		-	-	0.40	-	-	-	0.41	0.35
O	Valence	-2.0	-2.3	-2.0	-1.7	-2.0	-1.8	-1.8	-1.9

One can also compare this structure with other perovskite-related transition metal oxides. The reduced neodymium titanate, $\text{Nd}_3\text{Ti}_4\text{O}_{12}$,⁶ for example, crystallizes in a similar structure with a perovskite-like TiO_6 corner-sharing octahedral bilayer, and a Ti_2O_{10} edge-shared octahedral layer. The Nd atoms lie in chains in the framework much like the La atoms in $\text{La}_5\text{Re}_3\text{MnO}_{16}$. An important difference in the two structural types is the manner in which the Ti octahedra are connected. Instead of having their apexes connected to the Ti_2O_{10} layer, the TiO_6 octahedra are linked by their four equatorial ligands to the next layer, and have their apexes linked to other TiO_6 octahedra which lie in chains in the network. The two structures both have extremely short metal-metal bonds, though, with Ti-Ti distances of 2.760(3) Å. Resistivity measurements on this material have shown that it is indeed

nonmetallic, and thus there is localization of free electrons in the structure which is more than likely due to the Ti-Ti bond. A similar measurement in our material would be crucial to determining the nature of the bonding in the Re-Re bioctahedra and characterizing the magnetic response.

Magnetism in $\text{La}_5\text{Re}_3\text{MnO}_{16}$

Perovskite and perovskite-related materials often exhibit fascinating low temperature magnetic behaviour which is commonly due to the layered stacking of the magnetic species. To investigate these properties, the magnetic susceptibility of single phase powder samples of $\text{La}_5\text{Re}_3\text{MnO}_{16}$ was measured. The magnetic susceptibility for polycrystalline $\text{La}_5\text{Re}_3\text{MnO}_{16}$ is displayed in Figures V and VI for a field of 0.05 T. There are clearly three features of interest in the response: (1) a low temperature phase of possible short range magnetic ordering at temperatures lower than about 50 K, as evidenced by the difference in the FC and ZFC data, (2) a magnetic transition at about 160 K, and (3) Curie-Weiss behaviour in the range 400 K – 600 K. Figure VI shows this high temperature response more explicitly. The high temperature data can be fit to the Curie-Weiss law:

$$(2) \quad \chi = C/(T - \theta_c)$$

where χ is the molar susceptibility, C is the Curie constant, and θ_c is the Weiss temperature. The Curie constant was found to be 4.43(4) emu·K/mol, which is consistent with Mn^{2+} ($S = 5/2$) as the only magnetic species (the spin-only Curie constant is 4.375 emu·K/mol for $S = 5/2$). The Weiss temperature of $\theta_c = -48(5)$ K indicates the presence of antiferromagnetic coupling between the moments.

Figure V. The magnetic susceptibility as a function of temperature for an applied field of 0.05 T. Note the divergence in the FC and ZFC runs at low temperatures in the insert.

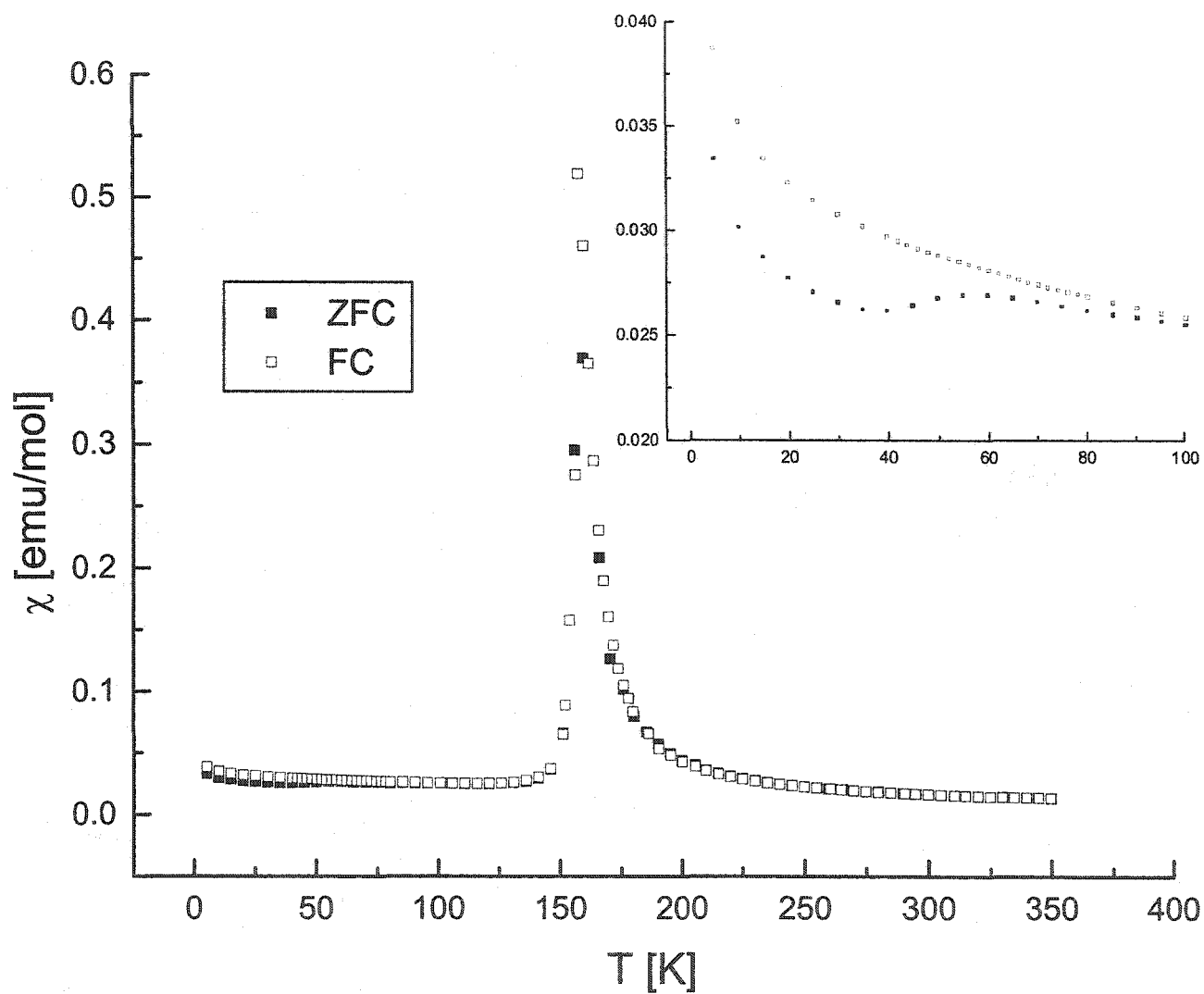
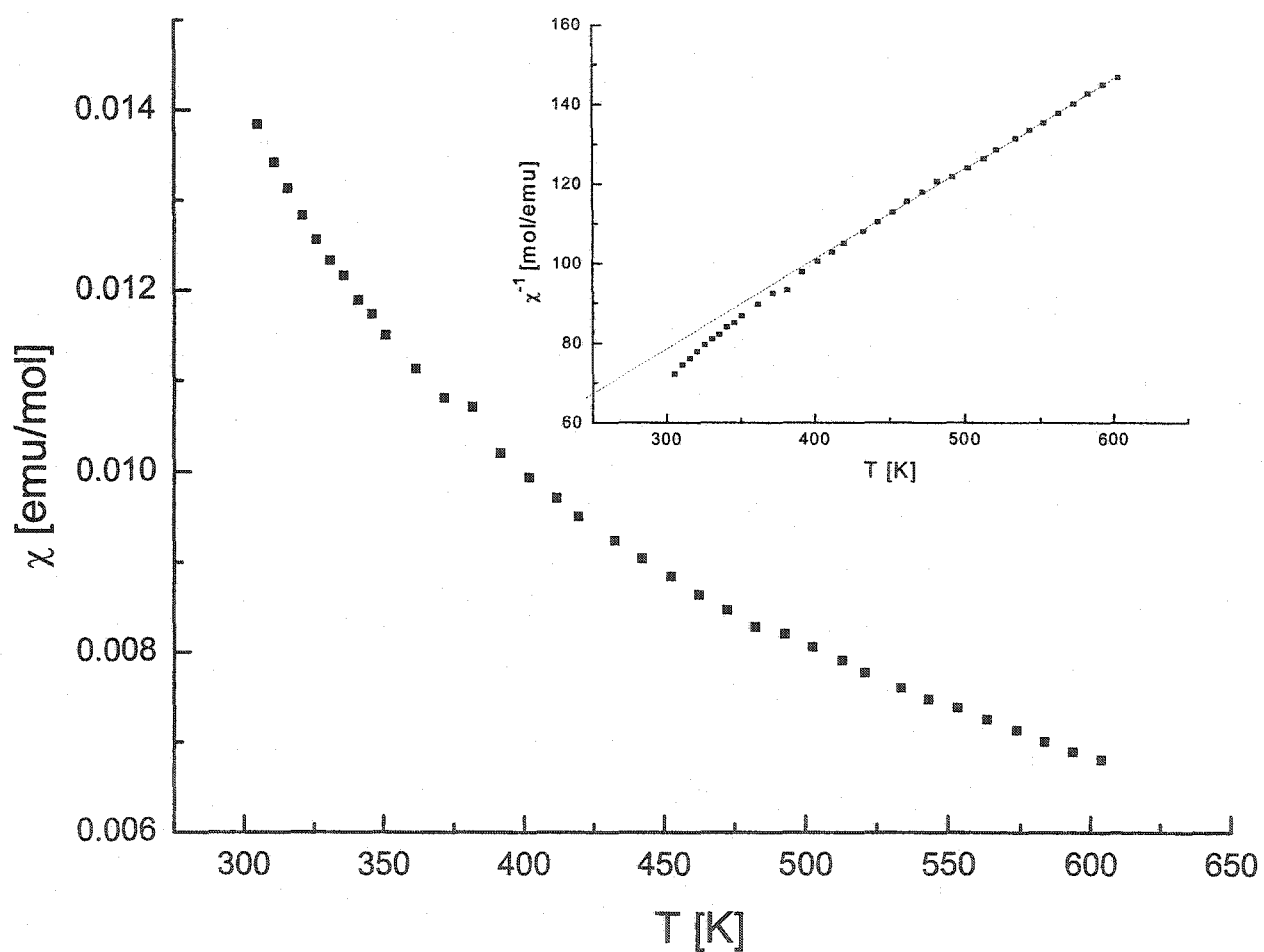


Figure VI. The high temperature magnetic susceptibility as a function of temperature for an applied field of 0.05 T. The insert shows the inverse susceptibility with a linear regression based upon the Curie-Weiss law (2), which gives a Curie constant of 4.43(4) emu K/mol (corresponding to $S = 2.52(2)$) and a Weiss temperature of $\theta = -48(5)$ K.

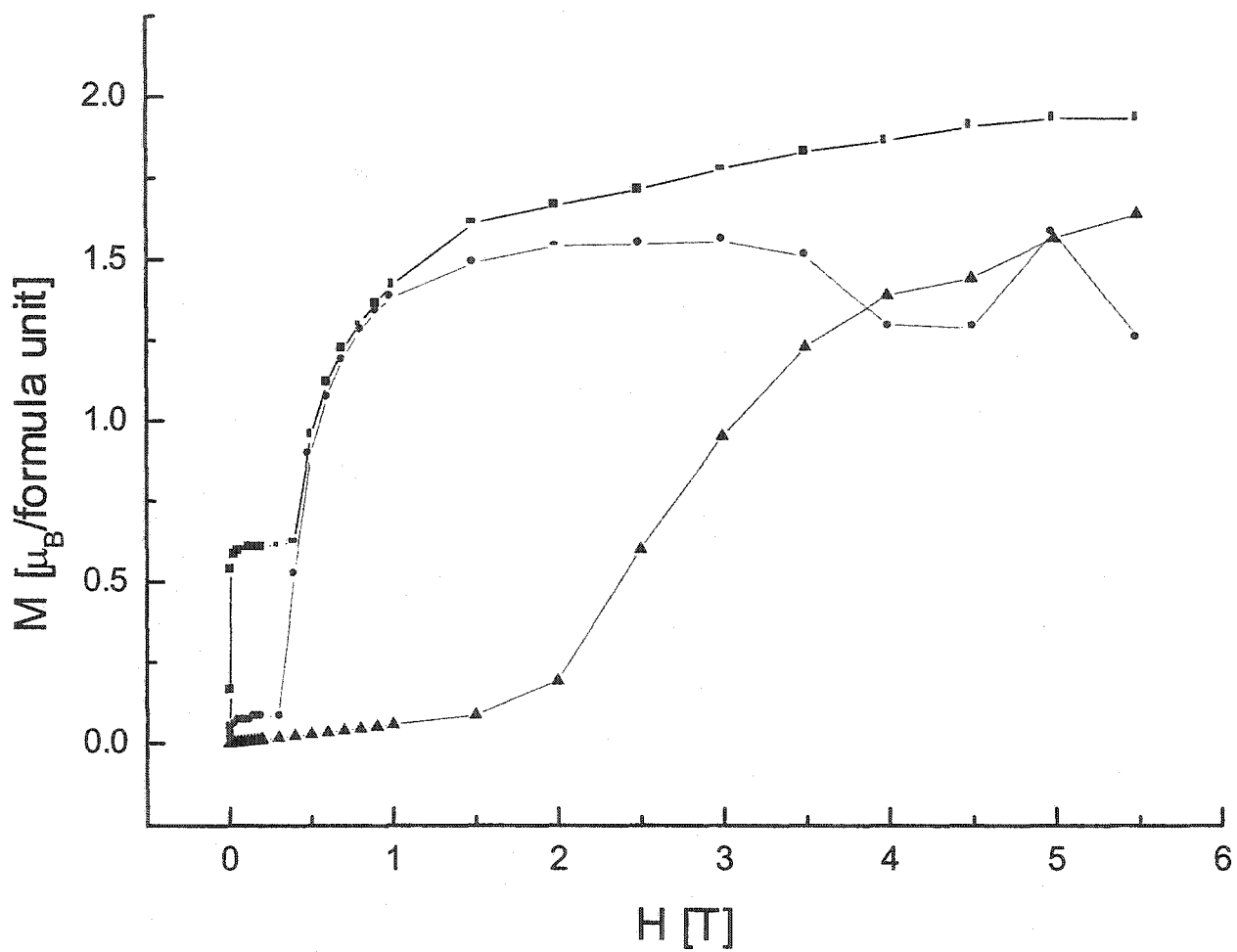


In an effort to understand further the magnetic susceptibility measurements, the magnetization of the sample as a function of magnetic field was measured for three temperatures: 5 K, 60 K, and 120 K (see Figure VII). At 5 K, the response indicates antiferromagnetic alignment of the moments up until a field of about 2 T, beyond which the magnetization grows more rapidly to a value of $1.6 \mu_B$ at about 5.5 T. At 60 K and 120 K however, there is a notable difference in the magnetic response. At both temperatures, there is an initial sharp rise in the magnetization, followed by a plateau to about 0.4 T. After this critical field has been reached, there is another sharp rise to apparent saturation at about $2 \mu_B$ by 2 T. The maximum saturation moment for Mn^{2+} ($S = 5/2$) is $5 \mu_B$. These observations point to a complex magnetic structure and H-T phase diagram for this material.

Other aspects of the magnetism are also puzzling at this stage. For example there is apparently no contribution from Re^{5+} to the magnetic susceptibility. In a localized electron picture, Re^{5+} is an $S = 1$ ion and a spin-only Curie constant of $1.00 \text{ emu}\cdot\text{K/mol } Re^{5+}$ would be expected, although this value may be reduced by spin-orbit coupling.

One can imagine at least two mechanisms by which the Re^{5+} moments might be quenched, multiple bond formation and electron delocalization. For example, the Re(1) atoms reside in the bi-layer consisting of edge-sharing Re-O octahedra with very short Re-Re distances, as noted previously. It is natural to propose the existence of Re-Re double bonds which would provide moment quenching for these sites. This seems to be a likely scenario, as the bond distance of 2.4068 \AA is consistent with double bonds in other systems, such as halo metal-atom clusters, which have double bonds of length 2.42 \AA .⁹ Other systems exist which have this Re-Re bonding in edge-shared bioctahedra.¹⁰ Of particular relevance is the system $K_4[Re_2O_2(C_2O_4)_4]\cdot 3H_2O$, which has Re-Re edge-shared octahedra with oxygen ligands. The metal-metal distance has been reported as 2.36 \AA ,¹¹ which is comparable to the Re-Re distance in $La_5Re_3MnO_{16}$. The shorter bond distance and lower oxidation state (+4) in this case indicates the presence of a triple bond. Since the Re-Re bond distance in $La_5Re_3MnO_{16}$ is slightly longer, it is more probable that there is double bonding on the Re(1) site involving a $5d^2-5d^2$ interaction.

Figure VII. Magnetization as a function of applied field for 5 K (■), 60 K (●) and 120 K (▲).



The next issue concerns the electrons on the Re(2) site. One can imagine that if a pathway can be devised to delocalize the electrons on this site, then the Re *d*-electrons which are not involved with the Re-Re double bonds form a Fermi surface (of, no doubt, quite a complex topology) and, thus, the compound should be metallic. While there is no direct evidence for this hypothesis, the magnetic properties, especially the relatively high transition temperature provides indirect support. For example given the dilute nature of the Mn²⁺ magnetic centers, that the Mn-containing layers are well separated by 10.24 Å and the fact that no Mn-O-Mn superexchange pathways exist, it is very difficult to understand a critical temperature as high as 160 K without the intervention of a conduction electron mediated spin coupling mechanism such as RKKY.

As a counter argument to the above, one should note that there are no Re(2)-O-Re(2) connections in the pervoskite layer or with the Re₂O₁₀ units; only Re(2)-O-Mn-O-Re(2) or Re(2)-O-Mn-O-Re(1) pathways exist. In similar materials, there is evidence for local moments on the Re ions.¹² Thus, if there is a local moment on Re(2), one must consider a ferrimagnetic model for the Re(2)-Mn layers. The magnetization results lend some support to this, as the saturation of the moment only reached about 2 μ_B per formula unit, which is shy of the value expected for Mn²⁺ (5 μ_B). The ordering at 160 K would then involve a cross-over from 2d to 3d magnetic order. The low temperature FC-ZFC irreversibility might result from a spin canting. There are very few examples of layered ferrimagnetic materials and these hypotheses merit further investigation.

Elements of the above models can be verified by further studies. For example neutron diffraction can determine if all of the ordered magnetic moment is associated with the Mn sites and transport or optical measurements would disclose metallic behaviour.

ACKNOWLEDGEMENTS

The authors would like to express their gratitude to Prof. I. D. Brown, who assisted with the bond valence calculations, and to M. Bieringer, who assisted with the powder synthesis. C. R. Wiebe gratefully acknowledges support for this work from the Natural Sciences and Engineering Research Council in the form of a PGS B. This project was also supported through a research grant to J. E. Greedan through NSERC.

REFERENCES

- 1) R. J. D. Tilley, *Endeavor* **14**, 124 (1990).
- 2) R. M. Hazen, *Sci. Amer.* **358**, 52 (1988).
- 3) J. G. Bednorz and K. A. Müller, *Z. Phys. B.* **64**, 189 (1986).
- 4) N. L. Morrow and L. Katz, *Acta Cryst.* **B24**, 1466 (1968).
- 5) M. Ledesert, Ph. Labbe, W. H. McCarroll, H. Leligny, and B. Raveau, *J. Solid State Chem.* **105**, 143 (1993).
- 6) B. Hessen, S. A. Sunshine, T. Siegrist, and R. B. Van Dover, *J. Solid State Chem.* **105**, 107 (1993).
- 7) A. Perrin and M. Sergent, *New J. Chem.* **12**, 337 (1988).
- 8) A. S. Willis, 1998, VaList for GSAS.
- 9) F. A. Cotton, *Inorganic Chem.*, **4**, 334 (1965).
- 10) F. A. Cotton and R. A. Walton, *Multiple Bonds between Metal Atoms*, J. Wiley and Sons, New York (1982).
- 11) T. Lis, *Acta Cryst.* **B31**, 1594 (1975).
- 12) A. W. Sleight, J. Longo, and R. Ward, *Inorg. Chem.* **1**, 245 (1962).

APPENDIX: MAGNETIC STRUCTURE OF $\text{La}_5\text{Re}_3\text{MnO}_{16}$ **EXPERIMENTAL***Preparation of $\text{La}_5\text{Re}_3\text{MnO}_{16}$*

An alternate route to synthesizing large single phase quantities was discovered based upon the following solid state reaction:



Stoichiometric quantities of the above reagents were ground in an agate mortar and pestle to produce a homogenous mixture. Pellets were pressed and placed into a platinum capsule which was then sealed into a quartz tube under a vacuum of $\sim 10^{-5}$ Torr. This vessel was placed in a tube furnace and heated twice at 1050°C for 48 hrs with a regrinding step between firings. The yields from the above were essentially quantitative, allowing the preparation of several grams for neutron diffraction experiments.

X-Ray Diffraction

The polycrystalline product was analyzed using a Guinier-Hågg camera with $\text{Cu K}_{\alpha 1}$ radiation ($\lambda = 1.54056 \text{ \AA}$) and high purity silicon powder as an internal standard. The lattice constants were obtained using LSUDF and the single crystal data as a starting model.

Neutron Diffraction

Neutron scattering experiments were completed on the product using the Dualspec C2 beamline operated by the Neutron Program for Materials Research of the National

Research Council of Canada at the Chalk River Laboratory. The neutron wavelength was $\lambda = 2.3688(2)$ Å. The sample was sealed in a vanadium can in a He atmosphere with an indium wire gasket. Data were obtained over the angular range $5^\circ < 2\theta < 114.9^\circ$, with a step width of 0.1° at several temperatures from 10 K to 250 K.

The data were analyzed using the program FULLPROF 3.5d Rietveld refinement package. The program BONDS was used to calculate bond distances and angles.

RESULTS AND DISCUSSION

X-ray Diffraction

All of the reflections (41 lines) were indexed using a triclinic cell of symmetry C-1. The cell constants were in good agreement with the single crystal results, verifying that the material is of the same phase ($a = 7.988(1)$ Å [7.984(7)], $b = 8.053(3)$ Å [8.020(3)], $c = 10.215(2)$ Å [10.255(8)], $\alpha = 90.14(2)^\circ$ [90.19(4)°], $\beta = 95.18(2)^\circ$ [95.29(3)°] and $\gamma = 89.89(3)^\circ$ [90.17(4)°]). The values in square brackets are those from the single crystal experiment.

Crystal Structure

The crystal structure of $\text{La}_5\text{Re}_3\text{MnO}_{16}$ was refined using the neutron powder diffraction data and the program FULLPROF 3.5d. The refinement is displayed in Figure VIII, and the results are tabulated in Tables VI and VII. The agreement between the single crystal room temperature x-ray diffraction experiments and the 250 K powder neutron diffraction experiments is quite reasonable.

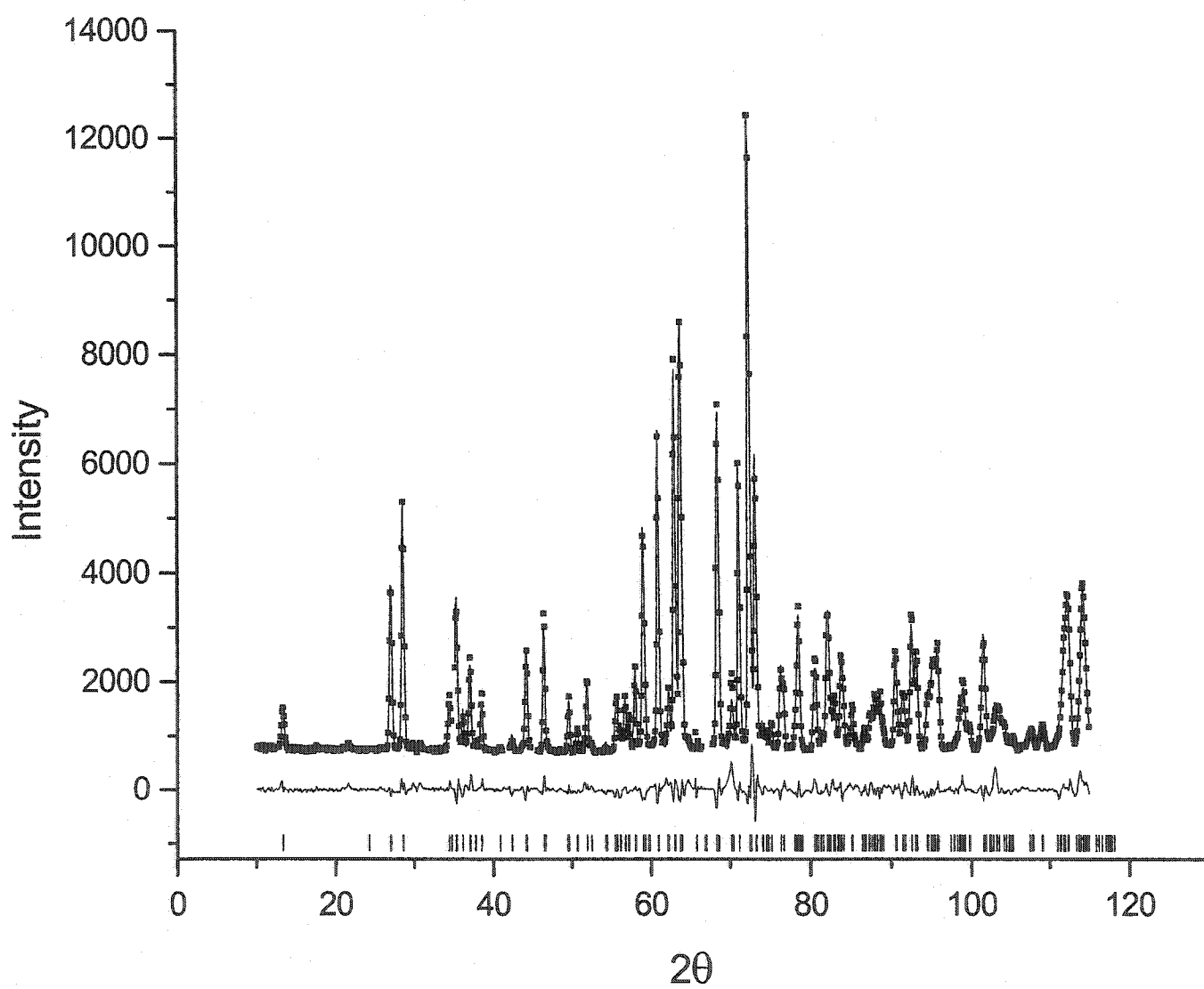
Table VI: Positional parameters refined from powder neutron diffraction data for $\text{La}_5\text{Re}_3\text{MnO}_{16}$ for 10 K and 250 K.

	x (10K)	y (10K)	z (10K)	x (250K)	y (250K)	z (250K)	B (\AA^2)
La1	0.230(2)	0.740(2)	0.797(2)	0.227(1)	0.743(1)	0.799(1)	0.78(24)
La2	0.227(2)	0.263(2)	0.793(2)	0.228(1)	0.282(2)	0.789(1)	0.78(24)
La3	0.5	0.5	0.5	0.5	0.5	0.5	0.78(24)
Re1	0.053(1)	0.494(2)	0.392(1)	0.053(1)	0.496(1)	0.393(1)	0.38(16)
Re2	0	0	0	0	0	0	0.38(16)
Mn	0	0.5	0	0	0.5	0	0.51(20)
O1	0.189(2)	0.504(4)	0.565(2)	0.189(2)	0.508(3)	0.564(1)	0.76(54)
O2	0.276(2)	0.497(4)	0.316(2)	0.275(1)	0.493(2)	0.320(1)	0.76(54)
O3	-0.042(2)	0.503(4)	0.196(1)	-0.042(1)	0.500(2)	0.200(1)	0.76(54)
O4	0.072(2)	-0.015(3)	0.181(2)	0.073(2)	-0.011(2)	0.179(1)	0.76(54)
O5	0.034(2)	0.734(4)	0.366(3)	0.034(2)	0.733(2)	0.363(1)	0.76(54)
O6	0.038(3)	0.261(4)	0.367(3)	0.036(2)	0.264(2)	0.371(2)	0.76(54)
O7	-0.058(2)	0.249(3)	0.001(2)	-0.059(1)	0.244(2)	0.004(1)	0.76(54)
O8	0.240(2)	0.062(2)	-0.026(2)	0.238(2)	0.059(1)	-0.028(1)	0.76(54)

Table VII: Cell parameters, magnetic moments and agreement indices for $\text{La}_5\text{Re}_3\text{MnO}_{16}$ for 10 K and 250 K.

	10 K	250 K
Mn moment (μ_B)	3.9(1)	0
Re moment (μ_B)	1.0(1)	0
a (\AA)	7.9660(5)	7.9836(4)
b (\AA)	8.0084(5)	8.0208(3)
c (\AA)	10.2095(7)	10.2269(5)
α ($^\circ$)	90.185(6)	90.181(4)
β ($^\circ$)	95.193(4)	95.182(3)
γ ($^\circ$)	89.933(6)	89.944(5)
Volume (\AA^3)	648.65(7)	652.20(5)
R_p	5.16	4.55
R_{wp}	6.77	6.30
R_{exp}	2.53	2.68
χ^2	7.14	5.53
Bragg R-factor	5.03	5.20
R - F	3.70	3.88
Magnetic R-factor	22.7	-

Figure VIII: Rietveld refinement of the 250K neutron diffraction data for $\text{La}_5\text{Re}_3\text{MnO}_{16}$. The open circles represent the data, the solid line is the fit and the difference is shown below. The tick marks show the Bragg peak positions.



Magnetic Structure

The transition reported in this material at $T_N \sim 160$ K is accompanied by a series of magnetic Bragg peaks, indicating a long-range ordered magnetic ground state, as shown in figure IX. This is not entirely surprising considering the size of the magnetic susceptibility peak at this temperature (see figure V). Careful indexing of these new peaks in the original monoclinic cell leads to a magnetic unit cell which is twice the size, namely $a_{\text{mag}} = a$, $b_{\text{mag}} = b$ and $c_{\text{mag}} = 2c$ (or a $(0, 0, \frac{1}{2})$ ordering wavevector). Figure X displays the temperature dependence of these features, which clearly demonstrate the choice of T_N . However, there is at least one magnetic Bragg peak which cannot be indexed on this cell, and requires a $k = (1/2, 1/2, 1/2)$ wavevector. There is a similar peak in the high angle data that is severely overlapped by chemical Bragg peaks. These features have a different temperature dependence though, and are excluded from the refinement of the magnetic structure. They may have a correlation with the low temperature susceptibility features, but more data is needed to confirm this. The most likely explanation would be that there is a spin reorientation in the Re-Mn planes which would give this feature, or there is a small Mn oxide impurity that orders at a lower temperature regime.

With an ordering wave vector of $(0\ 0\ \frac{1}{2})$ a natural choice for a trial magnetic structure is one analogous to the so-called A-type structure in perovskites, where planes of ferromagnetically coupled **ab** layers are coupled antiferromagnetically with respect to the **c**-axis which would account for the doubling of the **c**-axis in the magnetic cell. In this case the intraplanar coupling between the different Mn and Re moments could be in principle ferromagnetic or antiferromagnetic and both models were tried. The absence of magnetic reflections of the type $(0\ 0\ L)$, except for a very weak $(0\ 0\ 2)$ peak, indicates that the net moment direction is roughly parallel to the **c**-axis.

For the 10 K dataset a model in which the Re moments were antiparallel to the Mn moments within the layers and with the layers coupled antiparallel was tried with initial moment values of $4.5\mu_B$ on Mn^{2+} and $1.5\mu_B$ on Re^{5+} (i.e. nearly the spin only values) and the direction parallel to the **c**-axis. The moment values at were refined with the aid of soft

constraints to $3.9(1) \mu_B$ on Mn and $1.0(1) \mu_B$ on Re, not unreasonable values. Initial models in which the intraplanar Re – Mn coupling was ferromagnetic, refined rapidly to antiparallel alignments. The orientation of the Re and Mn moments with respect to the c-axis was also refined, given the presence of a weak (0 0 2) peak and slightly different angles were obtained, with the Mn moments nearly parallel to c and the Re moments aligning $\sim 18^\circ$ with respect to c. The results of the combined chemical structure/ magnetic structure refinements are listed in Tables 1 and 2 for the 10 K data and the data refinement for 10 K is shown in Figure XI. Figure XII displays the magnetic structure associated with the $\mathbf{k} = (0\ 0\ \frac{1}{2})$ wave vector.

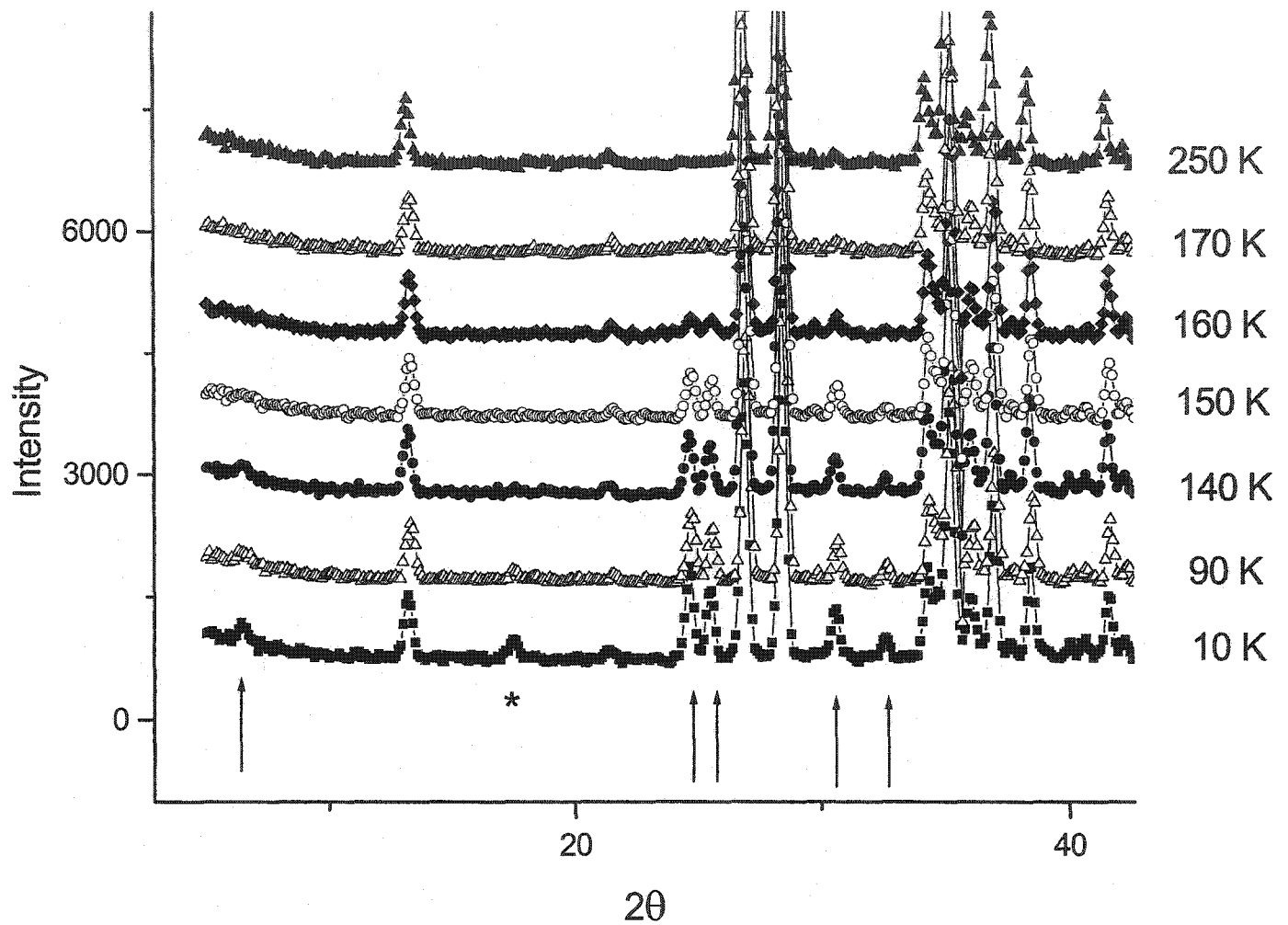


Figure IX: Low angle neutron diffraction data for $\text{La}_5\text{Re}_3\text{MnO}_{16}$ at selected temperatures showing the development of new reflections below 160 K. The magnetic reflections belonging to $k = (0\ 0\ \frac{1}{2})$ are marked by arrows and the reflection belonging to $k = (\frac{1}{2}\ \frac{1}{2}\ \frac{1}{2})$ is marked by a star (*).

Figure X: The temperature dependence of the strongest magnetic reflections belonging to the $\mathbf{k} = (0\ 0\ \frac{1}{2})$ magnetic structure along with an additional weak reflection indexed with $\mathbf{k} = (\frac{1}{2}\ \frac{1}{2}\ \frac{1}{2})$.

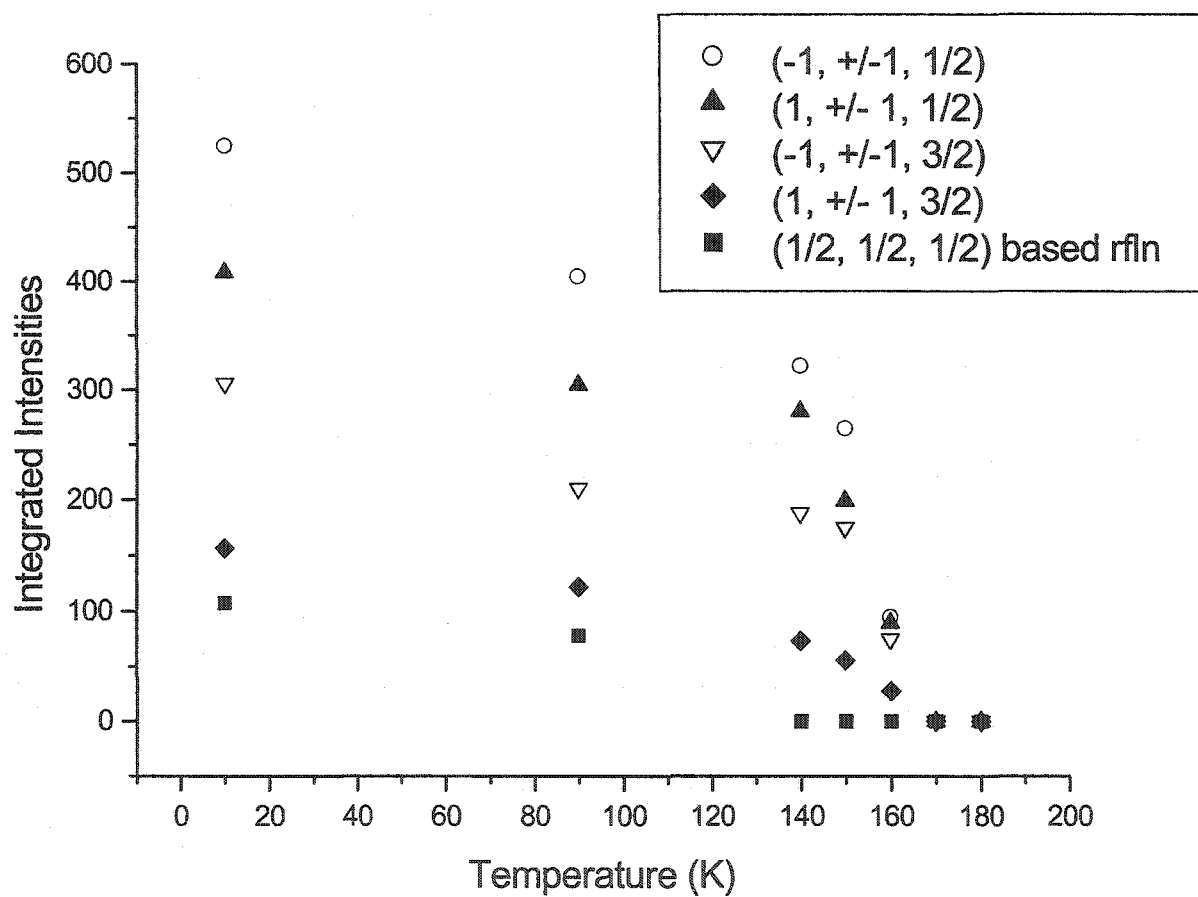


Figure XI: Simultaneous crystal structure/magnetic structure Rietveld refinement of the 10 K data for $\text{La}_5\text{Re}_3\text{MnO}_{16}$. The open circles are the data, the solid line is the fit, the difference plot is shown below and the crystal structure reflections (top) and the magnetic structure reflections (bottom) are marked.

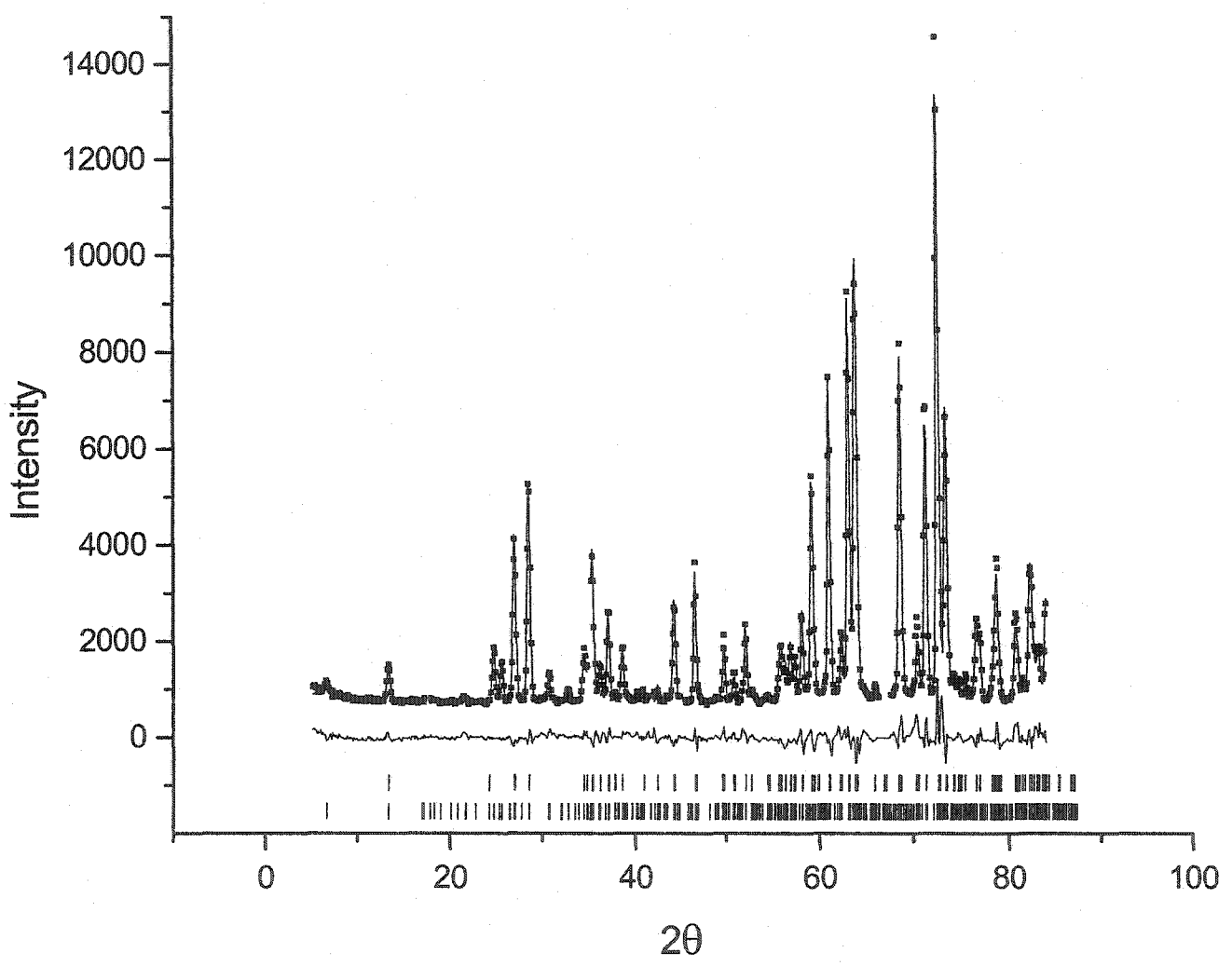
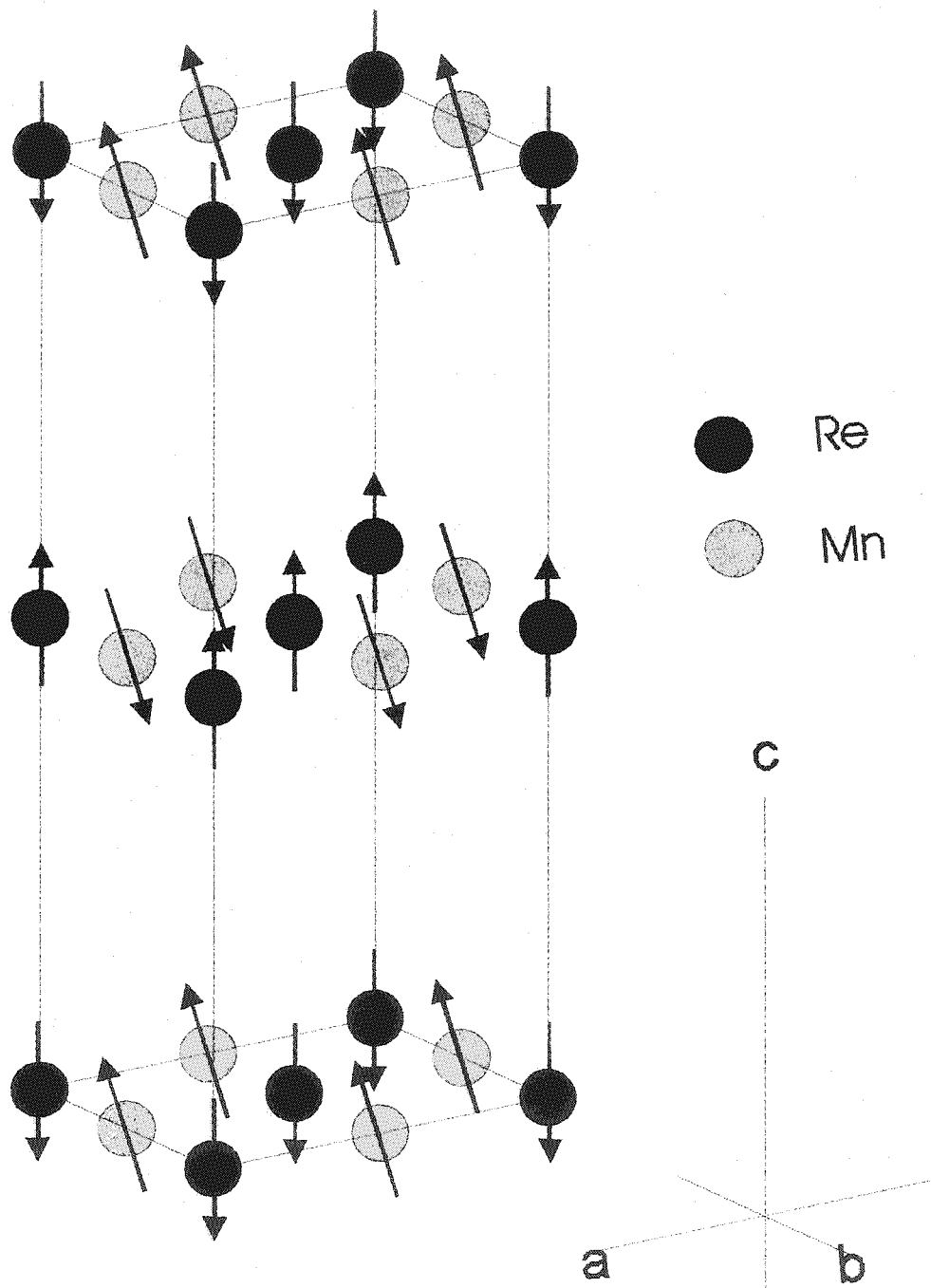


Figure XII: The refined magnetic structure for $\text{La}_5\text{Re}_3\text{MnO}_{16}$ 

FUTURE WORK

There are as of yet several unanswered questions concerning the bulk behaviour of $\text{La}_5\text{Re}_3\text{MnO}_{16}$. Although the magnetic structure has been elucidated, there is still the matter of the $(\frac{1}{2} \frac{1}{2} \frac{1}{2})$ reflections which appear at temperatures much lower than T_N . These are more than likely due to a spin reorientation in the Re-Mn planes, but more detailed measurements are needed to prove this. The ordered moments are also slightly lower than expected, which may indicate an incorrect magnetic structure, or some electron delocalization. The added complication of a Re-Re bond in the dimer layers makes such a determination more difficult, and transport and/or optical measurements are needed to investigate this further.

It has recently been demonstrated that the $\text{La}_5\text{Re}_3\text{MnO}_{16}$ structure is quite robust to substitution within the Re-Mn layer. Dr. Lisheng Chi has synthesized members of the $\text{La}_5\text{Re}_3\text{XO}_{16}$ series, with $X = \text{Fe}, \text{Ni}, \text{Co},$ and Mg .¹³ In the first three cases, he has noted a shift in T_N which is commensurate with the spin on the lattice sites (see table VIII). The magnetic structure of these materials is almost identical to the $\text{La}_5\text{Re}_3\text{MnO}_{16}$ parent compound, albeit a slight canting of the moments within the plane. The relative ease of these substitutions provides the possibility of a detailed study of the ordering mechanism of this series, which would be somewhat exotic considering the exchange paths within the layers that involve a Re-Re bond. It is believed that these materials are all highly two dimensional, with only weak interactions between the perovskite layers. In light of this, it is surprising that the Néel temperatures are quite high in these materials, pointing towards interesting physics that may be at play.

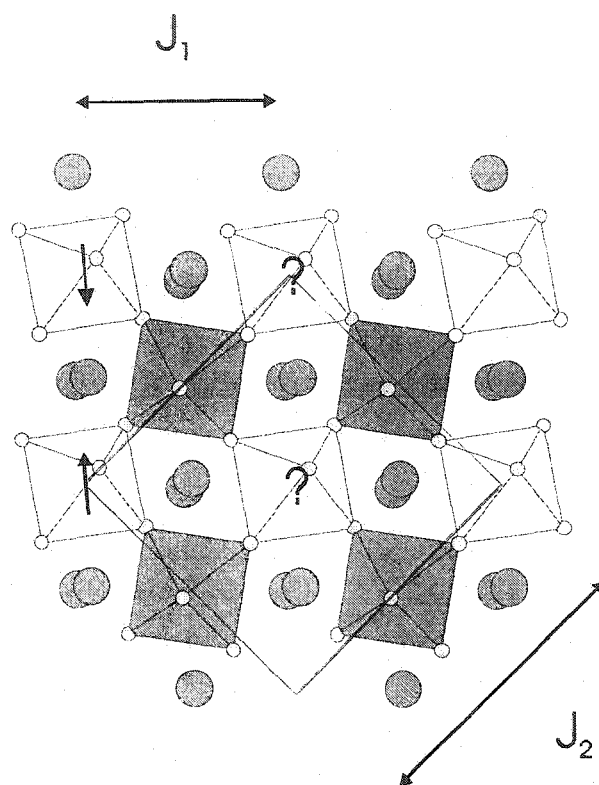
Table VIII: Néel temperatures for the series $\text{La}_5\text{Re}_3\text{XO}_{16}$ ($\text{X} = \text{Fe}, \text{Co}, \text{Ni}$)¹³

	Electronic configuration on X	Néel temperature
$\text{La}_5\text{Re}_3\text{FeO}_{16}$	$4d^6$	155 K
$\text{La}_5\text{Re}_3\text{CoO}_{16}$	$4d^7$	33 K
$\text{La}_5\text{Re}_3\text{NiO}_{16}$	$4d^8$	36 K*
		14 K*

* This material may have two transitions which are apparent from the DC susceptibility data.

For the case of the diamagnetic substitution of Mg within the perovskite layer, no such transition is noted in the magnetic susceptibility. In fact, there is only a broad feature that has a maximum at ~ 60 K. Attempts have been made to understand this behaviour by fitting this feature to a model of 2D spin correlations,¹⁴ but there has been little success. It is now believed that this behaviour can be due to frustration. The Re $S=1$ spins form a square lattice in the a-b plane. With diamagnetic Mg^{2+} ions linking the Re atoms via a Re-O-Mg-O-Re bond, the super-exchange interaction now prefers an antiferromagnetic arrangement of the spins in a magnetically ordered state (see figure XIII). For $J_1 \sim J_2$, which should be a reasonable assumption based upon the diffuse nature of the $5d^2$ orbitals and the similar exchange pathways, the bonding requirements cannot be met for an ordered ground state, and thus frustration should be expected. The novelty of this route to frustration is that the Re atoms now lie in well-separated layers in the ab-plane, which is a rare geometry. The facile nature of the substitution process provides promise that a varied set of frustrated materials can be synthesized based upon this motif, and studied in more detail.

Figure XIII: Possible magnetic frustration in $\text{La}_5\text{Re}_3\text{MgO}_{16}$. If J_1 and J_2 are approximately equal, then the Re moments in the ab plane will not have their bonding criteria met.



ACKNOWLEDGEMENTS

The authors acknowledge the assistance of Dr. J. S. Gardner of the Neutron Program for Materials Research of the NRC of Canada in collecting the neutron diffraction data. This work was supported by the Natural Science and Engineering Research Council (NSERC) of Canada through a research grant to J. E. G.. C. R. W. acknowledges support in the form of a PGS B from NSERC and a OGSST from the government of Ontario.

REFERENCES

- 13) L.-S. Chi, A. E. G. Green, R. Hammond, C. R. Wiebe, and J. E. Greedan, work in progress.
- 14) J. E. Lines, *J. Phys. Chem. Solids*, **31**, 101 (1970).

Chapter Five

Spin Glass Behaviour in the $S=1/2$ FCC

Ordered Perovskite $\text{Sr}_2\text{CaReO}_6$

The next two chapters detail the work done on the ordered FCC perovskites $\text{Sr}_2\text{CaReO}_6$ and $\text{Sr}_2\text{MgReO}_6$. Both of these materials form frustrated networks of $S=1/2$ Re^{6+} cations. Chapter Five incorporates the article “Spin Glass Behaviour in the $S=1/2$ FCC Ordered Perovskite $\text{Sr}_2\text{CaReO}_6$ ”, which has recently been published in Physical Review B (Physical Review B, Volume 65, 144413/1-144413/9, 2002).

Spin Glass Behavior in the $S = 1/2$ FCC Ordered Perovskite $\text{Sr}_2\text{CaReO}_6$

C. R. Wiebe, J. E. Greedan, and G. M. Luke

*The Brockhouse Institute for Materials Research, McMaster University, Hamilton, ON
L8S 4M1, Canada*

J. S. Gardner

*Neutron Program for Materials Research, NRC, Chalk River Labs, Chalk River, ON
K0J 1J0, Canada*

ABSTRACT

The ordered perovskite $\text{Sr}_2\text{CaReO}_6$ of monoclinic symmetry (space group $P2_1/n$, $a = 5.7556(3)$ Å, $b = 5.8534(3)$ Å, $c = 8.1317(4)$ Å, $\beta = 90.276(5)^\circ$ at $T = 4$ K) has been synthesized using standard solid-state chemistry techniques. The difference in the size and charge of the cations induces an ordering of the B site Ca^{2+} and Re^{6+} ions which leads to a distorted FCC lattice of spin-1/2 Re^{6+} ($5d^1$) moments. DC magnetic susceptibility measurements indicate a maximum at $T_G \sim 14$ K and an irreversibility in the FC and ZFC data at ~ 22 K that is believed to be caused by the geometric frustration inherent in the FCC structure. Neutron scattering measurements confirm the absence of magnetic long range order, and μSR experiments indicate the presence of an abrupt spin freezing at T_G . Specific heat measurements reveal a broad anomaly typical of spin glasses and no sharp feature. 65% of the spin entropy is released at low temperatures. The low temperature data do not show the expected linear temperature dependence, but rather a T^3 relationship, as is observed, typically, for antiferromagnetic spin waves. The material is characterized as an unconventional, essentially disorder-free, spin glass

INTRODUCTION

The topic of geometric frustration has been at the forefront of condensed matter physics for the last decade due to the remarkable variety of interesting magnetic ground states observed.¹⁻³ The availability of lattice types which can accommodate the requisite triangular motif of spins coupled with the variety of magnetic species to place on these sites has led to the discovery of a number of materials which have been central to the development of this new subfield of magnetism. Some of these systems appear to order on intermediate length scales at low temperatures, such as the garnet $\text{Gd}_3\text{Ga}_5\text{O}_{12}$.⁴ Others, instead, exhibit phase transitions to disordered or very short range ordered states such as the unconventional spin glasses $\text{SrCr}_{9p}\text{Ga}_{12-9p}\text{O}_{19}$ ⁵ and $\text{Y}_2\text{Mo}_2\text{O}_7$.⁶ In the last few years, the focus of study has shifted to a search for more exotic states such as the spin liquid, which arises due to quantum effects from networks of frustrated spin-1/2 moments, or the spin ice, which is related to the problem of proton disorder in hexagonal water ice first discussed by Pauling.⁷ For example, the pyrochlore, $\text{Dy}_2\text{Ti}_2\text{O}_7$, has been identified as a spin ice material.⁸ Such discoveries provide the impetus to look for new materials.

Despite this high level of interest, the number of examples of frustrated systems with isolated spin-1/2 moments is relatively small. LiNiO_2 for example, is believed to have a quantum spin liquid ground state which is stabilized by short ranged ferromagnetic correlations,⁹ but sample quality is an issue which is still being addressed. Spin liquid characteristics have been found in other materials such as $\text{Tb}_2\text{Ti}_2\text{O}_7$ where Tb^{3+} is an effective $S = 1/2$ ion at low temperatures.¹⁰ Attention has turned recently to less conventional $S = 1/2$ systems such as those based on Re^{6+} ($5d^1$). For example, $\text{Li}_4\text{MgReO}_6$ where the Re^{6+} sublattice consists of a three dimensional array of face-sharing tetrahedra has been synthesized and characterized.¹¹ Its behavior is spin glass like with some unconventional features. While the Re^{6+} sublattice is disorder free, mixing of Li^+ and Mg^{2+} on adjacent sites may induce the spin glass like ground state. To date the number of systems with very little disorder and well-defined $S = 1/2$ moments on frustrated lattices is still small.

The perovskites have historically proved themselves to be extremely robust structures that can accommodate a wide variety of cations on the A and B sites. For certain combinations of oxidation states and cation radii, cation ordering is well known to exist, such as in the perovskites $A_2BB'O_6$ (B^{2+} , B'^{6+}).¹² These ordered sublattices of B and B' sites form two interpenetrating FCC networks, which do indeed fall into the class of frustrated materials, since an FCC lattice is comprised of a network of edge-shared tetrahedra. The number of systems that have been investigated as candidates for geometric frustration on FCC lattices is relatively small as well. Sr_2NbFeO_6 for example, with $S = 5/2$ $3d^5$ Fe^{3+} spins, has demonstrated spin glass behavior according to Rodriguez *et al*,¹³ however the B-site ordering is incomplete in this material. Recently, the $S=1$ systems Sr_2NiTeO_6 and Sr_2NiWO_6 have been studied by Iwanaga *et al*, but they have been found to order at low temperatures.¹⁴ Reports of $S = 1/2$ materials of this class are sparse.

This paper details the synthesis and characterization of a new spin-1/2 frustrated material with $Re^{6+} 5d^1$ ions on an FCC lattice. The perovskite Sr_2CaReO_6 exhibits frustration effects in the absence of detectable disorder on the Re sites. This is one of the few detailed studies to our knowledge of an ordered spin-1/2 system on an edge-shared network of tetrahedra.

EXPERIMENTAL PROCEDURES

Polycrystalline samples of Sr_2CaReO_6 were prepared by firing stoichiometric quantities of SrO (99.9%, Fisher), CaO, (99.99%, Cerac) and ReO_3 (99.9%, Rhenium Alloys, Inc) under vacuum for 60 hours at 900° C in platinum crucibles:



The reactants SrO and CaO were first prefired under vacuum for 12 hours at 400° C

to eliminate surface impurities and remove any absorbed water. The final product was found to be multiphasic, so a subsequent regrinding and refiring stage was needed to isolate a single monoclinic phase product.

The quality of the final product was analyzed using a focussing Guinier- Hagg camera with copper $K_{\alpha 1}$ radiation and a high purity Si powder as an internal standard. No impurities were initially detected by this technique. The oxygen stoichiometry was measured using thermogravimetric analysis, by heating the sample to 900° C under flowing hydrogen.

Neutron diffraction was also carried out on this material using the C2 diffractometer at the National Research Council's Neutron Programme for Materials Research in Chalk River, Canada. Two different wavelengths were employed to investigate the possibility of magnetic ordering (2.3688(3) Å) and to obtain an accurate structural refinement (1.3284(2) Å). The powder patterns were obtained in a temperature range of 4 K – 40 K using a helium cryostat.

DC Magnetic susceptibility data were obtained using a Quantum Design MPMS SQUID magnetometer at McMaster University. Field cooled (FC) and zero field cooled runs (ZFC) were carried out over a temperature range of 2 K to 350 K with applied magnetic fields of 0.01 T and 0.1 T. Isothermal magnetization data were obtained at temperatures of 5 K, 25 K and 40 K in applied fields to 5.5 T.

The heat capacity was measured using an Oxford Instruments Calorimeter, a probe in the Oxford Instruments MagLab system. The sample was a pellet weighing 26.75 mg, and a small known portion of Wakefield grease was applied to insure good thermal contact for which a correction was made. The measurements were completed between 4 K and 35 K using the relaxation method. The sample itself was attached to a sapphire platform which has a Cernox-chip thermometer for temperature control. Measurements at both zero field and an applied field of 6 T were taken in the same temperature range for the Sr_2CaReO_6 sample.

The μ SR experiments were completed at TRIUMF in Vancouver, Canada. The measurements were carried out over a temperature range of 2.5 K – 39.5 K with zero applied magnetic field.

RESULTS AND DISCUSSION

PART A: CRYSTAL STRUCTURE

After the initial firing, the reaction product was found by powder x-ray diffraction to consist of two phases, one monoclinic and the other cubic, by indexing the lines using the search routine DICVOL.¹⁵ Regrinding and refiring under vacuum yielded only the monoclinic phase as the final product.

The space group was determined to be $P2_1/n$ in analogy with the $\text{Ca}_2\text{SrReO}_6$ phase reported by Chamberland and Levasseur.¹⁶ As noted, it is isostructural with the monoclinic Ca_3WO_6 phase. Similar structures have been reported before by Jung and Demazeau¹⁷ for the iridium analogue $\text{Sr}_2\text{CaIrO}_6$ and the related compound $\text{Sr}_2\text{NiTeO}_6$, by Iwanaga *et al.*¹² The unit cell constants at room temperature were found to be $a = 5.7582(3) \text{ \AA}$, $b = 5.8346(3) \text{ \AA}$, $c = 8.1787(4) \text{ \AA}$, and $\beta = 90.245(3)^\circ$ using the program LSUDF¹⁸. There were no impurity lines found. Previously, an orthorhombic cell with similar lattice parameters ($a = 5.76 \text{ \AA}$, $b = 5.85 \text{ \AA}$, $c = 8.21 \text{ \AA}$),¹⁹ and a cubic cell with $a = 8.198(5) \text{ \AA}$ have been reported for this material.¹⁶ No reports of the monoclinic structure have been published to date, but it is likely that the small deviation from orthorhombic symmetry was not detected in earlier efforts. This distortion becomes more pronounced at low temperatures (table I).

The crystal structure was refined from neutron powder diffraction data at 4 K using the Rietveld refinement suite FULLPROF.²⁰ The refinements indicated a small impurity at $d = 2.14 \text{ \AA}$ which could not be indexed. This peak was excluded in the final refinements (see figure I). The final atomic positions at 4 K are listed in table II.

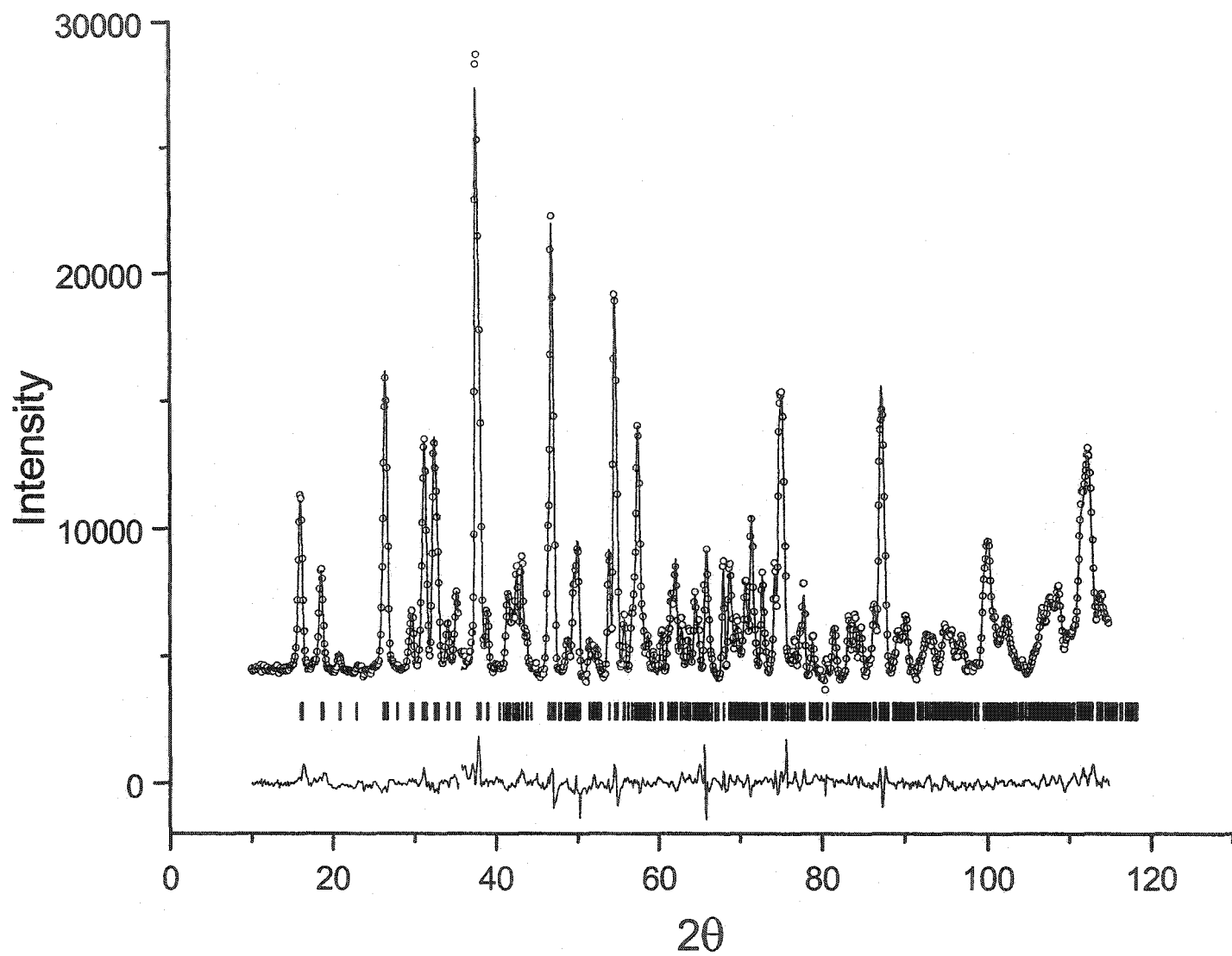


Figure I: Powder neutron diffraction refinements of $\text{Sr}_2\text{CaReO}_6$ at $T = 4 \text{ K}$ with $\lambda = 1.3284(2) \text{ \AA}$ neutrons. ($R_p = 7.87$, $R_{wp} = 9.03$)

	Sr ₂ CaReO ₆ , 4 K	Sr ₂ CaReO ₆ , 295 K	Sr ₂ CaWO ₆ , 295 K
a	5.7556(3) Å	5.7582(3) Å	5.7657(2) Å
b	5.8534(3)	5.8346(3)	5.8496(3)
c	8.1317(4)	8.1787(4)	8.1927(4)
β	90.276(5) °	90.245(3) °	90 °

Table I: Lattice parameters for Sr₂CaReO₆ at 4 K (short wavelength neutron data) and 295 K (x-ray data) as determined by powder diffraction. The material used as a model for the lattice contribution to the heat capacity, orthorhombic Sr₂CaWO₆, is referenced as well for comparison (x-ray data).

	x	y	z	B	Site
Sr	0.0096(8)	0.0421(4)	0.2477(8)	0.80(10)	4e
Ca	0.5	0.0	0.0	0.56(8)	2d
Re	0.5	0.0	0.5	0.54(8)	2c
O1	0.2664(8)	0.3109(8)	0.0384(7)	0.86(10)	4e
O2	0.1861(8)	-0.2342(9)	0.0468(6)	0.96(10)	4e
O3	-0.0822(7)	0.4769(7)	0.2256(5)	0.82(10)	4e

Table II: Refined lattice positions and temperature factors for Sr₂CaReO₆ ($\lambda = 1.3284(2)$ Å) at 4 K

The ordered perovskite structure of monoclinic Sr₂CaReO₆ is shown in figures II and III. The distortion away from cubic symmetry is due to two factors: the presence of a relatively small cation on the A site and the mismatch of cations on the B and B' sites. A choice of Ba²⁺ for the A site, which has a significantly larger ionic radius than Sr²⁺,²¹ (1.75 Å

compared to 1.58 Å for XII coordinated sites) results in a readily obtained cubic structure, $\text{Ba}_2\text{CaReO}_6$, by the same synthesis techniques.²² The larger framework in this case provides more volume for the B sites and thus a more accommodating structure. A choice of a smaller cation than Ca^{2+} on the B site, such as Mg^{2+} which has an ionic radii more similar in size to Re^{6+} , results in a tetragonal unit cell as in $\text{Sr}_2\text{MgReO}_6$ (Ca^{2+} has a radius of 1.14 Å, as compared to 0.86 Å and 0.69 Å for Mg^{2+} and Re^{6+} VI coordinated sites respectively).²³ The possibility of disorder on the B sites is more likely here though, with such similar sizes of cations. The goal in the synthesis of $\text{Sr}_2\text{CaReO}_6$ was to find a material with an ordered array of Re^{6+} moments on an FCC lattice to study the effects of geometric frustration in the absence of disorder.

Nonetheless, the possibility for cation disorder was investigated in the refinements by allowing for site mixing among the A, B, and B' cation sites. All of the atoms refined to full occupancy on their respective sites to within 1%. Disorder in this structure is highly unlikely due not only to the differences in sizes of the cations, but also due to the large difference in formal charge on the B and B' site ions. The electrostatic repulsion between the Re^{6+} cations is a significant ordering mechanism.

The bond lengths of the Re^{6+} and Ca^{2+} octahedra are listed in figures II and III, and noted in table III. All of the octahedra are distorted, with unequal apical and equatorial bond lengths as indicated. A valence bond sum analysis was carried out using VALIST²⁴ to determine the oxidation state of the Re ions. The elongated bonds on the Re octahedra gave slightly higher values for the valence (7+ rather than 6+), and the Ca octahedra being similarly distorted gave slightly higher values as well (2.5+ rather than 2+). The high values for the Re site reflect the poorly known valence bond parameters for the Re^{6+} species. To address this problem, a thermogravimetric analysis in flowing hydrogen was completed to fully reduce the sample by heating to 900 ° C. The expected reaction is



The experimental weight loss of 10.25 % correlated quite well with the expected

weight loss of 10.14 % assuming full oxygen stoichiometry, and thus an oxidation state of Re^{6+} . The final product, a dull yellow colored solid, was investigated using x-ray diffraction on the Guinier-Hagg apparatus mentioned above and was found to contain Re metal and a mixture of poorly crystallized $\text{Sr}_x\text{Ca}_{1-x}\text{O}$ phases. The oxygen stoichiometry was assumed to be 6.0, but in the final refinements of the neutron data, the occupancy factors for each oxygen site were allowed to vary to check for defects. The values refined to their full occupancies to within 1%.

Table III: Bond distances and angles for $\text{Sr}_2\text{CaReO}_6$ at $T = 4 \text{ K}$ and $T = 20 \text{ K}$ as determined by powder neutron diffraction ($\lambda = 1.3284(2) \text{ \AA}$). There are no appreciable changes due to the phase transition at $T_G \sim 14 \text{ K}$.

	4 K	20 K
Re – O1	1.907(4) Å	1.899(5) Å
Re – O2	1.921(5)	1.925(5)
Re – O3	1.904(4)	1.908(4)
Ca – O1	2.291(4)	2.297(4)
Ca – O2	2.300(5)	2.295(5)
Ca – O3	2.280(4)	2.280(4)
Re – Re	5.7518(3)	5.7483(3)
	5.7640(2)	5.7652(2)
	5.7835(2)	5.7859(2)
	5.8494(3)	5.8468(2)
Re – O2 – Ca	152.562(184) °	152.445(179) °
Re – O1 – Ca	155.278(172)	155.356(168)
Re – O3 – Ca	152.269(162)	152.442(156)

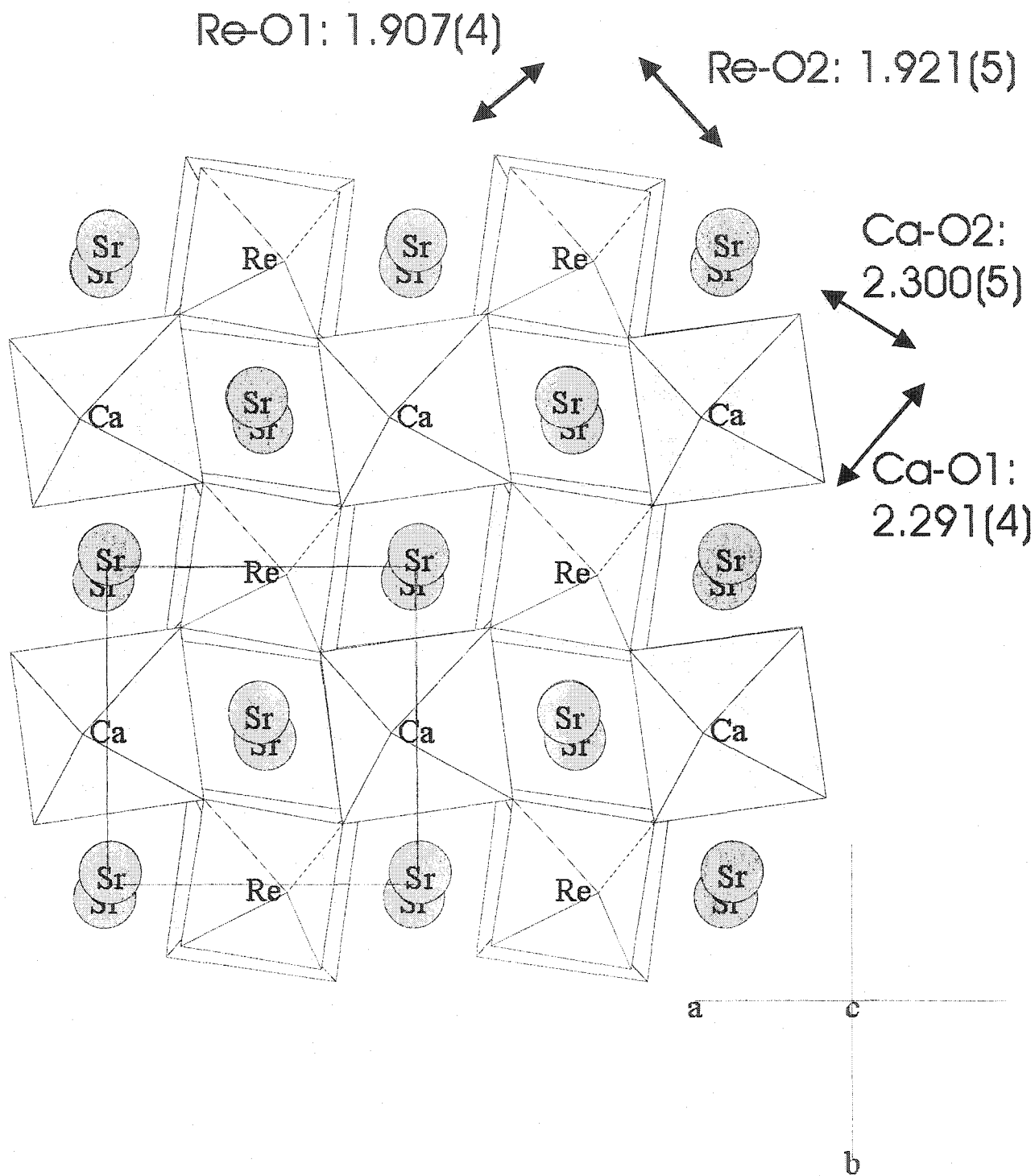


Figure II: The crystal structure of $\text{Sr}_2\text{CaReO}_6$ as viewed from the ab plane at $T = 4$ K. Note the distortion of the Ca and Re octahedra.

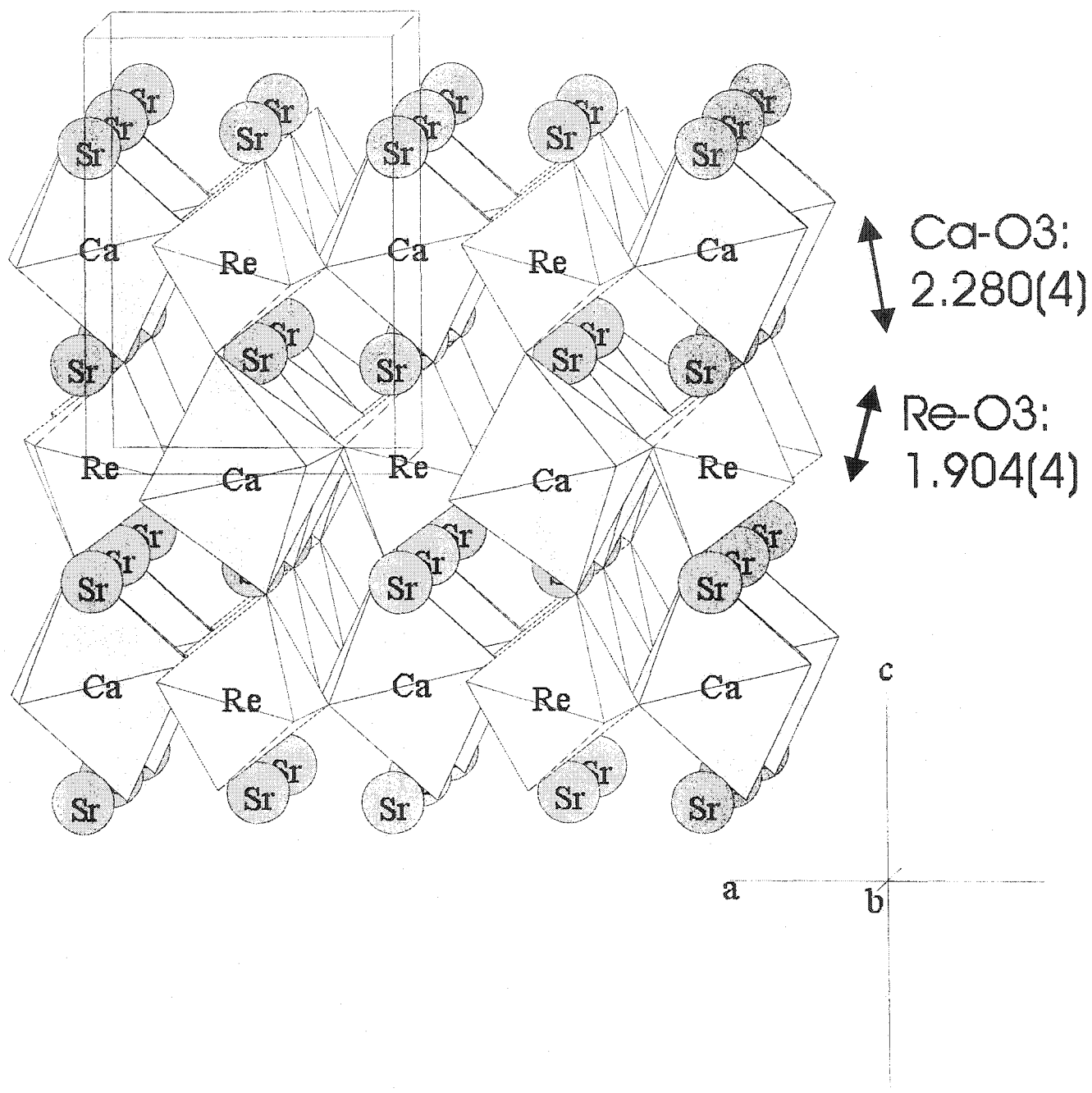


Figure III: The crystal structure of $\text{Sr}_2\text{CaReO}_6$ as viewed from the ac plane.

Since the magnetic interactions between the Re moments are mediated via superexchange mechanisms, the bond angles for the Re-O-Ca-O-Re pathways are important to note at this point. Due to the significant tilting in the octahedra of the distorted structure, these angles vary greatly from the ideal 180° for the perfect cubic structure, as indicated in table III.

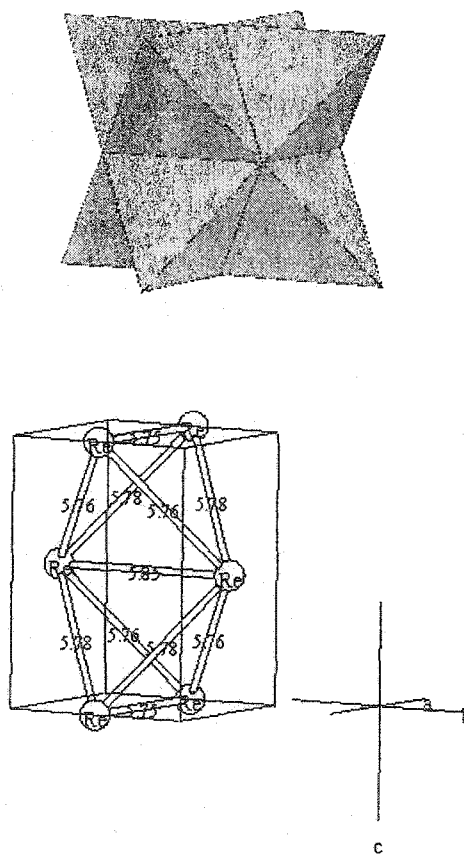


Figure IV: The ordered Re ions in the FCC-based lattice form a network of edge-shared tetrahedra as indicated above. The corresponding Re-Re distances are noted in the figure below.

The underlying topology of the magnetic sublattice, however, suggests that magnetic frustration should be observed due to the Re^{6+} ordering on the FCC lattice. Figure 4 shows the isolated Re sublattice with respect to the unit cell. The bond distances have been indicated in angstroms. Although these distances are slightly different from one another due to the low symmetry of the monoclinic framework, they all lie within a few percent of the mean distance ($\sim 5.8 \text{ \AA}$), and the magnetic exchange constants are expected to be similar for nearest neighbors on all of the Re sites.

PART B: MAGNETIC SUSCEPTIBILITY EXPERIMENTS

The magnetic response of $\text{Sr}_2\text{CaReO}_6$ was expected to be quite weak due to the dilute nature of the magnetic sublattice and relatively small size of the Re^{6+} moment. Previous DC susceptibility measurements on the ordered perovskite $\text{Sr}_2\text{CaReO}_6$ in the range of 80 K – 300 K suggested Curie-Weiss behavior, with $\theta = -189 \text{ K}$ and an effective moment of $\mu_{\text{eff}} = 1.08 \mu_{\text{B}}$ based upon a fit to:¹⁶

(1)

$$\chi = C/(T - \theta)$$

where $\mu_{\text{eff}} = \sqrt{8 C}$. The values obtained here by fitting over the temperature range of 170 K – 250 K (see inset, figure V) are $\mu_{\text{eff}} = 1.659(6) \mu_{\text{B}}$ and $\theta = -443(6) \text{ K}$ (after applying a diamagnetic correction). This indicates strong antiferromagnetic interactions among the Re moments, a requirement for geometric frustration. The strong antiferromagnetic interactions are perhaps unexpected in this material, considering the distorted exchange pathways and small values for the Re $S = \frac{1}{2}$ moments. One possible reason for this result is due to the extended nature of the 5d orbitals, which provide good overlap regardless of the deviations in bond angle. One can compare this system with the monoclinic Ni analogue $\text{Sr}_2\text{NiTeO}_6$, with a $3d^8$ configuration, $S = 1$, on the Ni^{2+} site, which has a Weiss constant of -240 K .¹⁴ From mean field theory, one can compute values for the nearest neighbor exchange constant as

(2)

$$J_{nn}/k = \frac{\theta_c}{12(2/3)S(S+1)}$$

The ratio of J_{nn}/k for $\text{Sr}_2\text{CaReO}_6$ relative to $\text{Sr}_2\text{NiTeO}_6$ is 5:1, which illustrates the more extended nature of the 5d orbitals relative to 3d orbitals.

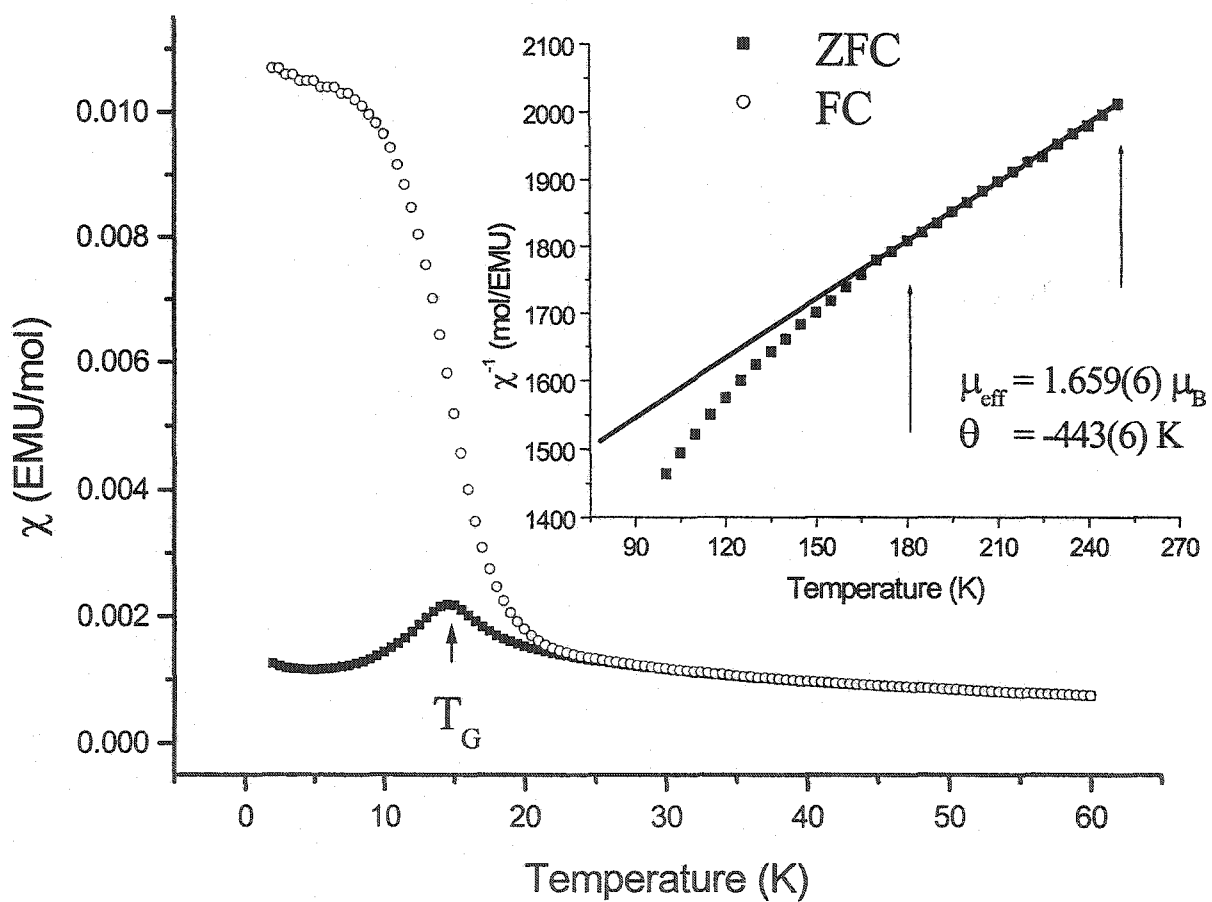


Figure V: DC magnetic susceptibility results for powder $\text{Sr}_2\text{CaReO}_6$ samples. The inset shows the inverse susceptibility, and the fit to the Curie-Weiss law as indicated in the text.

The value obtained for the effective moment falls slightly shy of the theoretical value for a $5d^1$ system, which is expected to be $1.73 \mu_B$ for $S = 1/2$. It is well known, however, that Re^{6+} in an octahedral environment has a reduced magnetic moment due to spin-orbital coupling and crystal-field effects. These spin orbital contributions have been noted to reduce the moment in related systems as well, such as $\text{Li}_4\text{ReMgO}_6$, which has an effective moment of $1.14(1) \mu_B$ on the Re^{6+} sites.¹⁰ Reduced moments are also a signature of geometrically frustrated systems, with many known cases in the literature.²

Another common feature of geometrically frustrated materials is a divergence in the field-cooled and zero field-cooled susceptibility at low temperatures, indicative of a highly degenerate magnetic ground state. The cusp like feature that is observed in figure V is seen in other frustrated materials, such as the pyrochlore spin glass $\text{Y}_2\text{Mo}_2\text{O}_7$, which has a network of corner-shared tetrahedra.⁶ A major difference in the magnetic response of our sample is a divergence in the susceptibility at $T \sim 23$ K which occurs at temperatures much higher than the transition temperature of $T_G \sim 14$ K, where the cusp is located. This suggests the presence of magnetic correlations which set in at a higher temperature scale than T_G .

Additional evidence for frustration effects in this material is seen in the Curie-Weiss fit to the inverse susceptibility, which lies above the data at low temperatures, inset, figure V. This departure from Curie-Weiss behavior is not well understood, but it is believed to be due to orphan spins, or spins due to defects, for systems that display structural disorder.² However, this feature is seen in frustrated materials with very little or no structural disorder as well, such as the spin ice $\text{Dy}_2\text{Ti}_2\text{O}_7$ ⁸ or the spin glass, $\text{Y}_2\text{Mo}_2\text{O}_7$.⁶ Clearly, an explanation for this characteristic still lacks solid theoretical grounding, but progress is being made.²⁵

Finally, a frustration index, f_{frus} , is typically used as a measure of the degree of frustration in a magnetic material, which is defined as:

(3)

$$f_{\text{frus}} = |\theta| / T_{\text{ord}}$$

where θ is the Weiss temperature as extracted from the high temperature Curie-Weiss fits, and T_{ord} is a transition temperature. Typically, for geometrically frustrated materials,

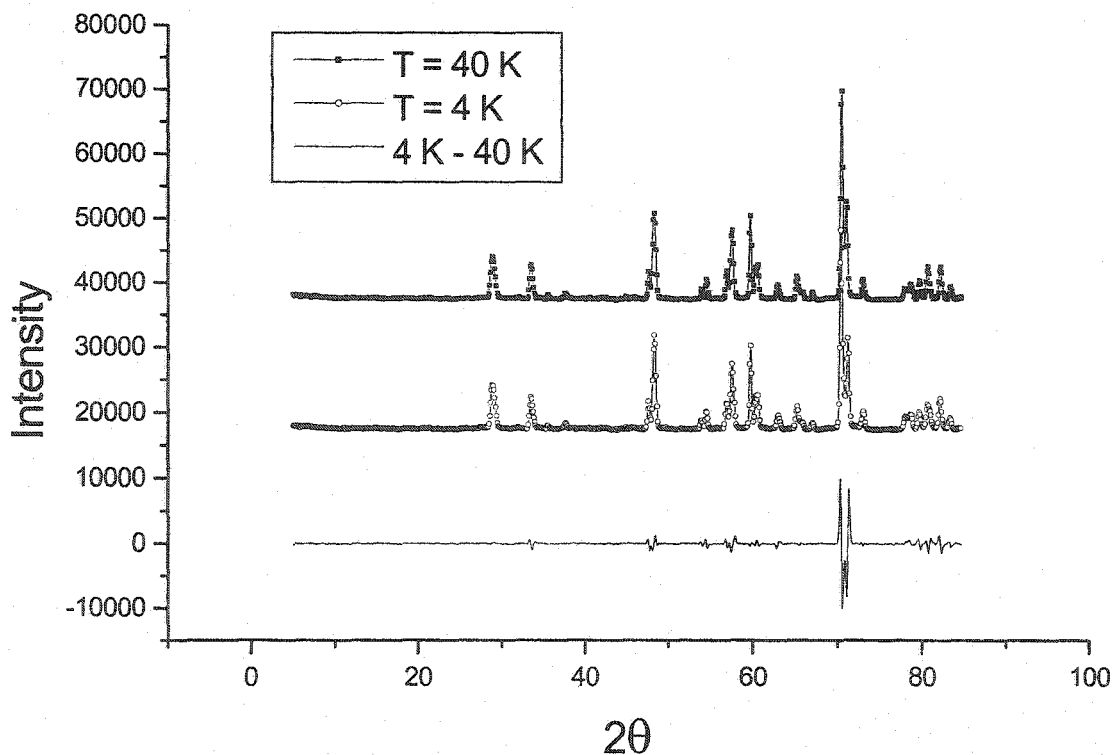
$f_{\text{frus}} > 10$. The f_{frus} for $\text{Sr}_2\text{CaReO}_6$ can be estimated at ~ 31 . In comparison to other perovskites, $\text{Sr}_2\text{NbFeO}_6$ has a $f_{\text{frus}} \sim 30$ and is a spin glass, but the role of B site disorder is unclear.¹³ The $S = 1$ ordered analogues $\text{Sr}_2\text{NiTeO}_6$ and Sr_2NiWO_6 have lower indices of $f_{\text{frus}} \sim 7$ and $f_{\text{frus}} \sim 3$, and they form ordered ground states.¹⁴ The observation of glassy magnetic behavior is thus expected for $\text{Sr}_2\text{CaReO}_6$ as well.

The cusp like feature and divergence in the FC/ZFC susceptibility is a tell-tale sign of a spin glass transition, yet these features have also been seen in samples that exhibit long range magnetic ordering. Even though the magnetic sublattice is highly frustrated, such an ordering is always possible, and to investigate this a series of low temperature neutron scattering experiments were completed to probe the magnetic ground state. Measurements were done with long wavelength neutrons ($2.3688(3) \text{ \AA}$) for very long counting intervals at a medium flux source, but no evidence for long range magnetic ordering was detected down to 4 K (see figure 6). Given the very small moment expected on the Re^{6+} spin- $1/2$ site, it is not clear that a complex ordering would be detectable using this technique. Thus, the diffraction patterns expected for a variety of simple ferromagnetic and antiferromagnetic arrangements were simulated using FULLPROF with a moment size of $1 \mu_B$ on each site. Most FCC materials order in a few types of magnetic structures, and some of these were investigated in detail.^{26,27} For example, a simple stacking of Re^{6+} moments of magnitude $1 \mu_B$ in a type-I ordering ($Q = (0, 0, 1)$) yielded Bragg peaks which were on the order of 2% of the intensity of the strongest structural peak. This is clearly within the detection limits of the instrument, and thus, if magnetic ordering of this type were present it would have been observed. While the evidence is to the contrary, the existence of magnetic ordering cannot be precluded on this basis alone. No significant lattice distortion, which may be expected with an ordering transition, was noted in the vicinity of T_G .

Magnetization measurements performed on this sample in fields up to 5.5 T provided further evidence for the absence of long range magnetic order, since no saturation of the moment was found even to low temperatures (see figure VII). Evidence for hysteresis was observed, which was most prominent at 5 K, below T_G . As the temperature was increased, the size of the remnant magnetization was reduced greatly, until it was almost negligible at

40 K. Magnetic hysteresis is typical in spin glass materials due to the large number of degenerate ground states that can be accessed at virtually negligible energy cost. By this criterion, then, and given the absence of any evidence for ferromagnetism, it is reasonable to conclude that $\text{Sr}_2\text{CaReO}_6$ is a spin glass. It is unusual, though, that spin glass behavior would be observed at all, since such systems arise due to chemical disorder on the magnetic sites, such as in the alloys CuMn .²⁸ The powder neutron diffraction results indicate no such disorder down to the 1% level of detectability. There are cases of spin glass behavior in the absence of disorder in other frustrated systems, such as $\text{Y}_2\text{Mo}_2\text{O}_7$ (which has $f_{\text{frus}} \sim 10$), but in even these cases, evidence for an ill-defined disorder has been claimed in recent XAFS measurements.²⁹ Further measurements on $\text{Sr}_2\text{CaReO}_6$ may reveal small levels of disorder as well.

Figure VI: Powder neutron diffraction profiles at $T = 4$ K and $T = 40$ K with $\lambda = 2.3688(3)$ Å. Note the absence of magnetic Bragg peaks in the difference profile below. The shift observed is due to a slight relaxation of the lattice as the temperature is increased.



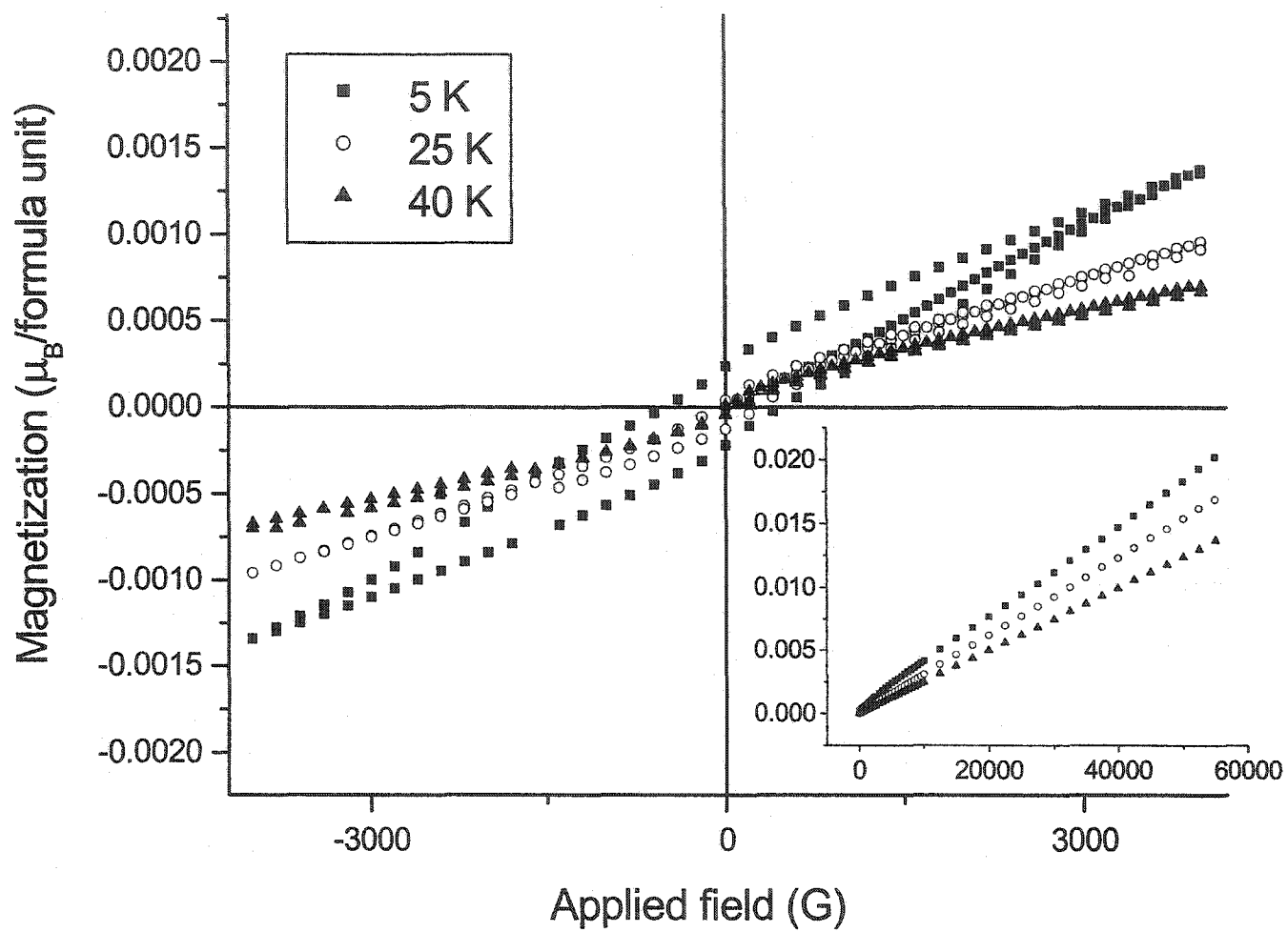


Figure VII: DC magnetization measurements as a function of field for $T = 5$ K, $T = 25$ K and $T = 40$ K. Note the strong hysteresis at $T = 5$ K. The inset shows the high field measurements, which show no signs of saturation.

PART C : μ SR MEASUREMENTS

μ SR has long been used to study the dynamics of spin glasses and related systems. For small S spin systems in particular, muons are perhaps the best probe of the low temperature magnetic ground state within a broad frequency range.

Figure VIII shows several zero field-cooled scans taken between $T = 2.5$ K and $T = 28$ K. The two component nature of the spectra is immediately evident below $T_G \sim 14$ K, as opposed to the single component high temperature scans which is characteristic of a paramagnetic response. This characteristic two-component signal indicates a quasi-static distribution of internal magnetic fields developing below T_G , as noted in other spin glasses.^{6,30} The fit to the spectra indicated in figure VIII are modeled after Uemura's original treatment of these line shapes in his pioneering μ SR work on AuFe and CuMn alloys:²⁸

(4)

$$G(t) = \frac{1}{3} \left[\exp \left[- (4\alpha_d^2 t / \nu)^{1/2} \right] \right] + \frac{2}{3} \left[1 - \frac{\alpha_s^2 t^2}{(4\alpha_d^2 t / \nu + \alpha_s^2 t^2)^{1/2}} \right] \exp \left[- (4\alpha_d^2 t / \nu + \alpha_s^2 t^2)^{1/2} \right]$$

In this equation, ν is the spin fluctuation rate, and α_s and α_d are the static and dynamic spin components. The fits to the spectra are more phenomenological than quantitative descriptions of the data. More detailed analysis which would include modeling of the spin relaxation function for this system would be needed to extract a proper fluctuation rate, for example. It suffices to conclude at this point that the behavior is typical of a spin glass.

The relative absence of a fluctuating component to the spectra indicates that a large percentage of spins are frozen at low temperatures. Although the signal is weak due to the small moment, it is also clear that there is no periodic modulation in the line shape. This precludes the existence of magnetic ordering, which would show such a modulation due to muon precession in an ordered field.

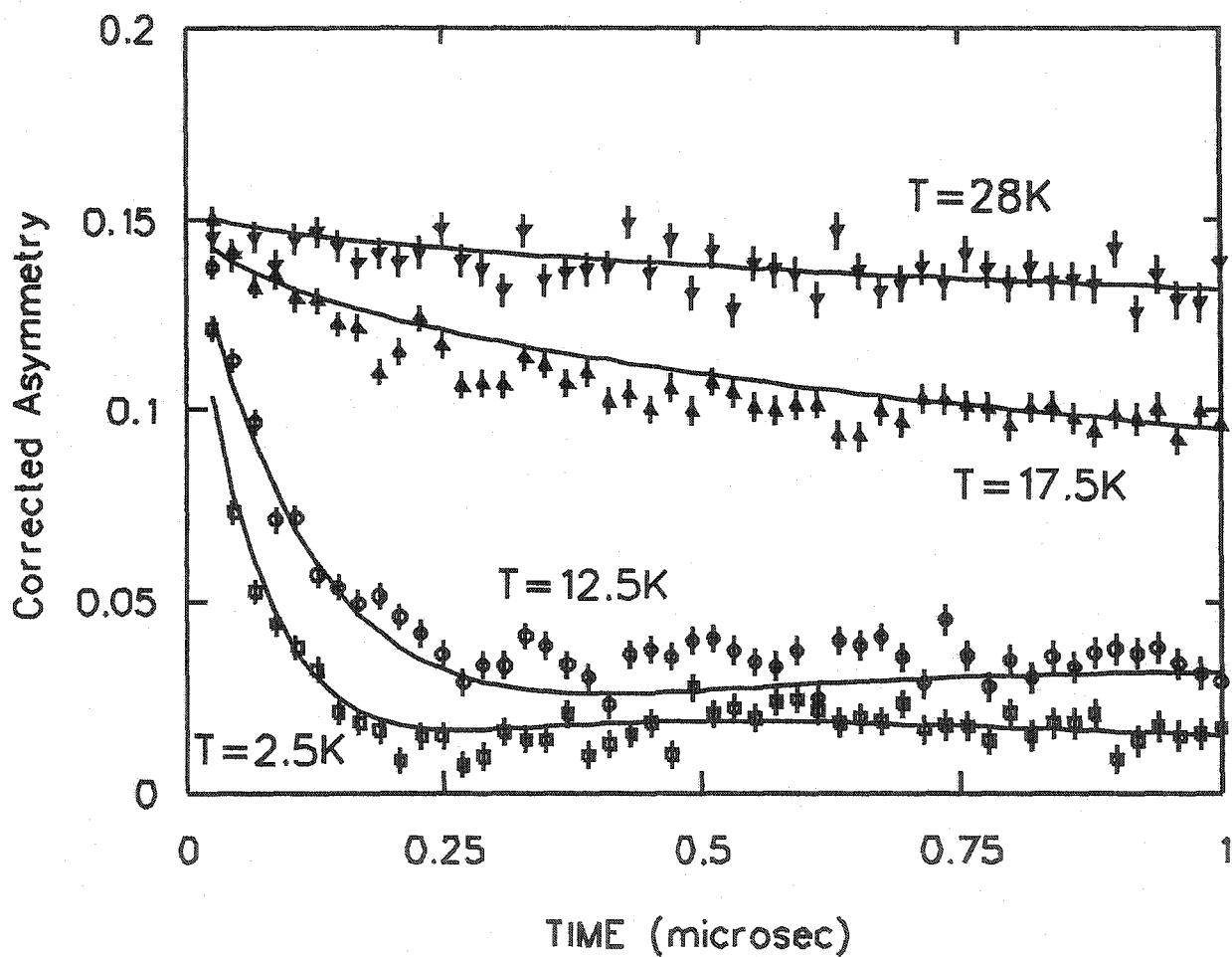


Figure VIII: ZF μ SR measurements of $\text{Sr}_2\text{CaReO}_6$ at $T = 2.5\text{ K}$, 12.5 K , 17.5 K , and 28 K . The fits are based upon a generic spin glass relaxation function as described in the text.

Although it seems like this system is a typical spin glass from the μ SR measurements, there are several departures from convention which merit further discussion. First, the signal is somewhat weak, which is expected due to the small magnetic moment, but since it is feeble, it is truly difficult to tell if there is a weak ordering signal buried in the background. There could indeed be short ranged magnetically ordered clusters forming that are virtually undetectable by this technique. One would expect spin fluctuations at temperatures slightly higher than T_G to be visible in the spectra³¹, but the nature of the transition itself is rather abrupt, with only the slightest hint of a second component appearing at $T = 17.5$ K. It is not surprising to see spin clusters starting to freeze out at temperatures higher than T_G , for our susceptibility measurements have a FC/ZFC divergence at $T \sim 23$ K. However, it is surprising that the second component develops quickly below T_G . The conventional way of understanding spin glasses is in the formation of islands of frozen spins which slowly develop as one passes through the transition. In our system, however, there is relatively little change in the muon signal from 12.5 K to 2.5 K, which suggests that the spins freeze out rather abruptly. One can compare this behavior to what is seen in the related material $\text{Li}_4\text{MgReO}_6$, for example, which has a gradual formation of the glassy state as indicated by μ SR measurements.¹¹ However, in this material, there is no cusp in the susceptibility, just a very weak FC/ZFC divergence at ~ 12 K, and there is also the presence of disorder on the Mg/Li sites, but not the Re^{6+} sites.¹¹ In contrast, the pyrochlore $\text{Y}_2\text{Mo}_2\text{O}_7$ has no or very little disorder, but there are significant spin fluctuations observed with μ SR and inelastic neutron scattering up to ~ 40 K, and thus a very slow development of the spin glass state as well.^{6,31} The abrupt nature of the transition in $\text{Sr}_2\text{CaReO}_6$ is unusual and worthy of further investigation.

PART D : HEAT CAPACITY MEASUREMENTS

Although the μ SR experiments provide compelling evidence for an unconventional spin glass ground state, the existence of a long or short-range magnetic ordering for example may be overlooked due to the local nature of the probe's interactions. For example, in the FCC antiferromagnet GdInCu_4 ,²⁶ a transition to a partially ordered state occurs in which glassy layers of Gd moments are interspersed with ordered layers. The magnetic susceptibility for this material is very similar to $\text{Sr}_2\text{CaReO}_6$, with a FC/ZFC divergence at temperatures higher than the cusp-like feature, which is due to a weak ordering followed by a spin glass transition. It is conceivable that μ SR experiments would be relatively insensitive to this set of transitions, and other factors such as the existence of multiple oxygen sites for the muon to reside on may further complicate the interpretation of the results. Specific heat measurements would provide more definitive evidence about the ground state. For example, a lambda-like anomaly would be present in the case of long range magnetic ordering, albeit diminished in magnitude due to the small moment. Spin glass behavior, on the other hand, would result in a broad feature centered about T_G .

The results of the heat capacity measurements in an applied field of 0 T and 6 T are shown in figure IX. A broad and smeared out anomaly is readily visible in the data in the vicinity of T_G , and there is no sign of a lambda type feature that would be expected for a magnetically ordered system. In addition, the robustness of the anomaly with respect to field is unexpected in conventional spin glasses.³²

In an effort to extract the magnetic component to the specific heat, the non-magnetic analogue Sr_2CaWO_6 was synthesized and measured. Stoichiometric quantities of prefired SrCO_3 , CaCO_3 (99.999%, Cerac), and WO_3 (99.98%, Alfa-Aesar) were intimately ground, pressed into pellets, and fired in air up to 1350 ° C for 12 hours. A regrinding and refiring step was needed with rapid quenching to isolate the final product and avoid a Sr_2WO_5 impurity. The resulting product was orthorhombic, with lattice parameters in agreement with the literature³³ (see table I). Unfortunately, the difference in the underlying lattice symmetry gave rise to a quantitatively different heat capacity, and a straight subtraction of

the two data sets was not a feasible route to determining the magnetic heat capacity C_m . Instead, a different approach was taken. The Debye temperature as a function of temperature was determined for Sr_2CaWO_6 using the Debye specific heat expression:

(5)

$$C = 9R(\theta_D / T)^3 \int_0^{\theta_D / T} \frac{x^4 e^x}{(e^x - 1)^2} dx$$

The same procedure was done for $\text{Sr}_2\text{CaReO}_6$, and the two data sets were scaled by a single constant such that the Debye temperatures were in agreement at temperatures higher than the magnetic transition. The lattice contribution for $\text{Sr}_2\text{CaReO}_6$ was then calculated down to low temperatures with the rescaled data, and subtracted from the total heat capacity to estimate the magnetic contribution (see figures IX and X). It is worth noting that the lattice contribution to the heat capacity is low compared to the magnetic contribution for the $T \sim T_G$ regime. This suggests that further calculations with the magnetic heat capacity, such as the entropy removal at low temperatures, will be relatively unaffected by details of the estimated lattice contribution.

The final result for C_m clearly accentuates the broad signature typical for short-ranged correlations that are seen in spin glasses (figure X). The extensive nature of the peak suggests that magnetic correlations may set in at higher temperatures, which is echoed by the μSR measurements which indicate a slight glassiness as high as 17.5 K. It is interesting to compare the specific heat anomaly with the susceptibility results, which show a broad peak as well centered about T_G , and a FC/ZFC dependence which diverges at higher temperatures (~ 23 K). This behavior is somewhat reminiscent of what is observed in the pyrochlore $\text{Y}_2\text{Mo}_2\text{O}_7$, which has a smeared out heat capacity anomaly that has been interpreted as a signal of short-ranged ordering at $T_G \sim 22.5$ K.³⁴ Subsequent neutron scattering measurements have confirmed that these correlations persist to $T \sim 40$ K in the form of low-energy spin fluctuations. Further neutron work may show a similar result for the dynamics of $\text{Sr}_2\text{CaReO}_6$.

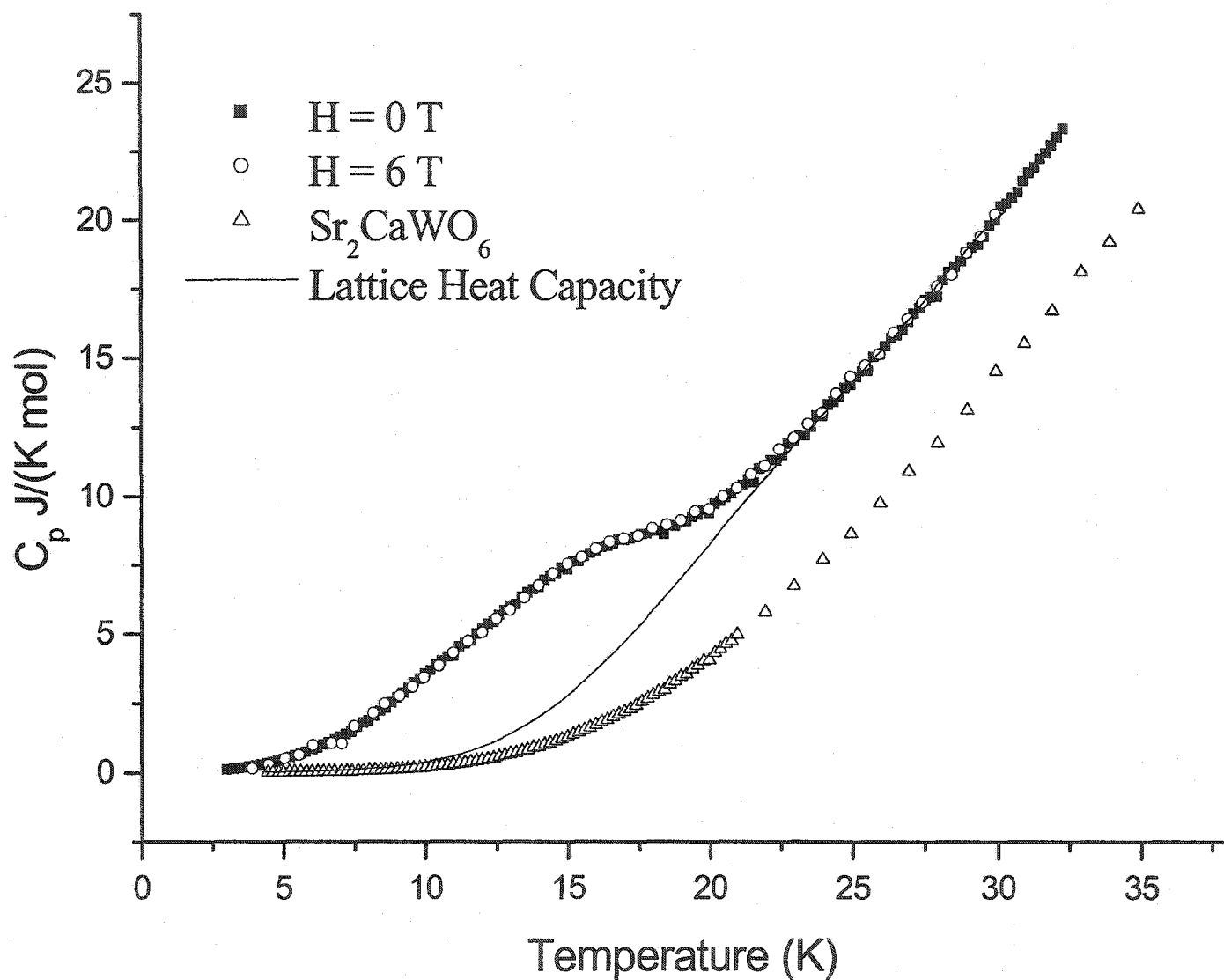


Figure IX: The heat capacity of $\text{Sr}_2\text{CaReO}_6$ at $H = 0$ T and $H = 6$ T, the heat capacity of the lattice model compound Sr_2CaWO_6 at $H = 0$ T, and the calculated lattice heat capacity of $\text{Sr}_2\text{CaReO}_6$ based upon the model material.

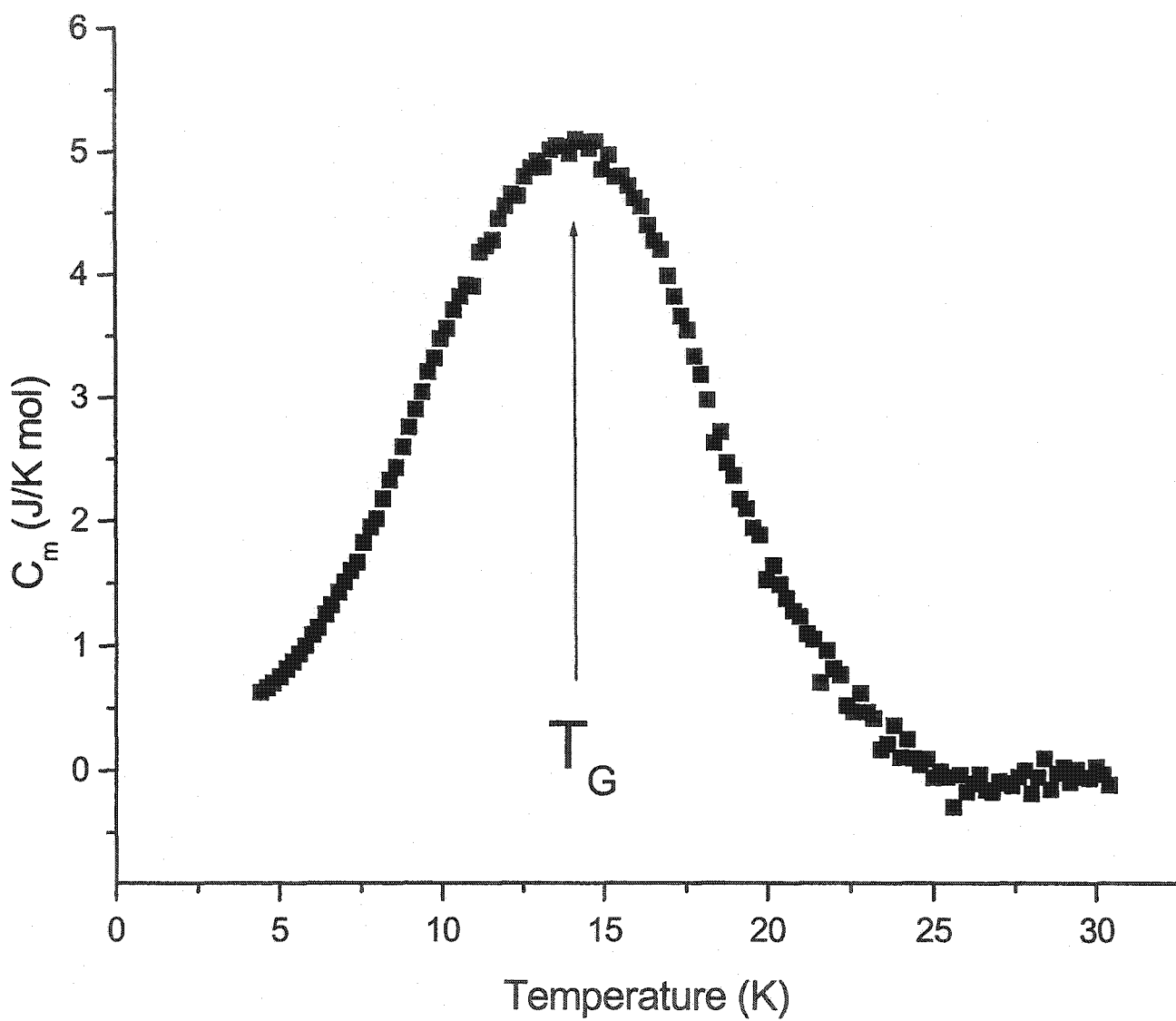


Figure X: The magnetic heat capacity of $\text{Sr}_2\text{CaReO}_6$ calculated by subtracting the lattice component.

A striking difference between the two systems is the absence of a linear dependence of C_m with temperature for $\text{Sr}_2\text{CaReO}_6$ below T_G . This linear variation has been noted for $\text{Y}_2\text{Mo}_2\text{O}_7$ ³⁴ and related compounds such as $\text{Y}_2\text{Mn}_2\text{O}_7$ ³⁵ and suggests a low temperature density of states which is independent of energy as would be expected for spin glasses. To determine the power law for $\text{Sr}_2\text{CaReO}_6$, a logarithmic plot of the heat capacity as a function of temperature was made (see figure XI inset). The calculated exponent was 2.897(5) for $T < 10$ K. Since the lattice component should be negligible in this region, it is somewhat surprising to find $C \sim T^3$. The strong T^3 dependence is shown more clearly in figure XI, with an excellent fit to $C_m \sim T^3$. Unusual temperature dependencies of the heat capacity at low temperatures have been found in other frustrated systems, with the most notable example being SCGO, which has $C \sim T^2$ which has been ascribed to 2D antiferromagnetic spin waves from large 2D correlated domains.³⁶ Another more recent example is the case of LiNiO_2 , which has a complex spin glass like ground state and a $T^{2.5}$ specific heat dependence.³⁷ One possible origin for the appearance of the T^3 term in $\text{Sr}_2\text{CaReO}_6$ is from spin waves. For a long range ordered 3D AF, one would expect $C \sim T^3$ from a spin wave contribution.³⁸ However, from the geometry of the frustrated lattice, and from the evidence presented previously in this paper, it is unlikely that this system exhibits long range order, or at least it is unlikely that the bulk of the material orders. A more plausible explanation for this feature is that there is a difference in the dynamical response of this material when compared to other spin glasses rather than an ordering mechanism. In analogy with SCGO, which has large but finite 2D correlated regions of spins, one would expect $\text{Sr}_2\text{CaReO}_6$ to have large but finite 3D correlated regions of spins, and hence the T^3 heat capacity term in the absence of magnetic ordering.

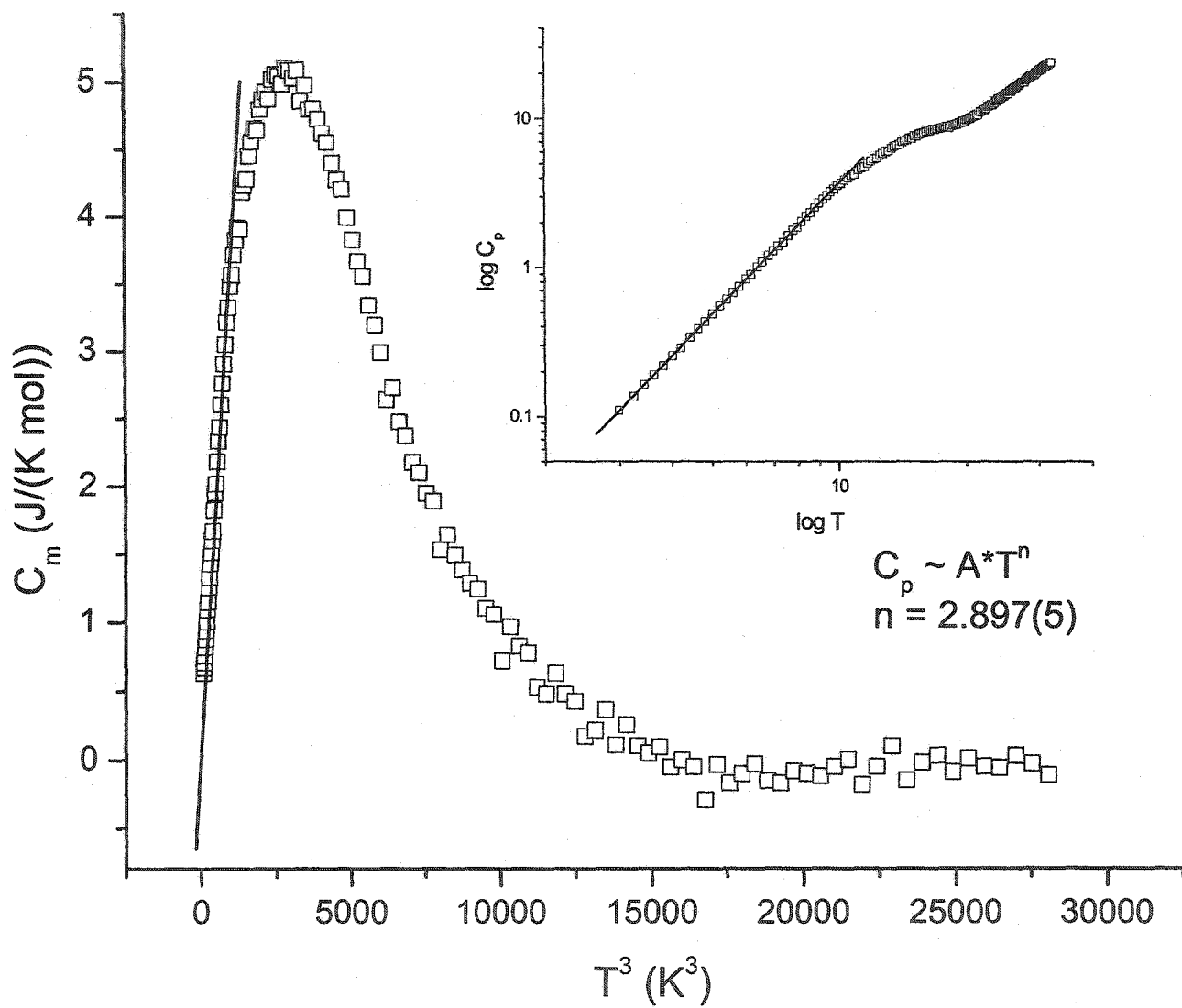


Figure XI: The magnetic heat capacity of $\text{Sr}_2\text{CaReO}_6$ as a function of T^3 . The inset shows the heat capacity as a function of temperature on a logarithmic scale (base 10), emphasizing the T^3 dependence.

It is possible that due to inhomogeneities in the sample, there may be regions of ordered clusters of moments, with the rest of the material remaining in a spin glass state. Theoretical studies on the nearest-neighbor FCC Heisenberg antiferromagnet have shown that spin dilution on the order of 15% is enough to drive the system from an ordered state to spin glass one.³⁹ It is possible that small levels of local disorder can generate separate domains of spin glassy and ordered states by this mechanism. Furthermore, these studies have shown that the transition to the long ranged ordered state is very sharp and first order in nature. Evidence for an abrupt first order transition is seen in the μ SR experiments, but the heat capacity data do not show any sharp features. This feature may be obscured if there is only partial ordering in the sample, but even a sharp spike should be visible. It is indeed conceivable as well that the transition itself may be first order and spin glassy,⁴⁰ rather than due to regions of ordered and spin glassy domains, but substantial proof to support either scenario is not available from this study. Indeed, the only evidence for the abrupt nature of the transition is in the μ SR experiments, and this is only noted in the context of other spin glasses, which typically have very gradual transitions.

Integration of the low temperature magnetic specific heat is a measure of the magnetic entropy by the following relationship:

(6)

$$S = \int_0^T (C_m / T) dT$$

The total magnetic entropy integrated over the entire temperature range of the anomaly is 3.73 J/K/mol for 1 formula unit of $\text{Sr}_2\text{CaReO}_6$. This is $\sim 64.7\%$ of the expected value of $R \ln(2S+1)$ for 100% of the spins freezing. At the magnetic transition itself, only $\sim 35.3\%$ of the entropy is recovered, indicating that most of the entropy removal occurs above T_G , as would be expected for a spin glass.³² One can compare these results with the monoclinic $S=1$ FCC ordered system $\text{Sr}_2\text{NiTeO}_6$ which shows a lambda anomaly at $T_N \sim 28$ K indicative of magnetic ordering and a continuous phase transition.¹⁴ Nonetheless, magnetic susceptibility measurements show evidence for magnetic correlations at $T \sim 35$ K

by a FC/ZFC divergence at temperatures higher than the cusp at T_N . In this case, approximately 70% of the entropy is recovered at the magnetic transition, but the ground state is ordered rather than glassy. As the Ni^{2+} ions in Sr_2NiTeO_6 have $S = 1$, this seems to suggest that it is the $S = \frac{1}{2}$ moment on Re^{6+} that induces the spin glass ground state in Sr_2CaReO_6 . Further experiments are clearly needed to explore this possibility.

CONCLUSIONS

Magnetic susceptibility, neutron scattering, μ SR and specific heat data on the B-site ordered perovskite Sr_2CaReO_6 are all consistent with unconventional glass behavior below $T_G \sim 14$ K. Among the unconventional features are the thermal abruptness of the spin-freezing transition from μ SR, the FC-ZFC divergence above T_G from susceptibility and the very unusual T^3 dependence of the low temperature specific heat. Further work is needed to explore the spin dynamics and magnetic microstructure of this material.

ACKNOWLEDGEMENTS

The authors would like to thank Ron Donaberger for his technical assistance with the neutron scattering experiments at Chalk River. The authors would also like to acknowledge M. J. P. Gingras for his critical reading of this manuscript. C. R. Wiebe gratefully acknowledges financial support for this work in the form of a PGS B from the National Sciences and Engineering Research Council, and a OGSST from the government of Ontario. This work was also supported through research grants to J. E. Greedan and G. M. Luke from the National Sciences and Engineering Research Council and to G. M. Luke from the Canadian Institute for Advanced Research. The MAGLAB experimental apparatus was purchased through funding from the CFI and ORDCF.

References

- (1) G. Aeppli and P. Chandra, *Science*, **275**, 177 (1997).
- (2) A. P. Ramirez in *Handbook of Magnetic Materials*, edited by K. H. J. Buschow, (North-Holland, Amsterdam, 2001) **13**, 423.
- (3) J. E. Greedan, *Journal of Mat. Chem.*, **11**, 37 (2001).
- (4) O. Petrenko, C. Ritter, M. Yethiraj, D. McK. Paul, *Phys. Rev. Lett.*, **80**, 4570 (1998)
- (5) S.-H. Lee, C. Broholm, G. Aeppli, T. G. Perring, B. Hessen, A. Taylor, *Phys. Rev. Lett.*, **76**, 4424 (1996)
- (6) J. S. Gardner, B. D. Gaulin, S.-H. Lee, C. Broholm, N. P. Raju, J. E. Greedan, *Phys. Rev. Lett.*, **83**, 211 (1999).
- (7) L. Pauling, *The Nature of the Chemical Bond*, 3rd ed. (Cornell University Press, Ithaca, 1960).
- (8) M. J. Harris, S. T. Bramwell, D. F. McMorrow, T. Zeiske, K. W. Godfrey, *Phys. Rev. Lett.*, **79**, 2554 (1997).
- (9) L. F. Feiner, A. M. Oles, J. Zaanen, *Phys. Rev. Lett.*, **78**, 2799 (1997).
- (10) J. S. Gardner, S. R. Dunsiger, B. D. Gaulin, M. J. P. Gingras, J. E. Greedan, R. F. Kiefl, M. D. Lumsden, W. A. MacFarlane, N. P. Raju, J. E. Sonier, I. Swainson, Z. Tun, *Phys. Rev. Lett.*, **82**, 1012 (1999).
- (11) M. Bieringer, N. P. Raju, G. Luke, J. E. Greedan, *Phys. Rev. B*, **62**, 6521 (2000).
- (12) J. Longo and R. Ward, *J. Am. Chem. Soc.*, **83**, 2816 (1961).
- (13) R. Rodríguez, A. Fernández, A. Isalgué, J. Rodríguez, A. Labarta, J. Tejada, X. Obradors, *J. Phys. C.*, **18**, L401 (1985).
- (14) D. Iwanaga, Y. Inaguma, M. Itoh, *Mat. Res. Bull.*, **35**, 449 (2000).
- (15) DICVOL Version: 24/11/98.
- (16) B. L. Chamberland and G. Levasseur, *Mat. Res. Bull.*, **14**, 401 (1979).
- (17) D.-Y. Jung and G. Demazeau, *J. Solid State Chem.*, **115**, 447 (1995).
- (18) LSUDF: least square unit-cell refinement package run with GUCOS.
- (19) A. W. Sleight, J. Longo, R. Ward, *Inorganic Chem.*, **1**, 245 (1962).

- (20) FULLPROF Version 3.5d (Oct. 98).
- (21) R. D. Shannon, *Acta Cryst.* **A32**, 751 (1976).
- (22) C.R. Wiebe, J. E. Greedan, G. M. Luke, J. S. Gardner, I. Swainson, in press.
- (23) A. Ferretti, D. B. Rogers, and J. B. Goodenough, *J. Phys. Chem. Solids*, **26**, 2007 (1965).
- (24) A. S. Wills, 1998, VaList for Windows.
- (25) R. Moessner and A. J. Berlinsky, *Phys. Rev. Lett.*, **83**, 3293 (1999).
- (26) H. Nakamura, N. Kim, M. Shiga, R. Kmiec, K. Tomala, E. Ressouche, J. P. Sanchez, B. Malaman, *J. Phys: Conden. Matter*, **11**, 1095 (1999).
- (27) J. S. Smart, *Effective Field Theories of Magnetism* (Saunders College, Philadelphia, 1966).
- (28) Y. J. Uemura, T. Yamazaki, D. R. Harshman, M. Senba, E. J. Ansaldo, *Phys. Rev. B.*, **31**, 546 (1985).
- (29) C. H. Booth, J. S. Gardner, G. H. Kwei, R. H. Heffner, F. Bridges, M. A. Subramanian, *Phys. Rev. B*, **62**, R755 (2000).
- (30) G. A. Petrakovskii, K. S. Aleksandrov, L. N. Bezmaternikh, S. S. Aplesnin, B. Roessli, F. Semadeni, A. Amato, C. Baines, J. Bartolomé, M. Evangelisti, *Phys. Rev. B.*, **63**, 18, (2001).
- (31) S. R. Dunsiger, R. F. Kiefl, K. H. Chow, B. D. Gaulin, M. J. P. Gingras, J. E. Greedan, A. Keren, K. Kojima, G. M. Luke, W. A. MacFarlane, N. P. Raju, J. E. Sonier, Y. J. Uemura, W. D. Wu, *Phys. Rev. B*, **54**, 9019 (1996).
- (32) J. A. Mydosh, *Spin Glasses, An Experimental Introduction* (Taylor and Francis, London, 1993).
- (33) F. Zhengmin, L. Wenxiu, L. Dongcai, *Scientia Sinica*, **26**, 835 (1983).
- (34) N. P. Raju, E. Gmelin, R. K. Kremer, *Phys. Rev. B*, **46**, 5405 (1992).
- (35) J. N. Reimers, J. E. Greedan, R. K. Kremer, E. Gmelin, M. A. Subramanian, *Phys. Rev. B*, **43**, 3387 (1991).
- (36) A. P. Ramirez, G. P. Espinosa, A. S. Cooper, *Phys. Rev. Lett.*, **64**, 2070 (1990).

- (37) Y. Kitaoka, T. Kobayashi, A. Koda, H. Wakabayashi, Y. Niino, H. Yamakage, S. Taguchi, K. Amaya, K. Yamaura, M. Takano, A. Hirano, R. Kanno, *J. Phys. Soc. Japan*, **67**, 3703 (1998).
- (38) J. A. Eisele and F. Keffer, *Phys. Rev.*, **96**, 929 (1954).
- (39) C. Wengel, C. Henley, A. Zippelius, *Phys. Rev. B.*, **53**, 6543 (1996).
- (40) Private communication with Prof. M. J. P. Gingras.

Chapter Six

Frustration-driven Spin Freezing in the S=1/2 FCC Perovskite Sr₂MgReO₆

The final chapter of this thesis details the work on Sr₂MgReO₆, the tetragonal analogue of Sr₂CaReO₆. This paper is being submitted to the journal Physical Review B (November, 2002).

Frustration-driven Spin Freezing in the $S = 1/2$ FCC Perovskite $\text{Sr}_2\text{MgReO}_6$

C. R. Wiebe, J. E. Greedan, P. P. Kyriakou and G. M. Luke

*The Brockhouse Institute for Materials Research, McMaster University, Hamilton, ON
L8S 4M1, Canada*

J. S. Gardner

*Neutron Program for Materials Research, NRC, Chalk River Labs, Chalk River, ON
K0J 1J0, Canada*

I. M. Malureanu, P. L. Russo, A. T. Savici and Y.J. Uemura

*Department of Physics, Columbia University, New York, New York
10027, USA*

ABSTRACT

The ordered perovskite $\text{Sr}_2\text{MgReO}_6$ of tetragonal symmetry ($I4/m$, $a = 5.5706(2)$ Å, $c = 7.9277(5)$ Å) has been synthesized and characterized by x-ray and neutron diffraction, TGA, DC susceptibility, heat capacity and μSR experiments. Despite the similar ionic radii, the B site cations Re^{6+} and Mg^{2+} appear to be ordered due to the charge difference of the species. The Re^{6+} magnetic ions form a distorted FCC lattice of $S=1/2$ species, which is a frustrated topology of edge-shared tetrahedra. The frustration inherent to the structure is responsible for a weak glassiness evidenced by a cusp at ~ 50 K in the DC susceptibility, a weak but broad heat capacity anomaly and a low temperature μSR lineshape characteristic of a spin glass state. A broad and strongly field dependent maximum in the DC susceptibility suggests that magnetic correlations persist to ~ 175 K. This is accompanied by a divergence in the field-cooled and zero-field cooled susceptibility. The anisotropic nature of the super-

exchange pathways due to the tetragonal distortion is thought to disrupt the ideal frustrated environment and lead to weaker glassiness than $\text{Sr}_2\text{CaReO}_6$, which has $T_G \sim 14$ K, and a large specific heat anomaly. In contrast, $\text{Sr}_2\text{MgReO}_6$ has a small anomaly, and only about 3% of the entropy is released at $T_G \sim 50$ K, which is comparable to other unconventional spin glasses such as the jarosite $(\text{H}_3\text{O})\text{Fe}_3(\text{SO}_4)_2(\text{OH})_6$ ($\sim 6\%$).

INTRODUCTION

Some of the most fascinating phenomena in condensed matter physics are due to the consequences of competing interactions.¹ Anderson's prediction of the unusual and interesting physics that would arise out of these systems has been realized experimentally in a wide variety of materials², from high T_C superconductors³ to molecular crystals⁴ to geometrically frustrated antiferromagnets⁵. In the latter case, the inability of the sublattice to magnetically order often leads to exotic ground states that continue to challenge theories in solid state magnetism. In particular, the study of $S=1/2$ species on frustrated lattices has been the target of current research with the promise of a "spin liquid" state that is thought to arise in the quantum limit.^{6,7} The spin liquid, a dynamic state that is stabilized by the formation of rapidly fluctuating spin singlets, was first postulated by Pauling⁸ in his Resonating Valence Bond model (and later by Anderson), but surprisingly very few ideal spin liquids have been discovered since his prediction.

The current trend in the search for this elusive ground state is centered around low dimensional systems. Evidence for liquid like behaviour has been noted for 2D layered systems such as the kagomé-based $\text{SrCr}_9\text{pGa}_{12-p}\text{O}_{19}$ ⁹ and $\text{Ba}_2\text{Sn}_2\text{Ga}_3\text{ZnCr}_7\text{O}_{22}$ ¹⁰ but very few three dimensional spin liquids have been well characterized. Most three dimensional systems in fact show spin glassiness, such as the pyrochlore $\text{Y}_2\text{Mo}_2\text{O}_7$, in which the moments "freeze out" and only short range order is observed.¹¹ There are a few exceptions, such as $\text{Tb}_2\text{Ti}_2\text{O}_7$, which enters a "cooperative paramagnetic state" at low temperatures,¹² but overall the literature is lacking clear examples of three dimensional liquid like materials.

The perovskites have largely been overlooked as structures which can be used as a framework for frustrated magnetic sublattices. Ordered structures of the form $A_2BB'O_6$ have been demonstrated to be extremely stable to substitution of various ions upon the B site, which form ordered FCC sublattices.¹³ This provides the opportunity to study frustration effects, as the FCC lattice forms a network of edge shared tetrahedra. Traditionally, most FCC materials enter long range ordered ground states, and it is indeed this lattice which was first studied as the classical example of an ordered antiferromagnet by early neutron scattering measurements on oxides such as MnO.¹⁴ However, in these materials, near neighbour and next-nearest neighbour interactions compete and eventually favour the formation of an ordered ground state. It is when one substitutes magnetic ions beyond the 4d elements that orbital effects become more important for the magnetic exchange interactions and a lack of long range order is observed. The magnetism of the 5d electrons in the Re cation has recently caught the attention of many solid state physicists. For example, the ferromagnetic half-metallic species Sr_2FeReO_6 ¹⁵ and the superconducting pyrochlore $Cd_2Re_2O_7$ ¹⁶ have been objects of fruitful study as of late.

This paper details the first in depth study of the ordered perovskite, Sr_2MgReO_6 , which was synthesized for the purpose of investigating the combination of quantum magnetism upon a highly frustrated sublattice. The analogous material Sr_2CaReO_6 , which is a distorted perovskite of monoclinic symmetry, shows spin glass behaviour with $T_G \sim 14$ K.¹⁷ Due to the FCC network of $S=1/2$ Re^{6+} cations, several conventional spin glass like features were seen, such as a cusp in the DC susceptibility, the lack of long range magnetic order, magnetic hysteresis and spin freezing noted by μ SR experiments. However, a few unusual properties were discovered as well. The appearance of a low temperature field-independent specific heat anomaly with a T^3 dependence in particular suggested that a spin singlet ground state may be present which is stabilized by strong 3D spin fluctuations. The magnetic character of Sr_2MgReO_6 , which has tetragonal rather than monoclinic symmetry, is markedly different from the Ca material, but these new properties can be understood by investigating the differences in the crystal structure and the magnetic exchange paths. The properties of these two materials will be compared to $S = 1$ analogues (Sr_2NiMO_6 , $M = W$ or

Te) to emphasize the role of quantum effects in this low spin system.

EXPERIMENTAL PROCEDURES

Powder samples of $\text{Sr}_2\text{MgReO}_6$ were synthesized by combining stoichiometric amounts of SrO (99.9%, Fisher), MgO (99.95%, Alfa-Aesar) and ReO_3 (99.9%, Rhenium Alloys Inc.), and then firing under vacuum for 60 hours in platinum crucibles at 900°C . The starting materials SrO and MgO were pre-fired under vacuum for 12 hours at 400°C in separate ceramic containers to removed any absorbed water or surface impurities.

The quality of the final product was tested using a focussing Guinier-Hägg camera of copper $\text{K}_{\alpha 1}$ radiation and Si powder as an internal standard. After several firings, no impurities were ascertained using this technique. Thermogravimetric analysis was used to determine the oxygen stoichiometry by reducing the sample in a hydrogen atmosphere at 900°C .

A Bruker D8 diffractometer using Cu K_{α} radiation was used to obtain high quality x-ray diffraction patterns. The software package FULLPROF¹⁸ was used to obtain the room temperature crystal structure.

This material was also examined using neutron diffraction at the C2 beamline of the National Research Council's Neutron Program for Materials Research in Chalk River, Canada. Using a neutron wavelength at $\lambda = 1.3285(3)\text{ \AA}$, and FULLPROF¹⁸ we analyzed the structure between 6 K and room temperature.

The DC magnetic susceptibility was measured using a Quantum Design MPMS SQUID magnetometer at McMaster University. Field cooled (FC) and zero field cooled (ZFC) scans were made over a temperature range of 2 K to 350 K under various applied magnetic fields. Isothermal magnetization scans were also obtained at 5 K and 250 K in fields of 4000 G.

An Oxford Instruments Calorimeter probe in the Oxford Instruments MAGLAB apparatus was used to measure the heat capacity of this sample. A pellet of mass 12.19 mg

was attached to the probe using a measured portion of Wakefield grease (for which a correction was made using software provided by Oxford Instruments). The measurements were made between 3 K and 70 K using the relaxation method. Measurements were also completed on the lattice standard Sr_2MgWO_6 over the same temperature range to calculate the lattice contribution to the specific heat. The measurements were carried out in a similar fashion with a pellet of mass 9.80 mg.

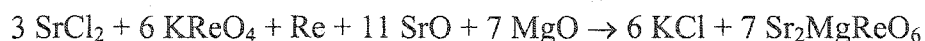
μSR experiments were completed at the M15 beamline at TRIUMF in Vancouver, Canada. The measurements were made over a temperature range of 2.5 K to 130 K in a small applied longitudinal field of 65 G. A series of longitudinal field measurements up to 2065 G were made at 5 K.

RESULTS AND DISCUSSION

PART A: CRYSTAL STRUCTURE

Initial analysis of powder x-ray diffraction using the search routine DICVOL¹⁹ indicated that the sample was single phase. Subsequent neutron diffraction measurements showed that there was indeed a small MgO impurity (0.6 %) in the sample not detected using x-rays. Since no other impurities were found, this was assumed to be due to either a small weighing error or an incomplete reaction

The original structural work on this sample was done by Ferretti, Rogers, and Goodenough,²⁰ who made these samples by firing stoichiometric amounts of SrCl_2 , KReO_4 , Re, SrO, and MgO in sealed evacuated tubes followed by washing well with water to remove KCl.



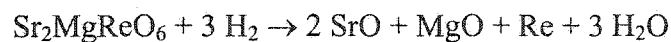
Attempts to synthesize the sample by this method were unsuccessful. Several other reactions

were tried, such as reacting $\text{Sr}(\text{NO}_3)_2$ or SrCO_3 with ReO_3 and MgO under vacuum, but all of these were unsuccessful as well. The method described earlier and identical used to produce $\text{Sr}_2\text{CaReO}_6$, was found to be the best.

Ferretti *et al.* reported the structure to be tetragonal, but only listed the ratio of the lattice parameters c/a to be 1.005. No cell constants or space group were recorded. A proper indexing of the Bragg peaks determined the space group to be $I4/m$. The ratio of our lattice parameters is in good agreement with Ferretti *et al.* although the unit cell is slightly different. Our room temperature lattice parameters, as determined from Rietveld refinement of x-ray diffraction data (see figure I), were $a = 5.5670(1) \text{ \AA}$ and $c = 7.9318(2) \text{ \AA}$ (see table I).

Structure refinements were also done at 6 and 298 K using neutron diffraction data. The results are listed in table I, with the full diffraction pattern displayed in figures II and III. The small MgO impurity is noted as the second set of tickmarks in the diffraction pattern. The calculated weight percentage of MgO was found to be 0.6 % by Rietveld refinement.

As these samples were prepared under vacuum, there was some concern about the oxygen stoichiometry. A defect structure would be difficult to detect by x-ray diffraction or with the limited Q -space surveyed by our neutron diffraction experiments (which were primarily used to detect magnetic ordering and disorder on the cation sites). Several TGA experiments were conducted to reduce $\text{Sr}_2\text{MgReO}_6$ to SrO , MgO and Re metal under flowing hydrogen to measure the weight loss, and thus the oxygen stoichiometry:



The final solid state products were confirmed by x-ray powder diffraction using a Guinier-Hägg camera to ensure that the reaction was complete. The theoretical weight loss was 9.96 %. The average of several of these reactions was 9.75(10)% weight loss. Thus, the sample is nearly stoichiometric with respect to oxygen. The slight deficiency may be due to the small amount of excess MgO remaining in the sample, which would lower the expected weight loss.

Figure I: Powder x-ray diffraction refinements of $\text{Sr}_2\text{MgReO}_6$ at $T = 298 \text{ K}$ with $\text{Cu K}\alpha$ radiation. ($R_p = 12.2$, $R_{wp} = 17.4$)

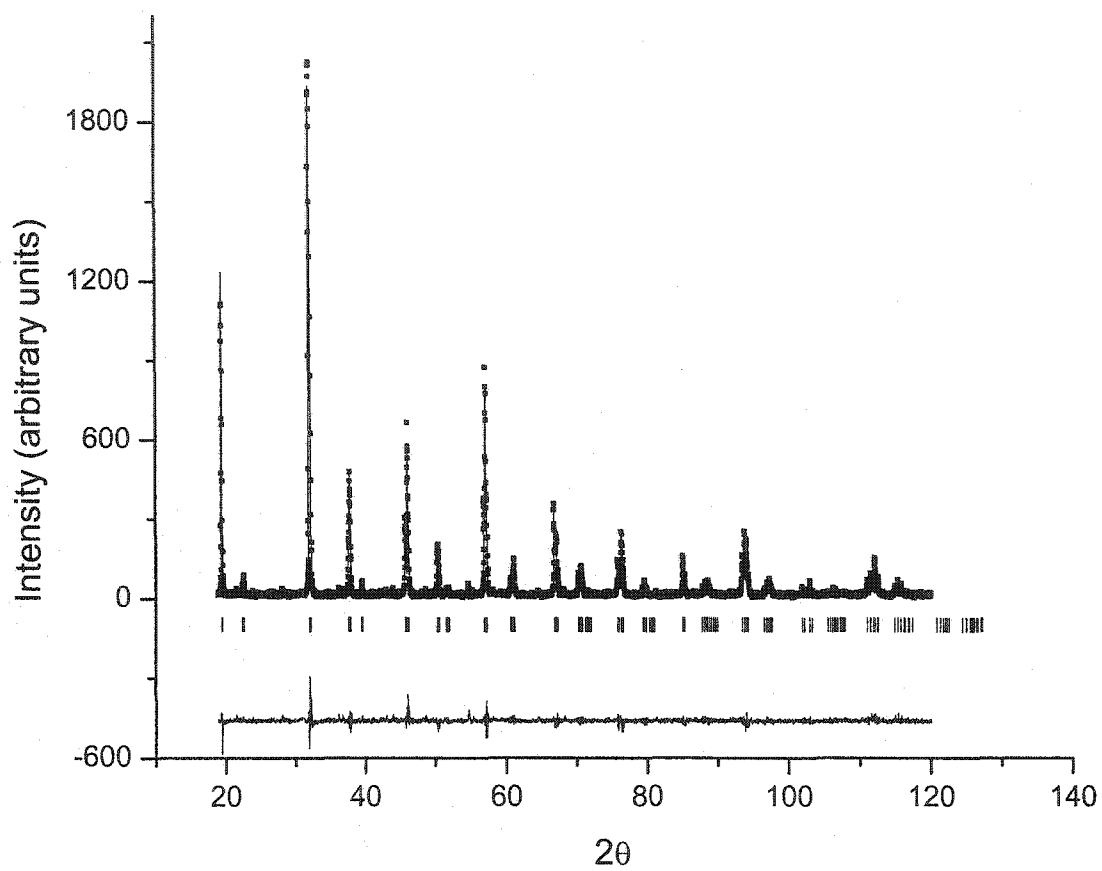
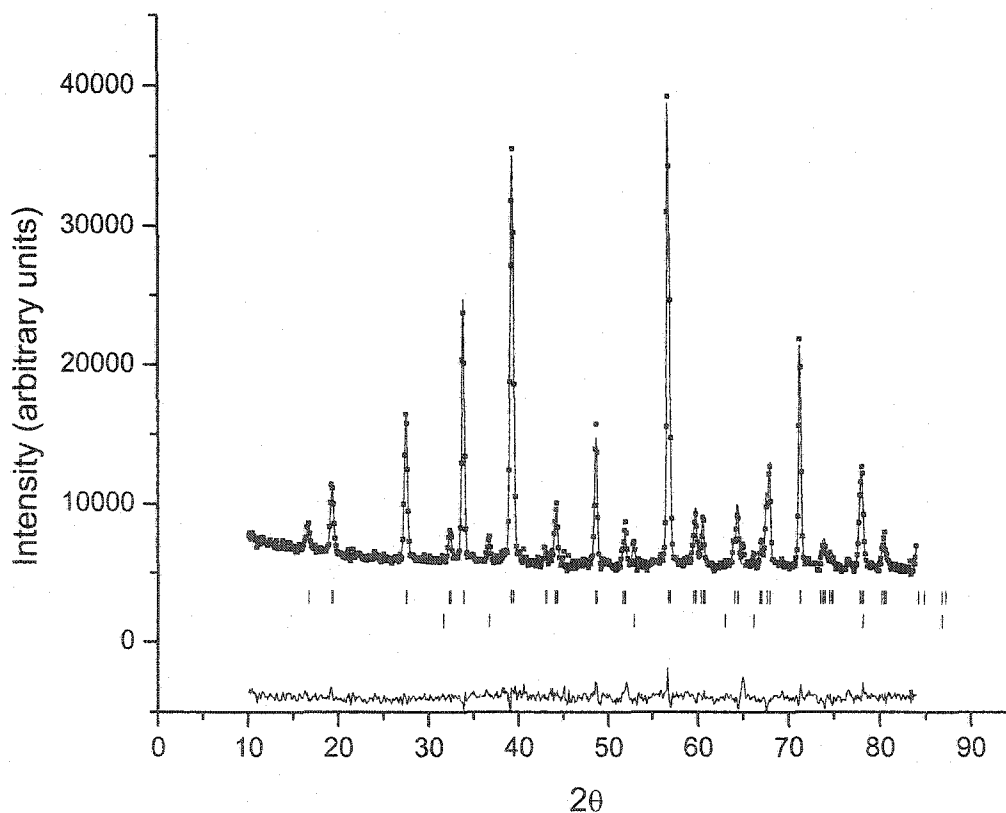


Table I: Lattice parameters for $\text{Sr}_2\text{MgReO}_6$ at 6 K (neutron data) and 295 K (neutron and x-ray data) as determined by powder diffraction. The material used as a model for the lattice contribution to the heat capacity, Sr_2MgWO_6 , is referenced as well for comparison (x-ray data).

	neutron data		x-ray data	
	$\text{Sr}_2\text{MgReO}_6$, 6 K	$\text{Sr}_2\text{MgReO}_6$, 295 K	$\text{Sr}_2\text{MgReO}_6$, 295 K	Sr_2MgWO_6 , 295 K
	(Å)	(Å)	(Å)	(Å)
a	5.5350(6)	5.5706(2)	5.5670(1)	5.5816(1)
c	7.9724(9)	7.9277(5)	7.9318(2)	7.9420(1)

Figure II: Powder neutron diffraction refinements of $\text{Sr}_2\text{MgReO}_6$ at $T = 6$ K with $\lambda = 1.3285(3)$ Å. ($R_p = 10.8$, $R_{wp} = 10.8$)



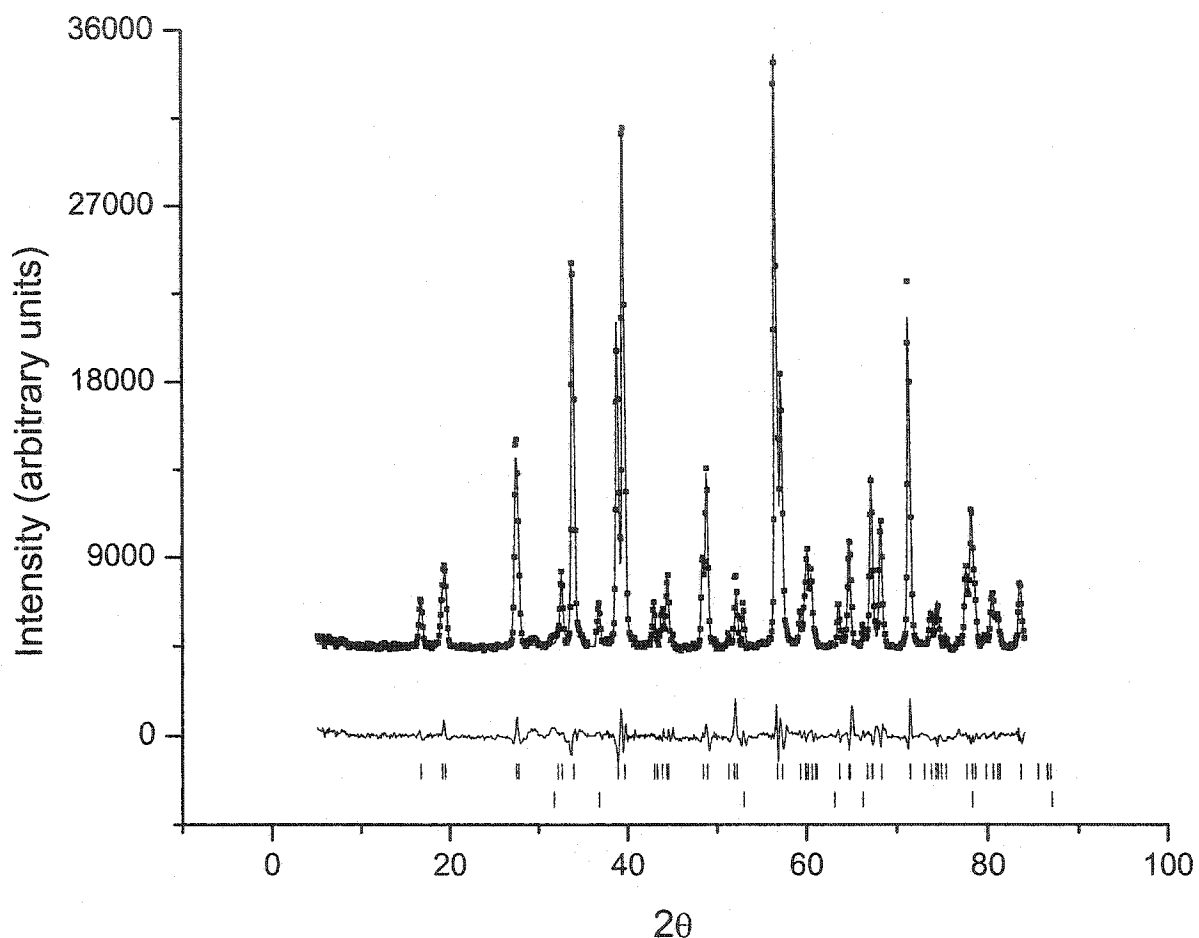


Figure III: Powder neutron diffraction refinements of $\text{Sr}_2\text{MgReO}_6$ at $T = 298 \text{ K}$ with $\lambda = 1.3285(3) \text{ \AA}$. The rising background at low Q is from air scattering, and a blank run was made to confirm this. ($R_p = 14.6$, $R_{wp} = 11.9$)

The crystal structure of $\text{Sr}_2\text{MgReO}_6$, is shown in figures IV and V. The similar size of the Re and Mg octahedra led to several detailed refinements of the structure using models of disorder upon these sites. However, all of the parameters refined to an ordered structure in both the neutron and x-ray work. The electrostatic repulsion between the Re^{6+} and Mg^{2+}

species is thought to be a significant ordering mechanism. The significant difference in ionic radii (0.86 and 0.69 Å for Mg and Re with VI coordination²¹) will also aid the cation ordering. The relatively large size of the Sr²⁺ cation excluded the possibility of disorder on this site as well (which is 1.18 Å for VI coordination). The oxygen sites were allowed to vary in the final refinements, but they did not change appreciatively.

Figure IV: The crystal structure of Sr₂MgReO₆ as viewed from the ac plane.

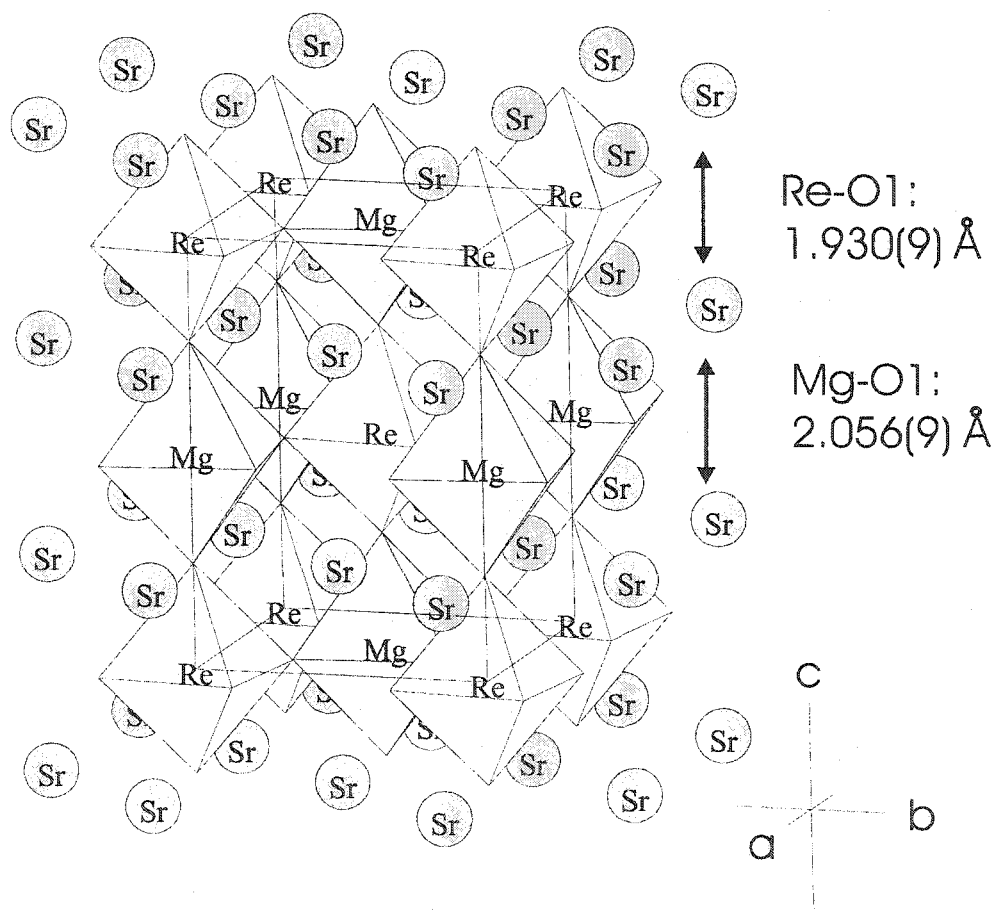
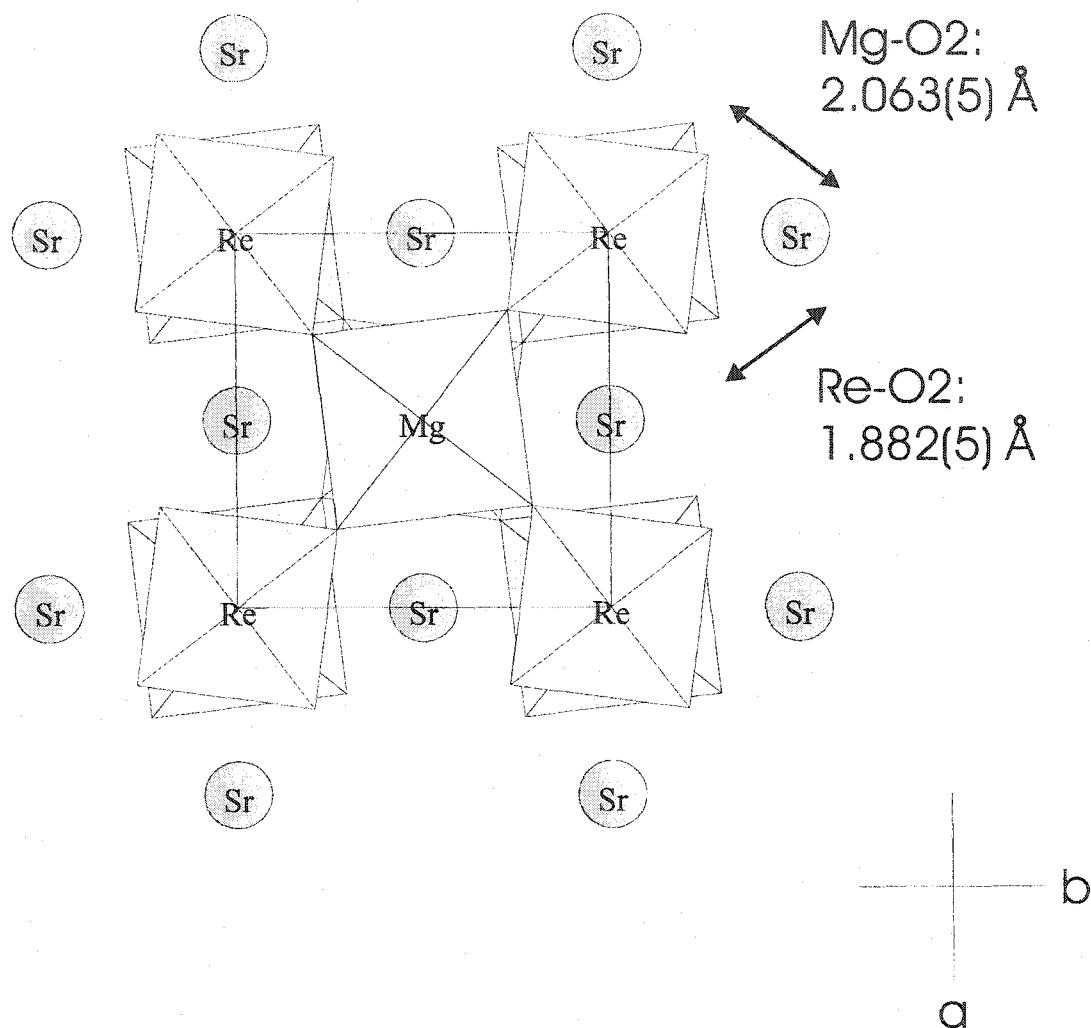
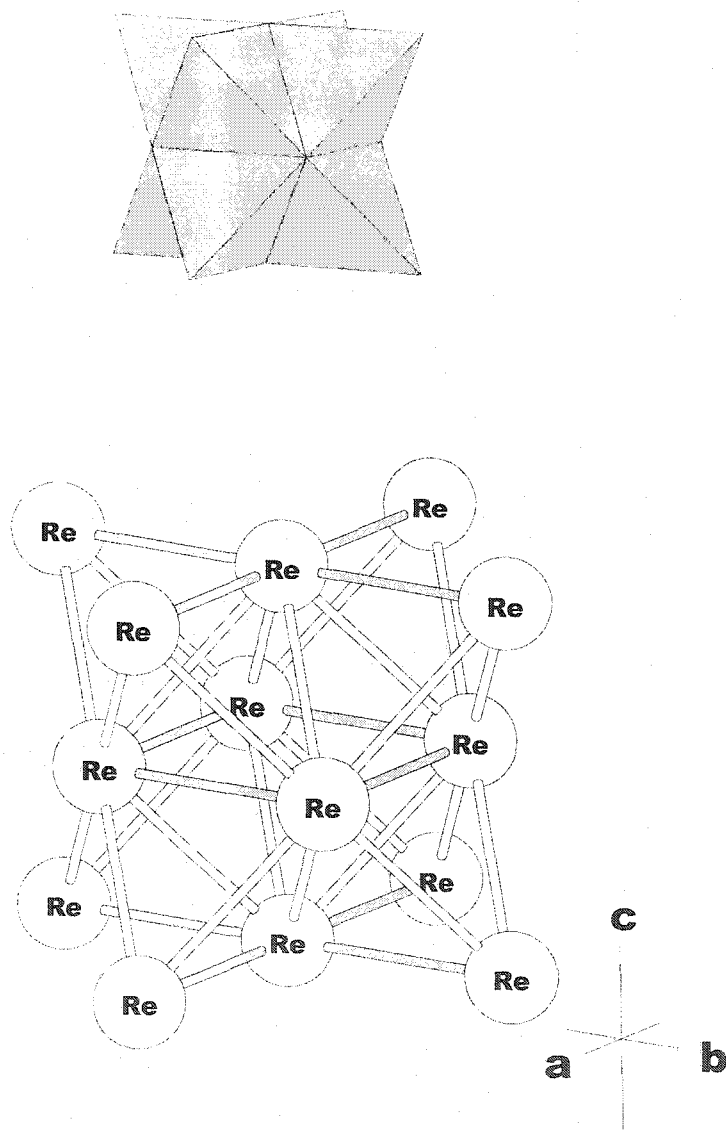


Figure V: The crystal structure of $\text{Sr}_2\text{MgReO}_6$ as viewed from the ab plane.



The ideal material to study the magnetic properties of FCC magnetic sublattices would be the cubic case, as all of the bond angles and exchange paths would be identical for the interconnected tetrahedra. In the case of $\text{Sr}_2\text{MgReO}_6$, the structure is tetragonal, and the exchange paths are anisotropic. The Re-O-Mg bond angles are $180.00(36)^\circ$ along the c -direction, but they are distorted in the ab plane to $165.57(19)^\circ$, as shown in figure IV (at 6 K). The tetragonal distortion also results in slightly different Re-Re bond distances, but these agree to within 1% (see figure VI). The significant differences in bond angles, and thus 5d orbital overlap, is believed to play a much more important role.

Figure VI: The FCC ordered sublattice of $\text{Sr}_2\text{MgReO}_6$. The two different Re-Re bond distances are marked as $5.5350(6) \text{ \AA}$ (shaded bonds) and $5.5864(4) \text{ \AA}$ (unshaded bonds).



It is worth noting that this distortion away from cubic symmetry has been observed for the Ca analog $\text{Sr}_2\text{CaReO}_6$. It is believed that the relatively small size of the A cation facilitates this distortion to a monoclinic structure. Indeed $\text{Ba}_2\text{CaReO}_6$ with its larger Ba^{2+} cation (1.61 Å compared to Ca^{2+} of 1.44 Å) is cubic. It is believed that $\text{Ba}_2\text{MgReO}_6$ would be cubic and suitable for further studies.

Table II: Refined lattice positions and temperature factors for $\text{Sr}_2\text{MgReO}_6$ ($\lambda = 1.3285(3)$ Å) at 6 K

	x	y	z	B (Å ²)	Site
Sr	0	0.5	0.25	0.456(10)	4d
Mg	0	0	0.5	0.10(1)	2b
Re	0	0	0	0.07(1)	2a
O1	0	0	0.242(1)	0.493(8)	4e
O2	0.2700(9)	0.2066(7)	0	0.565(10)	8h

The structural difference between $\text{Sr}_2\text{CaReO}_6$ and $\text{Sr}_2\text{MgReO}_6$ is due to the relative sizes of the B site cations. In the monoclinic case ($\text{Sr}_2\text{CaReO}_6$), the difference between Ca^{2+} and Re^{6+} is large, which leads to a distortion of their respective octahedra to fill space. In the case of Mg^{2+} and Re^{6+} , the sizes are very similar, and thus the distortion is only a slight twisting in the ab plane.

Due to the centrosymmetric crystal structure presented here the previously reported room temperature ferroelectric phase²² and the associated Jahn-Teller distortions are difficult to imagine. Neutron data suggests that there is a slight elongation of the Re-O bonds in the c-direction, but this small variation (1.930(9) Å for Re-O1 and 1.882(5) Å for Re-O2 at 6 K) makes it hard to justify Re^{6+} as a true Jahn-Teller active ion in this material. However, it should be noted that Re-O bond distances are significantly more distorted than the $\text{Sr}_2\text{CaReO}_6$ Re octahedra (1.907(4) Å for Re-O1, 1.921(5) Å for Re-O2, and 1.904(4) Å for Re-O3). There is no such distortion for the Mg-O distances, which change very little from 6

K to 295 K. In general, Jahn-Teller effects are more subtle for t_{2g}^1 configurations than for e_g^1 , and it is difficult to confirm whether or not this is a real effect in this material based upon this study alone. The literature of Jahn-Teller effects in Re^{6+} species is very sparse.

Table III: Bond distances and angles for $\text{Sr}_2\text{MgReO}_6$ at $T = 6$ and $T = 298$ K as determined by powder neutron diffraction. There are no appreciable changes due to the phase transition at $T_G \sim 50$ K.

	6 K	295 K
Re – O1	1.930(9) Å	1.933(17) Å
Re – O2	1.882(5)	1.900(8)
Mg – O1	2.056(9)	2.031(17)
Mg – O2	2.063(5)	2.058(8)
Re – Re	5.5830(6)	5.5706(2)
	5.5864(4)	5.5882(2)
Re – O2 – Mg	165.57(19) °	165.458(16) °
Re – O1 – Mg	180.000(36)	179.972(41)

PART B: MAGNETIC SUSCEPTIBILITY EXPERIMENTS AND NEUTRON DIFFRACTION

Although $\text{Sr}_2\text{MgReO}_6$ has been known for some time, there are no detailed reports of the magnetic properties. Ferretti *et al.* found that $\text{Sr}_2\text{MgReO}_6$ had a room temperature resistivity that is in the semi-conductor to insulator regime of at least $10^5 \Omega\text{-cm}$.²⁰ The conclusion was that the *d*-electrons were localized on the rhenium sites rather than forming a band structure such as in the parent compound ReO_3 . Other than this brief entry, there are no other published results on this material.

Even with full localization on the Re sites, the magnetic susceptibility was expected to be weak, since the electronic configuration is $5d^1$ and the magnetic ions are quite dilute. It was found that a Curie-Weiss regime did not develop in this sample until at least 450 K. The resulting fit in figure VII was made to the following relationship:

(1)

$$\chi = C/(T - \theta) + \alpha$$

where $\mu_{\text{eff}} = \sqrt{8C}$, θ is the Weiss temperature, and α is a temperature-independent paramagnetic term (TIP). A correction for the diamagnetism of the sample was made before the Curie-Weiss fits were completed. In the range of 450 K – 600 K and under a field of 1 T, the Weiss temperature was found to be $\theta = -426(58)$ K and $\mu_{\text{eff}} = 1.72(9) \mu_{\text{B}}$. A very small TIP of $\alpha = 0.00009(2)$ EMU/mol was found. These values are consistent with $\text{Sr}_2\text{CaReO}_6$ (where $\mu_{\text{eff}} = 1.659(6) \mu_{\text{B}}$ and $\theta = -443(6)$ K), re-enforcing the similarities of these two materials. With similar exchange paths and Re-Re distances, it is no surprise that such a comparison can be made. The large and negative Weiss temperature indicates the presence of strong antiferromagnetic interactions, and the value for the effective moment agrees well with the ideal spin-only $S = 1/2$ case of $1.73 \mu_{\text{B}}$.

The lack of a Curie-Weiss regime until very high temperatures is somewhat unusual, as most geometrically frustrated materials tend to exhibit this behaviour to temperatures

much lower than θ . The reason for this discrepancy is that there is a weak feature in the susceptibility which appears at ~ 175 K (see figure VIII). This broad maximum is only present at low fields, and believed to have a long tail that persists to high temperatures. In fields greater than ~ 500 G, the feature is lost in the background but a clear FC/ZFC divergence is seen which persists to ~ 250 K.

Figure VII: DC magnetization measurements as a function of temperature at $H = 100$ G. Note the cusp at ~ 50 K and broad feature at ~ 175 K. The insert shows the Curie-Weiss fit to the high temperature data, which as taken in a field of $H = 10000$ G.

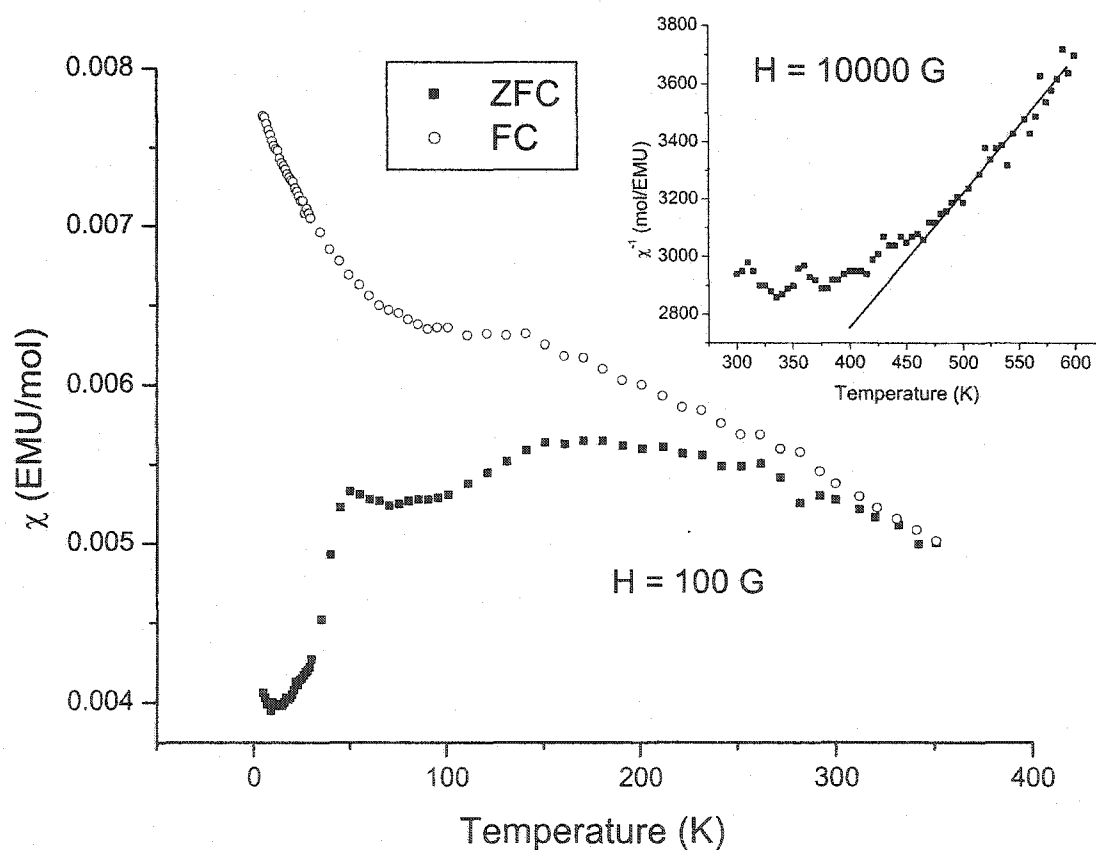


Figure VIII: DC magnetic susceptibility runs for $H = 100$ G, 500 G and 1000 G. Note the disappearance of the 50 K feature and the loss of the broad maximum at 175 K as the field increases.

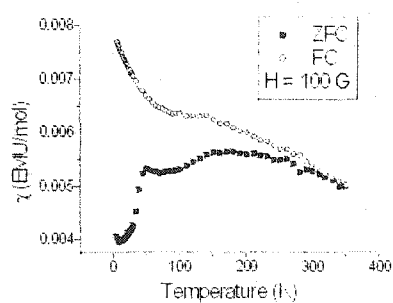
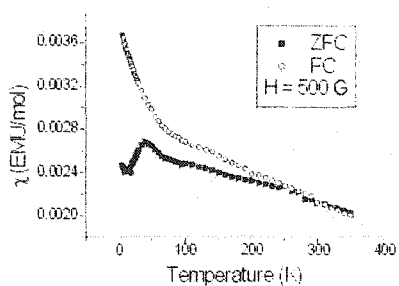
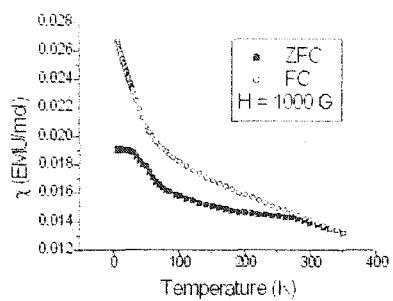
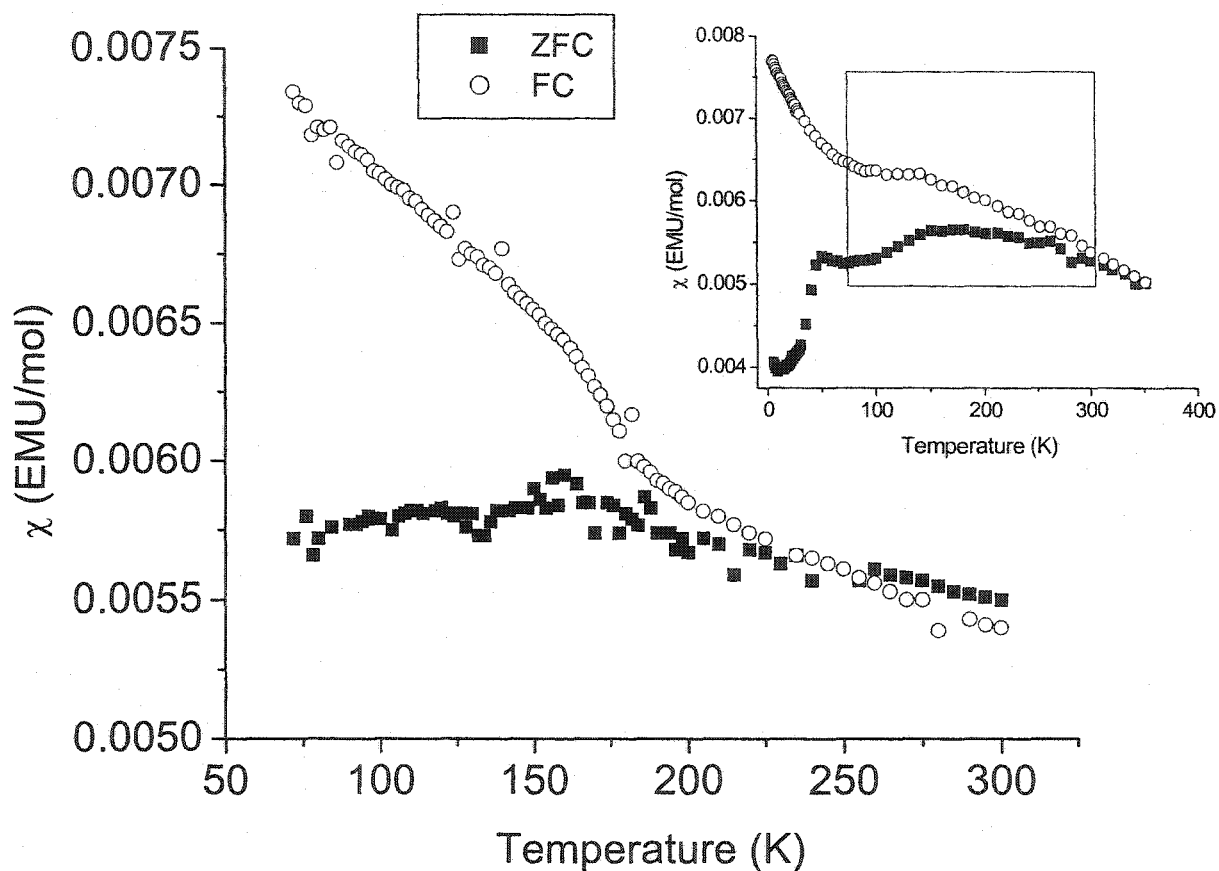


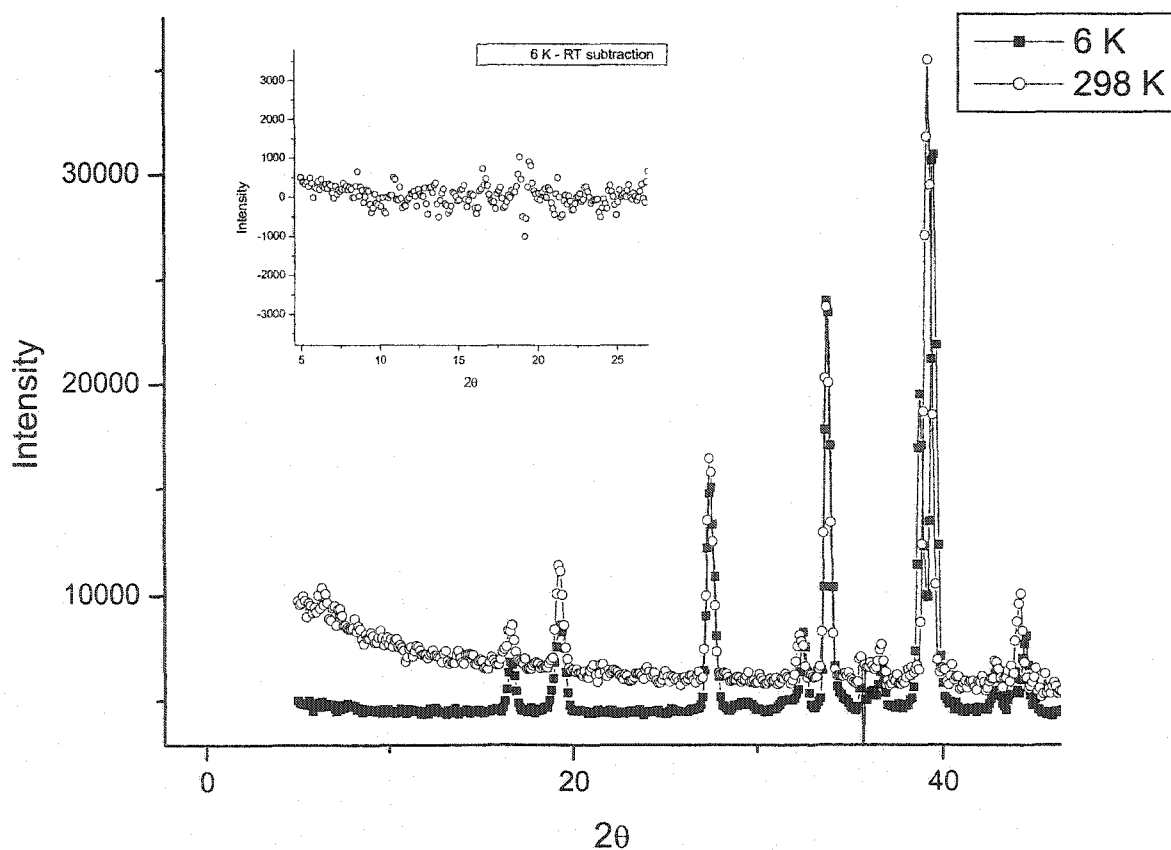
Figure IX: The magnetic susceptibility taken with the RSO mode, clearly showing the FC/ZFC divergence at ~ 175 K. The insert shows the corresponding susceptibility range in the same field of 100 G taken in DC mode.



The other notable feature in the data is the cusp and strong FC/ZFC divergence at ~ 50 K. This is most prominent in the 100 G data set, but evidence is clearly seen to higher fields as a broad maximum. Neutron diffraction measurements were made at 6 K and room temperature using short wavelength neutrons ($\lambda = 1.3285(3)$ Å) to search for magnetic ordering. There were no unusual anomalies found in the difference plot between the diffraction data taken at 298 K and 6 K (see inset to figure X). However, a caveat is needed here when precluding the existence of magnetic ordering: the Re^{6+} ($S=1/2$) moment size is

very small, and the magnetic ions comprise only 10 % of the atoms in the lattice. Even if the transition at ~ 50 K in the magnetic susceptibility was a signature of a long range ordered ground state, it might be difficult to discern such a feature using neutron scattering at a medium flux reactor (and with a small sample size of ~ 4 g). Simulations show that for an ordered Re^{6+} moment of $1.00 \mu_B$, the resulting magnetic Bragg peaks from a type-I structure typical of FCC lattices would be on the order of $\sim 1\%$ of the strong structural peaks.¹⁷ While these would be observable, any reduction in the ordered moment (common for a frustrated system) or a more complex magnetic structure would render these reflections indistinguishable from the background. Other methods were needed to elucidate the nature of the magnetic ground state.

Figure X: Powder neutron diffraction scans taken at 6 K and 298 K with $\lambda = 1.3285(3)$ Å. The difference plot is shown in the insert, which indicates no long range ordering. A background term was applied to the high temperature data before the subtraction to account for air scattering (by means of a blank run).



One can compare this system to the $S = 1$ analogue Sr_2NiWO_6 , which has a Weiss constant of -175 K .²³ As described in the work on $\text{Sr}_2\text{CaReO}_6$, the difference in these values can be understood in terms of the more extended nature of the 5d orbitals as compared to the 3d. According to mean-field theory, the nearest-neighbor exchange constants for an FCC lattice can be calculated by:

(2)

$$J_{nn}/k = \frac{\theta_c}{12(2/3)S(S+1)}$$

Thus, the ratio of J_{nn}/k is 6:1 for $\text{Sr}_2\text{MgReO}_6$ relative to Sr_2NiWO_6 , which is indicative of the larger spatial extent of the 5d orbitals. This is comparable to 5:1 ratio found in $\text{Sr}_2\text{CaReO}_6$.¹⁷

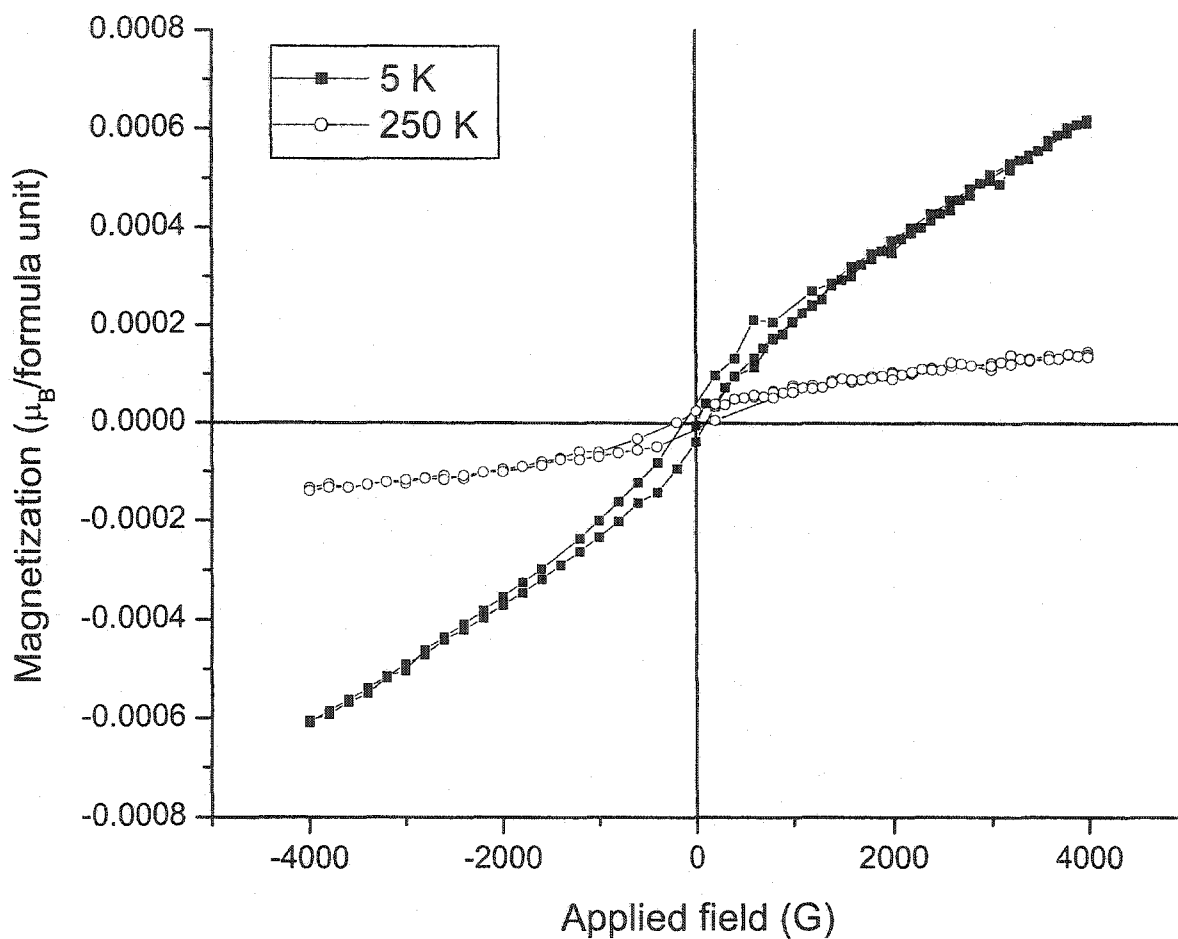
The transition at 50 K in $\text{Sr}_2\text{MgReO}_6$ is remarkably similar to what is seen in Sr_2NiWO_6 , which has a broad maximum at $\sim x \text{ K}$ and a Néel temperature of $T_N = 54 \text{ K}$. However, no FC/ZFC divergence was seen in the Ni analogue. This history dependence is a common property of frustrated systems which show glassy behaviour, such as the pyrochlore $\text{Y}_2\text{Mo}_2\text{O}_7$. However, the broad maximum seen at $\sim 175 \text{ K}$ in $\text{Sr}_2\text{MgReO}_6$ suggests that magnetic correlations set in at a much higher temperature regime than T_G . This is also implied with $\text{Sr}_2\text{CaReO}_6$, which has a glassy transition at $\sim 14 \text{ K}$, but a FC/ZFC divergence which appears at $\sim 23 \text{ K}$. In the case of $\text{Sr}_2\text{MgReO}_6$, the strong anisotropy of the exchange paths, which are $180.00(36)^\circ$ in the ac plane and $165.57(19)^\circ$ in the ab plane, might bring a one-dimensional character to the magnetism, which could manifest itself as a broad feature in the susceptibility. There is no evidence for this speculation other than the magnetic susceptibility results, as all other techniques described in this paper failed to find any hint of this. However, even with the extended nature of the 5d orbitals and the considerable overlap which is found regardless of deviations from 180° , it is easy to imagine that the difference between the two paths is enough to disrupt the symmetry and cause a preferential ordering along the c axis. $\text{Sr}_2\text{CaReO}_6$ is virtually isotropic, with respect to exchange pathways, with the bond angles having a mean of $\sim 153^\circ$. The magnetic properties echo this as a sharp cusp

at $T_G \sim 14$ K, and an otherwise featureless susceptibility indicative of no preferred exchange pathways, and thus only one collective transition at T_G .

Similar temperature dependent magnetic susceptibilities have been noted in other perovskites, such as SrLaFeSnO_6 .²⁴ A broad maximum is observed in the response at ~ 39 K, with a FC/ZFC divergence that sets in at about 250 K. In this material, Fe^{3+} , a $3d^5$ species, is the magnetic ion in a highly disordered lattice of cations. Attfield *et al.* postulate that this behaviour is due to spin clustering which sets in at very high temperatures. An analogy is made with LaFeO_3 , which has a T_N of 750 K. SrLaFeSnO_6 can be thought of as a diluted version of this lattice, with a correspondingly lower Néel temperature. The disorder in this material leads to short-range spatial correlations at ~ 250 K, which becomes long-ranged at $T_N = 1.7$ K. There is no evidence for long range order in $\text{Sr}_2\text{MgReO}_6$ at least down to 2 K. Furthermore, the lack of disorder and a fundamentally different cation environment complicates the comparison between SrLaFeSnO_6 and $\text{Sr}_2\text{MgReO}_6$. Nonetheless, the appearance of these features in the susceptibility supports our claim of high temperature spin correlations.

Hysteresis loops were also measured at 5 K and 250 K (see figure XI). A very small hysteresis was noted in both data sets. The origin of this effect is unknown, however it is not surprising considering the high temperature FC/ZFC divergence noted in this sample (for $T > 250$ K). This is further evidence for spin clustering that occurs in this temperature regime.

Figure XI: Magnetic hysteresis runs at 5K and 250 K. A small temperature dependent hysteresis is observed.



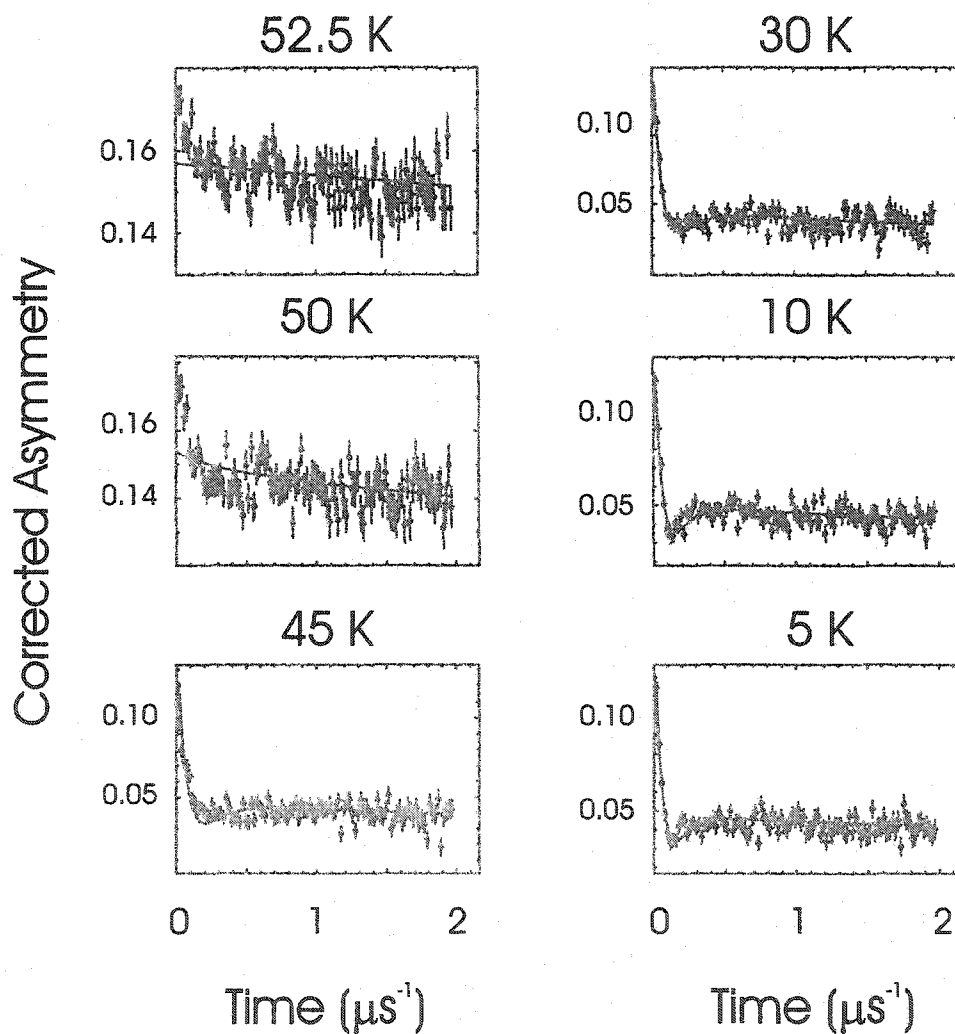
PART C : μ SR MEASUREMENTS

The technique of μ SR is well established as a standard tool in the repertoire of the modern condensed matter physicist. The remarkable sensitivity of the muon to local fields and fluctuations thereof, over a wide range of time scales places μ SR as one of the best

methods to measure quantum magnetism.

Our measurements were taken in a small applied longitudinal field of 65 G at the M15 beamline at TRIUMF in the temperature range $2 \text{ K} < T < 52.5 \text{ K}$; typical spectra are shown in Figure XII. The small field served to decouple any relaxation from nuclear dipole moments (of typical strength of a few gauss) but was weak enough not to affect the relaxation of electronic origin.

Figure XII: LF- μ SR data as a function of temperature. The fits are to Uemura's spin glass function, as described in the text. Note the dramatic change in lineshape above $T_G \sim 50 \text{ K}$.



The spectra at all temperatures were well described by Uemura's spin glass relaxation function ²⁶:

(4)

$$G(t) = \frac{1}{3} \left[\exp \left[- (4\alpha_d^2 t / \nu)^{1/2} \right] \right] + \frac{2}{3} \left[1 - \frac{\alpha_s^2 t^2}{(4\alpha_d^2 t / \nu + \alpha_s^2 t^2)^{1/2}} \right] \exp \left[- (4\alpha_d^2 t / \nu + \alpha_s^2 t^2)^{1/2} \right]$$

where α_s and α_d are the static and dynamic portions of the moment respectively, and ν is the fluctuation rate. The development of a static portion of the moment is apparent from the two-component form of the relaxation seen below about 50 K (see Figure XII). The order parameter is $Q = (\alpha_s/\alpha)^2$

$$(5) \quad Q = \left(\frac{\alpha_s}{\alpha} \right)^2 \quad \text{where } \alpha^2 = \alpha_s^2 + \alpha_d^2$$

As $\alpha_d \rightarrow 0$, the Uemura function reduces to a Lorentzian Kubo-Toyabe function:

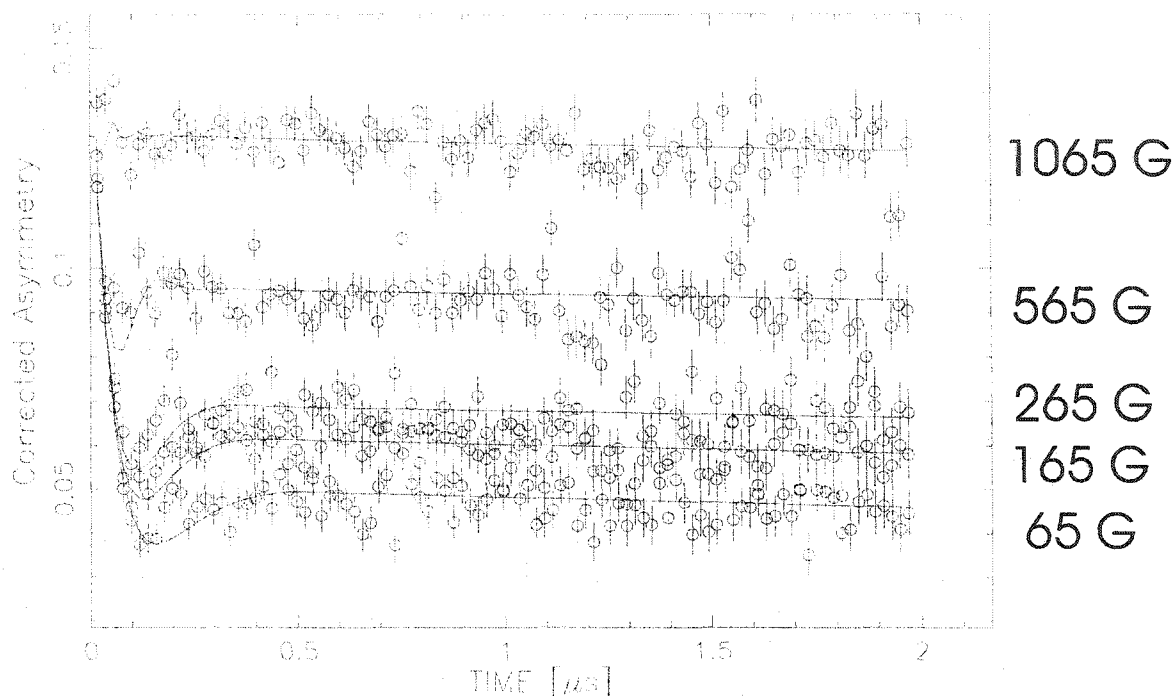
(6)

$$G(t) = \frac{1}{3} + \frac{2}{3} [1 - \alpha_s t] \exp(-\alpha_s t)$$

which is appropriate for a dilute source of randomly aligned magnetic moments. The Lorentzian function gave an essentially identical fit to the low temperature data.

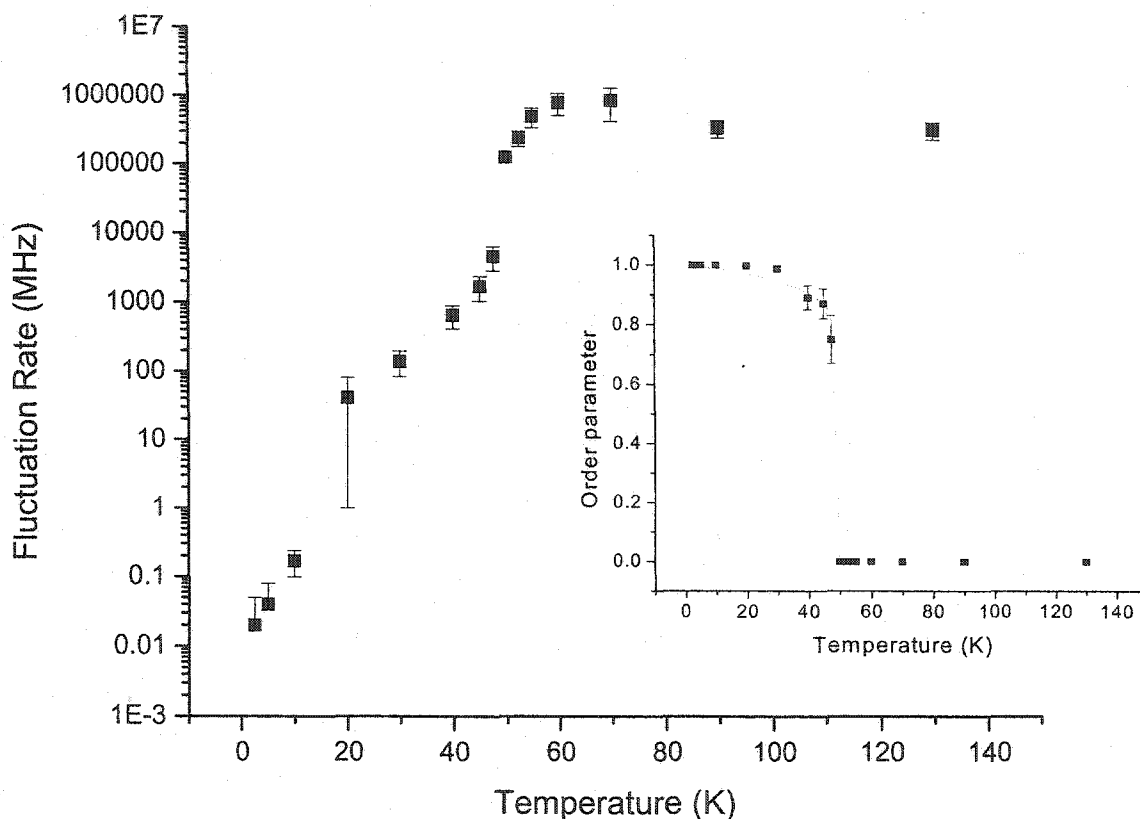
It is worth indicating at this point that several longitudinal field scans were made to confirm the origin of these spectra. Field scans up to 1065 G successfully decoupled the signal, as shown in figure XIII. This directly shows that the response is from the frozen moments within the sample. The fits to the data are Lorentzian, which as suggested above are identical to Uemura's function in the low temperature limit, and easier to handle numerically with a large applied longitudinal field.

Figure XIII: LF- μ SR runs as a function of field at $T = 5$ K. The fits to the data are Lorentzian functions as described in the text. This shows that the signal is successfully decoupled in moderate fields.



The two-component nature of the low temperature spectra is readily apparent from the data and is typical of spin glass behaviour. The appearance of a second component at $T_G \sim 50$ K agrees well with the DC susceptibility measurements that indicate a glass-like state at this temperature. This feature grows over a temperature range of about a decade, in sharp contrast to the situation in $\text{Sr}_2\text{CaReO}_6$, in which the lineshape changes dramatically over a few kelvin. Nonetheless, the extraction of an order parameter, Q , from Uemura's function can be made to illustrate the nearly first-order nature of the transition.

Figure XIV: The fluctuation rate as a function of temperature, indicating moment freezing below T_G . The insert shows the static order parameter, Q , as a function of temperature. The line is a guide to the eye.



As figure XIV shows, the freezing of moments is very abrupt. Power law fits to the order parameter were made to attempt to find the universality class of this material, but no sensible exponents could be found to properly account for the observed behaviour. Figure XIV also displays the fluctuation rate as a function of temperature, which is correlated with the appearance of the static order parameter below T_G . Above T_G , the moments are paramagnetic, leading to a nearly temperature independent fast fluctuating rate. It is quite likely that these measurements are very near, or beyond the detection limits of this

technique. However, at the transition itself, there is a rapid drop in the fluctuation rate. From 50 K to 10 K, there is a decrease of over six orders of magnitude. This is a clear signal for spin freezing. Below 10 K, the fluctuation rate is very small, or virtually undetectable in this limit. This is evident in the flat background of the lineshape, which indicates very slow fluctuations. This is what one would expect for a glassy system: a slowing down of moments over a wide range of frequencies ($\sim 10^8$),²⁷ persistent fluctuations at low temperatures, and a high temperature paramagnetic regime (hence the temperature independent response in the extremes).

In comparison to other spin glasses, such as $\text{Sr}_2\text{CaReO}_6$, the data are qualitatively similar. The spin glass function provides an excellent fit, which is further evidence for spin freezing, and the transition itself is rather abrupt. However, $\text{Sr}_2\text{MgReO}_6$ has a much more pronounced minimum in the spectra. There is also more quantitative evidence in this work which confirms that the material is glassy by showing a dramatic fall of the fluctuation rate below T_G . More measurements are clearly needed in the $\text{Sr}_2\text{CaReO}_6$ material for a proper comparison.

In broader terms, the characteristic spectra of $\text{Sr}_2\text{MgReO}_6$ are very akin to what is seen in other geometrically frustrated spin glasses. $\text{Y}_2\text{Mo}_2\text{O}_7$ has this characteristic at low temperatures, with a pronounced minimum at short time scales and an impressive drop in fluctuation rate below T_G .²⁸ In contrast though, there are significant dynamics above T_G that were later identified by neutron scattering to be due to low energy magnetic excitations. No strong correlation could be found with the high temperature FC/ZFC divergence present in the susceptibility in $\text{Sr}_2\text{MgReO}_6$. If there were short-ranged ordering for example in this sample, this would be present as a weak precession or another spin glass lineshape superimposed upon the spectra. Since no such feature is present, we must conclude that there is none, or at least no such ordering which occurs over time scales accessible to both neutrons and μSR , which is over nine orders of magnitude. Given this information, one may propose that this feature in the susceptibility is due to a "frustration" component, as suggested by Limot's work on SCGO.²⁹ Ga-NMR measurements on this material indicated that magnetic correlations persist up to an intermediate temperature scale of ~ 50 K, which is

very much higher than $T_G \sim 2$ K for SCGO. Evidence for this effect is in a weak maximum in the susceptibility, which has been interpreted as due to strong 2D correlations. Likewise, the effects seen in $\text{Sr}_2\text{MgReO}_6$ at ~ 175 K may be due to the weak magnetism associated with the frustrated 3D FCC lattice, although an analytical term which can describe such a feature in the quantum limit is unknown. The absence of such a term in the magnetic susceptibility of $\text{Sr}_2\text{CaReO}_6$ suggests that the anisotropy in $\text{Sr}_2\text{MgReO}_6$ may play a role. Indeed, the preferential exchange path along the c-axis may induce some one dimensional character to the magnetism which manifests itself in the magnetic susceptibility. It is difficult to discern the origin of the response without further measurements though.

PART D : HEAT CAPACITY MEASUREMENTS

Heat capacity measurements of $\text{Sr}_2\text{MgReO}_6$ are shown in figure XV. As shown in the insert, the low temperature behaviour follows the empirical law

(7)

$$C(T) = \gamma T + \beta T^3$$

where $\gamma = 1.89(24)$ mJ/(K²mol) and $\beta = 0.361(2)$ mJ/(K⁴mol). This is comparable to what is observed in other magnetic insulators such as $\text{Li}_4\text{MgReO}_6$.³⁰ However, the γ component for $\text{Li}_4\text{MgReO}_6$ is larger, which has been interpreted as a signature of the linear specific heat dependence observed in spin glasses. No such term is observed in $\text{Sr}_2\text{MgReO}_6$.

Upon inspection, it appears that there is no sharp magnetic anomaly in the heat capacity. Once more, the field scans up to 1 T do not reveal any new features, confirming that the magnetism is weak. However, the ordered perovskite Sr_2MgWO_6 was prepared as a lattice standard to properly calculate the magnetic component of the specific heat. This material was synthesized by combining stoichiometric amounts of SrCO_3 (99.999%, Cerac), MgCO_3 (99.999%, Cerac), and WO_3 (99.98%, Alfa-Aesar), pressing the mixture into pellets, and firing at 1350° C in air. The resulting product was confirmed to be single phase and isostructural to $\text{Sr}_2\text{MgReO}_6$ by x-ray diffraction (see table I). This lattice standard was

measured using the same method as $\text{Sr}_2\text{MgReO}_6$. A sample mass of 9.80 mg was mounted with a small portion of Wakefield grease upon the sample stage. The experiments were performed over the same temperature range.

Figure XV: The heat capacity as a function of temperature and field for $\text{Sr}_2\text{MgReO}_6$. The insert is a fit to $C = \gamma T + \beta T^3$, with $\gamma = 1.89(24)$ mJ/(K²mol) and $\beta = 0.361(2)$ mJ/(K⁴ mol).

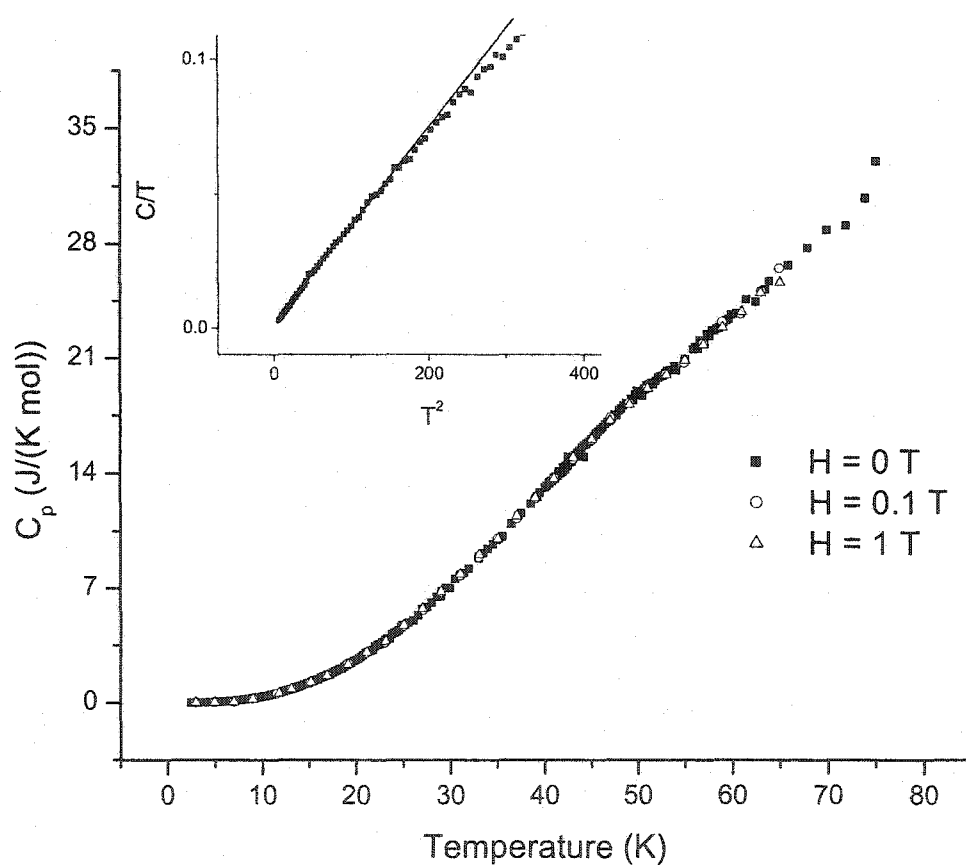
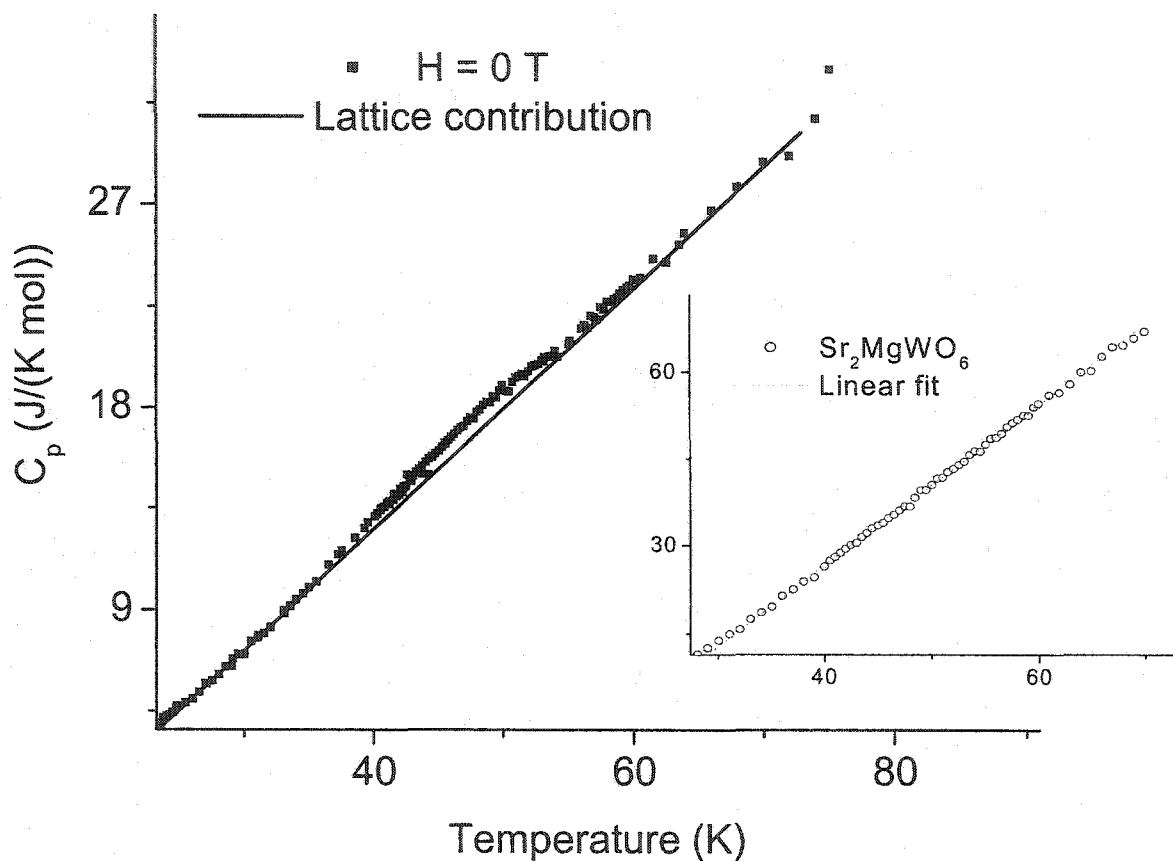


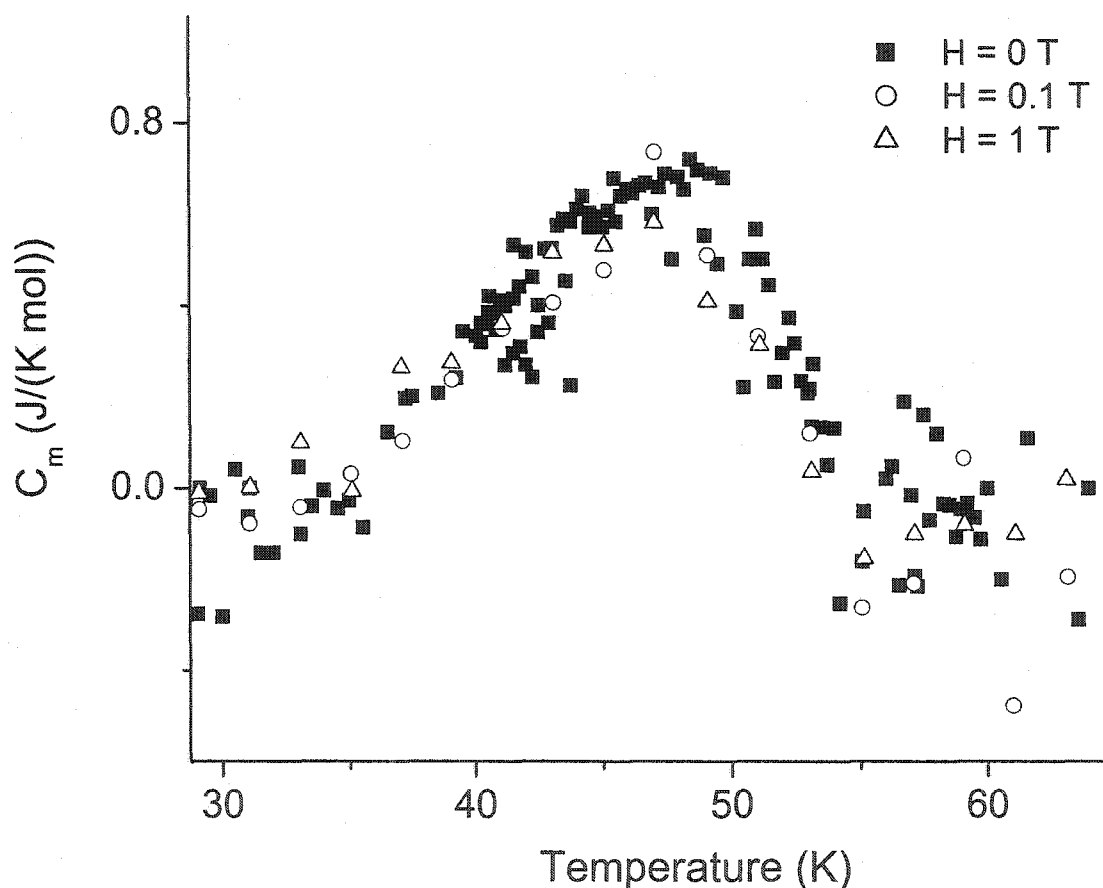
Figure XVI: The scaled lattice component is plotted with the raw data, suggesting that a weak magnetic component is present. The insert shows the linear dependence of the lattice standard Sr_2MgWO_6 as a function of temperature.



The resulting heat capacity is shown in figure XVI. A scaled lattice portion was calculated and subtracted from the total heat capacity of $\text{Sr}_2\text{MgReO}_6$. It is now clear that there is an anomaly in the vicinity of $T_G \sim 50 \text{ K}$. However, the feature is very weak and it is difficult to determine a proper lineshape to describe the transition. A lambda-like anomaly would be indicative of long range ordering for example, whereas a broad distribution would be more suggestive of spin glassiness. In this case, it is clear that there is no long-range order, as there are no magnetic Bragg peaks at low temperatures, no saturation of the

magnetic moment from the DC susceptibility, characteristic glassy behaviour from μ SR measurements, and now a broad feature in the heat capacity at $T_G \sim 50$ K.

Figure XVII: The magnetic specific heat, as determined by a subtraction of the lattice portion. Note the unchanged feature as a function of field.



It is interesting to note that there appears to be very little change in the magnetic heat capacity as a function of applied field (figure XVII). This result was seen in the Ca analogue, which had a very broad field-independent specific heat anomaly centered at $T_G \sim 14$ K. The layered kagomé system SCGO also has such a feature, which shows a similar robustness under applied fields. Ramirez *et al.* have suggested that such a response is

typical of what is seen in spin-singlet stabilized ground states, which would be impervious to high magnetic fields due the dynamic nature of the quantum system.³¹ If this is true, then this is tantalizing evidence that $\text{Sr}_2\text{CaReO}_6$ and $\text{Sr}_2\text{MgReO}_6$ have singlet magnetism playing a crucial role at low temperatures. The effect is greater in the Ca analogue, which has a larger entropy removal at low temperatures ($\sim 65\%$), presumably due to the isotropic exchange pathways. In $\text{Sr}_2\text{MgReO}_6$, the entropy removal, as calculated from integrating the magnetic component of the heat capacity from 30 K to 60 K:

(8)

$$S = \int_0^T (C_m / T) dT$$

is extremely small : 0.16738 J/(mol K). This is only about 3 % of the ideal amount of $R \ln (2S+1) = 5.7628 \text{ J}/(\text{mol K})$. However, it is comparable to what is observed in the jarosite $(\text{H}_3\text{O})\text{Fe}_3(\text{SO}_4)_2(\text{OH})_6$, which has $\sim 6\%$ entropy removal from the magnetic transition.³² In contrast though, there is no broad anomaly at the transition in this material. In spite of this absence, $(\text{H}_3\text{O})\text{Fe}_3(\text{SO}_4)_2(\text{OH})_6$ is characterized as a spin glass with $T_G \sim 19 \text{ K}$, and only short-ranged order at low temperatures. The spin-fluid nature of this material is evident in the T^2 heat capacity dependence at low temperatures. A power law dependence of $\text{Sr}_2\text{MgReO}_6$ cannot be made in comparison, as the anomaly is very weak, and does not persist to low temperatures.

As a final note, one can now readily compare the $S=1/2$ systems to their $S=1$ analogues to emphasize the role that quantum spins play upon frustrated lattices. Both $S=1$ materials Sr_2NiWO_6 and $\text{Sr}_2\text{NiTeO}_6$ entered a long range ordered state at $T_N = 54 \text{ K}$ and 28 K respectively. In contrast, the $S=1/2$ materials show glassy transitions at $T_G = 50 \text{ K}$ and 14 K for $\text{Sr}_2\text{CaReO}_6$ and $\text{Sr}_2\text{MgReO}_6$ respectively. The similarities between the two “ordering” temperatures re-enforce the close structural relationships of the two families of compounds. It is remarkable that the two sets of compounds show similar ordering temperatures yet the $S=1/2$ systems show no long range magnetic ordering. If we are indeed investigating the quantum limit, it may be that this is due to the formation of a liquid-like ground state. As

mentioned before, the lack of a response of the magnetic heat capacity as a function of field has been classified as a fingerprint of a spin singlet ground state. Although this conclusion cannot be reached in this study for the $S = 1/2$ $\text{Sr}_2\text{MgReO}_6$ (and $\text{Sr}_2\text{CaReO}_6$ previously reported) there is certainly adequate proof that glassy behaviour is observed in the absence of chemical disorder, which is markedly different from the $S=1$ cases. Further experiments, are required to elucidate the role of quantum magnetism in these $S=1/2$ compounds.

CONCLUSIONS

The B-site ordered $S=1/2$ FCC perovskite, $\text{Sr}_2\text{MgReO}_6$, has been synthesized and characterized to be a spin glass with $T_G \sim 50$ K. However, several unusual features, such as a mysterious broad maximum in the susceptibility at ~ 175 K (seen at low applied fields), and evidence for a weak but field-independent heat capacity anomaly at T_G suggest that there is much left to be understood in this material. The susceptibility anomaly is not echoed in any other measurement, and is hypothesized to be due to one-dimensional spin correlations induced by the strong 180° superexchange paths along c . The specific heat anomaly, which has no visible change upon application of magnetic fields, may be due to singlet magnetism.

ACKNOWLEDGEMENTS

The authors are grateful for the hospitality of Chalk River Labs and TRIUMF during the course of this work. Technical support from Ron Donaberger (Chalk River) and Syd Kreitzman (TRIUMF) is greatly appreciated. C. R. Wiebe would like to acknowledge support through an NSERC PGS B and an OGSST. This work was also supported by grants to J. E. Greedan and G. M. Luke through NSERC, and additional funding to G. M. Luke by the CIAR. The MAGLAB experimental apparatus was purchased through funding from the CFI and ORDCF.

References

- (1) *Magnetic Systems with Competing Interactions*, ed. by H. T. Diep (World Scientific, NY, 1994)
- (2) P. Anderson, *Mat. Res. Bull.*, **8**, 153 (1973).
- (3) J. Orenstein and A. J. Millis, *Science*, **288**, 468 (2001).
- (4) L. O. Manuel and H. A. Ceccatto, *Phys. Rev. B*, **60**, 9489 (1999).
- (5) J. E. Greedan, *Journal of Mat. Chem.*, **11**, 37 (2001).
- (6) C. Lhuillier and G. Misguich, *cond-mat/0109146* (2001).
- (7) B. Canals and C. Lacroix, *Phys. Rev. Lett.*, **80**, 2933 (1998).
- (8) L. Pauling, *The Nature of the Chemical Bond* (Cornell University Press, Ithaca, 1960).
- (9) X. Obradors, A. Labarta, A. Isalgue, J. Tejada, J. Rodriguez, M. Pernet, *Solid State Comm.*, **65**, 189 (1988).
- (10) I. S. Hagemann, Q. Huang, X. P. A. Gao, A. P. Ramirez, R. J. Cava, *Phys. Rev. Lett.*, **86**, 894 (2001).
- (11) J. S. Gardner, B. D. Gaulin, S.-H. Lee, C. Broholm, N. P. Raju, J. E. Greedan, *Phys. Rev. Lett.*, **83**, 211 (1999).
- (12) J. S. Gardner, S. R. Dunsiger, B. D. Gaulin, M. J. P. Gingras, J. E. Greedan, R. F. Kiefl, M. D. Lumsden, W. A. MacFarlane, N. P. Raju, J. E. Sonier, I. Swainson, Z. Tun, *Phys. Rev. Lett.*, **82**, 1012 (1999).
- (13) J. Longo and R. Ward, *J. Am. Chem. Soc.*, **83**, 2816 (1961).
- (14) C. G. Shull, E. O. Wollan, W. A. Strauser, *Phys. Rev.*, **81**, 483 (1950).
- (15) H. Kato, T. Okuda, Y. Okimoto, Y. Tomioka, K. Oikawa, T. Kamiyama, Y. Tokura, *Phys. Rev. B*, **65**, 144404, (2002).
- (16) M. Hanawa, Y. Muraoka, T. Tayama, T. Sakakibara, J. Yamaura, Z. Hiroi, *Phys. Rev. Lett.*, **87**, 187001 (2001).
- (17) C. R. Wiebe, J. E. Greedan, G. M. Luke, J. S. Gardner, *Phys. Rev. B*, **65**, 144413 (2002).

- (18) FULLPROF Version 3.5d (Oct. 98).
- (19) DICVOL Version 24/11/98.
- (20) A. Ferretti, D. B. Rogers, and J. B. Goodenough, *J. Phys. Chem. Solids*, **26**, 2007 (1965).
- (21) R. D. Shannon, *Acta Cryst.* **A32**, 751 (1976).
- (22) V. V. Gagulin, *Segnetoelektriki P'ezoelektriki*, **4**, 128 (1987).
- (23) D. Iwanaga, Y. Inaguma, M. Itoh, *Mat. Res. Bull.*, **35**, 449 (2000).
- (24) M. P. Attfield, P. D. Battle, S. K. Bollen, T. C. Gibb, R. J. Whitehead, *J. Solid State Chem.*, **3**, 591 (1993).
- (25) A. P. Ramirez in *Handbook of Magnetic Materials*, edited by K. H. J. Buschow (North-Holland, Amsterdam, 2001), Vol. 13, p. 423.
- (26) Y. J. Uemura, T. Yamazaki, D. R. Harshman, M. Senba, E. J. Ansaldo, *Phys. Rev. B.*, **31**, 546 (1985).
- (27) J. A. Mydosh, *Spin Glasses, An Experimental Introduction* (Taylor and Francis, London, 1993).
- (28) S. R. Dunsiger, R. F. Kiefl, K. H. Chow, B. D. Gaulin, M. J. P. Gingras, J. E. Greedan, A. Keren, K. Kojima, G. M. Luke, W. A. MacFarlane, N. P. Raju, J. E. Sonier, Y. J. Uemura, W. D. Wu, *Phys. Rev. B*, **54**, 9019 (1996).
- (29) L. Limot, P. Mendels, G. Collin, C. Mondelli, B. Ouladdiaf, H. Mutka, N. Blanchard, M. Mekata, *cond.-mat./0111540* (2002).
- (30) M. Bieringer, N. P. Raju, G. M. Luke, J. E. Greedan, *Phys. Rev. B*, **62**, 6521 (2000).
- (31) A. P. Ramirez, B. Hessen, M. Winkelmann, *Phys. Rev. Lett.*, **84**, 2857 (2000).
- (32) A. S. Wills, A. Harrison, S. A. M. Mentink, T. E. Mason, Z. Tun, *Europhys. Lett.*, **42**, 325 (1998).

Chapter Seven

Conclusions

A variety of different techniques (x-ray and neutron diffraction, DC magnetic susceptibility, heat capacity, and μ SR experiments) have been employed to investigate the magnetic properties of several perovskite-based materials. The first two materials, $\text{CaMnO}_{3-\delta}$ and $\text{La}_5\text{Re}_3\text{MnO}_{16}$, were found to adopt long range ordered magnetic ground states, while the latter two, $\text{Sr}_2\text{CaReO}_6$ and $\text{Sr}_2\text{MgReO}_6$ were found to exhibit unconventional spin frozen ground states (due to the geometric frustration of the FCC lattice).

Several important questions were addressed with the study of $\text{CaMnO}_{3-\delta}$. One very basic result was a simple confirmation of the G-type structure which was solved for the end member of the series CaMnO_3 (by Wollan and Koehler nearly 40 years ago) and expected for the lightly doped material $\text{CaMnO}_{2.94}$. Surprisingly, there are very few recent magnetic structure determinations of the undoped parent material. Another important result is the existence of a charge-ordered phase for $\text{CaMnO}_{2.89}$. It is remarkable that such a phase coexists with the G-type ordered structure. This charge ordering may play a role in the dramatic increase in the MR of this material (from 20 % in $\text{CaMnO}_{2.94}$ to 40 % in

CaMnO_{2.89}), but the mechanism for such an increase is unknown. The existence of a small impurity phase, which was only detected with the long wavelength neutron diffraction experiments in this thesis, may also be important.

The “pillared perovskite” material La₅Re₃MnO₁₆ is the first in a new series of materials based upon perovskite-like layers of ReO and MnO octahedra and Re₂O₁₀ dimers. Single crystal x-ray diffraction data, taken with the appropriate absorption corrections, have been used to determine the crystal structure. The very short Re-Re bond distance of 2.4068(5) Å suggests that a Re-Re double bond may be present in the dimers which separate the perovskite layers. Despite the large distances between the layers of about 10 Å, the material is found to order at T_N ~161 K. The magnetic structure, which is detailed in the appendix, was determined to be a simple A-type stacking along the c-direction, with a slight spin canting. The appearance of a few weak Bragg peaks at lower temperatures may be indicative of a spin-reorientation within the layers. Future work by Dr. Chi of the Greedan group has recently shown that one can easily substitute ions within the perovskite layer to form the series La₅Re₃XO₁₆ (X = Fe, Ni, Co, and Mg). All of these materials, except for the Mg, exhibit long range ordered ground states. The Mg material may be geometrically frustrated, and is worthy of more in depth studies.

The last topic of this thesis concerns the ordered FCC S=1/2 perovskites Sr₂XReO₆ (X = Ca, Mg). These materials were synthesized to investigate the effects of quantum magnetism upon a frustrated lattice. Sr₂CaReO₆ is monoclinic, whereas Sr₂MgReO₆ is tetragonal. Both of these were found to exhibit spin-freezing at T_G ~14 K (Sr₂CaReO₆) and T_G ~50 K (Sr₂MgReO₆), as evidenced by irreversibilities in the DC magnetic susceptibility, the absence of long range order by elastic neutron scattering measurements, broad heat capacity anomalies, and μ SR lineshapes characteristic of spin glasses. It is worth noting that the spin glass transition temperature of ~50 K for Sr₂MgReO₆ is unusually high, and uncharacteristic of frustrated systems. Several other unconventional properties were discovered, such as a T³ magnetic specific heat dependence for Sr₂CaReO₆, and field independent heat capacity anomalies for both materials. This suggests that interesting spin dynamics may be present, such as those commonly found for spin liquid like ground states.

A comparison is made with two analogous $S=1$ materials, $\text{Sr}_2\text{NiTeO}_6$ and Sr_2NiWO_6 , which order at $T_N \sim 28$ K and $T_N \sim 54$ K respectively. The quantum nature of the $S=1/2$ materials is hypothesized to be driving the transition to new magnetic ground states which are a direct consequence of the geometric frustration inherent in the lattice.